

EARTHQUAKE CHARACTERISTICS AS IMAGED BY THE
BACK-PROJECTION METHOD

A dissertation presented

by

Eric Daniel Kiser

to

The Department of Earth and Planetary Sciences

in partial fulfillment of the requirements

for the degree of

Doctor of Philosophy

in the subject of

Earth and Planetary Sciences

Harvard University

Cambridge, Massachusetts

April 2012

©2012 Eric Daniel Kiser

All rights reserved.

EARTHQUAKE CHARACTERISTICS AS IMAGED BY THE BACK-PROJECTION METHOD

ABSTRACT

This dissertation explores the capability of dense seismic array data for imaging the rupture properties of earthquake sources using a method known as back-projection. Only within the past 10 or 15 years has implementation of the method become feasible through the development of large aperture seismic arrays such as the High Sensitivity Seismograph Network in Japan and the Transportable Array in the United States. Coincidentally, this buildup in data coverage has also been accompanied by a global cluster of giant earthquakes ($M_w > 8.0$). Much of the material in this thesis is devoted to imaging the source complexity of these large events. In particular, evidence for rupture segmentation, dynamic triggering, and frequency dependent energy release is presented. These observations have substantial implications for evaluating the seismic and tsunami hazards of future large earthquakes.

In many cases, the details of the large ruptures can only be imaged by the back-projection method through the addition of different data sets and incorporating additional processing steps that enhance low-amplitude signals. These improvements to resolution can also be utilized to study much smaller events. This approach is taken for studying two very different types of earthquakes. First, a global study of the enigmatic intermediate-depth (100-300 km) earthquakes is performed. The results show that these events commonly have sub-horizontal rupture planes and suggest

dynamic triggering of multiple sub-events. From these observations, a hypothesis for the generation of intermediate-depth events is proposed. Second, the early aftershock sequences of the 2004 Mw 9.1 Sumatra-Andaman and 2011 Mw 9.0 Tohoku, Japan earthquakes are studied using the back-projection method. These analyses show that many events can be detected that are not in any local or global earthquake catalogues. In particular, the locations of aftershocks in the back-projection results of the 2011 Tohoku sequence fill in gaps in the aftershock distribution of the Japan Meteorological Agency catalogue. These results may change inferences of the behavior of the 2011 mainshock, as well as the nature of future seismicity in this region. In addition, the rupture areas of the largest aftershocks can be determined, and compared to the rupture area of the mainshock. For the Tohoku event, this comparison reveals that the aftershocks contribute significantly to the cumulative failure area of the subduction interface. This result implies that future megathrust events in this region can have larger magnitudes than the 2011 event.

CONTENTS

ABSTRACT	iii
CONTENTS	v
LIST OF FIGURES	ix
LIST OF TABLES	xiii
ACKNOWLEDGEMENTS	xiv
1 INTRODUCTION	1
2 METHOD AND DATA	7
2.1 Introduction	7
2.2 The Back-Projection Method	8
2.2.1 Empirical Corrections	9
2.2.2 Combining Seismic Phases	11
2.2.3 Combining Seismic Arrays	13
2.2.4 The Coherency Function	15
2.3 Seismic Array Data	16
2.3.1 The High Sensitivity Seismograph Network	17
2.3.2 The USArray Transportable Array	17
2.3.3 Additional Seismic Networks	18

3	INTERMEDIATE-DEPTH EARTHQUAKES	19
3.1	Introduction	19
3.2	Data and Data Processing	21
3.3	Results	25
3.3.1	Tonga-Kermadec	26
3.3.2	Vanuatu	27
3.3.3	Hindu Kush	32
3.3.4	Java	32
3.3.5	Alaska	35
3.4	Discussion	37
3.4.1	Robustness of Composite Ruptures	39
3.4.2	Properties of Composite Ruptures	44
3.4.3	Depth Variation of Individual Subevents	46
3.5	The Proposed Mechanism of Intermediate-Depth Earthquakes	47
3.5.1	Possible Fault Orientations	48
3.5.2	Previously Proposed Mechanisms	49
3.5.3	Proposed Mechanism for Intermediate-Depth Earthquakes	52
3.6	Summary	57
4	SEGMENTATION	58
4.1	Introduction	58
4.2	Data and Data Processing	59
4.3	Results and Discussion	60
4.3.1	The 2007 August 15 Mw 8.0 Pisco, Peru Earthquake	62
4.3.2	The 2007 September 12 Mw 8.4 and Mw 7.9 Mentawai Islands, West Sumatra Earthquakes	63

4.3.3	The 2009 September 29 Mw 8.1 Samoa Islands Earthquake . . .	66
4.3.4	The 2010 February 27 Mw 8.8 Maule, Chile Earthquake	70
4.3.5	Triggered Slip on Adjacent Segments	71
4.3.6	High-Frequency Energy and the Seismogenic Zone	73
4.4	Summary	74
5	FREQUENCY-DEPENDENCE	75
5.1	Introduction	75
5.2	The 2010 Mw 8.8 Maule, Chile Earthquake	76
5.2.1	Data and Data Processing	76
5.2.2	Results	78
5.3	The 2011 Mw 9.0 Tohoku, Japan Earthquake	84
5.3.1	Data and Data Processing	86
5.3.2	Results	88
5.4	Summary	94
6	AFTERSHOCK DETECTION	96
6.1	Introduction	96
6.2	2011 Tohoku, Japan Aftershock Sequence	97
6.2.1	Data and Data Processing	97
6.2.2	Large Aftershocks and Interface Failure	98
6.2.3	The First 25 Hours of Aftershocks	103
6.2.4	Comparison with the JMA Catalogue	104
6.2.5	Waveforms from Undetected Events in Local Data	112
6.2.6	Comparison with the NEIC Catalogue	115
6.3	2004 Sumatra Aftershock Sequence	116
6.3.1	Data and Data Processing	117

6.3.2	The First Hour and a Half	117
6.3.3	Comparison with the NEIC Catalogue	117
6.3.4	Coseismic Aftershocks	118
6.4	Summary	123
7	FUTURE WORK	125
7.1	The Back-Projection Method	125
7.2	Deep Earthquakes	126
7.3	Understanding Rupture Complexity	126
	Appendices	128
A	RESOLUTION	128
A.1	Introduction	128
A.2	Lateral Resolution	128
A.2.1	Distance and Azimuth Coverage	129
A.2.2	Regional Lateral Resolution	133
A.3	Depth and Time Resolution	138
A.3.1	Synthetic Ruptures in Depth and Time	140
A.4	Low Amplitude Detection	142
A.5	The Horizontal Plane Setup	144
A.6	The Effect of Depth Phases on Shallow Events	145
A.7	Directivity	147
A.8	Summary	151
B	TABLES OF MARCH 11TH AND 12TH TOHOKU EVENTS	153
	BIBLIOGRAPHY	177

LIST OF FIGURES

Figure 2.1	STACKS OF SEISMIC PHASES	14
Figure 2.2	HI-NET STATION DISTRIBUTION	17
Figure 2.3	TA STATION DISTRIBUTION	18
Figure 3.1	EARTHQUAKE DISTRIBUTION VS. DEPTH	20
Figure 3.2	EFFECT OF THE TAPER FUNCTION	24
Figure 3.3	SEISMIC PHASES AND DISTRIBUTION OF INTERMEDIATE-DEPTH EARTHQUAKES	26
Figure 3.4	TONGA-KERMADEC EARTHQUAKES	28
Figure 3.5	VANUATU EARTHQUAKES	30
Figure 3.6	HINDU KUSH EARTHQUAKES	33
Figure 3.7	JAVA EARTHQUAKES	35
Figure 3.8	ALASKA EARTHQUAKE	37
Figure 3.9	SYNTHETIC TRIGGERING	40
Figure 3.10	SYNTHETIC TEST WITH A COMPLEX SOURCE-TIME FUNCTION	41
Figure 3.11	EFFECTS OF THE CRUST AND WATER LAYERS	43
Figure 3.12	DYNAMIC TRIGGERING	46
Figure 3.13	PROPOSED MECHANISM	56
Figure 4.1	COMBINING STACKS	60
Figure 4.2	RAY PATHS OF P AND CORE PHASES	61

Figure 4.3	THE AUGUST 15, 2007 PISCO, PERU EARTHQUAKE	64
Figure 4.4	THE SEPTEMBER 12, 2007 MW 8.4 MENTAWAI ISLANDS EARTHQUAKE	65
Figure 4.5	THE SEPTEMBER 12, 2007 MW 7.9 MENTAWAI ISLANDS EARTHQUAKE	67
Figure 4.6	THE SEPTEMBER 29, 2009 SAMOA ISLANDS EARTHQUAKE .	69
Figure 4.7	THE FEBRUARY 27, 2010 MAULE, CHILE EARTHQUAKE . .	72
Figure 5.1	MAULE MAINSHOCK SOURCE REGION AND DATA	77
Figure 5.2	ALIGNED SEISMOGRAMS FROM THE FEBRUARY 27, 2010 CHILE EARTHQUAKE	79
Figure 5.3	IMAGED ENERGY AT HIGH FREQUENCIES FOR THE MAULE MAINSHOCK	81
Figure 5.4	HIGH- (1-5 Hz) AND INTERMEDIATE- (0.5-1 Hz) FREQUENCY BACK-PROJECTION RESULTS FOR THE MAULE MAINSHOCK	83
Figure 5.5	NORTHERN AND SOUTHERN SEGMENTS OF THE 2010 CHILEAN EARTHQUAKE	84
Figure 5.6	COMPARISON BETWEEN THE HIGHEST AND LOWEST FRE- QUENCY BACK-PROJECTION RESULTS FOR THE MAULE MAINSHOCK	85
Figure 5.7	INDIVIDUAL HI-NET, F-NET, AND TA BACK-PROJECTION RESULTS FOR THE MAULE MAINSHOCK	85
Figure 5.8	TOHOKU SOURCE REGION AND DATA COVERAGE	87
Figure 5.9	TOHOKU MAINSHOCK RESULTS	90
Figure 5.10	FREQUENCY DEPENDENCE IN LONGITUDE AND TIME	91
Figure 5.11	TOHOKU TOTAL RUPTURE AREA	93
Figure 6.1	TOHOKU PLATE INTERFACE FAILURE	99

Figure 6.2	RUPTURE AREAS OF FORESHOCKS AND AFTERSHOCKS . . .	101
Figure 6.3	TRIGGERED SEISMICITY	102
Figure 6.4	PROCEDURE FOR AFTERSHOCK PICKING	105
Figure 6.5	DISTRIBUTION OF BACK-PROJECTION AFTERSHOCKS	106
Figure 6.6	SEISMICITY RATE OF BACK-PROJECTION AFTERSHOCKS . .	106
Figure 6.7	DISTANCE, AZIMUTH, AND TIME BETWEEN JMA AND DE- TECTED BACK-PROJECTION AFTERSHOCKS	108
Figure 6.8	COMPARISON OF JMA MAGNITUDE AND DETECTED BACK- PROJECTION EVENT AMPLITUDES	108
Figure 6.9	NUMBER OF EVENTS VS. NOISE-TO-SIGNAL RATIO	109
Figure 6.10	PERCENTAGE OF UNDETECTED EVENTS VS. TIME	110
Figure 6.11	JMA AFTERSHOCKS NOT DETECTED BY THE BACK-PROJECTION TECHNIQUE	110
Figure 6.12	MAGNITUDE OF UNDETECTED JMA EARTHQUAKES	111
Figure 6.13	ADDING BACK-PROJECTION EVENTS TO THE JMA CATA- LOGUE	112
Figure 6.14	LOCAL DATA FOR AN EVENT IN THE JMA CATALOGUE . .	113
Figure 6.15	LOCAL DATA FOR AN EVENT NOT IN THE JMA CATALOGUE	114
Figure 6.16	NEIC MAGNITUDE OF DETECTED BACK-PROJECTION EARTH- QUAKES	115
Figure 6.17	COMPARISON OF BACK-PROJECTION EVENTS TO THE NEIC CATALOGUE	116
Figure 6.18	2004 SUMATRA AFTERSHOCK SEQUENCE	118
Figure 6.19	THE FIRST AFTERSHOCK OF THE 2004 SUMATRA EARTH- QUAKE	119
Figure 6.20	TIME-DEPENDENT DETECTION: MAGNITUDE 6.8	121

Figure 6.21	TIME-DEPENDENT DETECTION: MAGNITUDE 7.4	122
Figure 6.22	DETECTION CAPABILITY SUMMARY	123
Figure A.1	SYNTHETIC SEISMOGRAM	130
Figure A.2	EFFECTS OF DISTANCE AND AZIMUTH COVERAGE	132
Figure A.3	PERU SYNTHETIC TESTS	135
Figure A.4	MENTAWAI ISLANDS SYNTHETIC TESTS	136
Figure A.5	SAMOA ISLANDS SYNTHETIC TESTS	138
Figure A.6	MAULE, CHILE SYNTHETIC TESTS	139
Figure A.7	DEPTH-TIME RESOLUTION	141
Figure A.8	SYNTHETIC RUPTURES	143
Figure A.9	LOW AMPLITUDE DETECTION	144
Figure A.10	CARTOON OF HORIZONTAL PLANE ASSUMPTION	146
Figure A.11	THE HORIZONTAL PLANE SETUP	146
Figure A.12	BACK-PROJECTION RESULTS USING AFTERSHOCK WAVEFORMS	148
Figure A.13	POINT SOURCE ENERGY KERNELS	149
Figure A.14	TA DIRECTIVITY	150
Figure A.15	HI-NET AND F-NET DIRECTIVITY	152

LIST OF TABLES

Table 3.1	TONGA EARTHQUAKES	29
Table 3.2	VANUATU EARTHQUAKES	31
Table 3.3	HINDU KUSH EARTHQUAKES	34
Table 3.4	JAVA EARTHQUAKES	36
Table 3.5	ALASKA EARTHQUAKE	38
Table B.1	MARCH 11TH TOHOKU BACK-PROJECTION AFTERSHOCKS .	153
Table B.2	MARCH 12TH TOHOKU BACK-PROJECTION AFTERSHOCKS .	173

ACKNOWLEDGEMENTS

This dissertation would not have been possible without the support of my family and friends. Since my first day in graduate school, my advisor, Miaki Ishii, has been patient with me and enthusiastic about my research. Her guidance has made my time at Harvard a very enjoyable and memorable experience. I thank my parents for always encouraging me to strive for excellence in everything I do. These lessons have served me well throughout my academic career. I am also grateful to my older brother for his invaluable advice during my undergraduate and graduate studies. Finally, I would like to thank my wife, Amanda Hughes, for her constant love and support.

CHAPTER 1

INTRODUCTION

The past decade has seen a cluster of large earthquakes around the world. The effects of these events, which include strong ground shaking, the generation of tsunami waves, and triggering of aftershock sequences, have been devastating, with around 260,000 fatalities and billions of dollars in economic loss (<http://earthquake.usgs.gov>). This cluster of events is not unusual when compared to the last century of seismicity. For example, during the fifteen years between 1950 and 1965 there was a similar cluster of giant earthquakes, which included two of the three largest recorded events, the 1964 Mw 9.2 Prince William Sound, Alaska and 1960 Mw 9.5 Chile earthquakes [Kanamori, 1977]. Though this cluster has been thoroughly studied [e.g., Wyss and Brune, 1967; Kanamori, 1970, 1977; Fukao and Furumoto, 1979; Ruff and Kanamori, 1983; Barrientos and Ward, 1990; Johnson and Satake, 1993; Christensen and Beck, 1994; Johnson et al., 1994; Lorenzo-Martin et al., 2006], limited data coverage for much of this time period only allows for very general information of earthquake characteristics to be determined (e.g., focal mechanisms, body and surface wave magnitudes, and rupture duration). A more indirect way of studying these events is to make interpretations of the mainshock ruptures by evaluating the locations of aftershocks with respect to hypocenters of the mainshocks. The distribution of aftershocks was, and still is, used

to estimate the rupture areas of the mainshocks, and guided many of the assumptions and conclusions made in these studies [e.g., Wyss and Brune, 1967; Kanamori, 1970, 1977; Fukao and Furumoto, 1979; Ruff and Kanamori, 1983; Johnson and Satake, 1993; Christensen and Beck, 1994; Johnson et al., 1994].

The World Wide Standardized Seismographic Network (WWSSN) was deployed in the early 1960's and greatly increased the data sets of the later earthquakes in the 1950's and 1960's giant earthquake cluster. The improved station coverage allowed for a more detailed study of the 1964 Mw 9.2 Prince William Sound, Alaska earthquake than other events in this cluster. In particular, estimates on the rupture direction and distribution of moment release with time were greatly improved [e.g., Kanamori, 1970; Christensen and Beck, 1994].

During the next 40 years between giant earthquake clusters, advances were made in the methods used for studying earthquake properties [e.g., Brune, 1970; Dziewoński et al., 1981; Hartzell and Helmberger, 1982; Olson and Apsel, 1982; Dziewoński and Woodhouse, 1983; Boatwright and Choy, 1986; Cohee and Beroza, 1994; Cotton and Campillo, 1995; Zeng and Anderson, 1996; Sekiguchi et al., 1996; Antolik et al., 1999; Ji et al., 2002; Frankel, 2004; Venkataraman and Kanamori, 2004]. The most popular genre of methods that were developed during this time was slip modeling, in which seismic data are inverted for slip on a predetermined fault plane [e.g., Hartzell and Helmberger, 1982; Olson and Apsel, 1982; Cohee and Beroza, 1994; Cotton and Campillo, 1995; Zeng and Anderson, 1996; Sekiguchi et al., 1996; Antolik et al., 1999; Ji et al., 2002; Frankel, 2004]. This approach can provide detailed estimates for the spatial and temporal evolution of slip that adequately matches the data, however, there are certain drawbacks to this modeling approach [e.g., Olson and Apsel, 1982; Hartzell and Heaton, 1983; Beresnev, 2003; Mai et al., 2007; Lay et al., 2010a]. For example, rupture constraints commonly have to be applied to stabilize the inversion.

These constraints vary from the rupture velocity to the orientation and dimensions of the fault onto which slip is modeled. Differences in these subjective decisions can lead to dramatic changes in the distribution of slip [e.g., Beresnev, 2003].

In addition to improvements in the methods used for studying earthquakes, the 40 years of relative seismic quiescence saw a dramatic increase in the number, distribution, and quality of seismic data. One highlight of this expansion was the development of the Global Seismographic Network (GSN) in the late 1980's. As the name suggests, this network is distributed throughout the world and currently has around 190 stations. An additional milestone in the increase of seismic data occurred with the development of the High Sensitivity Seismograph Network (Hi-net) in Japan following the 1995 Kobe earthquake [Okada et al., 2004; Obara et al., 2005]. This network, which can more accurately be described as an array, currently has around 800 stations distributed throughout Japan. It was the development of this array, as well as others like it, that allowed for the first application of the back-projection method used throughout this dissertation.

The main ideas behind back-projection, which utilizes the coherency of waveforms within seismic arrays to image the source of seismic waves, have been used in the oil industry for decades for imaging impedance contrasts in the subsurface [e.g., Claerbout, 1976]. In fact, applications of these ideas for earthquake source studies began in the 1980's for relatively small local earthquakes with varying degrees of success [e.g., McMechan et al., 1985]. Despite these early efforts, array processing techniques only became commonplace in earthquake source studies after three significant occurrences. The first of these has already been discussed, and was the development of dense, large aperture seismic arrays, such as the Hi-net array in Japan. The second was to develop an array processing technique that utilized teleseismic data. This approach allows for the detailed study of earthquakes from around the world, instead

of just in areas which happen to have a dense seismic array, and is one of the key elements that distinguishes the back-projection method from its predecessors [Ishii et al., 2005]. The final occurrence was the 2004 Mw 9.1 Sumatra-Andaman earthquake. Using teleseismic Hi-net data, the enormous 1300 km long rupture was imaged in the first back-projection analysis [Ishii et al., 2005]. The Ishii et al. [2005] study demonstrated the two major advantages of the back-projection method. First, the method requires very little *a priori* information to be implemented. This means that many of the rupture properties that are imposed in the slip modeling approaches can be directly estimated from the back-projection results. The second advantage of the back-projection method is that it is fast, and therefore, if implemented in near-real time, could be very useful for mitigating seismic hazards following large earthquakes. This second point initially gained the most appreciation throughout the earth science community, though a large amount of work is still needed to implement such a system. Following the pioneering study of Ishii et al. [2005], the back-projection method has been modified and applied to earthquakes from a variety of locations [e.g., Walker et al., 2005; Ishii et al., 2007; Nelson et al., 2008; Honda and Aoi, 2009; Walker and Shearer, 2009; D’Amico et al., 2010; Kiser and Ishii, 2011; Kiser et al., 2011; Meng et al., 2011; Wang and Mori, 2011a; Kiser and Ishii, 2012a,b]. The general trend of these studies has been to add more processing steps and combinations of data to the back-projection analysis to improve resolution and image small-scale details of rupture [e.g., D’Amico et al., 2010; Kiser et al., 2011].

This emphasis on complex rupture behavior is understandable given the diverse subjects to which this information can be applied. Perhaps the most important of these topics is evaluating the seismic gap hypothesis [e.g., McCann et al., 1979]. This hypothesis argues that the strain accumulated along the plate interface of subduction zones is released through a series of large earthquakes, and therefore gaps in the

distribution of recent, large ruptures can be interpreted as regions with the highest seismic potential. This simple view of subduction zones has been subjected to considerable scrutiny in recent years. For example, GPS studies have revealed large spatial variations in the amount of coupling along plate interfaces, and in certain regions, the strain needed to generate large events will either never accumulate or take a much longer time than expected based upon the convergence rate [e.g., Fournier and Freymueller, 2007; Chlieh et al., 2008; Loveless and Meade, 2010; Moreno et al., 2010]. In addition, multiple studies have revealed the importance of post-seismic deformation following large earthquakes for releasing significant strain in areas adjacent to the mainshock rupture area [e.g., Perfettini et al., 2010]. These additional features of the subduction zones lead to a very complex spatial and temporal distribution of strain release, and requires detailed descriptions of the rupture process to adequately evaluate how the strain release from seismic events fits into this system.

Detailed analyses of rupture behavior are also critical for evaluating laboratory work and numerical dynamic models of slip which attempt to understand the physical processes that act during ruptures. These studies are focused on how parameters such as temperature, pressure, material properties, and the stress state influence rupture behavior, and in some cases the constitutive relationships that govern the changes in stress during rupture [e.g., Raleigh and Paterson, 1965; Chernak and Hirth, 2010; Bizzarri, 2011; Brantut et al., 2011]. Many of these results can be related directly to seismological observations [e.g., Bizzarri, 2010]. For example, recent numerical work has shown that the local rupture velocity of an event, which can be estimated particularly well with the back-projection method, correlates with the ratio between shear and normal stress [Ben-David et al., 2010].

This dissertation utilizes high-quality seismic array data to investigate the ruptures associated with recent large earthquakes. The results are used to evaluate

tectonic factors and physical mechanisms that control ruptures, and to determine the information that can be quickly obtained for hazard assessment. Chapter 2 describes the back-projection method used for studying earthquake sources, and how this method can be modified to better resolve different aspects of the rupture process. Chapter 3 shows results from a global study of large, intermediate-depth earthquakes. These events are rarely destructive, but there is still much debate regarding the physical mechanisms that allow them to occur. Therefore, much of the discussion is focused on evaluating the constraints that can be placed on the mechanisms of these events given their source properties. Chapter 4 addresses the rupture segmentation of five recent large, shallow earthquakes. It is argued that this segmentation is controlled by the tectonic environments of the ruptures and has a strong influence on the hazards associated with these events. Chapter 5 discusses frequency-dependent rupture properties. This is a relatively new approach to studying large earthquakes that provides insights into the mechanisms and hazards of megathrust events. Chapter 6 moves to smaller events and investigates the capability of the back-projection method for detecting aftershocks. Chapter 7 discusses future directions for the research presented in this dissertation, and back-projection in general. Finally, Appendix A discusses the resolution of the back-projection method, and Appendix B presents tables of the back-projection aftershock catalogue from the Tohoku region that is discussed in Chapter 6.

CHAPTER 2

METHOD AND DATA

2.1 INTRODUCTION

Over the past 25 to 30 years, the source properties of both deep and shallow earthquakes have most commonly been studied using slip modeling approaches [e.g., Hartzell and Helmberger, 1982; Olson and Apsel, 1982; Cohee and Beroza, 1994; Cotton and Campillo, 1995; Zeng and Anderson, 1996; Sekiguchi et al., 1996; Antolik et al., 1999; Ji et al., 2002; Frankel, 2004; Rhie et al., 2007]. Though these methods have been widely used, many studies have revealed limitations associated with *a priori* constraints required to stabilize the inversions for slip [e.g., Olson and Apsel, 1982; Hartzell and Heaton, 1983; Beresnev, 2003; Mai et al., 2007; Lay et al., 2010a]. For example, the assigned parameters used in slip modeling include the fault plane dimensions and geometry. Such constraints for shallow earthquakes are obtained based upon geologic studies or aftershock distributions [e.g., Olson and Apsel, 1982]. However, multiple studies have shown that this information can be misleading when trying to identify rupture planes [e.g., Perfettini et al., 2010]. In addition, for intermediate-depth and deep-focus earthquakes, there is no surface expression of the rupture and often very few aftershocks [e.g., Frohlich, 1987], making detailed estimates on the

rupture plane dimensions and orientation difficult. In order to circumvent this problem, waveforms from deep earthquakes are typically inverted onto one of the nodal planes from the focal mechanism [e.g., Antolik et al., 1999]. This practice inherently limits the information that can be gained from source studies of these deeper events. Additional constraints that are commonly applied to slip models include the rupture direction and speed. As the results in Chapters 3-5 will show, there can be substantial variability in these parameters during a single event, hence constraining an earthquake source to be a simple unilateral rupture with a constant speed misses much of the complexity of these events and can lead to fictitious features.

The back-projection technique used in this thesis requires very little *a priori* knowledge, and therefore is a more deterministic approach to studying earthquake sources. This approach has become feasible in recent years through the availability of high-quality data from large-aperture dense arrays such as the High Sensitivity Seismograph Network (Hi-net) in Japan [Okada et al., 2004; Obara et al., 2005]. The application of the back-projection method to a number of large earthquakes has shown that it is a quick and efficient way to determine some important properties of earthquake sources, such as total rupture area, rupture direction, and rupture speed [e.g., Ishii et al., 2005, 2007; Walker et al., 2005; Nelson et al., 2008; Honda and Aoi, 2009; Walker and Shearer, 2009; Kiser and Ishii, 2012a,b].

2.2 THE BACK-PROJECTION METHOD

The back-projection technique is similar to other methods that utilize the time-reversal property of seismic waves [e.g., McMechan et al., 1985; Rietbrock and Scherbaum, 1994; Ekström et al., 2003; Kao and Shan, 2004, 2007; Baker et al., 2005; MacAyeal et al., 2006; Allmann and Shearer, 2007; Kao et al., 2008]. It was first used to study

the December 26, 2004 Sumatra-Andaman earthquake [Ishii et al., 2005], and has since been used to study both shallow and deep earthquakes [e.g., Ishii et al., 2005, 2007; Walker et al., 2005; Nelson et al., 2008; Honda and Aoi, 2009; Walker and Shearer, 2009; Kiser and Ishii, 2011; Wang and Mori, 2011a; Kiser et al., 2011; Meng et al., 2011; Kiser and Ishii, 2012a,b].

The back-projection method time-reverses seismograms from a seismic array to a grid of potential source locations around the hypocenter using predicted travel times based upon a one-dimensional Earth model such as IASP91 [Kennett, 1991]. The seismograms are stacked at each grid point, i.e.,

$$s_i(t) = \sum_{k=1}^K u_k(t + t_{ik}),$$

where $s_i(t)$ is the stacked seismogram at the i th grid point, $u_k(t)$ is the seismogram recorded at the k th station, t_{ik} is the predicted travel time between grid i and station k , and K is the total number of recorded seismograms. The grid points can be set up as a single horizontal plane or in three dimensions, depending on the aspect of rupture that needs to be investigated. The propagation of a rupture can be imaged by tracking the times and locations of high-amplitudes in the stacks. Therefore, this method is used for imaging relative energy release, and does not provide direct information about slip.

2.2.1 EMPIRICAL CORRECTIONS

The one-dimensional Earth model used in the back-projection analysis does not include lateral variations which can produce deviations from theoretical travel times. To correct for these lateral variations, we cross correlate the initial few seconds of the P waveforms between stations within the array and align the waveforms [Ishii

et al., 2007]. This process empirically corrects for the lateral variations, and ensures a coherent stack at the hypocenter. The cross correlation procedure also provides amplitude and polarity information for each seismogram with respect to a reference waveform. Including this information modifies the expression for the stacks to

$$s_i(t) = \sum_{k=1}^K \alpha_k u_k (t + t_{ik} + \Delta t_k). \quad (1)$$

Here, Δt_k is the empirical time correction for each station obtained from the cross correlation procedure, and α_k is a weighting factor to ensure proper polarity and contribution from each trace. α_k can be defined to consider various effects such as array geometry [e.g., Ishii et al., 2007], but the simplest form is

$$\alpha_k = \frac{p_k}{A_k},$$

where p_k is the polarity and A_k is an amplitude factor for seismogram k . The factor p_k has a value of either 1 or -1. The amplitude factor A_k obtained during the cross correlation step normalizes all seismograms so that a small group of high amplitude seismograms do not dominate the stacking process. Including this amplitude factor means that only relative energy release can be imaged. The time and amplitude corrections are usually determined using the first arriving P waves from the earthquake on which the back-projection analysis is applied. However, when the first arriving P waves of the event of interest are difficult to align, one can use corrections from an event in the same region, and with a similar focal mechanism, that has more impulsive first-arriving P waves. It should also be noted that seismic phases other than P can be used in the back-projection analysis. When these phases are compressional waves along most of their ray paths, and have ray paths similar to the P wave paths, then

the same time corrections can be used for these phases that are determined from the P cross correlation analysis (See Section 2.2.2). However, when the seismic phases have much different ray paths or are shear waves, then a separate cross correlation of the seismic phase of interest is desirable.

2.2.2 COMBINING SEISMIC PHASES

We have expanded the above basic back-projection technique to include additional seismic wave arrivals observed within the same seismic array. The use of multiple seismic phases can improve resolution, especially with respect to depth if depth phases are included. The seismograms are stacked for each phase based upon predicted travel times and the time correction Δt_k obtained for the reference phase (usually P). The stacks from multiple phases are combined such that

$$s_i(t) = \sum_{j=1}^J \left| \sum_{k=1}^K \alpha_k u_k (t + t_{ik}^j + \Delta t_k) \right|,$$

where J is the total number of seismic phases used, and t_{ik}^j is the predicted travel time for the j th seismic phase between the i th grid point and the k th station.

A few additional steps are taken to reduce unwanted signal, and to enhance coherency between phase stacks. For example, the P wave for a relatively shallow earthquake arrives close to the depth phase pP , and its amplitude is typically much larger than the depth phase. The slownesses of the two phases are also similar enough that back-projection results using the depth phase arrival times will result in the depth-phase stack that includes large amplitude signals from the P -wave arrival. In order to suppress such signals, a taper function $f_{jk}(t)$ is used to eliminate arrivals before

the target phase. The taper function $f_{jk}(t)$ is defined as

$$f_{jk}(t) = \begin{cases} 0 & \text{for } t \leq t_{0k}^j - T/2 \\ \frac{1}{2} \left\{ \cos \left[\frac{2(t-t_{0k}^j)\pi}{T} \right] + 1 \right\} & \text{for } t_{0k}^j - T/2 < t < t_{0k}^j, \\ 1 & \text{for } t \geq t_{0k}^j \end{cases},$$

where t_{0k}^j is the predicted travel time of the j th phase to the k th station from the hypocenter, and T is the period of the cosine taper function that is used.

Another step taken when combining seismic phases is to apply an additional weighting factor (w_j) to the stacks of each seismic phase, so that one phase does not dominate the final result. The weighting factor (w_j) can be expressed in many different ways, with the most basic form being

$$w_j = \frac{A_{ref}^{max}}{A_j^{max}}.$$

Here A_{ref}^{max} is the maximum amplitude of the reference phase stacks and A_j^{max} is the maximum amplitude of the stacks of the j th phase being considered. If a majority of the phases have upward or downward takeoff directions, there will be a bias in the contribution to back-projected stacks if the above weighting factor is used. For example, when P , pP , and sP are used in the back-projection analysis, there will be a bias in the upward takeoff direction. We therefore modify the weighting factor for the depth phases to

$$w_j = \frac{c_j A_{ref}^{max}}{\sum_{l=2}^J c_l A_l^{max}},$$

where c_j is the maximum correlation coefficient between the reference stack and the j th depth phase stack at the hypocenter. The summation in the denominator begins at 2 because this weighting factor is not being applied to the P phase. The above

formulations are based upon maximum stack amplitudes. Alternatively, one can use the ratio of summed stacks or the amplitude information from a hypocentral stack cross correlation. We have investigated both of these approaches without any significant changes to the final results.

Finally, we apply the constraint that the stacks from different seismic phases sum coherently at the hypocenter. To accomplish this, a second empirical time shift (Δt_j) is obtained by cross correlating the different phase stacks against a reference phase stack at the hypocenter (Figure 2.1). Including these additional steps modifies the expression for the stacks at each grid point to

$$s_i(t) = \sum_{j=1}^J w_j \left| \sum_{k=1}^K f_{jk}(t) \alpha_k u_k (t + t_{ik}^j + \Delta t_k + \Delta t_j) \right|.$$

The stacks $s_i(t)$ give time and relative amplitude information of energy released by an earthquake, providing constraints on the rupture process.

2.2.3 COMBINING SEISMIC ARRAYS

The modifications made to the back-projection technique to incorporate multiple seismic arrays are similar to those for combining multiple seismic phases recorded at the same array. At each grid point, stacked seismograms are generated for the j th array, $s_{ji}(t)$, using Equation 1. The stacks from different arrays are then combined at each grid point giving the final stacks, $S_i(t)$, in the form

$$S_i(t) = \sum_{j=1}^J w_j |s_{ji}(t + \Delta t_j)|,$$

where J is the number of seismic arrays being considered, w_j is the array-specific weighting factor, and Δt_j is the array-specific time correction. The weighting fac-

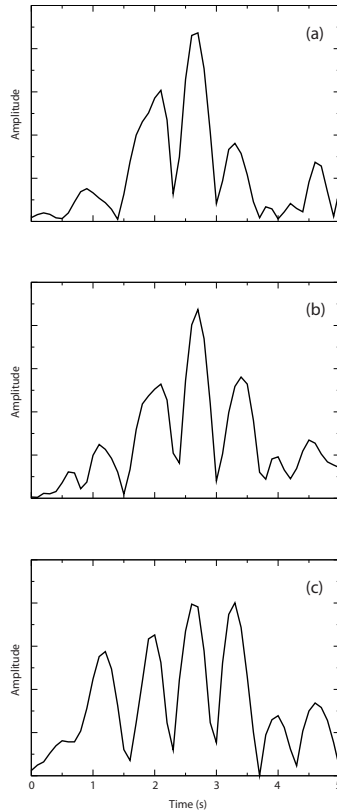


Figure 2.1: The absolute amplitudes of the first 5 seconds of stacks from three seismic phases, P (a), pP (b), and sP (c), at the hypocenter after phase-specific time shifts (Δt_j) have been applied. These stacks are from the September 8, 2008, Mw 6.9 earthquake. Time is with respect to the hypocentral time.

tor and time correction act to normalize individual array contributions and enhance coherence, respectively. The weighting factor takes the form

$$w_j = \frac{A_{ref}^{max}}{A_j^{max}},$$

where A_{ref}^{max} is the maximum absolute amplitude of the reference seismic array stack at the hypocenter, and A_j^{max} is the maximum absolute amplitude of the hypocentral stack of the j th seismic array. In order to ensure that stacks from different arrays combine coherently, the absolute values of the hypocentral stacks from different arrays are cross-correlated against the absolute values of the hypocentral reference stack. The absolute values are used to avoid changes in the polarity of the waveforms due to the location of seismic arrays with respect to the radiation pattern. The resulting

time shift, Δt_j , is applied to all of the stacks from the j th seismic array.

2.2.4 THE COHERENCY FUNCTION

During very large earthquakes or during periods of rigorous seismic activity, it is common to have multiple sources of energy with varying amplitudes. As demonstrated in Section A.4, using the linear stacking approach, where seismograms are simply summed after being time shifted, the largest amplitude source amongst a number of sources can dominate the resulting back-projection image. Therefore, an additional processing step needs to be incorporated into the back-projection analysis to reduce the dependence of the results on amplitude information. Multiple approaches have been developed to address this problem. The most common of these approaches is to apply n -th root stacking. Here, the n -th root, n is normally chosen between 2 and 6, of the seismograms is taken before the stacking process. The amplitude of the resulting stacks will depend more upon the coherency of the waveforms being stacked, instead of the amplitude of these waveforms. Following the stacking process, the amplitudes of the stacks are raised to the n -th power. This last step emphasizes the peaks of coherent waveforms. Though this method has been widely used, we do not prefer the technique, because it typically leads to a series of very discrete pulses of energy that are difficult to interpret in terms of the rupture parameters.

For this thesis, the low amplitude features of a propagating rupture are enhanced using an additional post-stack processing step that determines the similarity between waveforms in the linear stack and the waveforms in the seismograms. This step calculates a coherency function, $x_i(t)$ at the i th grid point as

$$x_i(t) = \frac{1}{K} \sum_{k=1}^K \frac{p_k \sum_{\tau=t}^{t+T} [u_k(\tau + t_{ik} + \Delta t_k) \cdot s_i(\tau)]}{\sqrt{\sum_{\tau=t}^{t+T} u_k^2(\tau + t_{ik} + \Delta t_k)} \sqrt{\sum_{\tau=t}^{t+T} s_i^2(\tau)}}.$$

This function is the average correlation value between individual, time shifted seismograms, $u_k(t)$, and the stack at the i th grid point, $s_i(t)$. T is the time window of the correlation. This time window should include multiple cycles of the waveforms, and therefore increases when using lower frequency data. p_k is the polarity correction at station k obtained from the initial waveform correlation step. A more thorough approach would be to calculate the average correlation between every pair of seismograms within each time window, however, this will dramatically increase the processing time of the analysis.

2.3 SEISMIC ARRAY DATA

Seismic arrays were originally developed to monitor nuclear explosions in the late 1950's [e.g., Carpenter, 1965]. This initial application, as well as the subsequent increase in popularity of these arrays such as in exploration seismology [e.g., Claerbout, 1976], is promoted by the fact that the recorded seismic waveforms are highly coherent between stations. This coherency allows for the application of processing techniques that enhance signals that may not be observed in the records of single stations. In addition, the spatial coverage of seismic arrays allows one to determine the azimuth and incident angle at which individual seismic waves are arriving, which is important for determining the source of the seismic waves [Gu, 2009, and references therein]. In this thesis, data is primarily used from the High Sensitivity Seismograph Network (Hi-net) in Japan and the USArray Transportable Array (TA). These two arrays provide the best combination of high-quality data, station density, abundance of stations, and large aperture.

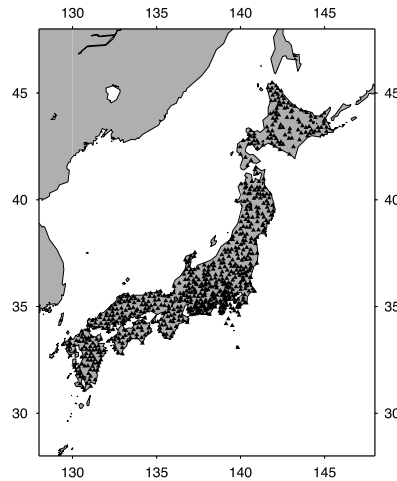


Figure 2.2: Distribution of the seismic stations (black triangles) in the High Sensitivity Seismograph Network (Hi-net) array throughout Japan. As of February 27, 2010 there are 776 stations.

2.3.1 THE HIGH SENSITIVITY SEISMOGRAPH NETWORK

Implementation of Hi-net began after the Kobe earthquake in 1995, and data from the array have been available since October 2000 [Okada et al., 2004; Obara et al., 2005]. There are currently around 800 stations in this array with a targeted station spacing of 20 km (Figure 2.2). Borehole short-period instruments (100 samples/second) are placed around 100 m depth. These sites are recording 3 components of ground motion, though only the vertical component is used in this dissertation.

2.3.2 THE USARRAY TRANSPORTABLE ARRAY

In contrast, TA consists of 400 high-quality three-component broadband seismometers with a targeted station spacing of 70 km (<http://www.usarray.org/researchers/obs/transportable>). This temporary array stretches from the northern to the southern border of the continental United States (Figure 2.3). It was first deployed in the west coast states in August of 2007, and has been moving eastward since then. Only the vertical components in these arrays are used in this dissertation.

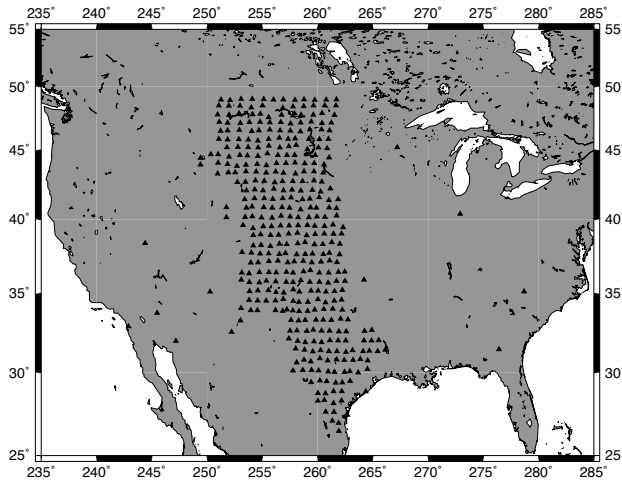


Figure 2.3: Distribution of the seismic stations (black triangles) in the Transportable Array (TA) throughout the United States. As of February 27, 2010 there are 390 stations.

2.3.3 ADDITIONAL SEISMIC NETWORKS

An additional seismic array used in this thesis is the Full Range Seismograph Network (F-net) of Japan [Okada et al., 2004]. This array has around 70 broadband stations with a station spacing of 100 km. In some cases, other seismic networks in the United States and Canada are combined with TA to produce a single seismic array across North America. These networks include the Caltech Regional Seismic Network (Caltech/USGS), Global Seismograph Network (IRIS), International Miscellaneous Stations, University of Utah Regional Network (University of Utah), Berkeley Digital Seismograph Network (Berkeley Seismological Laboratory), University of Oregon Regional Network (University of Oregon), Canadian National Seismograph Network (Geological Survey of Canada), United States National Seismic Network (ANSS Data Collection Center), and ANZA Regional Network (IGPP, University of California, San Diego).

CHAPTER 3

INTERMEDIATE-DEPTH EARTHQUAKES

3.1 INTRODUCTION

Deep earthquakes occur at pressure and temperature conditions which should prohibit brittle failure, and yet many of the rupture characteristics of deep earthquakes are similar to those of shallow events, such as double-couple focal mechanisms [Frohlich, 2006]. Traditionally, these earthquakes have been divided into two categories: intermediate-depth (60-300 km) and deep-focus (300-700 km) events [e.g., Wadati, 1929]. This classification is motivated by the bimodal distribution in the number of earthquakes with depth, where an exponential decrease in the number of earthquakes occurs from 60 km to about 300 km followed by an increase between 400 and 600 km which quickly drops off between 650 and 700 km [e.g., Flinn and Engdahl, 1965; Frohlich, 1989, Figure 3.1]. Studies of source characteristics (e.g., rupture complexity and aftershock productivity) and conditions within the subducting slab (e.g., stability of hydrous minerals) also broadly support this division of deep earthquakes [e.g., Ringwood, 1975; Houston and Vidale, 1994; Persh and Houston, 2004]. In this chapter, we focus on the intermediate-depth earthquakes occurring at depths between 100 and 300 km.

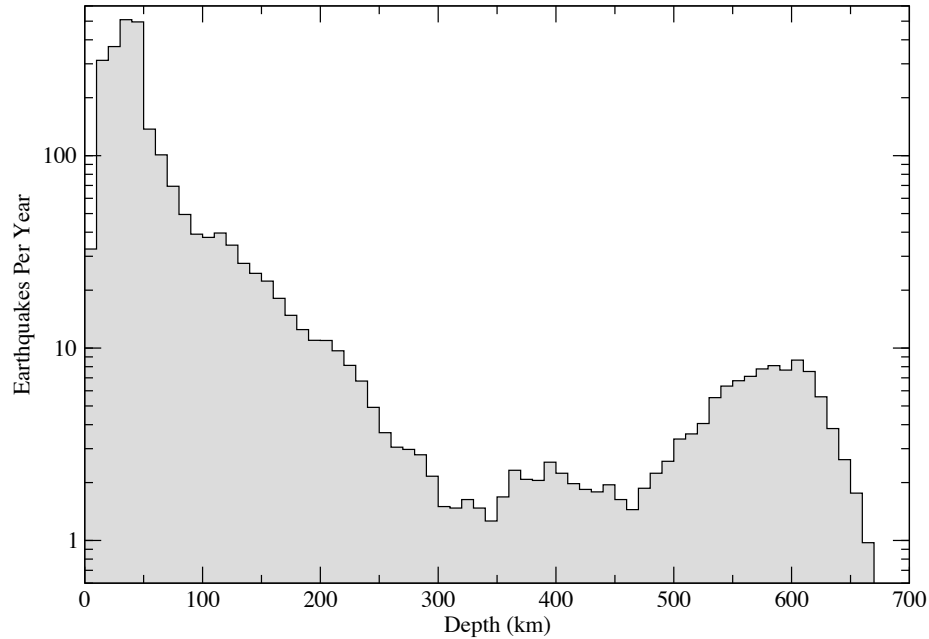


Figure 3.1: Seismicity rate as a function of depth. The events have been grouped into 10 km bins, and are from the NEIC catalogue between 1973 and 2011.

Many hypotheses have been proposed to explain the occurrence of intermediate-depth earthquakes, such as dehydration embrittlement and shear localization [e.g., Raleigh and Paterson, 1965; Ogawa, 1987; Hobbs and Ord, 1988; Kirby et al., 1996; Hacker et al., 2003; Keleman and Hirth, 2007]. In addition to work from the mineral physics community, these hypotheses are developed and tested based upon earthquake source studies. In general, these studies have only given very general descriptions of the rupture properties. For example, a recurring theme of many intermediate-depth earthquake studies is the identification of double seismic zones within the subducting slab, where one plane of seismicity takes place near the top of the slab and is separated from the deeper plane of seismicity by 5-40 km [e.g., Engdahl and Scholz, 1977; Hasagawa et al., 1978; Samowitz and Forsyth, 1981; Kawakatsu, 1985; Abers, 1992; Smith et al., 1993; Araujo and Suarez, 1994; Kao and Liu, 1995; McGuire and Wiens, 1995; Reyners et al., 1997; Kao and Rau, 1999; Comte et al., 1999; Cassidy and

Waldhauser, 2003]. This observation is used in support of the idea that dehydration of hydrous minerals within the upper crust and mantle is involved in the generation of intermediate-depth earthquakes [e.g., Peacock, 2001; Hacker et al., 2003]. Other source studies have tried to analyze individual ruptures, and determined parameters such as the impulsiveness, duration, direction, and aftershock production of the rupture [e.g., Vidale and Houston, 1993; Houston and Vidale, 1994; Bos et al., 1998; Houston et al., 1998; Antolik et al., 1999; Campus and Das, 2000; Houston, 2001; Persh and Houston, 2004; Warren et al., 2007, 2008]. Most of these studies are either designed to examine a very narrow aspect of the rupture [e.g., Houston and Vidale, 1994] or impose very subjective constraints on the rupture in an attempt to gain a more detailed description of the source [e.g., Antolik et al., 1999]. In addition, many of these studies investigate the systematic differences between intermediate-depth and deep-focus earthquakes [e.g., Vidale and Houston, 1993; Persh and Houston, 2004] more than the rupture properties of the intermediate-depth earthquakes alone. The results and discussion in Chapter 3 are unique in two ways. First, it is one of the few source studies that focuses solely in the rupture parameters of intermediate-depth earthquakes to gain insights into their mechanisms, instead of describing them in a relative sense with respect to shallow or deep-focus earthquakes. Second, the multi-phase back-projection method allows us to describe intermediate-depth ruptures at a much higher level of detail than previous studies.

3.2 DATA AND DATA PROCESSING

This chapter uses unfiltered data from the High-Sensitivity Seismograph Network (Hi-net) in Japan. Three phases are used in the back-projection analysis: P , pP , and sP (Figures 3.2 and 3.3a). The difference in takeoff direction between P and the

depth phases, pP and sP , produces very good depth resolution when all three phases are combined.

In order to obtain the empirical correction for lateral variations in the velocity structure of the Earth, Δt_k , a cross-correlation analysis is applied to P waves. The waveforms are cross-correlated in a 4-second time window, which is allowed to shift by ± 2 seconds, around the predicted arrival times based upon the one-dimensional velocity model IASP91 [Kennett and Engdahl, 1991]. A cluster analysis is applied [e.g., Romesburg, 1984] to identify the largest group of seismograms with high waveform similarity to generate the first reference stack. This reference stack is then cross-correlated with each seismogram, as in the first step, and those with a correlation coefficient above 0.6 are stacked to produce the second reference stack. This step is repeated five times to generate a final reference stack. Each seismogram is then correlated with this final reference stack to obtain the polarity (p_k), the amplitude factor (A_k), and the relative time shift (Δt_k). Only the first arriving P waves are cross-correlated and the same time shifts are used to correct every seismic phase considered. The cross-correlation technique can be applied to any individual seismic phase, but the depth phases (pP and sP) considered in this study typically have low signal-to-noise ratios, making the cross-correlation procedure less effective.

The low signal-to-noise ratios of the depth phases compared to the P phase also demonstrate the necessity for using the taper function $f_{jk}(t)$. The taper function prevents the high amplitude P waves from contaminating the depth phase stacks (Figure 3.2). The period T over which the taper function goes from 1 to 0 is fixed at 10 seconds. Varying this value has little effect on the final results as long as it is a short enough time window to down-weight the P waves and long enough to avoid generating artifacts due to an abrupt cutoff. The taper function can also suppress signals from the depth phases if these phases arrive significantly before the

predicted arrival. This possibility is evaluated by shifting the taper function gradually up to 5 seconds before the theoretical arrival time and monitoring the correlation coefficients between the P stack and depth phase stacks at the hypocenter. If the depth phase signal arrives earlier than predicted, then the shifted taper function should allow more of the depth phase signal to be present in the depth phase stacks. This would increase the correlation coefficient between the stacks at the hypocenter. In contrast, if the depth phase arrives at or later than the predicted time, then only noise and the P waveform is down-weighted by the original taper function, leading to a lower correlation coefficient using the shifted taper function. Seven of the events have correlation coefficients for one of the depth phases that become larger when the shifted taper function is used, hence we choose to apply the shifted taper function in the back-projection analysis for these cases. However, in general, shifting the taper function has little effect on the back-projection results.

The form of the weighting factor for each phase w_j can change depending on the seismic phases being used (Chapter 2). There are five earthquakes for which one of the depth phases is predicted to have an amplitude much smaller than the P phase (10% or less) based upon Global CMT solutions [e.g., Dziewoński et al., 1981; Dziewoński and Woodhouse, 1983; Woodhouse and Dziewonski, 1984; Ekström et al., 2005]. For these events, only the higher amplitude depth phase is used with weighting specified by the basic weighting factor. Finally, the phase-dependent time shift (Δt_j) is obtained by cross correlating the depth phase stacks at the hypocenter with the hypocentral P stack.

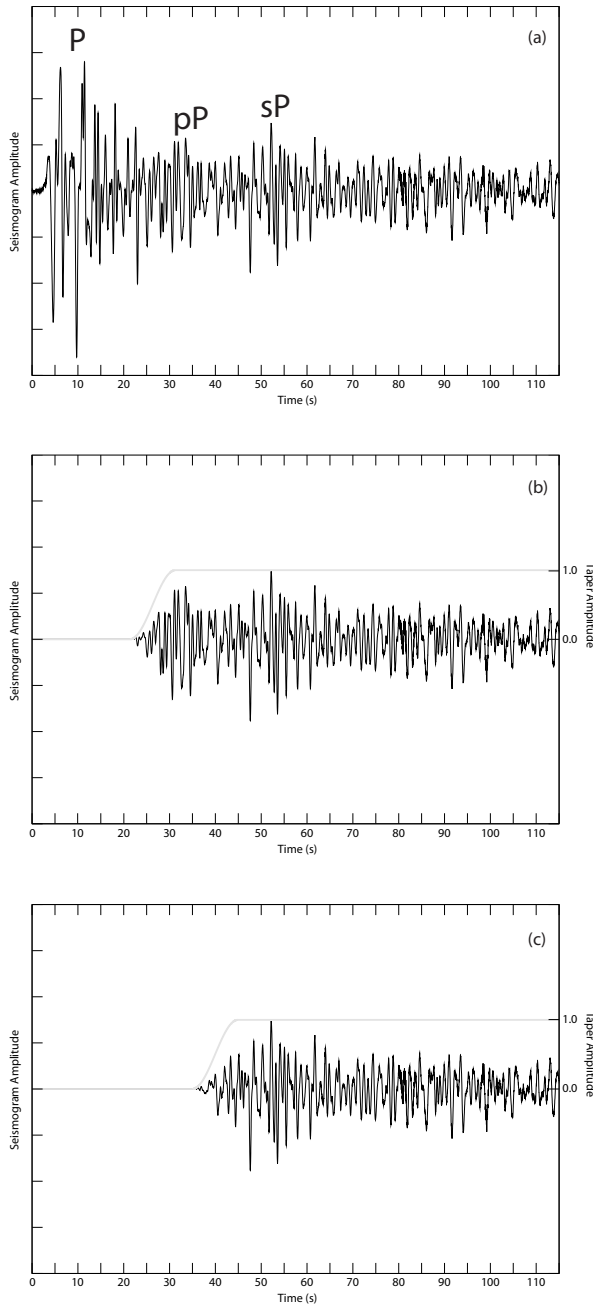


Figure 3.2: (a) Seismic record from the September 8, 2008, Mw 6.9 event in Vanuatu. This record comes from station ASHH in the Hi-net array. The P , pP , and sP seismic phases are all labeled. Time is with respect to the P wave arrival. (b) The same seismic record after the taper function (light grey line) is applied at the theoretical pP arrival time. (c) Same as (b) except applied to sP .

3.3 RESULTS

The multi-phase back-projection analysis is applied to 22 intermediate-depth earthquakes (Tables 3.1-3.5 and Figure 3.3). These events occurred between October 2000 and April 2010, and are at teleseismic distances from the Hi-net array. The moment magnitudes and depths of these events, as reported by the USGS (<http://earthquake.usgs.gov/regional/neic/>), range from 6.5 to 7.8 and 103 to 280 km, respectively. For all of these earthquakes, a box of grid points centered at the hypocenter is defined with dimensions of 2.4 degrees in latitude, 2.4 degrees in longitude, and 160 km in depth. The grid spacing, which is based upon the average resolution in latitude, longitude, and depth, is set to 0.4 degrees, 0.4 degrees, and 5 km, respectively. We choose the 75% contour of the maximum stack amplitude to estimate the depth extent and duration of each event (Tables 3.1-3.5). This choice is somewhat arbitrary, however, it captures the major features for most of the earthquakes.

Using this contour level, many of the events (14 out of 22) show similar depth-time behavior to the synthetic ruptures in Section A.3.1 in that they have one episode of energy release that is continuous in depth and time. The remaining 8 earthquakes have multiple regions of high amplitude energy that are well separated in time and/or depth. In order to systematically categorize events consisting of a single or multiple sub-events, we use the selection criterion that the initiation depths of the sub-events need to be separated by at least 15 km. When this criterion is met, we refer to the event as composite. When the depth separation is less than 15 km, the events are labeled simple. In addition, the observed depth extent of individual sub-events can be classified into two groups, one with limited depth range and another showing energy release over a much larger depth interval. Most of the sub-events are of the first group, with 23 out of 30 sub-events having depth extents of 15 km or less (Tables 3.1-3.5).

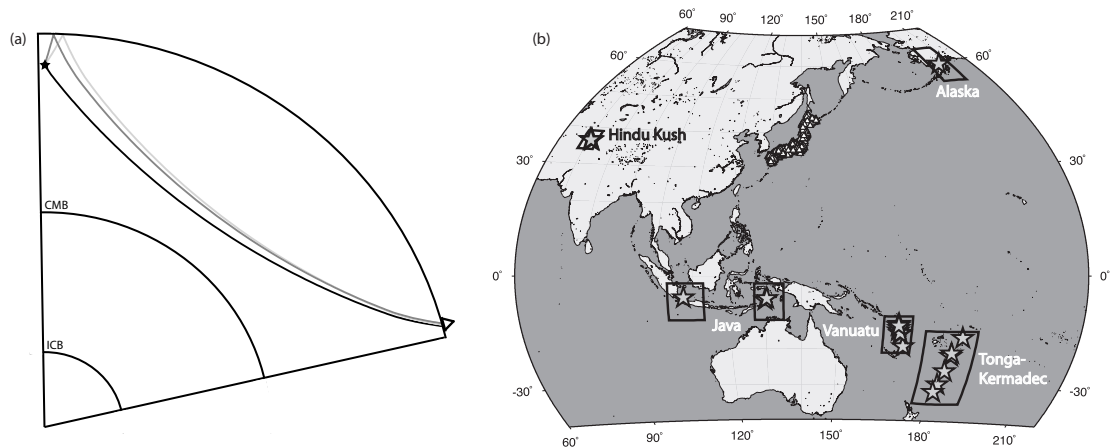


Figure 3.3: (a) The ray paths of the P (black line), pP (dark grey), and sP (light grey) phases from the source (star) to the receiver (triangle). The difference in the takeoff directions between the P phase and depth phases (pP and sP) results in excellent vertical resolution when stacks from each phase are combined. (b) Locations of the 22 earthquakes studied (grey stars) relative to the Hi-net array (white triangles). The black boxes are the areas displayed in Figures 3.4 through 3.8.

We refer to these sub-events as sub-horizontal ruptures. In the following subsections, we discuss results for events in each region shown in Figure 3.3.

3.3.1 TONGA-KERMADEC

The Tonga-Kermadec trench subducts the 70-100 Myr old Pacific plate beneath the Indo-Australian Plate at a rate which increases to the north from rates of 16 to 24 cm/yr [Bevis et al., 1995]. The hypocentral depths of six events in this region range from 129 to 212 km, and their moment magnitudes vary between 6.5 and 7.8 (<http://earthquake.usgs.gov/regional/neic/>) (Figures 3.4). Four of the events are interpreted as simple ruptures (Figures 3.4a, d, e, and f). The depth extent of these events varies from 0 km to 25 km, and their durations range from 12 to 14 seconds (Table 3.1). The remaining 2 earthquakes are composite events, with two sub-events separated in depth by 25 and 30 km (Figures 3.4b and c, respectively).

The event duration of these composite events is slightly longer than the simple events, 15 to 16 seconds (Table 3.1).

3.3.2 VANUATU

Along the Vanuatu subduction zone, the Indo-Australian plate is subducting beneath the Pacific plate. There are large variations in the subduction rates along the trench, ranging from 3 cm/yr to 17 cm/yr [e.g., Bergeot et al., 2009]. Figure 3.5 shows the regional distribution of earthquakes and the back-projection results. These events have magnitudes and depths that range from 6.5 to 7.2 and 103 to 228 km, respectively (<http://earthquake.usgs.gov/regional/neic/>). Five of the earthquakes from Vanuatu have simple ruptures with depth extents of 5 km or less (Figures 3.5a, b, c, f, and g). The duration of these events ranges from 14 to 15 seconds. The August 1, 2007, Mw 7.2 event (Figure 3.5g) from this group seems to have complexity beyond the single rupture, however, all of this complexity is weak, at energy levels below the 75% level. The northernmost and deepest event from this region also has a single rupture which propagates upward and downward with time, though the upward propagation dominates (Figure 3.5e). South of these simple events are two composite events. The August 7, 2006, Mw 6.8 earthquake is composed of 3 sub-events (Figure 3.5d). The largest depth separation between any two of these sub-events is 75 km. The second composite event (Mw 6.6) occurred on November 6, 2003 (Figure 3.5h). Two features of this earthquake warrant clarification. First, even though there are three separate depth ranges bounded by the 75% contour, the initiation depths of the deeper two are separated by less than 15 km. Therefore, based upon the definitions given above, this earthquake is classified as having only two rupture planes (Table 3.2). Second, there is low amplitude energy that is visible at about 25 seconds after the hypocentral time at a depth of 50 km. This is an artifact that arises

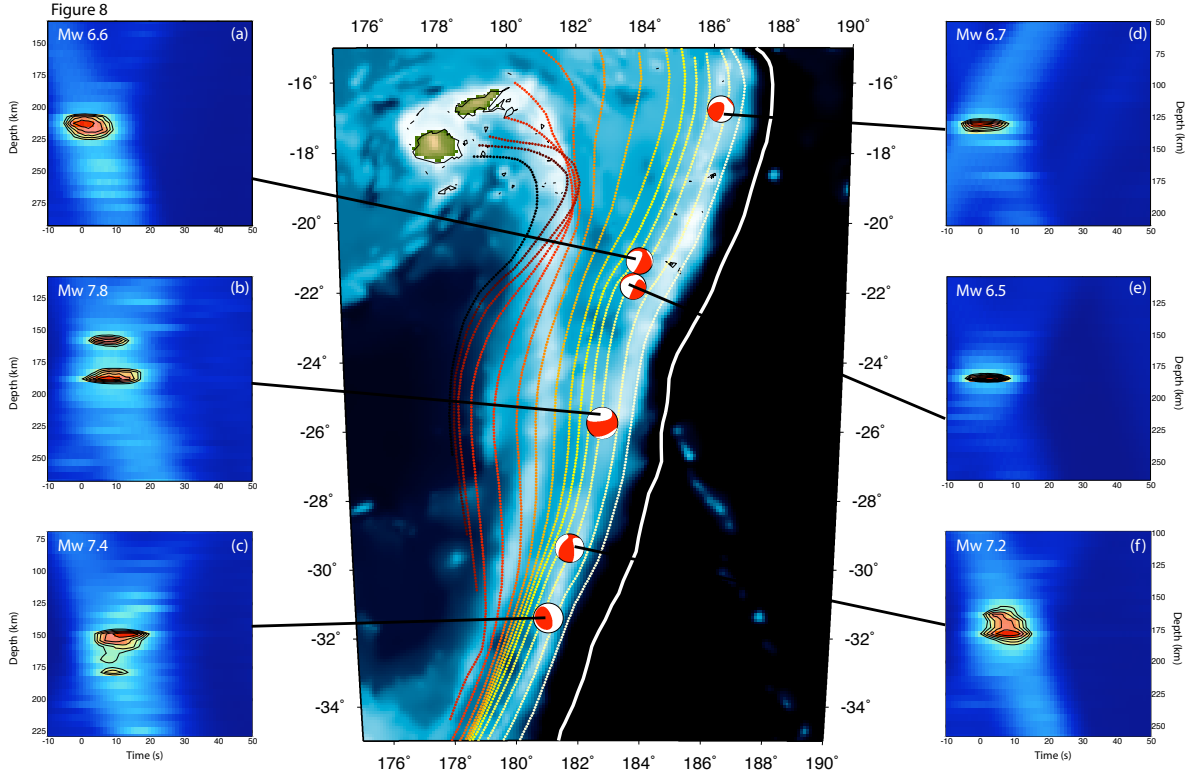


Figure 3.4: Summary of locations, focal mechanisms from the Global CMT catalogue [e.g., Dziewoński et al., 1981; Dziewoński and Woodhouse, 1983; Woodhouse and Dziewoński, 1984; Ekström et al., 2005], and the back-projection results of the earthquakes studied in the Tonga-Kermadec region. The map in the center shows the region with background color showing the bathymetry (ETOPO5; <http://www.ngdc.noaa.gov/mgg/global/etopo5.html>). The solid white line is the trench location. The dotted lines are the slab contours from 50 to 700 km (white to dark red) in 50 km increments. The panels labeled (a) through (f) show the back-projection results in the depth and time dimensions. The magnitudes and hypocentral depths are from the National Earthquake Information Center (NEIC) catalog (<http://earthquake.usgs.gov/regional/neic/>). The background colors indicate high (dark red) and low (dark blue) stack amplitudes. See Table 3.1 for a summary of the results. (a) The July 27, 2003 event with magnitude Mw 6.6 at a depth of 212 km. (b) The December 9, 2007 event with magnitude Mw 7.8 at a depth of 152 km. (c) The May 16, 2006 event with magnitude Mw 7.4 at a depth of 152 km. (d) The January 25, 2004 event with magnitude Mw 6.7 at a depth of 129 km. (e) The July 4, 2001 event with magnitude Mw 6.5 at a depth of 184 km. (f) The June 3, 2001 event with magnitude Mw 7.2 at a depth of 178 km.

Date & Time	Lat	Lon	Dep	Mw	# Rup.	Rup. Dep	Vert. Ext.	Event Dur.	Cumul. Dur.	Phases Used	Epsil.	Fig.
06/03/01 02:41:57	-29.67	-178.63	178	7.2	1	178	-20 +5	14	14	pP,sP	-0.05	3.4f
07/04/01 07:06:31	-21.73	-176.71	184	6.5	1	184	0	12	12	pP,sP	0.10	3.4e
07/27/03 02:04:11	-21.08	-176.59	212	6.6	1	212	-5 +10	14	14	pP,sP	-0.07	3.4a
01/25/04 11:43:11	-16.83	-174.20	129	6.7	1	129	+5	13	13	sP	0.13	3.4d
05/16/06 10:39:23	-31.81	-179.31	153	7.4	2	153 178	+15 0	15	22	pP,sP	0.16	3.4c
12/09/07 07:28:20	-26.00	-177.51	157	7.8	2	157 187	0 -5	16	26	pP,sP	-0.25	3.4b

Table 3.1: Summary of the Tonga-Kermadec events analyzed with the back-projection technique and the Hi-net data in Japan. The first five columns give hypocentral date and time (UTC), latitude, longitude, depth, and moment magnitude, obtained from the National Earthquake Information Center (<http://earthquake.usgs.gov/regional/neic/>). The column “# Rup.” gives the number of sub-events with a minimum of 15-km depth separation as described in the main text. For each sub-event, the depth at its initiation is given in the “Rup. Dep” column. The depth extent for each sub-event is summarized in the “Vert. Ext.” column, with the value given in increments of 5 km, and the sign indicating the direction, i.e., positive for downward propagation and negative for upward propagation. Sub-events with both positive and negative entries indicate bivertical rupture. The following two columns give duration information inferred from the back-projection results. The “Event Dur.” is the duration of the entire event. In contrast, the “Cumul. Dur.” gives the sum of the durations of sub-events. Large differences between these two values indicate that there is significant overlap of the sub-event ruptures in time. The “Phases Used” column shows the depth phases that have been combined with the P -wave stacks. In most cases, both pP and sP phases are used, except when the source mechanism is such that pP is not excited well. The next to last column gives the ϵ value that represents the non-double-couple component of the event (see main text for definition). The final column gives the corresponding back-projection plot for each earthquake. Note that on average, the uncertainties in depth and time are ± 5 km and ± 5.0 seconds, respectively.

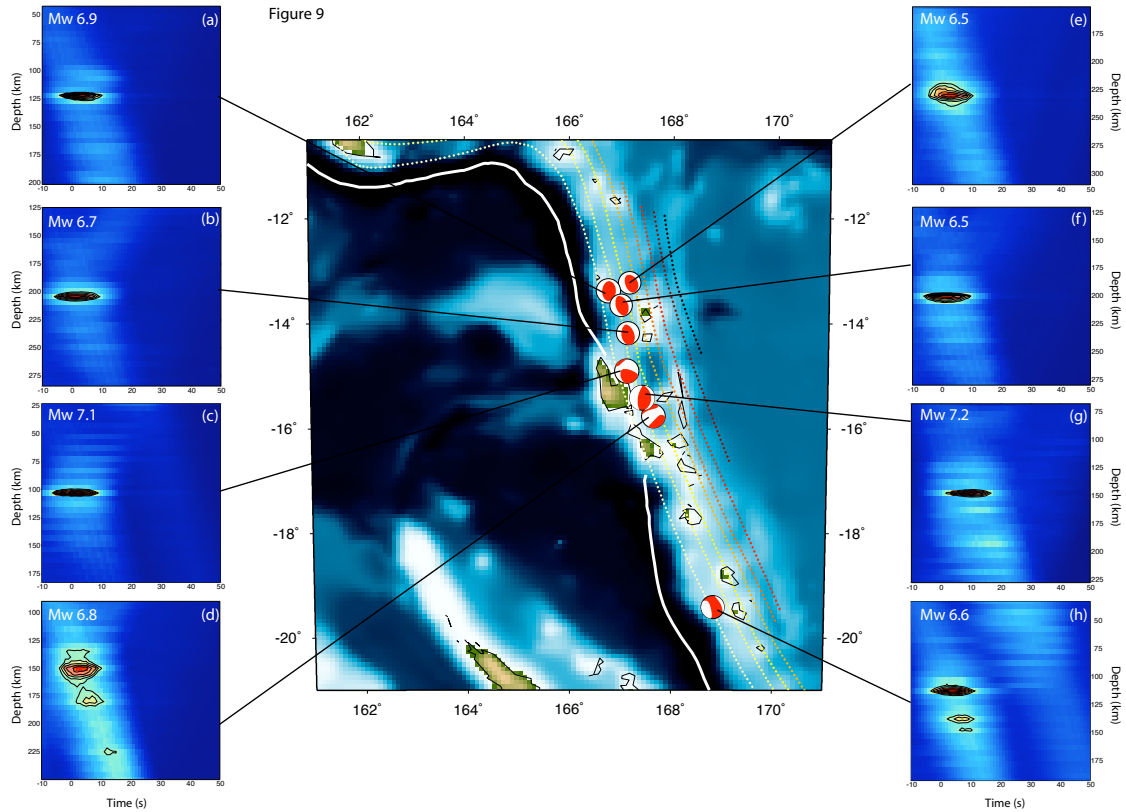


Figure 3.5: Same as Figure 3.4 for events in Vanuatu. The slab contours are from 50 to 400 km. See Table 3.2 for a summary of the results. (a) The September 8, 2008 event with magnitude Mw 6.9 at a depth of 110 km. (b) The February 8, 2005 event with magnitude Mw 6.7 at a depth of 206 km. (c) The January 9, 2001 event with magnitude Mw 7.1 at a depth of 103 km. (d) The August 7, 2006 event with magnitude Mw 6.8 at a depth of 149 km. (e) The April 9, 2004 event with magnitude Mw 6.5 at a depth of 228 km. (f) The March 4, 2010 event with magnitude Mw 6.5 at a depth of 176 km. (g) The August 1, 2007 event with magnitude Mw 7.2 at a depth of 120 km. (h) The November 6, 2003 event with magnitude Mw 6.6 at a depth of 113 km.

for shallow events due to the pP phase arrival within the P -wave window used in the back-projection analysis. If the back-projection method is applied to events shallower than 100 km, the amplitude of this artifact can become large at times close to the hypocentral time, complicating source imaging and degrading the depth resolution.

Date & Time	Lat	Lon	Dep	Mw	# Rup.	Rup. Dep	Vert. Ext.	Event Dur.	Cumul. Dur.	Phases Used	Epsil.	Fig.
01/09/01 16:49:28	-14.93	167.17	103	7.1	1	103	0	14	14	pP,sP	0.11	3.5c
11/06/03 10:38:04	-19.26	168.89	113	6.6	2	113 138	-5 +10	14	22	pP,sP	-0.29	3.5h
04/09/04 15:23:35	-13.17	167.20	228	6.5	1	228	-10 +5	14	14	pP,sP	0.10	3.5e
02/08/05 14:48:21	-14.25	167.26	206	6.7	1	206	0	14	14	pP,sP	0.03	3.5b
08/07/06 22:18:55	-15.80	167.79	149	6.8	3	149 179 224	-15 +15 -10 0	19	25	pP,sP	0.22	3.5d
08/01/07 17:08:51	-15.60	167.68	120	7.2	1	120	0	14	14	pP,sP	-0.01	3.5g
09/08/08 18:52:06	-13.50	166.97	110	6.9	1	110	0	14	14	pP,sP	0.13	3.5a
03/04/10 14:02:27	-13.60	167.16	176	6.5	1	176	+5	15	15	pP,sP	0.03	3.5f

Table 3.2: Summary of the Vanuatu events analyzed with the back-projection technique and the Hi-net data in Japan. The columns are the same as in Table 3.1.

3.3.3 HINDU KUSH

The intermediate-depth seismicity in Hindu Kush and Pamir is thought to be taking place within a remnant slab that has subducted beneath Eurasia during its collision with India around 55 Ma [e.g., Pavlis and Das, 2000]. A total of 4 earthquakes with magnitudes between 6.5 and 7.4 are studied from this region with depths between 187 and 230 km (Figure 3.6; Table 3.3). Three of these events have simple ruptures (Figures 3.6b, c, and d). For all three events, bivertical (upward and downward) energy propagation is observed. The durations range from 13 to 15 seconds, and the vertical extents range from 15 to 30 km. Some of the sub-events in this region have symmetric depth behavior (Figure 3.6b and d) that is similar to that observed for synthetic results (Section A.3.1). These symmetric low amplitude stacks may be artifacts, and therefore, part of the complexity seen may not reflect the actual rupture properties of the subevents. The fourth and largest event of this group of earthquakes (Mw 7.4) is composite and characterized by three sub-events. The two strongest sub-events which dominate the earthquake are separated by 75 km (Figure 3.6a). The total duration of this event is 21 seconds.

3.3.4 JAVA

Along the Java trench, the Indo-Australian plate subducts beneath the Eurasian plate. The age of the Indo-Australian plate at the subduction zone varies from 50 Myr in the east to 140 Myr in the west [e.g., Holcombe, 1977]. All three of the earthquakes from this region have relatively large magnitudes ($M_w \geq 6.9$). The main ruptures of all of these events also have large vertical extents (20-35 km) with mainly downward propagation (Table 3.4 and Figure 3.7). For two of these earthquakes, there are sub-events separated by 15 km or more, hence they are composite earthquakes

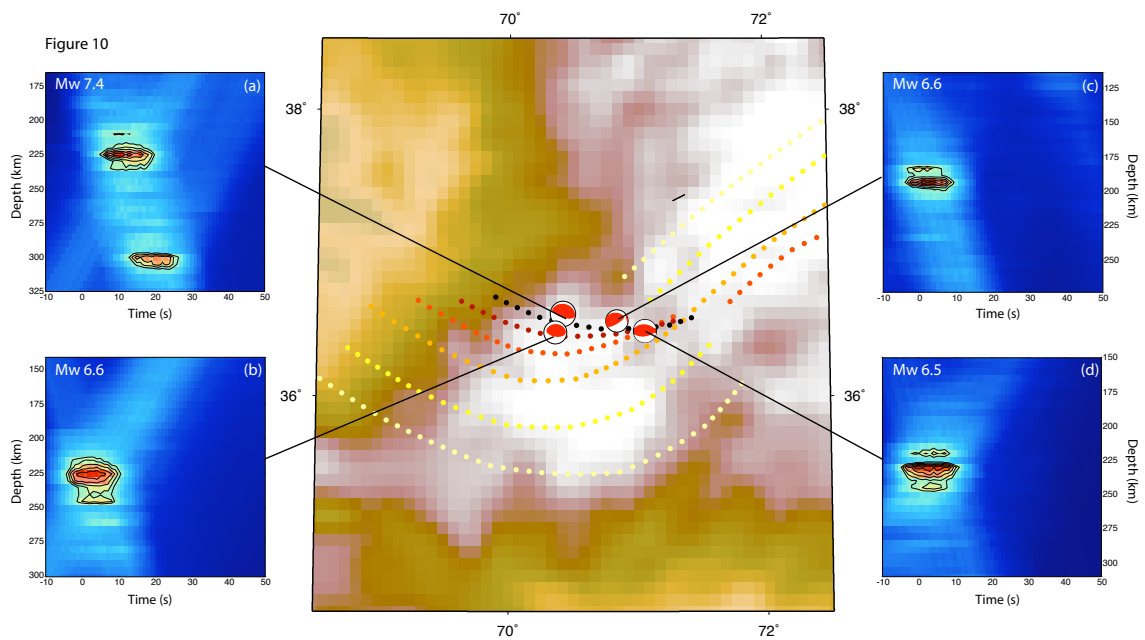


Figure 3.6: Same as Figure 3.4 for events in Hindu Kush. The slab contours are from 50 to 300 km. See Table 3.3 for a summary of the results. (a) The March 3, 2002 event with magnitude Mw 7.4 at a depth of 225 km. (b) The January 3, 2009 event with magnitude Mw 6.6 at a depth of 204 km. (c) The April 5, 2004 event with magnitude Mw 6.6 at a depth of 187 km. (d) The December 12, 2005 event with magnitude Mw 6.5 at a depth of 230 km.

Date & Time	Lat	Lon	Dep	Mw	# Rup.	Rup. Dep	Vert. Ext.	Event Dur.	Cumul. Dur.	Phases Used	Epsil.	Fig.
03/03/02 12:08:19	36.50	70.48	225	7.4	2	225	-15	21	27	sP	0.03	3.6a
						300	+10					
04/05/04 21:24:04	36.51	71.03	187	6.6	1	187	-10	13	13	pP,sP	0.01	3.6c
							+5					
12/12/05 21:47:46	36.36	71.09	230	6.5	1	230	-10	15	15	pP,sP	-0.04	3.6d
							+15					
01/03/09 20:23:20	36.42	70.74	204	6.6	1	204	-10	14	14	sP	0.09	3.6b
							+20					

Table 3.3: Summary of the Hindu Kush events analyzed with the back-projection technique and the Hi-net data in Japan. The columns are the same as in Table 3.1.

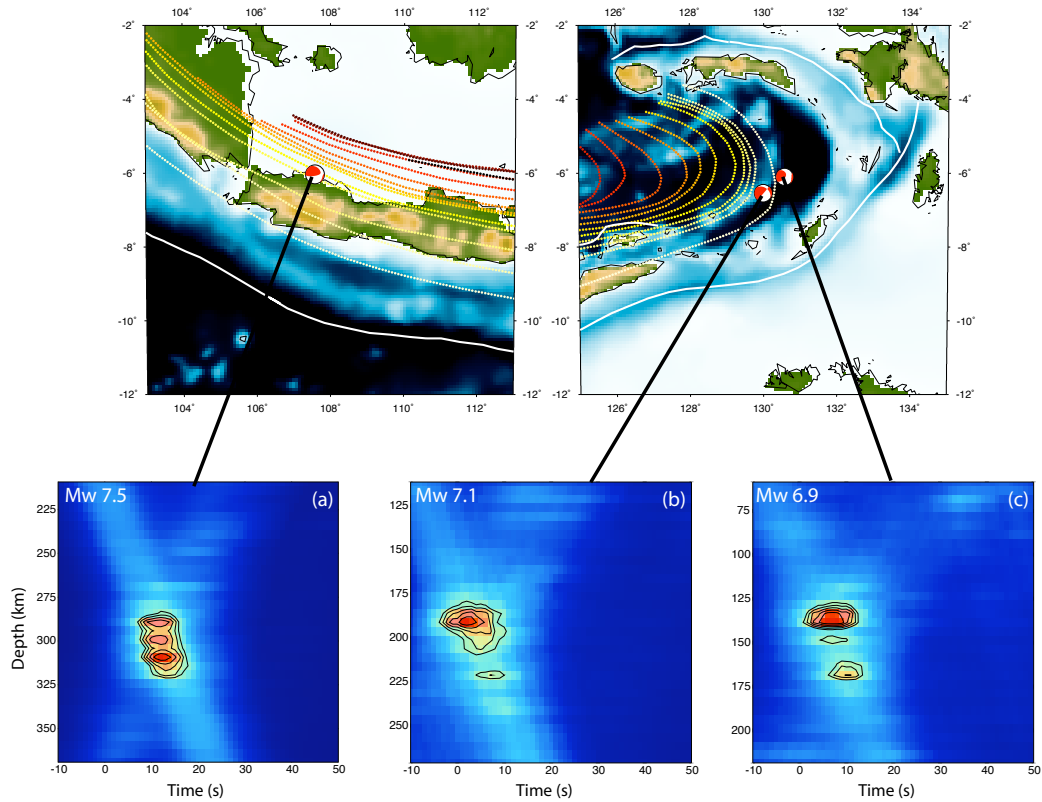


Figure 3.7: Same as Figure 3.4 for events in Java. The slab contours are from 50 to 700 km. See Table 3.4 for a summary of the results. (a) The August 8, 2007 event with magnitude Mw 7.5 at a depth of 280 km. (b) The March 2, 2005 event with magnitude Mw 7.1 at a depth of 191 km. (c) The October 24, 2009 event with magnitude Mw 6.9 at a depth of 138 km.

(Figures 3.7b and c). The event durations of the Java earthquakes range from 9 to 13 seconds.

3.3.5 ALASKA

In this region, the Pacific plate subducts beneath the North American plate along the Aleutian trench at a rate of 7 to 8 cm/yr, and unlike most sections of the Aleutian trench, convergence is perpendicular to the trench [Creager and Boyd, 1991]. The one earthquake studied in this region has a large strike-slip component based upon the Global CMT solution, and is observed to be a composite rupture (Figure 3.8).

Date & Time	Lat	Lon	Dep	Mw	# Rup.	Rup. Dep	Vert. Ext.	Event Dur.	Cumul. Dur.	Phases Used	Epsil.	Fig.
03/02/05 10:42:12	-6.53	129.93	191	7.1	2	191	-10	13	19	pP,sP	0.00	3.7b
						221	+15					
08/08/07 17:05:04	-5.86	107.42	280	7.5	1	280	-5	9	9	pP,sP	0.08	3.7a
							+30					
10/24/09 14:40:43	-6.13	130.38	138	6.9	2	138	-10	12	17	pP,sP	0.27	3.7c
						168	+10					
							-5					

Table 3.4: Summary of the Java events analyzed with the back-projection technique and the Hi-net data in Japan. The columns are the same as in Table 3.1.

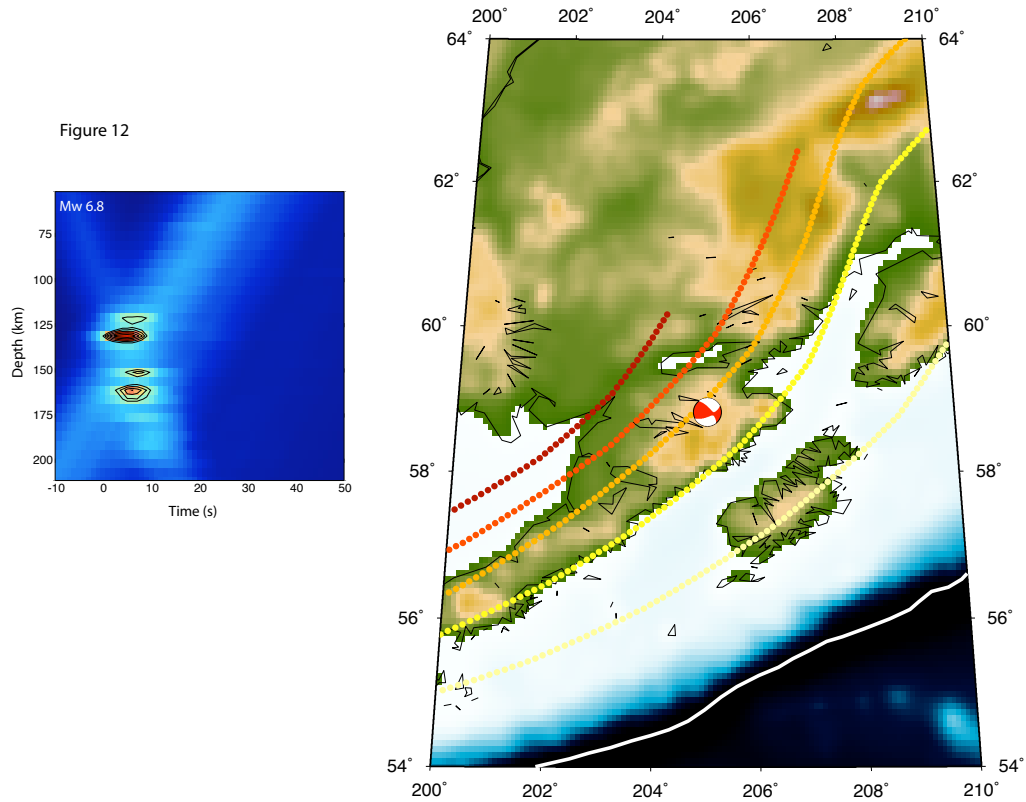


Figure 3.8: Same as Figure 3.4 for the event in Alaska. This earthquake occurred on July 28, 2001, had a magnitude M_w 6.8, and a hypocentral depth of 131 km. The slab contours are from 50 to 250 km. See Table 3.5 for a summary of the results.

The first rupture propagates 10 km upward, although the energy falls below the 75% level during this upward propagation. The second rupture starts 30 km below the initial rupture and propagates both upward and downward, and has a total vertical extent of 15 km. The event duration of this earthquake is 9 seconds.

3.4 DISCUSSION

The depth-time behavior of the 22 intermediate-depth events considered in this study can be interpreted in many different ways. However, we first address the issue of whether the complexities of the composite ruptures are artifacts of the back-projection method. In order to investigate the robustness of the complexities imaged by the back-

Date & Time	Lat	Lon	Dep	Mw	# Rup.	Rup. Dep	Vert. Ext.	Event Dur.	Cumul. Dur.	Phases Used	Epsil.	Fig.
07/28/01 07:32:43	59.03	-155.12	131	6.8	2	131 161	-10 -10 +5	9	15	sP	-0.03	3.8

Table 3.5: Summary of the Alaska events analyzed with the back-projection technique and the Hi-net data in Japan. The columns are the same as in Table 3.1.

projection technique, synthetic tests are presented in this section with a focus on the large Hindu Kush event which had the largest depth separation between two rupture planes. These tests support the conclusion that multiple planes of high amplitude energy are real features of the earthquakes.

3.4.1 ROBUSTNESS OF COMPOSITE RUPTURES

The composite earthquakes are potentially the most interesting observations of this study (e.g., Figure 3.6a). These results are partially supported by reports of similar complexity in other catalogues for some of the events we have analyzed [e.g., Starovoi et al., 2002]. We investigate whether complexities seen in the back-projection results are real features of the events or artifacts of the stacking procedure. Synthetic results show that high amplitude artifacts do not arise when the input source is simple (Figures A.7 and 3.9). However, this may not necessarily apply to very complex ruptures. To investigate this possibility, a more complex case is simulated by using the *P*-wave train recorded at a single station from the March 3, 2002 Hindu Kush event (Figure 3.6a) as the input source-time function for a synthetic test (Figure 3.10a). The hypocentral location of this complex synthetic source is fixed to that of the Hindu Kush event, i.e., 36.50°N, 70.48°E, and 225 km depth. If the second rupture observed in the March 3, 2002 Hindu Kush event is an artifact of the complex source-time function, then a similar artifact should be seen in the synthetic result. On the other hand, if the method can reliably constrain depth for the complex source-time function, then the synthetic result should have high amplitude stacks only at the assigned depth. Figure 3.10(b) shows the high amplitude energy is imaged at the hypocentral depth, although there is low amplitude energy above and below the assigned depth of 225 km. This result demonstrates that even for a very complex horizontal rupture, artifacts of high amplitude energy at different depths are suppressed by virtue of using multiple

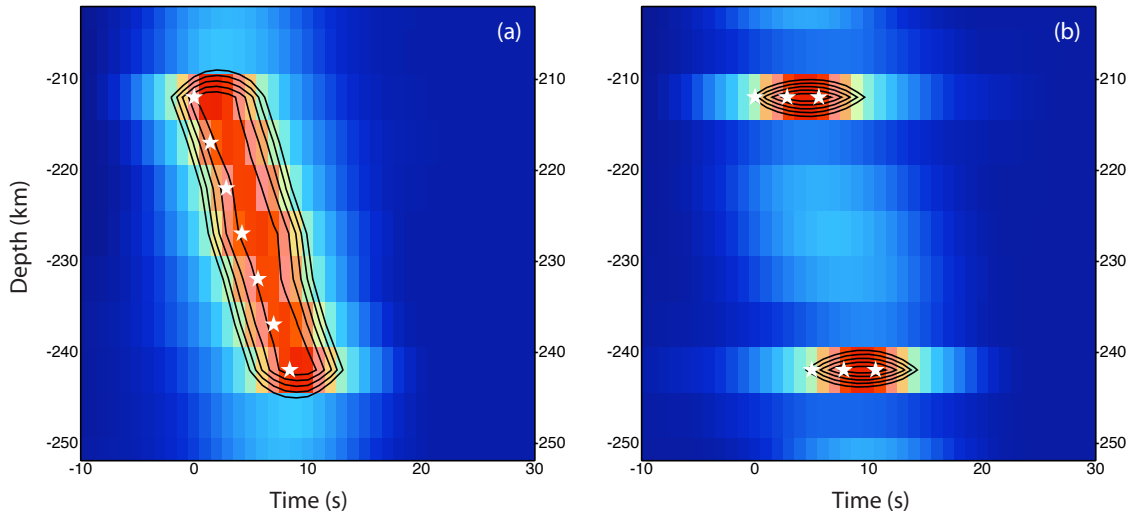


Figure 3.9: Back-projection results of a synthetic vertical and composite rupture. (a) Vertical rupture with a propagation velocity of 3.6 km/s. The white stars are the depths and times of the point sources. (b) Composite rupture with two horizontal sub-events. The rupture velocity of the individual sub-events is 3.6 km/s. The propagation velocity between the two sub-events is 6.0 km/s

seismic phases.

There is also the possibility that seismic phases not included in the back-projection analysis may cause the observed complexity. As demonstrated in Appendix A (Figure A.7) and discussed briefly for an event in the New Hebrides region (Figure 3.5h), moderately coherent stacks can result at depths and times close to the hypocenter when unwanted phases are present. To investigate this possibility, we focus on crustal and water phases, which have very similar ray paths as the depth phases used in this study. In particular, we consider arrivals due to underside reflections from the Moho and the sea surface. To determine the effect of these phases on back-projection results, the synthetic tests used in Figure A.7 are modified. For the original synthetic tests, seismograms include one Ricker wavelet for each assigned point source and each seismic phase chosen for that source, i.e., one Ricker wavelet for each of the P , pP , and sP arrivals. This approach is changed so that more Ricker wavelets arrive around

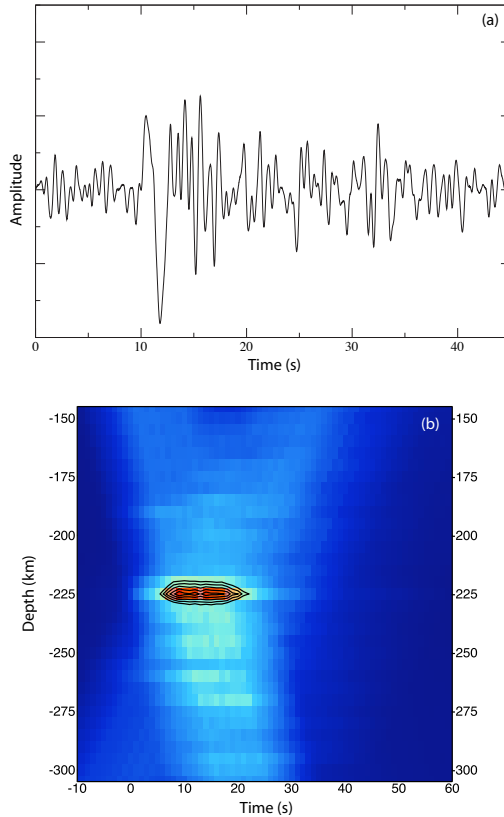


Figure 3.10: (a) The P waveform from the March 3, 2002 Hindu Kush earthquake recorded at station MIGH is used as the source-time function in the synthetic test for rupture complexity. (b) Back-projection result where the input source is located at 36.50° N, 70.48° E, and 225 km depth, i.e., a point source. For this synthetic test, only the P and sP seismic phases are used in the back-projection analysis since these are the phases used for the actual earthquake.

the depth phase time to mimic the crustal and water reflection phases while the P arrival consists of a single Ricker wavelet.

We determine the time shifts for the phases that interact with the crust and ocean using a 7 km thick crust, a 3 km thick ocean, and velocities from the one-dimensional model IASP91 [Kennett and Engdahl, 1991]. For the underside reflection at the Moho, a Ricker wavelet is assigned to arrive before both depth phases (pP and sP). For the pP phase, the time shift of -2.4 seconds is calculated using the two-way travel time of a P wave through the crust. For the sP phase, the time shift of -3.3 seconds is calculated by summing the one-way travel times of P and S waves in the crust. For both calculations, we make the approximation that the ray paths within the crust are vertical. To estimate the arrival times of the water phases, we use the two-way travel time of a P wave in the ocean. Once again, a vertical path is assumed, and the

time shift is 4.1 seconds with respect to the pP and sP arrival time. Figures 3.11(b) and (c) show that there is little change in the imaged energy of the depth phases for these synthetic tests compared to a single point source (Figures A.7b and c) although there is a slight extension in time. This is because the additional phases associated with the crust and ocean have origin times that are within or very close to the temporal uncertainty of the single point source (± 5 seconds). The combined result shows that the additional arrivals do not cause high amplitude artifacts at different depths, and produce results almost identical to a point. This approach assumes that phases associated with the crust and ocean can be represented by time shifted depth phases and ignores deviations in the slowness from the depth phases. These deviations in slowness are small, but if they were included when generating the synthetic seismograms, it would only decrease the stack amplitudes due to the fact that a different slowness would reduce coherent stacking of the additional phases using pP or sP arrival times. Therefore, the synthetic test shown in Figure 3.11 gives the maximum effect that can be produced by these phases.

We have only considered underside reflections in these synthetic tests and ignored multiple reflections within the crust and water column. Each reflection will change the slowness away from that of the slowness of the depth phases used in the back-projection analysis. Therefore, the stack amplitudes should be smaller than the underside reflections and contribute less to any possible artifacts. An additional source of complexity may be the seismic wave interactions with the subducting slab. We assume that any phases produced by these interactions would have lower amplitudes compared to the P and depth phases, however, only by fully modeling the wavefield can we confirm this assumption, and, therefore, slab interactions are a potential source of error. On the other hand, arrivals such as slab reflected phases would produce stacks with the same time dependence for various “sub-events” which is not

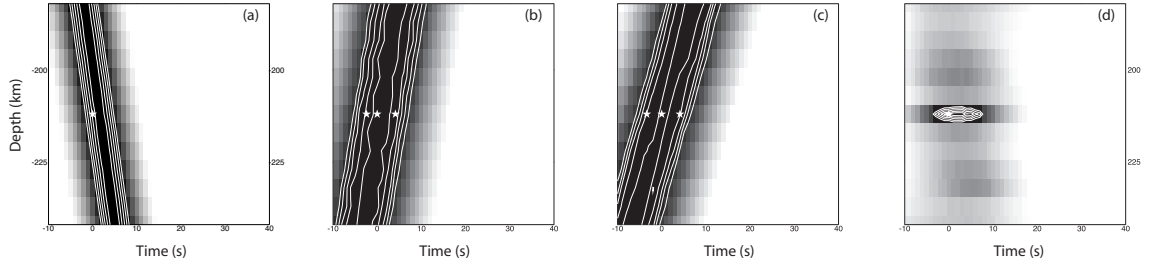


Figure 3.11: The back-projection result from a point source using only the P phase, as well as the back-projection result from the depth phases with additional sources included to simulate phases produced by bottom side reflections of the crust and the water surface. (a) The back-projection result from a single point source (black star) using only the P phase. (b) The back-projection result from three point sources (black stars) with the same hypocentral locations, but different origin times using pP travel times. The first star mimics the underside reflection at the Moho that arrives 2.4 seconds before the pP phase. This time is calculated using a 7 km thick crust with a P -wave velocity of 5.8 km/s from IASP91 [Kennett and Engdahl, 1991]. The second star is the hypocenter generating the P wave arrival. The third star mimics the underside reflection at the ocean surface that arrives 4.1 seconds after the pP phase. This time is calculated using a 3 km thick ocean with a P -wave velocity of 1.45 km/s from IASP91 [Kennett and Engdahl, 1991]. (c) The back-projection result from three point sources (black stars) with the same hypocentral locations, but different origin times using sP travel times. The first star mimics the underside reflection at the Moho that arrives 3.4 seconds before the sP phase. This time is calculated using a 7 km thick crust with P and S -wave velocities of 5.8 km/s and 3.36 km/s from IASP91, respectively [Kennett and Engdahl, 1991]. The second star is the hypocenter generating the P wave arrival. The third star mimics the underside reflection at the ocean surface that arrives 4.1 seconds after the sP phase. This time is calculated using a 3 km thick ocean with a P -wave velocity of 1.45 km/s from IASP91 [Kennett and Engdahl, 1991]. (d) The back-projection result using all three seismic phases with the simulated bottom side reflections included.

observed for most of the composite earthquakes. We believe that the artifacts due to the presence of a slab are not significant in most of our results.

3.4.2 PROPERTIES OF COMPOSITE RUPTURES

Based upon various resolution tests, we conclude that the imaged energy of the composite earthquakes is a real feature of rupture complexity. We explore this complexity further in this section. First, the timing of the individual sub-events for some of the composite events are such that dynamic triggering by seismic waves is likely to be involved in the activation of the second sub-event. For example, the March 3, 2002 Hindu Kush event shows a depth separation of 75 ± 5 km between individual sub-events. The time separation between the initiation of the two sub-events is about 8.5 ± 2.0 seconds, which implies that the minimum speed required to relate the two sub-events is around 8.8 ± 2.7 km/s (Figure 3.12). This velocity is in the range of compressional wave velocities, including those within the slab imaged from tomographic studies in the Hindu Kush region [e.g., Koulakov and Sobolev, 2006], but is too high for shear waves, which at 200 km depth have velocities around 4.5 km/s [Kennett and Engdahl, 1991]. The potential mechanism by which a compressional wave from one rupture would trigger a second rupture is discussed in a subsequent section. Another characteristic of the composite events is that often the individual sub-events have very different depth-time behavior. For example, the December 9, 2007, Mw 7.8 event has two ruptures which have considerable time overlap (Figure 3.4b). While the bottom rupture propagates upward with time, the top rupture maintains the same depth throughout its duration. This behavior suggests that the two ruptures are independent of one another.

The existence of multiple sub-events involving two independent faults can have effects on the non-double-couple component of the moment tensors [e.g., Houston,

1993]. This component is quantified using the parameter ϵ defined as $\epsilon = -\lambda_2 / \max(\lambda_1, \lambda_3)$ where λ values are the eigenvalues of the moment tensor with $\lambda_1 \geq \lambda_2 \geq \lambda_3$ [e.g., Ekström, 1994]. This parameter varies from 0.0 for a double-couple source to ± 0.5 for a purely non-double-couple source (i.e., compensated linear vector dipole). Using the Global CMT catalogue, the average absolute epsilon value of the events classified as “composite” in this study is 0.16, over twice that of the “simple” events (0.07). Furthermore, all five events with absolute epsilon values above 0.15 are imaged by the back-projection method as composite events. These results support the interpretation that sub-events are occurring as separate rupture planes.

Another property which may be related to the existence of composite events is the earthquake magnitude. Composite ruptures characterize most of the largest events studied, although there are a few smaller events ($M_w < 7.0$) which exhibit this behavior (e.g., Figure 3.5h). This observation suggests that the largest intermediate-depth earthquakes involve multiple faults, and that there could be predetermined rupture dimensions for any given region, which may be defined by preexisting faults in the slab. One test for this hypothesis is to determine the magnitude at which composite ruptures occur for different subduction zones or even different sections of the same subduction zone, though more than 22 events are needed to obtain statistically significant conclusions.

In addition, earthquake magnitude has been shown to be related to the duration of the event for shallow earthquakes in a relationship expected from a circular rupture model, i.e., $\tau \propto M_o^{1/3}$, where τ is the event duration and M_o is seismic moment [e.g., Vidale and Houston, 1993]. Multiple studies have investigated this relationship for intermediate-depth earthquakes [e.g., Vidale and Houston, 1993; Bos et al., 1998; Houston et al., 1998; Campus and Das, 2000; Houston, 2001; Persh and Houston, 2004], and found that the durations of the largest intermediate-depth events tend to be

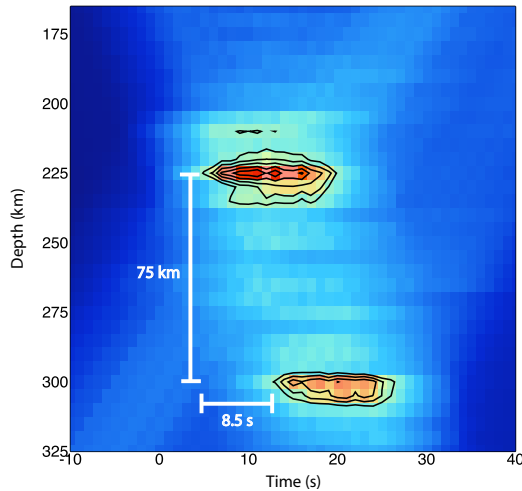


Figure 3.12: The back-projection results from the March 3, 2002 Mw 7.4 Hindu Kush event. The two ruptures of this event are separated by 75 km in depth and 8.5 seconds in time. This leads to a propagation velocity of 8.8 km/s, which is close to the P -wave velocity in this region.

shorter than expected from the magnitude-duration relationship observed for shallow earthquakes. The results presented in this manuscript offer a possible explanation for this behavior. If two faults are rupturing at the same time, the duration recorded on seismograms should be much shorter than the duration of an event on a single fault with the same magnitude. As Tables 3.1 through 3.5 show, summing the durations of individual sub-events leads to longer cumulative durations than the event durations discussed earlier. These observations may explain why the largest intermediate-depth earthquakes have shorter durations than expected, however, more data are needed to test this hypothesis.

3.4.3 DEPTH VARIATION OF INDIVIDUAL SUBEVENTS

In this subsection, we explore the implications of the sub-event vertical extents in terms of fault geometry, slip, and rupture propagation. The frequent observation of sub-events with limited depth extent is consistent with recent directivity studies that found a predominance of sub-horizontal rupture planes for large, intermediate-depth earthquakes [Warren et al., 2007, 2008]. Other studies have also observed this behavior for a small number of events [e.g., Suzuki and Kasahara, 1996; Antolik et al., 1999;

Tibi et al., 2002; Delouis and Legrand, 2007]. However, the back-projection method cannot distinguish sub-horizontal rupture propagation from a stationary source, i.e., energy release from the same point location over a period of time. This scenario is unlikely for most of the sub-events considered in this study in which the duration is significantly longer than the time uncertainty of ± 5 seconds, and based upon the magnitude, slip is expected to occur over a relatively large area. Another shortcoming of the back-projection technique is uncertainty in the slip direction. Thus, given the typical focal mechanisms of the earthquakes studied, the depth-limited sub-events can be interpreted as having slip vectors that are parallel to the propagation direction (i.e., slip on a sub-horizontal plane) or having vertical slip (i.e., slip perpendicular to the propagation direction). In the latter case of vertical slip, the fault will require an uncommon aspect ratio compared to typical slip observed at shallow depths, i.e., a very thin (depth dimension) and long (lateral dimension) fault. Regardless of the slip direction, our observations require significant lateral and limited depth extents of the fault, and following previous studies [e.g., Warren et al., 2007, 2008], we interpret the sub-events to have sub-horizontal rupture planes.

3.5 THE PROPOSED MECHANISM OF INTERMEDIATE-DEPTH EARTHQUAKES

The observations presented in this study show that most of the large, intermediate-depth earthquakes have small vertical extents of energy release, which we interpret as slip on shallowly dipping rupture planes. We also find that a significant number of these events have multiple rupture planes that are clearly separated in depth. These constraints provide insight into the possible mechanism of large, intermediate-depth events. In this section, we briefly review possible fault orientation scenarios, followed by a comparison of our findings with previously proposed mechanisms, and provide

a new hypothesis for the generation of large intermediate-depth earthquakes.

3.5.1 POSSIBLE FAULT ORIENTATIONS

The observation of shallow dipping rupture planes suggests that either an isobaric process is generating large, intermediate-depth earthquakes, or there are weak zones within the subducting slab that all have a sub-horizontal orientation [Warren et al., 2007, 2008]. For the latter case, one candidate for weak zones is faults generated in the outer rise of the subduction zone [e.g., Savage, 1969; Jiao et al., 2000; Ranero et al., 2005]. Multiple studies using a variety of methods, such as seabeam mapping, seismic reflection, and aftershock distributions, have imaged the orientation of outer-rise faults [e.g., Masson, 1991; Kobayashi et al., 1998; Ranero et al., 2003, 2005; Fromm et al., 2006; Hino et al., 2009]. These studies show that the outer-rise faults, associated generally with bending and subduction of the plate, strike sub-parallel to the trench. With the possible exception of Central America [e.g., Ranero et al., 2003], they also show the formation of horst-and-graben structures with conjugate faults dipping toward and away from the trench [e.g., Masson, 1991; Kobayashi et al., 1998; Ranero et al., 2005; Fromm et al., 2006; Hino et al., 2009], and dip angles typically varying between 30 and 60 degrees [e.g., Savage, 1969; Jiao et al., 2000]. During subduction, these faults are rotated by the angle of subduction which is typically between 40 and 60 degrees [e.g., Luyendyk, 1970; Cruciani et al., 2005], resulting in a set of faults that are nearly horizontal and vertical at depth (Figure 3.13a) [e.g., Savage, 1969; Jiao et al., 2000]. If these features are associated with intermediate-depth earthquakes, then an explanation must be provided for the preferential reactivation of sub-horizontal faults at depth.

Sub-horizontal rupture planes may also suggest the importance of isobaric processes in generating large, intermediate-depth earthquakes. One possibility is that

transformational faulting is generated through a phase change as minerals are subducted to higher pressures. The main problem with this hypothesis is that the minerals which undergo phase transformations at intermediate depths only make up a small percentage of the subducting slab, and therefore could not generate a large rupture [Green and Houston, 1995]. Alternatively, it is possible that fluids, which facilitate rupture, follow an isobaric path under certain conditions. We will revisit this fluid path argument in a later section.

3.5.2 PREVIOUSLY PROPOSED MECHANISMS

Unlike shallow earthquakes, high pressures at intermediate depths should prohibit crack formation and brittle failure due to simple strain accumulation. Hypotheses for the mechanism of intermediate-depth earthquakes are therefore much different than those of shallow events and include partial melting [e.g., Savage, 1969], transformational faulting [e.g., Green and Burnley, 1989], localized shear instabilities [e.g., Ogawa, 1987; Hobbs and Ord, 1988], localized viscous creep due to a grain-size difference within and outside the faults [Keleman and Hirth, 2007], and dehydration embrittlement [e.g., Raleigh and Paterson, 1965; Kirby et al., 1996; Hacker et al., 2003; Jung et al., 2004]. As will be explained below, both localized viscous creep and dehydration embrittlement are promoted by the presence of pre-existing faults. Based upon the observation of preferential sub-horizontal rupture plane orientations, we assume that intermediate-depth earthquakes are associated with pre-existing zones of weakness. Therefore, we will focus on localized viscous creep and dehydration embrittlement as possible mechanisms.

Localized Viscous Creep

Recent modeling work [Keleman and Hirth, 2007] has shown that shear heating due to localized viscous creep along fine-grained shear zones can produce instabilities and potentially generate earthquakes within the temperature range (600 to 800°C) commonly associated with intermediate-depth events [Peacock, 2001]. If these fine-grained weak zones within pre-existing faults are developed at the outer rise, this localized viscous creep mechanism would operate on both the sub-vertical and sub-horizontal faults. This is contrary to the observation that most large intermediate-depth earthquakes have sub-horizontal rupture planes [e.g., Suzuki and Kasahara, 1996; Delouis and Legrand, 2007; Warren et al., 2007, 2008, this study]. However, it may be possible to prevent reactivation of vertical faults at intermediate-depths if conditions for vertical and horizontal faults differ. For the localized viscous creep mechanism, the temperature and grain-size difference of the fault are the controlling parameters. If the temperature becomes too high, above 850°C [Keleman and Hirth, 2007], displacement will be accommodated by steady-state flow instead of instabilities. It has been observed that trenchward dipping faults (sub-vertical faults at intermediate-depths) are preferentially activated close to the trench [e.g., Masson, 1991]. This behavior is caused by the shear stresses imparted as the slab subducts beneath the overriding plate, which is likely to continue until the slab becomes coupled to the surrounding mantle. It is possible that preferential activation of these faults would cause an increase in their temperature and thus limit their rupture at intermediate-depths. This explanation is unsatisfactory, because heating due to rupture on vertical faults may also affect the temperature of the material surrounding the sub-horizontal faults. In addition, the preferential slip on the trench-ward dipping faults would also lead to smaller grain sizes for the nearly vertical faults compared to sub-horizontal faults.

This difference in the grain sizes within the fault gouge would promote slip on vertical faults based upon the localized creep mechanism. Therefore, localized viscous creep alone can not explain the observed tendency of rupture on sub-horizontal planes.

Dehydration Embrittlement

Another proposed mechanism that has become popular over the past twenty years is dehydration embrittlement [e.g., Raleigh and Paterson, 1965; Kirby et al., 1996; Hacker et al., 2003; Jung et al., 2004]. This mechanism argues that when water is released from hydrous minerals at depth, it increases the local pore pressure enough to counteract the confining pressure, allowing brittle failure. In order to account for the required existence of hydrous minerals, this mechanism is often described in association with faults that develop at the outer rise where water can propagate deep into the the mantle and hydrate the fault. This fault hydration at the surface would not create a significant difference in the amount of hydration between the faults that dip toward (vertical at intermediate-depths) and away from (horizontal at intermediate-depths) the trench. If anything, the preferential activation of the trench-ward dipping faults would allow more vertical faults to be hydrated. Therefore, without considering additional mechanisms, dehydration embrittlement of the outer-rise faults hydrated at the surface can not explain the predominance of sub-horizontal ruptures. Another potential problem is that the hydrous minerals must be preserved from the surface to great depths over many earthquake cycles. Finally, the stress changes from compressional waves should have a similar influence on the pore pressures of sub-horizontal and vertical faults, and therefore dehydration embrittlement alone can not explain the observed preferentially triggered sub-horizontal ruptures. Kuge et al. [2010] studied an earthquake in Tarapaca, northern Chile that occurred at a depth of 110 km, and observed two sub-events separated in depth, a result similar to those presented in this

manuscript. They propose that these sub-events represent the results of dehydration embrittlement in the upper crust and mantle [e.g., Peacock, 2001] during rupture of a fault that cuts through both, i.e., the sub-events correspond to the top and bottom seismicity of double Waditi-Benioff zones. This mechanism may be able to explain some of the back-projection observations at the shallowest depths considered here. However, many of the earthquakes we study take place deeper than the depths at which double seismic zones are observed.

3.5.3 PROPOSED MECHANISM FOR INTERMEDIATE-DEPTH EARTHQUAKES

The discussion in the previous section demonstrates that the available mechanisms for the occurrence of intermediate-depth earthquakes can not satisfy the observations of preferential activation of sub-horizontal rupture planes and P -wave triggering of sub-events. In this section, we propose a new mechanism for the generation of these earthquakes.

Subhorizontal Rupture Planes

The preference of sub-horizontal rupture planes at intermediate depths can be explained by considering post-subduction dehydration and pre-existing fault fabric. At the depths relevant to this study, i.e., between 100 and 300 km, the slab releases water as it reaches higher temperatures and pressures, and the water migrates toward the mantle wedge (Figure 3.13a). Some of this water will encounter the pre-existing faults along its migration path. The faults are characterized by smaller grain sizes compared to the surrounding material, and the difference in the grain sizes acts to concentrate water under these temperature and pressure conditions [Wark and Watson, 2000]. The water trapped in the faults can migrate along the fine-grained material, and once it reaches the interior of the slab where hydrous minerals are stable, the faults

can be replenished with hydrous minerals [e.g., Schmidt and Poli, 1998]. This water migration into the slab would be more efficient along the sub-horizontal faults since the pressure is nearly constant along these faults and the grain size difference inhibits farther vertical migration (Figure 3.13b). In contrast, water intersecting the vertical faults near the top surface of the slab experiences the same grain-size effect that tries to focus water within the fault zone, but downward migration into the serpentine stability zone within the slab must happen against the pressure gradient and buoyancy. This opposing force would likely limit the amount of water penetration into the slab interior and hence the rate at which sub-vertical faults can be replenished with hydrous minerals.

This difference in the rate at which hydration of sub-vertical and sub-horizontal faults can take place makes many more weaker sub-horizontal faults, allowing shear localization and instability to occur [e.g., Keleman and Hirth, 2007]. Once shear failure initiates, a temperature increase due to frictional heating and strain hardening [Chernak and Hirth, 2010] will dehydrate the hydrous minerals [e.g., Schmidt and Poli, 1998] to enhance the condition for slip. This constitutes a positive feedback mechanism where the temperature increase due to slip on one part of the fault causes dehydration of hydrous minerals on adjacent parts of the fault, promoting further slip. It is also possible that each rupture event will extend the damage zone into deeper and colder parts of the slab. The finer-grained material of these new damage zones will concentrate water and generate hydrous minerals, allowing replenishment and reactivation of pre-existing faults to greater depths.

There are a few points of this hypothesis which are worth reemphasizing. First, the mechanism described above does not necessarily apply to smaller events. The initiation of rupture due to the small grain size of the fault zone may be enough to produce small ruptures on faults of any orientation. However, the runaway dehy-

dration reaction will better accommodate the large rupture areas required for large earthquakes. Second, it has been suggested that fault zones would grow into the slab with each rupture. This growth would allow parts of the fault zones to remain within the cold slab, allowing for mineral hydration, even as this region becomes smaller as the slab warms. Finally, many studies have argued that outer rise faults are hydrated well into the mantle before subduction, and this hydration is what allows faults to be reactivated as depicted by double seismicity zones [e.g., Peacock, 2001; Ivandic et al., 2010]. The hypothesis proposed in this study does not preclude hydration at the surface, but puts more emphasis on hydration within the slab after subduction for generating large, intermediate-depth earthquakes. The faults are expected to lose water when an earthquake occurs, so the replenishment will also help explain the great depths to which earthquakes are observed.

Dynamic Triggering

The hypothesis for the preferential occurrence of rupture on sub-horizontal planes must also be consistent with the observation that dynamically triggered multiple ruptures commonly contribute to a large event. Theoretical work at low temperatures and pressures relevant for shallow-focus earthquakes has shown that for faults with significantly lower shear moduli, the pore pressures, and hence effective normal stress, are controlled by fault-normal stresses [Cocco and Rice, 2002]. Extending this argument to faults at depth, the interaction of the compressional wave, therefore, could reduce the effective normal stress on a hydrated fault through elevated pore pressure. If shear has already been localized on the fault through mechanisms such as viscous creep localization, the sudden reduction in effective normal stress will initiate slip. Our observations show that the triggered rupture planes are also sub-horizontal, and therefore, these faults may contain a sufficient amount of hydrous minerals to

experience the same positive feedback process proposed to explain the preferential slip on sub-horizontal faults.

Given the runaway dehydration mechanism, at least two conditions must be satisfied for two faults to ultimately rupture together. First, the stress state of the two faults must be very similar. Even with stress perturbations from seismic waves, the shear instability that initiates both ruptures requires hundreds of years of stress buildup before it becomes feasible [Keleman and Hirth, 2007]. Recent work on shallow earthquakes may be able to explain this fault synchrony. If two nearby faults have similar dimensions, orientations, and slip rates, then the static stress changes from rupture on each fault may, over the course of many earthquake cycles, bring the rupture cycles of the two faults into phase. When this occurs, the two faults will become locked in phase [Scholz, 2010]. It seems possible that this same synchronization mechanism would operate at intermediate depths.

The second condition is a high degree of hydration on the triggered fault. If faults near the initial rupture are relatively dry, the P waves may not reduce the effective normal stress enough for the initial slip (Figure 3.13c). Adequate hydration is also necessary for the positive feedback mechanism that would cause the second rupture to grow in size. The mechanism by which hydration synchronization occurs may be similar to the stress synchronization described above. If two faults are at different hydration stages, with one fault being well-hydrated and the other not at all hydrated, then rupture on the hydrated fault will make water available to the less hydrated fault. This should bring the second fault closer to failure, and bring the rupture cycles of the two faults closer to being in-phase. Both the stress change and hydration mechanisms should act together to bring nearby faults into synchrony, and may explain why triggering is so common at intermediate depths.

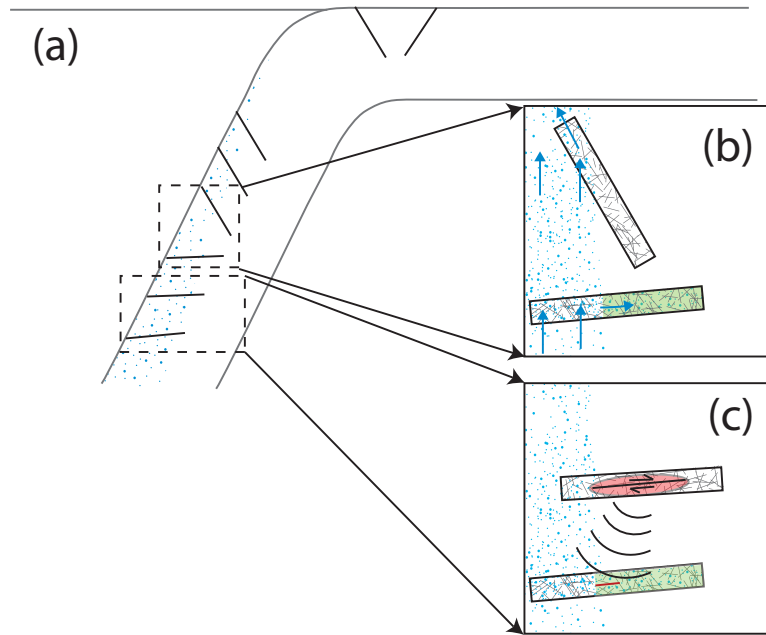


Figure 3.13: Cartoon of a slab subducting into the mantle with pre-existing fault fabric and the mechanisms responsible for the generation and triggering of intermediate-depth earthquakes. (a) Schematic of the orientation of the pre-existing faults (black lines) when they develop at the outer rise and after plate subduction. The blue stippled region depicts dehydration of the slab as it subducts into the mantle. (b) Enlarged view of the two conjugate faults (damage zones within the fault depicted by cross hatching) at intermediate depth. The blue arrows show propagation of water as it dehydrates from the slab and travels into the mantle wedge. Water would propagate deep into the slab more efficiently along a sub-horizontal fault with near constant pressure as opposed to a steeply dipping fault for which the grain-size difference may not be strong enough to effectively oppose the pressure gradient. The green region depicts the hydrated material. (c) Detailed schematic of the processes around pre-existing faults. Rupture on one sub-horizontal fault (red region with opposing arrows) generates seismic waves (curved black lines) that trigger slip (red line) on a second fault that has been weakened by water focusing and serpentinization. This initial slip will generate heat which will dehydrate the surrounding serpentine and lead to the positive feedback between dehydration embrittlement, slip, and heat generation discussed in the main text.

3.6 SUMMARY

A back-projection technique first used by Ishii et al. [2005] has been modified for better depth resolution using depth phases, and applied to study the depth-time behavior of twenty-two intermediate-depth earthquakes recorded at the Hi-net array in Japan. These earthquakes have a variety of magnitudes and source depths. We find that no single sub-event has a rupture extent in depth greater than 35 km, and most of the ruptures have vertical extents less than or equal to 15 km. This result supports previous studies that find a prevalence of shallow dipping rupture planes for large, intermediate-depth earthquakes [e.g., Suzuki and Kasahara, 1996; Delouis and Legrand, 2007; Warren et al., 2007, 2008]. We, therefore, interpret observations of planes with less than 15 km depth extent as slip on sub-horizontal faults created at the outer rise. The frequent occurrence of events with this geometry is explained with preferential focusing of water and subsequent generation of hydrous minerals in sub-horizontal faults. The second key observation from this study is that a significant portion of the earthquakes have multiple rupture planes separated in depth. Given the closeness in time and the separation distance of these ruptures, it appears that the seismic waves, specifically, the compressional waves, from one sub-event are triggering slip on a different fault. The conditions proposed to explain sub-horizontal ruptures also make these faults susceptible to being triggered by seismic waves from an abrupt reduction in the effective normal stress.

CHAPTER 4

RUPTURE SEGMENTATION

4.1 INTRODUCTION

One of the most important roles of seismology is characterizing the complexity of large earthquakes. Shortly after a large event, estimates of rupture parameters such as regions of highest slip, rupture speed, and rupture direction all contribute to assessing potential hazards, such as the generation of tsunamis and the intensity of ground shaking. In addition, it has been argued that large earthquakes are controlled by topographic features of the subducting plate and coupling along the subduction interface [e.g., von Huene et al., 1997; Moreno et al., 2010]. For such comparisons to be made, an accurate description of the source complexity is needed. We approach this problem by applying the multi-array back-projection technique (See Chapter 2) to determine the spatio-temporal behavior of energy release for the 2007 Mw 8.0 Pisco, 2007 Mw 8.4 & 7.9 Mentawai Islands, 2009 Mw 8.1 Samoa Islands, and 2010 Mw 8.8 Maule earthquakes.

4.2 DATA AND DATA PROCESSING

In this chapter, we use two seismic arrays, the High Sensitivity Seismograph Network (Hi-net) in Japan and the USArray Transportable Array (TA) in the United States. Only the vertical components in these arrays are used in this study, and data from both arrays are bandpass filtered between 1 and 5 Hz, with 1-second period waves dominating the signal.

As described in Chapter 2, when the multi-array back-projection analysis is used, there are two time corrections applied to the data, one to correct for lateral variations in the three-dimensional velocity structure of the Earth (Δt_k) and one to ensure that the hypocentral stacks add coherently from different arrays (Δt_j). Within each array, we cross-correlate each seismogram with a reference seismogram as outlined in Ishii et al. [2007] to obtain the time shift Δt_k . Δt_j is obtained by cross-correlating the hypocentral stacks from TA and Hi-net. For all five earthquakes, the TA stacks are used as the reference stacks.

In addition to these two time corrections, there are also two weighting factors α_k and w_j . The station-specific weighting factor, α_k , normalizes the seismograms within each array, and is obtained from the same cross-correlation procedure that determines Δt_k . The array-specific weighting factor, w_j , is the ratio of the maximum amplitudes of the hypocentral stacks from each array. Figure 4.1 shows an example of the hypocentral stacks from the Samoa Islands event after these time corrections and weighting factors have been applied.

This study investigates the 2007 Mw 8.0 Pisco, Peru, 2007 Mw 8.4 Mentawai Islands, 2007 Mw 7.9 Mentawai Islands, 2009 Mw 8.1 Samoa Islands, and 2010 Mw 8.8 Maule, Chile earthquakes. Four of these events have epicenters relative to Hi-net or TA that require the use of seismic phases other than the direct P phase, which is

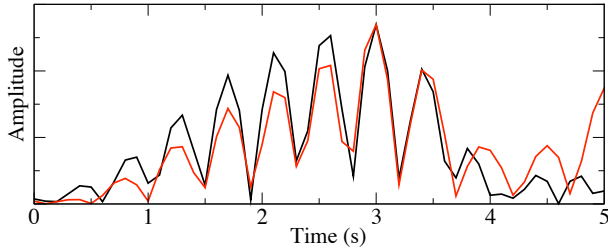


Figure 4.1: Back-projection stacks from TA (red) and Hi-net (black) at the epicenter of the 2009 Samoa Islands earthquake after the time correction Δt_j and weighting factor w_j is applied. Time is with respect to the epicentral time.

typically used in back-projection studies [e.g., Ishii et al., 2005, 2007; Walker et al., 2005; Walker and Shearer, 2009]. For the 2007 Peru event, the range of distances from the hypocenter to Hi-net is 133 to 150 degrees, hence there is a core phase triplication (e.g., *PKPab*, *PKPbc*, and *PKIKP*; Figure 4.2). Based upon visual inspection of the seismograms, we find that using the stations with distances at or greater than 146 degrees isolates a coherent *PKPbc* arrival, and this is the phase used in the back-projection analysis. Limiting the distance of the stations for this specific earthquake reduces the number of seismograms to 137. The range of distances of Hi-net stations from the hypocenter of the 2010 Chile event is 150 to 162 degrees. Limiting the stations used to distances of 155 degrees and greater results in a set of 367 seismograms with coherent *PKIKP* phase arrivals. The hypocenters of the two 2007 Mentawai Islands earthquakes are at distances between 121 and 141 degrees from TA such that the *PKIKP* phase is the first to arrive. No distance constraint is applied to the TA data for either of the Mentawai Islands events.

4.3 RESULTS AND DISCUSSION

For each of the five events studied, we estimate the rupture duration, rupture direction, rupture length, rupture speed, and the spatial distribution of energy release for the entire rupture. The rupture duration is estimated from the relative source-time function of the back-projection results. For the total duration, we choose the end

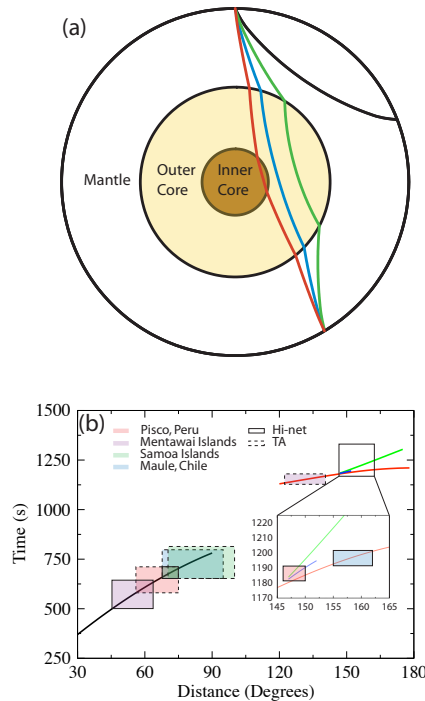


Figure 4.2: (a) Ray paths for the P (black), $PKPab$ (green), $PKPbc$ (blue), and $PKIKP$ (red) seismic phases. (b) Travel-time plot for the P (black), $PKPab$ (green), $PKPbc$ (blue), and $PKIKP$ (red) seismic phases. The inset shows the core phase triplication. The rectangles show the distance ranges of TA and Hi-net from the four regions studied.

of the rupture to correspond to the time at which the amplitude from the relative source-time function lowers to a value between 0.3 to 0.4 of the maximum value. This means that the estimates of total duration are probably lower bounds, since it can be argued that the end of the rupture occurs at the time when the amplitude is the same as at the hypocentral time (typically around 0.1 of the maximum amplitude). Rupture direction, rupture length, and rupture speed are calculated based upon the centers of the energy kernels at different times during the rupture. Earthquake sub-events are identified based upon dramatic changes in rupture direction and speed. For the earthquakes with multiple sub-events, rupture duration, rupture direction, rupture length, and rupture speed are estimated for each sub-event. To determine the spatial distribution of energy release for the entire earthquake, we select a contour that encloses an area that matches the moment magnitude given by the USGS earthquake catalogue assuming a typical stress drop of 30 bars [Kanamori, 1977,

<http://earthquake.usgs.gov/earthquakes/>]. The results of each earthquake are followed by a comparison of the rupture parameters with those from previous studies. In addition, we discuss the results in the context of rupture segmentation and the seismogenic zone.

4.3.1 THE 2007 AUGUST 15 MW 8.0 PISCO, PERU EARTHQUAKE

Figure 4.3(a) shows the distribution of energy release for the entire Pisco, Peru earthquake. This result indicates that the rupture is very compact. The relative source-time function shows that there are two distinct sub-events with durations of 20 seconds each (Figures 4.3b). The first sub-event propagates southeast from the epicenter at a speed of about 1.3 km/s, with a total rupture length of 25 km (Figures 4.3c). The second sub-event starts slightly updip of the terminus of the first sub-event, and has a larger amplitude of relative energy release than the first event. This rupture propagates north at a speed of 2.5 km/s, and has a rupture length of 50 km (Figures 4.3c). The spatial gap between the terminus of the first sub-event and the beginning of the second sub-event is about 15 km to the west and the temporal gap is about 25 seconds.

Numerous studies using seismic and geodetic data have investigated the rupture of the 2007 Peru event [e.g., Motagh et al., 2008; Pritchard and Fielding, 2008; Biggs et al., 2009; Hébert et al., 2009; Lay et al., 2010a; Perfettini et al., 2010; Sladen et al., 2010]. Most of these results have largest slip west or southwest of the Paracas Peninsula, with only minor moment release near the epicenter. The back-projection results showing low-amplitude energy release near the epicenter (sub-event 1) agree well with these previous studies. In addition, the timing of the high amplitude of the second sub-event imaged by the back-projection analysis, and its updip location with respect to the epicenter are consistent with previous work [Fritz et al., 2008; Motagh et al., 2008; Pritchard and Fielding, 2008; Biggs et al., 2009; Hébert et al., 2009; Sladen

et al., 2010]. However, in contrast to most studies which place this second rupture west or southwest of the Paracas Peninsula, the rupture imaged by back-projection is located north of the Paracas Peninsula. One possible explanation for the discrepancy comes from the fact that we are using high-frequency data (1-5 Hz). The slip south of the Paracas Peninsula may have a longer rise time, and may not efficiently radiate high-frequency energy [e.g., Madariaga, 1977]. A longer rise time is also consistent with efficient excitation of tsunami waves from this region. In addition to differences in the general locations, the second rupture, as imaged by back-projection, propagates north, back towards the epicenter, at a velocity significantly higher than the initial rupture. Both of the ruptures imaged using back-projection occur in a region of high interseismic coupling as determined using GPS data [Perfettini et al., 2010].

4.3.2 THE 2007 SEPTEMBER 12 MW 8.4 AND MW 7.9 MENTAWAI ISLANDS, WEST SUMATRA EARTHQUAKES

This pair of earthquakes took place on September 12, 2007 in the Mentawai Islands region in Indonesia and were separated by 12 hours from each other. The energy distribution for the first event (Mw 8.4) is shown in Figure 4.4(a). The back-projection result shows that most of the energy is released northwest of the epicenter. The relative source-time function shows a rupture duration of 90 seconds and energy is released continuously throughout the event, though there are two clear episodes of peak energy release (Figure 4.4b). The rupture propagates mostly unilaterally to the northwest for about 170 km (Figure 4.4c), which leads to an average rupture speed of 1.9 km/s. One interesting feature of the event is the down-dip propagation at a latitude of about 4 degrees south (Figure 4.4c). This down-dip propagation takes place 40 to 50 seconds after the hypocentral time, and is followed by an increase in the along-strike rupture velocity from 1.4 km/s to 2.5 km/s. The location of the down-

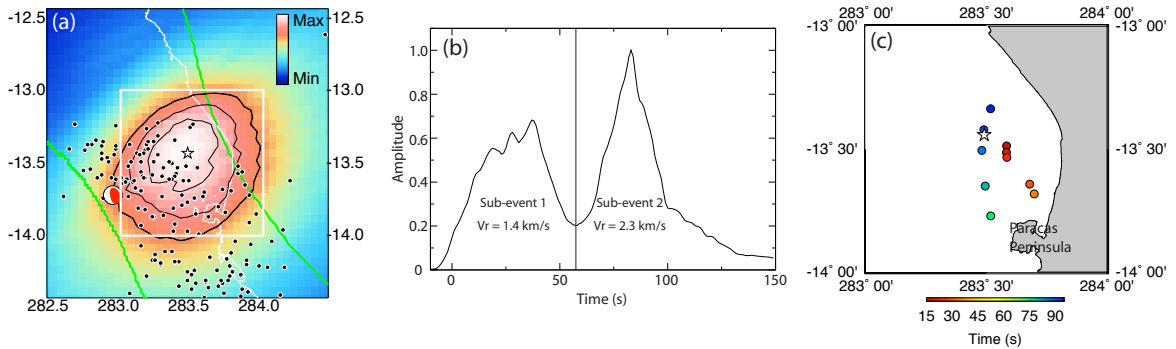


Figure 4.3: (a) Spatial distribution of the normalized energy released during this earthquake as imaged by the back-projection method. This figure is obtained by integrating the squared amplitude of the stacks over a time window of 15 seconds. The light grey lines are the contours of maximum energy release in 10% intervals. The focal mechanism is taken from the Global CMT Catalogue [Dziewoński et al., 1981; Dziewoński and Woodhouse, 1983, <http://www.globalcmt.org/>]. The epicenter (white star) and aftershock locations for the first three months following the mainshock (black circles) come from the National Earthquake Information Center (<http://earthquake.usgs.gov/earthquakes/>). The thick black contour is the 70% contour that represents the total rupture area for this event. The green lines are the upper and lower bounds of the seismogenic zone (Heuret *et al.* 2011). The white box is the region of (c). (b) Relative source-time function of the 2007 Peru event. The amplitude has been normalized so that the maximum amplitude is one. Time is with respect to the hypocentral time. (c) Locations (circles) of the imaged energy at different times during the rupture. The first sub-event occurs between 15 and 35 seconds after the hypocentral time. The second sub-event occurs between 75 and 95 seconds after the hypocentral time. For both sub-events, the locations are plotted every 5 seconds. The white star is the epicenter. The times on the scale are with respect to the hypocentral time.

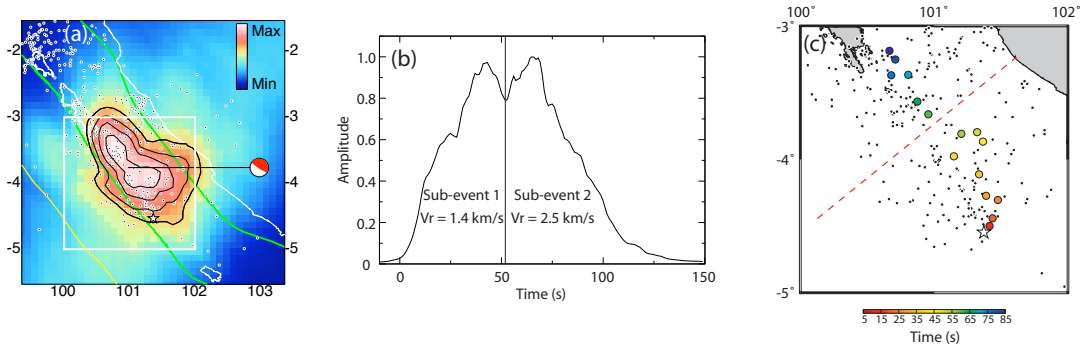


Figure 4.4: (a) The same as in Figure 4.3(a) except that the thick black contour is the 60% contour that represents the total rupture area for this event. The yellow line is the trench location. The CMT is offset from its location to show the changes in energy release better, and the black line connected to the CMT plot shows its actual location. (b) The same as Figure 4.3(b) except for the 2007 Mw 8.4 Mentawai Islands event. (c) The same as Figure 4.3(c). The red dashed line marks the break in the aftershocks for the first three months following the mainshock. The colored circles are plotted between 5 and 90 seconds after the hypocentral time every 5 seconds.

dip propagation also corresponds to a noticeable break in the aftershock distribution (Figure 4.4c)

The second event (Mw 7.9) begins down-dip of the terminus of the first event (Figure 4.5a). The majority of the energy is released northwest and updip of the epicenter (Figure 4.5a). The rupture is composed of two distinct high-amplitude sub-events with durations of 30 and 40 seconds. These sub-events are separated by 25 seconds of low amplitude energy release, which leads to a total duration of 95 seconds (Figure 4.5b). The along-strike length of the total rupture is about 150 km, leading to an average rupture speed of 1.6 km/s. The distribution of rupture locations has a distinct dumbbell shape showing that the main energy release had extensive propagation along the dip direction (Figure 4.5c). Note that this along-dip rupture makes the average rupture speed estimate of 1.6 km/s a lower bound. Between the two episodes of along-dip propagation, lower-amplitude energy is seen to travel

smoothly along strike. Dividing the rupture into three sub-events provides a much more complete rupture picture. The first sub-event propagates mainly down-dip to the north/northeast for a distance of 45 km and at a speed of 3.0 km/s. The second, low amplitude sub-event propagates along-strike to the northwest for about 40 km at a velocity of 2.7 km/s. Finally, the third sub-event propagates mostly down-dip to the northeast at a velocity of 2.0 km/s for a distance of 80 km.

A previous study of the September 12, 2007 Mentawai Islands earthquakes agrees well with the back-projection results of this study. Using GPS, coral, and InSAR data, Konca et al. [2008] determined a northwest trending distribution of slip away from the epicenter for both the 8.4 and 7.9 events. These results show a concentration of slip into two asperities for both events, consistent with results obtained in this study. In addition, Konca et al. [2008] also show extensive down-dip rupture of the asperities of the 7.9 event.

The rupture patterns imaged by the back-projection analysis for both events correlate well with the pattern of interseismic coupling along the Sunda subduction zone, where the regions of highest coupling also experienced the highest energy release [Chlieh et al., 2008; Konca et al., 2008]. The one exception to this conclusion is the first part of the Mw 8.4 event which takes place in a region of low coupling south of South Pagai Island, though the sparseness of GPS and coral data may make it difficult to determine the coupling in this region [Chlieh et al., 2008].

4.3.3 THE 2009 SEPTEMBER 29 MW 8.1 SAMOA ISLANDS EARTHQUAKE

Unlike the other events in this study, the 2009 Samoa Islands event is an intraplate event that occurred in the outer rise of the Tonga subduction zone. The energy release of this event is focused around the epicenter (Figures 4.6a). However, the relative source-time function reveals significant complexity with at least two sub-

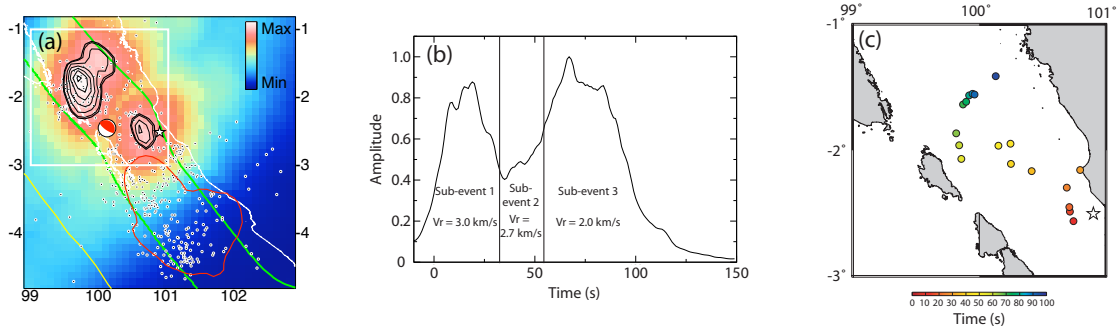


Figure 4.5: (a) The same as in Figure 4.3(a) except that the thick black contour is the 83% contour that represents the total rupture area for this event. The yellow line is the trench location, and the red contour is the 60% contour of the Mw 8.4 event (Figure 4.4a). (b) The same as Figure 4.3(b). (c) The same as Figure 4.3(c). The colored circles are plotted between 5 and 90 seconds after the hypocentral time every 5 seconds.

events composing the earthquake (Figures 4.6b). The first, weak sub-event begins at the epicenter and propagates north for around 15 seconds at an average speed of 1.8 km/s. The rupture length of this sub-event is 25 km (Figures 4.6c). The second sub-event, which releases most of the energy, originates about 50 km northwest and 10 seconds after the terminus of the first sub-event, and lasts 20 seconds with a rupture length of 40 km and a rupture velocity of 2.0 km/s to the southeast (Figures 4.6c). The propagation velocity between the end of the first sub-event and beginning of the second sub-event is about 5.0 km/s. This is much higher than the S wave speed at 10 to 20 km depth [Kennett and Engdahl, 1991, 3.4 km/s based upon IASP91].

The September 29, 2009 Samoa Islands earthquake has been modelled using seismic, GPS, and tsunami data [Beavan et al., 2010; Lay et al., 2010c; Okal et al., 2010]. Two of these studies argue for a “hidden” thrust event in addition to the normal event in the outer rise [Beavan et al., 2010; Lay et al., 2010c]. Using GPS and tsunami data, Beavan et al. [2010] prefers a model in which a thrust event with a long rise time ($>$

200 s) occurs on the subduction interface and precedes the outer rise normal event by about 2 minutes. In this model, the moment magnitude of the thrust event is slightly larger than the outer rise event that follows. A second model that could not be ruled out by Beavan et al. [2010] is that the thrust event occurs shortly after (< 50 s) the normal event and has a much shorter rise time than in the first model (< 100 s). This model agrees with Lay et al. [2010c] who model the earthquake using both body and surface waves. Their preferred model has two smaller interface thrust events (Mw 7.8) occurring 50 to 90 seconds and 90 to 130 seconds after the initiation of the Mw 8.1 outer rise normal event. The activation of the subduction interface is corroborated by increased seismic activity (Figure 4.6b). Most of the aftershocks occur west of the trench, and only a few aftershocks are located near the outer rise region.

In contrast to these studies, the back-projection results presented in this manuscript show no significant energy release west of the trench (Figure 4.6a). The earthquake is composed of two sub-events with very different rupture directions, but they are both located in the outer rise region. There are, however, low amplitude features in our results that may correspond to the thrust events argued by Lay et al. [2010c]. The largest of these low-amplitude features occurs 120 seconds after the epicentral time and almost 75 km west of the trench. This feature has the timing and location of an aftershock imaged in Lay et al. [2010c]. The next largest feature in the back-projection energy occurs at about the same time as the thrust events in Lay et al. [2010c], i.e., 80 seconds after event initiation. However, the location of this energy is east of the trench in the outer rise instead of along the subduction interface. This location offset of the thrust event is also evident in some of the supplementary back-projection results accompanying Lay et al. [2010c] in which seismic arrays other than F-net are used.

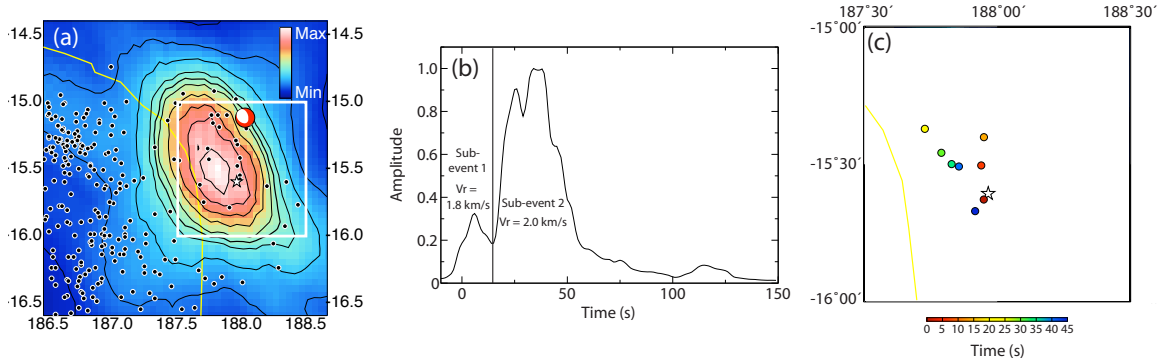


Figure 4.6: (a) The same as in Figure 4.3(a). This plot is made by integrating the squared amplitude of the stacks over a time window of 10 s. The thick black contour is the 45% contour that represents the total rupture area for this event. (b) The same as Figure 4.3(b) except for the 2007 Mw 8.1 Samoa Islands event. (c) The same as Figure 4.3(c). The first sub-event occurs between 0 and 14 seconds after the hypocentral time and the colored circles are plotted every 7 seconds. The second sub-event occurs between 25 and 45 seconds after the hypocentral time and locations are plotted every 5 seconds.

The exact location of the thrust event has important implications for future seismic hazards in the region. For example, if the thrust event did occur on the plate interface, a similar event in the near future may be unlikely. On the other hand, if the thrust event occurred in the outer rise, the aftershocks along the plate interface may be a sign of stress transfer from the outer rise to the plate interface which could lead to an interplate thrust event. Such a stress transfer has been documented south of the Samoa Islands region, along the Kermadec subduction zone [Habermann and Wyss, 1984]. A similar increase in seismicity along the plate interface is observed after the magnitude 7.3 July 2, 1974 outer rise event followed by a magnitude 8.0 thrust event on the plate interface on January 14, 1976 [Habermann and Wyss, 1984].

4.3.4 THE 2010 FEBRUARY 27 MW 8.8 MAULE, CHILE EARTHQUAKE

As demonstrated with the resolution tests in Section A.2.2, the Hi-net data does not provide substantial improvements to lateral resolution in the Chile region. Furthermore, the Hi-net data are noisy due to the large distance from the hypocenter and weak arrival of the core phase. While the rupture can be imaged using both arrays, TA provides very good lateral resolution for this event, and therefore we will only use data from this array.

The spatial extent of this event indicates that most of the rupture takes place north of the epicenter (Figures 4.7a). The relative source-time function suggests that the rupture is composed of at least two sub-events (Figures 4.7b). The first sub-event propagates bilaterally, both southwest and northeast away from the epicenter, though the northern rupture has a much higher amplitude (Figures 4.7c). The extent of this northern component of the rupture is 100 km, and it lasts about 45 seconds. This leads to an average rupture speed of 2.2 km/s. The second sub-event, as defined by the source-time function, is composed of two separate sub-events, one north of the epicenter and one south of the epicenter. The rupture north of the epicenter begins updip (about 75 km north/northwest) of, and shortly after (10 seconds), the northern terminus of the first sub-event, and has the largest energy release of all the sub-events (Figures 4.7b). The spatio-temporal gap between these two sub-events requires a propagation velocity of 7.5 km/s, only slightly below the P -wave speed at the hypocentral depth [Kennett and Engdahl, 1991, 8.0 km/s given by IASP91]. The northern rupture propagates north at an average speed of 2.9 km/s with an along-strike length of 175 km and a duration of 60 seconds (Figures 4.7c). In contrast, the rupture south of the epicenter has a substantially lower amplitude than the northern sub-events. This makes it difficult to image the southern rupture until

about 70 seconds after rupture initiation at which time an episode of stronger energy release occurs. This rupture is either a continuation of the southward propagation of the initial rupture or it is a rupture on a separate fault segment. There is a significant reduction in the rupture velocity to 0.8 km/s and a change in the rupture direction to the east. This sub-event lasts about 20 seconds, and has a length of 15 km (Figures 4.7c).

Most of the previous studies of the Mw 8.8 2010 Maule, Chile earthquake using seismic, geodetic, and tsunami data generally agree with the current study, with highest slip north of the epicenter [e.g., Delouis et al., 2010; Lay et al., 2010a; Moreno et al., 2010; Lorito et al., 2011]. However, there have been conflicting reports regarding whether the high slip patches correlate with regions of high interseismic coupling [Moreno et al., 2010; Lorito et al., 2011]. As with the Pisco, Peru and Mentawai Islands earthquakes, the two northern ruptures presented in this study correlate well with regions of high interseismic coupling, with the rupture jump occurring in a region of relatively low interseismic coupling [Moreno et al., 2010; Kiser and Ishii, 2011].

4.3.5 TRIGGERED SLIP ON ADJACENT SEGMENTS

Back-projection results from all five earthquakes show that these giant events are composed of multiple sub-events. Evidence for this segmentation varies between subtle changes in rupture speed to abrupt changes in rupture direction. As reported in Sections 4.3.1 through 4.3.4, sometimes there is a noticeable jump in the rupture location accompanying the transition from one sub-event to the next. In two cases, these jumps between the multiple ruptures occur where interseismic coupling along the subduction interface abruptly changes. For the 2010 Chile event, the jump occurs at about 35° S latitude where there is relatively low coupling [Moreno et al., 2010]. Similarly, the updip jump between the ruptures of the 2007 Pisco, Peru event occurs

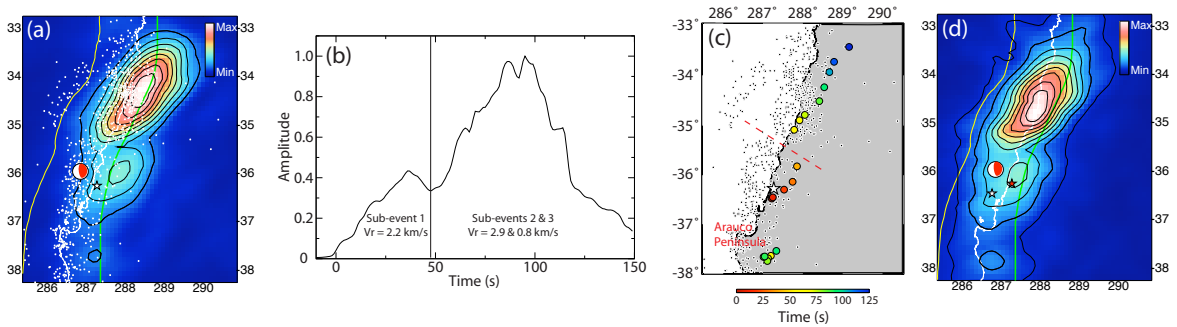


Figure 4.7: (a) The same as in Figure 4.3(a). This plot is made by integrating the squared amplitude of the stacks over a time window of 20 s. The thick black contour is the 23% contour that represents the total rupture area for this event. (b) The same as Figure 4.3(b). (c) The same as Figure 4.4(c) with the red dashed line showing a break in the aftershocks. (d) The same as (a) except using the hypocenter reported by the National Seismological Service in Chile. The white star is the epicenter reported by the National Seismological Service in Chile (36.47° S, 73.24° W) and the red star is the epicenter reported by NEIC.

at the edge of a high coupling zone, slightly north of where the Nazca Ridge subducts [Perfettini et al., 2010]. These comparisons suggest that seismogenic segmentation of the slab interface is partially controlled by factors that dictate interseismic coupling. Furthermore, updip jumps are observed to accompany rupture segmentation. Given that rupture close to the trench has high potential for large tsunami excitation [e.g., Kanamori, 1972], identifying regions where these updip jumps are likely to occur provides important information for defining regions that are most susceptible to tsunami hazard following large earthquakes.

In contrast to the interplate events, the 2009 Samoa Islands earthquake is an intraplate event that occurred in the outer rise of the Tonga subduction zone. In addition to our results, recent studies that relocated aftershocks of large outer rise events suggest that the rupture of multiple faults during large, outer rise earthquakes are a common occurrence [e.g., Fromm et al., 2006; Hino et al., 2009]. One explanation for this behavior comes from the fact that the lengths of outer rise faults are very

similar, and normally fall between 5 and 30 km as observed from bathymetry data [e.g., Masson, 1991]. These observations suggest that there is a mechanism that limits the length of outer rise faults, which would also limit the size of earthquakes that can occur on any one of these faults. Therefore, to generate a large outer rise event, rupture on multiple faults may be necessary.

4.3.6 HIGH-FREQUENCY ENERGY AND THE SEISMOGENIC ZONE

There are interesting spatial relationships between the rupture distributions obtained using back-projection and the seismogenic zone. Figures 4.3a, 4.4a, 4.5a, and 4.7a show that the majority of the imaged energy occurs within the seismogenic zones as determined from past seismicity in the different regions [Heuret et al., 2011]. In fact, within the along-strike range of the ruptures, almost the entire seismogenic zone is covered during three of the four interplate events (Figures 4.3a, 4.4a, and 4.5a). The one exception is the 2010 Maule, Chile earthquake which has substantial energy downdip of the bottom of the seismogenic zone. This may be a real feature of the rupture, however, it should also be noted that there are large variations in the hypocentral locations reported for this earthquake. Because back-projection results are relative to the assumed hypocentral location, using a different hypocenter causes a translation of the imaged energy. For example, the hypocenter reported by the National Earthquake Information Center is used in Figures 4.7 (a) and (c). However, the hypocenter reported by the National Seismological Service in Chile is significantly west of the NEIC location. Using the shifted hypocenter, the back-projection results also move west, and the energy release is almost entirely updip of the bottom of the seismogenic zone, which is more consistent with the observations from other large earthquakes (Figures 4.7d).

For both of the 2007 Mentawai Islands earthquakes and the 2010 Chile earth-

quake, the transition from one rupture segment to the next occurs directly after the rupture approaches the downdip limit of the seismogenic zone. This downdip rupture propagation is somewhat surprising given that it has been argued that updip rupture propagation is common for both continental and subduction zone earthquakes [e.g., Sibson, 1982; Kato and Seno, 2003]. However, since the bottom of the seismogenic zone is probably a region of high shear stress [e.g., Kato and Seno, 2003], if a rupture initiates away from this zone, it does not seem unreasonable that the rupture would propagate into this region. The discrepancy between this result and previous studies may be caused by the fact that we are using high-frequency data, as opposed to aftershock distributions or lower-frequency data typically used in finite-fault modelling.

4.4 SUMMARY

The distribution of stations from TA and Hi-net provides good coverage to image the rupture details of five recent large earthquakes using the multi-array back-projection method. The spatio-temporal distribution of energy release from all five events shows that these ruptures are segmented into sub-events with varying rupture directions and speeds. In some cases, gaps in the ruptures suggest that large earthquakes involve multiple fault segments that are triggered by slip on an adjacent segment. These rupture details are important for developing a better understanding of the tectonic parameters and conditions that control the size and dynamics of ruptures, and the seismic hazards associated with large earthquakes.

CHAPTER 5

FREQUENCY-DEPENDENT RUPTURE

5.1 INTRODUCTION

It is common for earthquake studies to focus on the general properties of a rupture. For example, average rupture velocity, rupture direction, rupture length, total rupture area, and regions of highest slip are traditionally viewed as the important parameters of any earthquake source study [e.g., Pritchard and Fielding, 2008; Biggs et al., 2009; Lay et al., 2010b, 2011b]. This is not surprising given that in most cases these parameters can be used to assess the hazards associated with an earthquake. However, as Chapter 4 shows, these broad descriptions of the sources misses much of the rupture complexity. This can influence the way hazards are assessed, and also have important consequences for testing different hypotheses of the physical mechanisms that act during ruptures. In this chapter, we attempt to gain new insight into the complexity of earthquake sources by imaging the rupture behavior of the Mw 8.8 2010 Maule, Chile and Mw 9.0 2011 Tohoku, Japan earthquakes using data filtered to different frequency ranges. The frequency of seismic waves are related to the rise time of slip at the source [e.g., Aki and Richards, 2002]. These rise times may be controlled by the material properties of the fault and processes acting during slip, and therefore by

studying sources at different frequencies, we may be able to gain insights into rupture mechanisms.

5.2 THE 2010 MW 8.8 MAULE, CHILE EARTHQUAKE

The February 27, 2010 Mw 8.8 Maule, Chile earthquake is the sixth largest event to occur in the past century. While the aftershock distribution for this event suggests a rupture length of 600 to 650 km, there is a wide range of finite fault models with highly variable slip distributions [e.g., Delouis et al., 2010; Lay et al., 2010b; Moreno et al., 2010]. For example, a seismological study by Lay et al. [2010b] finds that the highest slip occurred north of the epicenter, southwest of Santiago, which agrees with many of the finite-fault modelling studies that use seismic data [e.g., Delouis et al., 2010]. In contrast, the horizontal displacement measured by GPS stations (<http://sopac.ucsd.edu/dataArchive/>) is 25 times larger at Concepción (south of the epicenter) than at Santiago (north of the epicenter) (Figure 5.1a). A slip inversion using GPS data confirms that this displacement requires much more slip near Concepción than north of the epicenter [e.g., Moreno et al., 2010].

5.2.1 DATA AND DATA PROCESSING

We study the rupture properties of the Chilean event using data from the Full Range Seismograph Network (F-net) [Okada et al., 2004] and the High Sensitivity Seismograph Network (Hi-net) [Okada et al., 2004; Obara et al., 2005] of Japan and the Transportable Array (TA) in the United States (Figure 5.1b). The waveform of the first-arriving compressional wave recorded on the vertical component is used at each array. In order to investigate the frequency dependence of the Chilean event, the data are bandpass-filtered to three frequency ranges, 1 to 5 Hz, 0.5 to 1 Hz, and

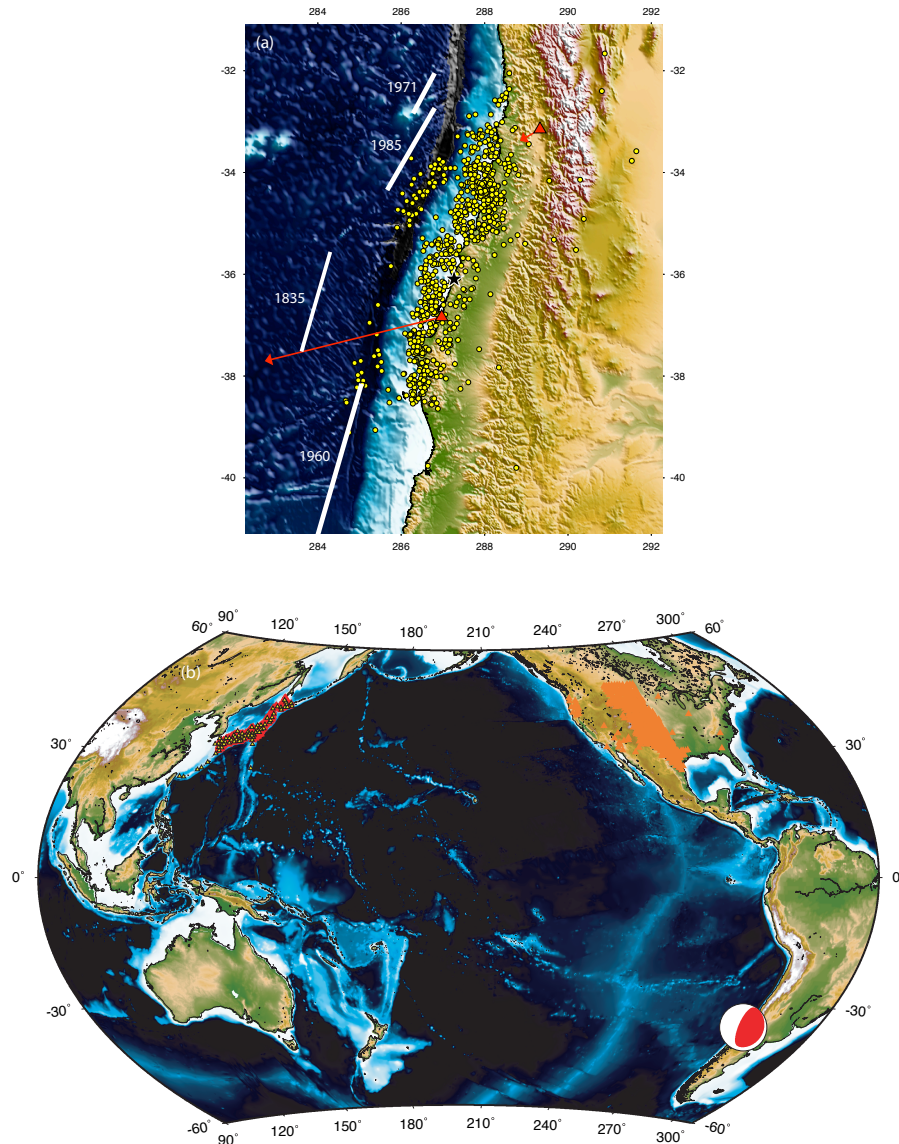


Figure 5.1: (a) The epicenter (black star) and aftershock distribution (yellow circles) of the 2010 Chile event 3 months following the mainshock. These locations are from the USGS National Earthquake Information Center (<http://earthquake.usgs.gov/>). The red triangles are the GPS stations that recorded the horizontal displacement (red vectors) one day after the event near Santiago (0.8 cm) and Concepción (20 cm) provided by the Scripps Orbit and Permanent Array Center (<http://sopac.ucsd.edu/>). The white lines show the approximate latitudinal extents of the most relevant large earthquakes in this region [e.g., Beck et al., 1998]. (b) TA (orange triangles), Hi-net (red triangles) and F-net (small yellow triangles) station distributions relative to the focal mechanism of the February 27, 2010 Chile earthquake from the Global CMT catalog [e.g., Dziewoński et al., 1981; Dziewoński and Woodhouse, 1983].

0.05 to 0.1 Hz, henceforth referred to as high-frequency, intermediate-frequency, and low-frequency, respectively (Figure 5.2). For the high- and intermediate-frequency results, spatial resolution comes mainly from the TA data, therefore we will only show these results (Appendix A). However, as we discuss later, the Hi-net data are vital to confirming some of the features observed in the TA results. For the low-frequency results, the F-net and TA data are combined to improve resolution (Appendix A).

5.2.2 RESULTS

As was outlined in Chapter 4, back-projection results using high-frequency data reveal that this event is composed of three rupture segments defined by different rupture velocities and amplitudes (Figure 5.3). Segment 1 is a north/south bilateral rupture (between about 36.5°S and 36°S) away from the epicenter, though the northward propagating rupture has higher amplitude energy release. This northward rupture lasts about 45 seconds and has a velocity of about 2.2 km/s (Figure 5.3). North of Segment 1 is Segment 2 (between about 35°S and 34°S), which has the highest amplitude energy release of all the segments at high frequency. It begins to rupture about 55 seconds after the hypocentral time, and propagates to the northeast for 60 seconds with a distinctly higher rupture velocity of around 2.9 km/s (Figure 5.3). In contrast, Segment 3 is located south of the epicenter at about 37.5°S, and is activated 70 seconds after the hypocentral time. This segment ruptures for 25 seconds at a rupture velocity of 0.8 km/s to the east, and has the weakest energy release of all the segments at high frequency (Figure 5.3). Note that the weak southern rupture of Segment 1 is obscured by the energy from the strong northern rupture, and therefore we cannot determine the rupture parameters that connect Segments 1 and 3. However, if we assume a continuous southern rupture, the rupture speed required between the epicenter and the initiation of Segment 3 is 2.2 km/s to the south, implying a

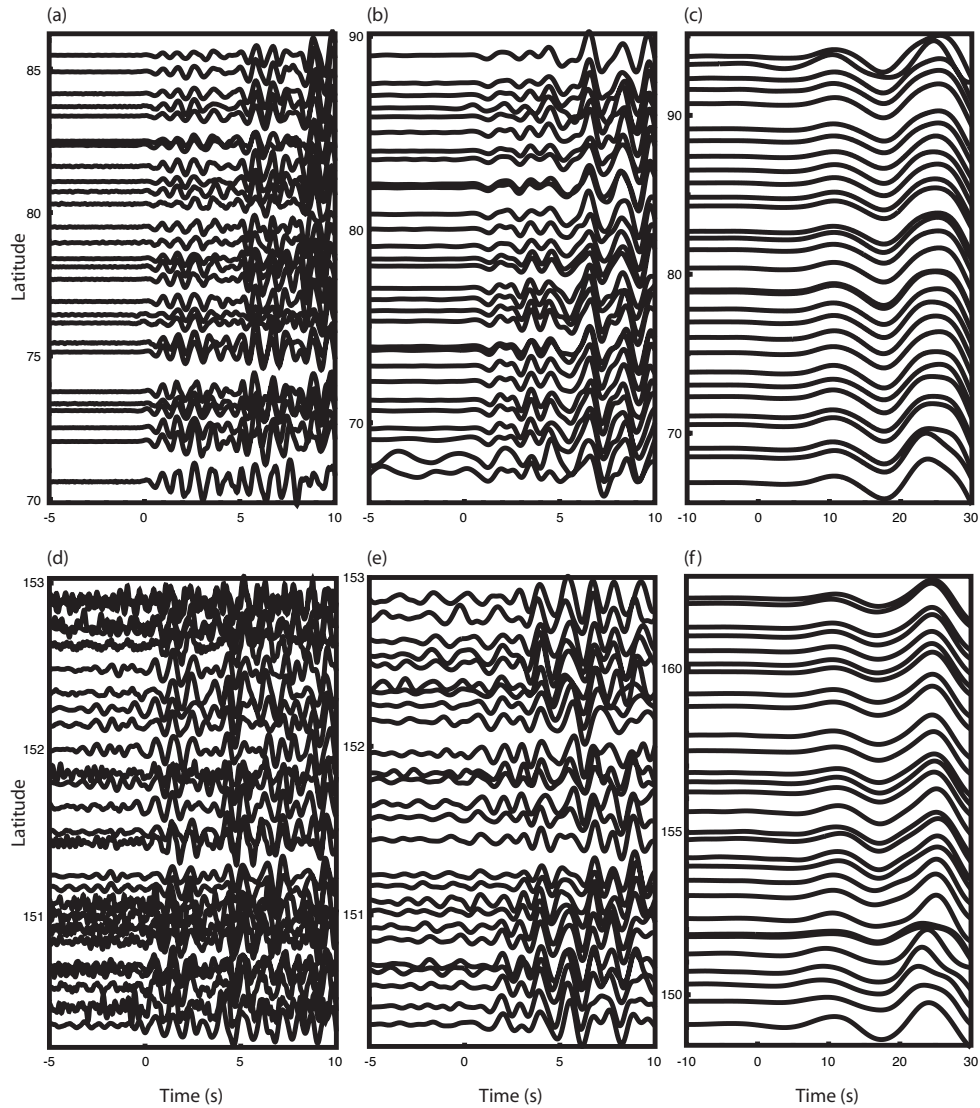


Figure 5.2: (a) TA data filtered between 1 and 5 Hz aligned at the theoretical P wave arrival time after cross correlation. Frequencies of 1 to 2 Hz dominate this signal. (b) The same as (a), except the TA data is filtered between 0.5 and 1 Hz. (c) The same as (a), except the TA data is filtered between 0.05 and 0.1 Hz. (d) The same as (a), except using Hi-net data aligned at the theoretical PKP bc arrival time. This data has a distance constraint between 150 and 153 degrees. This distance constraint avoids the core phase triplication and isolates the PKP bc arrival. (e) The same as (d), except the Hi-net data is filtered between 0.5 and 1 Hz. (f) The same as (c), except using F-net data aligned at the theoretical PKP df arrival time. PKP df dominates across F-net at low frequencies and therefore no distance constraint is needed.

dramatic decrease in rupture velocity and change in rupture direction at Segment 3. This segmentation of the slab interface is corroborated by historical seismicity of the region (Figures 5.3). The latitudinal extent of Segment 2 is consistent with the inferred rupture zone of the 1985 Mw 8.0 Valparaiso earthquake [e.g., Christensen and Ruff, 1986; Beck et al., 1998], and Segments 1 and 3 occur at the northern and southern regions, respectively, of the seismic gap between the 1985 and 1960 Chilean earthquakes, which has not slipped since the 1835 Darwin event (Figure 5.3) [e.g., Barrientos and Ward, 1990; Beck et al., 1998]. In addition, the boundary between Segments 1 and 2 coincides with a region of low interseismic coupling as inferred by continuous GPS data [Moreno et al., 2010]. The northern and southern extents of the 2010 earthquake have been argued to be controlled by visible surface features, i.e., the Juan Fernandez Ridge and the Mocha Fracture Zone [e.g., von Huene et al., 1997; Contreras-Reyes et al., 2008], but results presented here, and in Chapter 4, also indicate that regions of low interseismic coupling can act to segment a rupture.

We next investigate the frequency-dependent properties of each segment identified in the previous section using the three bandpass-filtered data. Figures 5.4a and 5.4b show that the high-frequency energy is radiated at the rupture front while the intermediate-frequency energy lags behind for Segments 1 and 2. The frequency-dependent characteristics of Segment 3 are slightly different than those of Segments 1 and 2. For this segment, both the high- and intermediate-frequency results are dominated by a single episode of energy release with slow propagation velocities. This slow speed, in the presence of imperfect spatial resolution, makes tracking of the energy at two frequencies difficult. However, the peak of the high-frequency energy is farther south than the intermediate-frequency energy (Figure 5.4c). These observations from all three segments can be interpreted as breaking of the fault at the rupture tip, releasing high-frequency energy, followed by slower slip behind the rupture front due

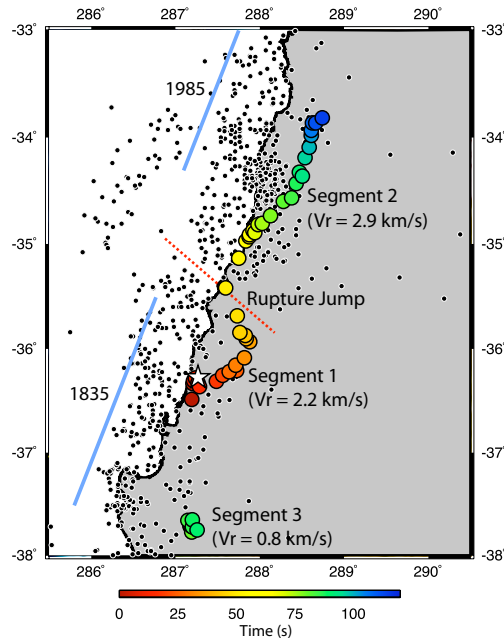


Figure 5.3: The large colored circles show the locations of imaged energy using high-frequency (1-5 Hz) TA data with the colors indicating the corresponding times with respect to the hypocentral time. The white star is the epicenter and the small black dots are the aftershocks. The labels indicate the three different rupture velocities (V_r) associated with this event and the northwest jump in the rupture between Segments 1 and 2. The dashed red line marks the gap in the aftershock distribution that corresponds to the change in rupture characteristics (i.e., a change in rupture velocity) and the interseismic coupling of the subduction zone [e.g., Moreno et al., 2010]. The light blue lines show the approximate latitudinal extents of the most relevant large earthquakes in this region [e.g., Beck et al., 1998].

to reduced friction. These types of rupture dynamics, which point to the importance of dynamic weakening of faults, have been proposed theoretically [e.g., McKenzie and Brune, 1972; Sibson, 1973, 1977; Richards, 1976; Lachenbruch, 1980; Mase and Smith, 1987; Melosh, 1996; Kanamori and Heaton, 2000; Brodsky and Kanamori, 2001; Rempel and Rice, 2006; Rice, 2006] and observed both experimentally [e.g., Di Toro et al., 2004; Hirose and Bystricky, 2007; Han et al., 2007; Famin et al., 2008; Nielsen et al., 2008] and for the 1999 Chi-Chi earthquake [Ma et al., 2003]. The reduction in friction caused by processes such as pore fluid thermal pressurization and frictional melt [e.g., Rempel and Rice, 2006; Nielsen et al., 2008] requires substantial slip, and therefore this effect should not apply to small earthquakes. The observation of frequency-dependent energy release suggests that small and large subduction zone earthquakes behave differently, and that one cannot simply scale the behavior of small events to understand the occurrence and mechanism of giant earthquakes. Another interesting observation from comparing high- and intermediate-frequency results is that both the northern edge of Segment 2 and the southern edge of Segment 3 are marked by bursts of high-frequency energy release that occur after the energy release at intermediate frequencies. We interpret these high-frequency features as the stopping phases that result from the sudden decrease in rupture velocity as the ruptures terminate [Savage, 1966].

The poor spatial resolution of low-frequency back-projection results makes it difficult to determine this energy's relationship to each of the three segments identified above (See Appendix A). However, there is adequate latitudinal resolution to determine that this energy peaks south of the epicenter, which is in contrast to high-frequency results where energy release prevails to the north (Figures 5.5 and 5.6). These results are confirmed with back-projection results using high-frequency data from Hi-net and low-frequency data from TA and F-net, individually (Figure 5.7),

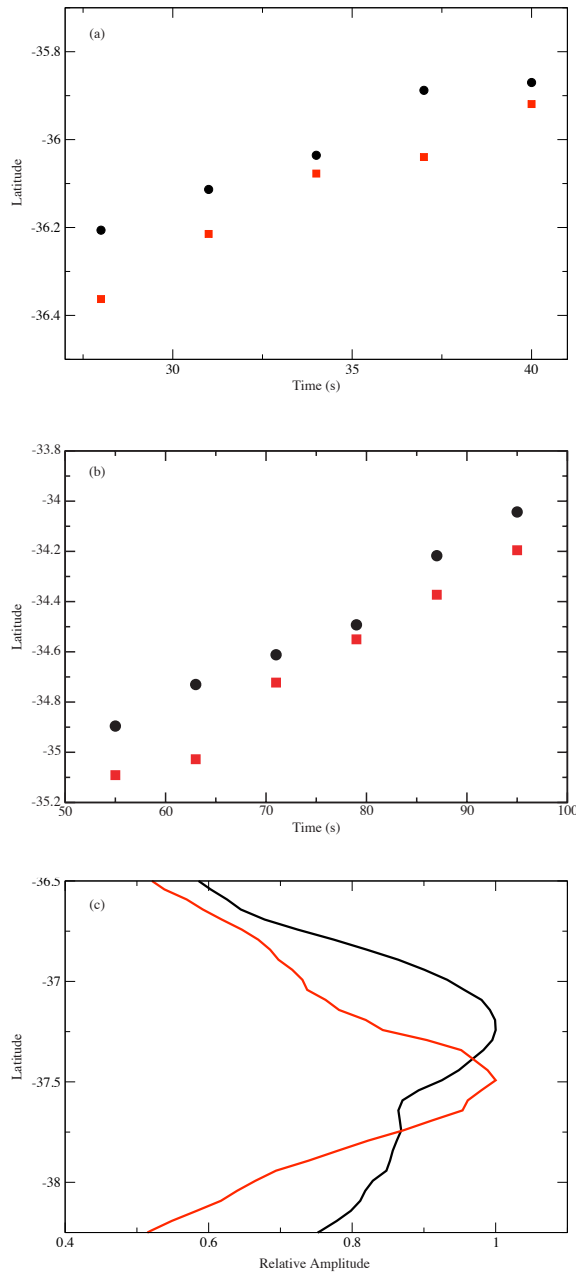


Figure 5.4: (a) Latitudes and times of the imaged energy from Segment 1 using high- (1-5 Hz; black circles) and intermediate-frequency (0.5-1 Hz; red squares) TA data. (b) Latitudes and times of the imaged energy from Segment 2 using high- (1-5 Hz; black circles) and intermediate-frequency (0.5-1 Hz; red squares) TA data. (c) Relative amplitude distribution with respect to latitude of the imaged energy from Segment 3 using high- (1-5 Hz; red line) and intermediate-frequency (0.5-1 Hz; black line) TA data.

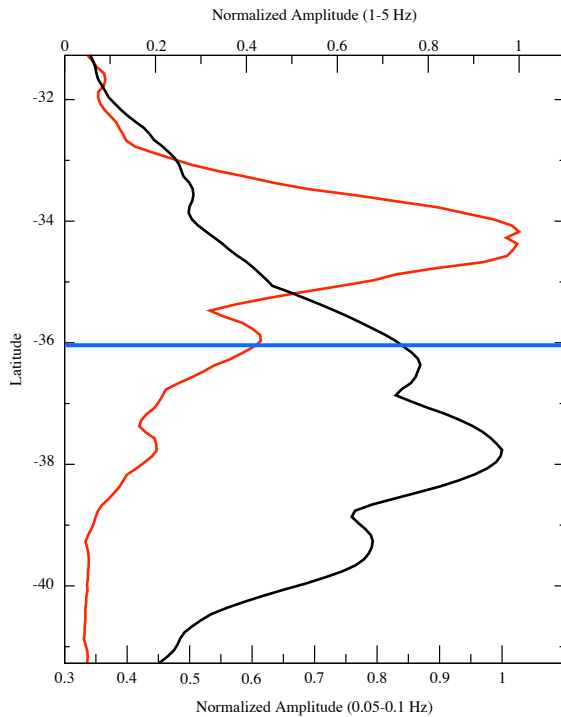


Figure 5.5: The relative amplitude variation of high- (1-5 Hz; red line) and low-frequency (0.05-0.1 Hz; black line) stacks as a function of latitude. The blue line is the epicentral latitude. The separation of the northern high-frequency rupture and the southern low-frequency rupture points out that this rupture took place on two mechanically different faults.

and are not the result of the directivity effect. This difference in frequency content suggests that the dynamics of slip change along the subduction zone during a single giant earthquake. Note that high-frequency energy release is largest on Segment 2 north of the epicenter where the rupture speed is high (2.9 km/s) and low-frequency energy release is largest near Segment 3 south of the epicenter where the rupture speed is low (0.8 km/s). This relationship between rupture speed and relative energy release at different frequencies suggests that the rupture velocity scales with the rise-time of slip [Aki and Richards, 2002]. It can therefore be interpreted that Segments 1 and 2 slipped fast while Segment 3 had slower slip.

5.3 THE 2011 MW 9.0 TOHOKU, JAPAN EARTHQUAKE

The March 11, 2011 Mw 9.0 Tohoku-oki earthquake is the fourth largest event to occur in the past century. The tsunami wave generated by this earthquake had a maximum

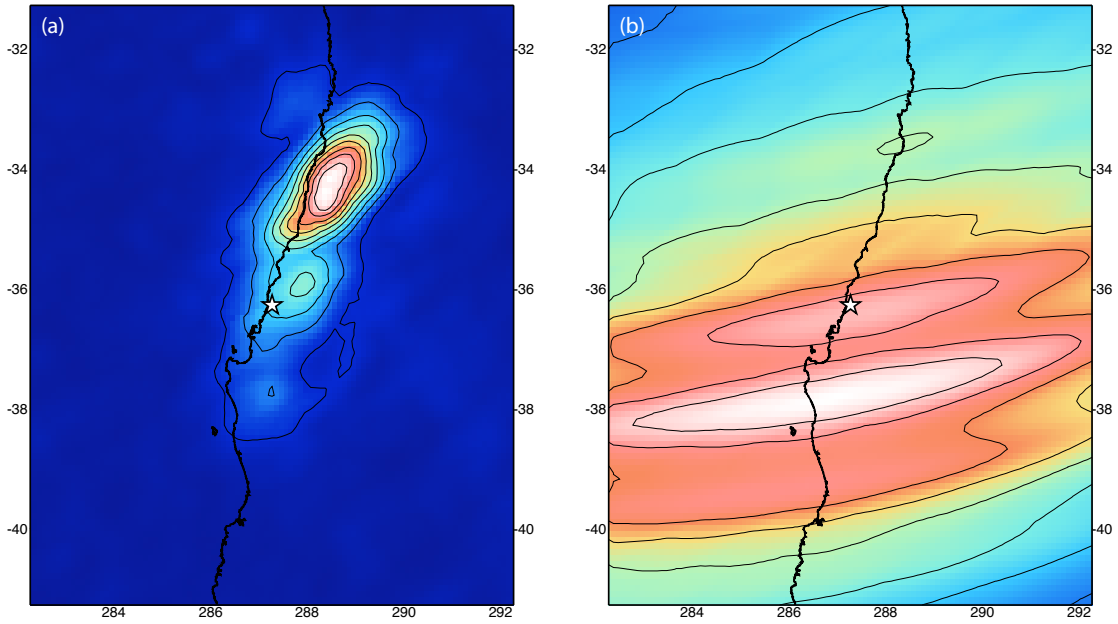


Figure 5.6: (a) High-frequency (1-5 Hz) back-projection result using TA data. Warmer colors represent high energy release and colder colors represent low energy release. The white star is the epicenter. (b) Low-frequency (0.05-0.1 Hz) back-projection result using TA and F-net data.

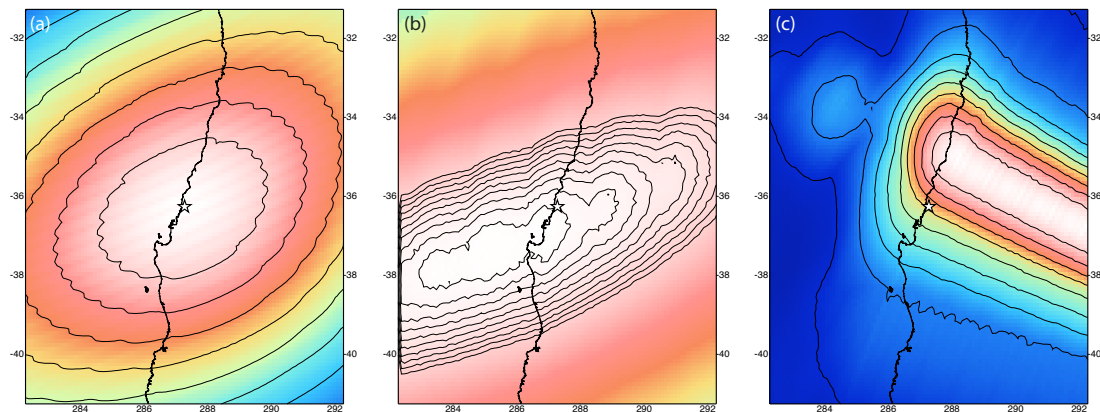


Figure 5.7: (a) Back-projection results using TA data filtered between 0.05 and 0.1 Hz. (b) Back-projection results using F-net data filtered between 0.05 and 0.1 Hz. (c) Back-projection results using distance constrained (150° - 153°) Hi-net data filtered between 1 and 5 Hz.

wave height between 10 and 20 m [Hiratsuka and Sato, 2011], devastating regions along the northeastern coast of Honshu, Japan. Initial results show that horizontal displacements measured on the seafloor near the epicenter reach values of 24 m [Sato et al., 2011]. In addition, slip models for this event show large variations, but in general, all have maximum slip near or updip of the epicenter [Hayes, 2011; Ammon et al., 2011; Fujii et al., 2011; Ide et al., 2011; Iinuma et al., 2011; Ito et al., 2011; Koper et al., 2011; Lay et al., 2011a,b; Maeda et al., 2011; Ozawa et al., 2011; Simons et al., 2011; Yoshida et al., 2011]. For many of these models, the mainshock region is substantially smaller than the area covered by aftershocks occurring on the subduction interface, which range from 35.0°N to 41.0°N and span most of the seismogenic zone (Figure 5.8a). This is in stark contrast to results of recent giant earthquakes, such as the 2010 Maule, Chile earthquake, where the aftershock distribution matches the ruptured fault extent [e.g., Kiser and Ishii, 2011].

5.3.1 DATA AND DATA PROCESSING

The high-frequency characteristics of the March 11, 2011 mainshock are analyzed using abundant observations from seismic stations in North America comprised by the following networks: USArray Transportable Array (IRIS and EarthScope), Caltech Regional Seismic Network (Caltech/USGS), Global Seismograph Network (IRIS), International Miscellaneous Stations, University of Utah Regional Network (University of Utah), Berkeley Digital Seismograph Network (Berkeley Seismological Laboratory), University of Oregon Regional Network (University of Oregon), Canadian National Seismograph Network (Geological Survey of Canada), United States National Seismic Network (ANSS Data Collection Center), and ANZA Regional Network (IGPP, University of California, San Diego) (Figure 5.8b). This group of stations acts as an array over most of North America.

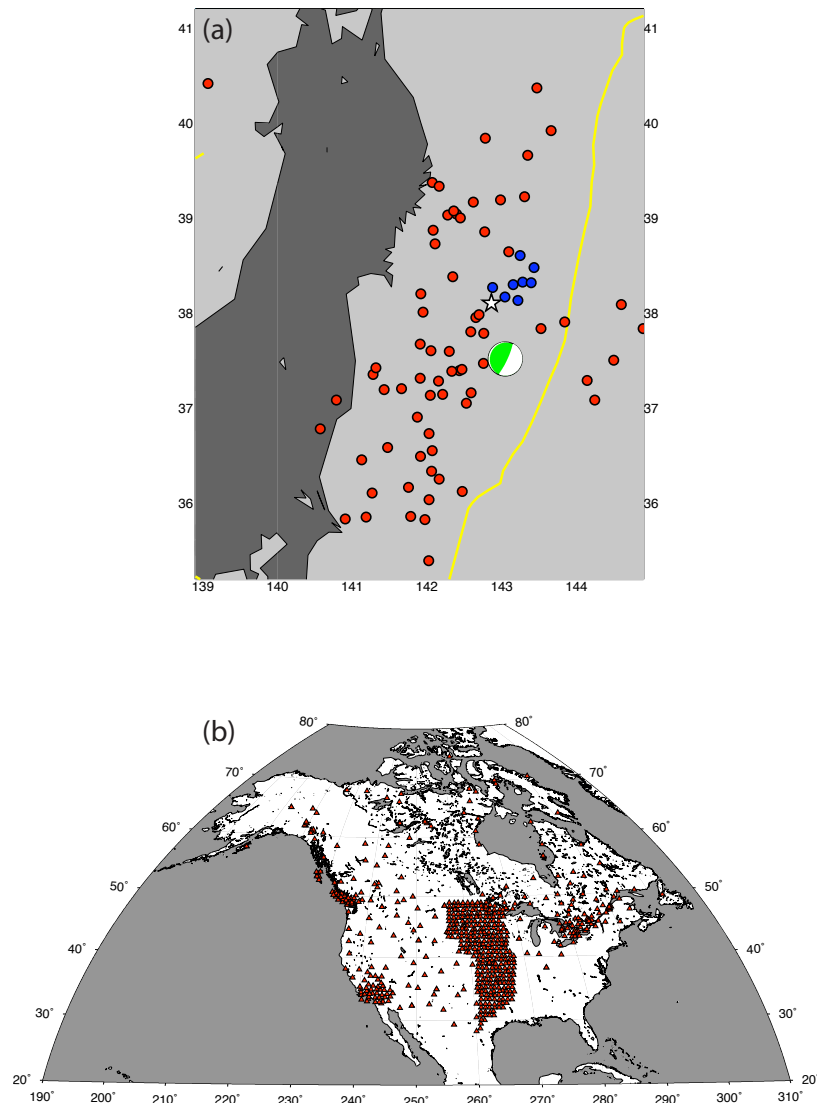


Figure 5.8: (a) The distribution of foreshocks (blue circles, $M \geq 6$) and aftershocks (red circles, $M \geq 6$) between March 9, 2011 and April 7, 2011 with respect to the mainshock (white star denoting the epicenter and green beach ball the Global CMT focal mechanism [Dziewonski and Woodhouse, 1983]). The yellow line is the Japan Trench. (b) Locations of seismic stations (red triangles) in North America. The USArray Transportable Array (IRIS and EarthScope), Caltech Regional Seismic Network (Caltech/USGS), Global Seismograph Network (IRIS), International Miscellaneous Stations, University of Utah Regional Network (University of Utah), Berkeley Digital Seismograph Network (Berkeley Seismological Laboratory), University of Oregon Regional Network (University of Oregon), Canadian National Seismograph Network (Geological Survey of Canada), United States National Seismic Network (ANSS Data Collection Center), and ANZA Regional Network (IGPP, University of California, San Diego) comprise this group of stations.

Though high-frequency data provide the most detailed information regarding the rupture, back-projection results using lower frequency data can show very different rupture characteristics than their high-frequency counterparts. Such a multi-frequency back-projection analysis is appropriate for the 2011 Tohoku-oki earthquake, because of its large magnitude and because reports from numerous studies have argued that high-frequency energy is concentrated at the downdip edge of the seismogenic zone, while the majority of slip occurred further updip near the epicenter and trench [e.g., Ide et al., 2011; Koper et al., 2011; Simons et al., 2011]. This large slip near the epicenter and trench should generate a strong low-frequency signal, resulting in frequency-dependent release of seismic energy [e.g., Polet and Kanamori, 2000]. To investigate such frequency dependence, the data are bandpass filtered to four frequency ranges: 0.8-2 Hz, 0.25-0.5 Hz, 0.1-0.2 Hz, and 0.05-0.1Hz.

5.3.2 RESULTS

The imaged source locations of high-frequency (0.8-2 Hz) energy release for the Tohoku earthquake show a very complex spatio-temporal rupture pattern (Figure 5.9a). To determine the relative amplitudes of energy release, we use results from linear stacking (Figure 5.9b), but rupture direction, duration, and velocity are determined by results from the coherency function (See Chapter 2; Figure 5.9a). At high frequency, this earthquake begins with downdip (northwest) propagation away from the epicenter at a velocity of about 0.8 km/s. This first episode of rupture lasts about 90 seconds (Figure 5.9a). This rupture episode shows a very diffuse distribution of energy release near its downdip limit. Following this downdip propagation, the rupture moves southwest, parallel to the Japan trench. This southwestward propagation lasts about 60 seconds, and includes the episode of highest amplitude energy release at about 95 seconds after the hypocentral time (Figure 5.9b). The average rupture

velocity of the southwest propagating rupture is very high at about 3.4 km/s. This high speed is in part due to a jump in the rupture of 70 km length (Figure 5.9a). The rupture velocities to the north and south of this jump are 2.7-3.3 km/s and 1.1-1.7 km/s, respectively. Between 36.5 and 37°N, the along trench propagation terminates, and rupture begins to propagate updip (southeast; Figure 5.9a). This updip propagation is weaker compared to earlier episodes, and lasts for about 20 seconds at a rupture velocity of 2.8-3.3 km/s (Figure 5.9a and 5.9b). The last rupture episode propagates to the northeast with a velocity of about 2.1-2.3 km/s and is very close to the trench (Figure 5.9a). This rupture has lowest amplitude high-frequency energy release and lasts about 45 seconds (Figures 5.9a and 5.9b). These results are similar to previous studies that also used back-projection or similar methods [Ishii, 2011; Wang and Mori, 2011b; Honda et al., 2011; Koper et al., 2011; Nakahara et al., 2011; Simons et al., 2011; Zhang et al., 2011]. In particular, imaged energy near the coast of Honshu and a large increase in rupture velocity during southwest propagation seem to be robust features of multiple studies, though imaged energy near the trench late in the rupture seems to be unique to the current study.

Using lower-frequency data (0.25-0.5 Hz) leads to slightly different back-projection results. For example, the rupture now begins with updip (northeast) propagation for 25 seconds at a rupture velocity of 0.4 km/s. The remaining rupture is very similar to the high-frequency results, though the 0.25-0.5 Hz results are updip of the 0.8-2 Hz results (Figure 5.9c; Figure 5.10). This updip shift in energy release locations continues when using data filtered at 0.1-0.2 Hz. In addition, updip propagation at the beginning of the rupture is more significant with a duration of 45 seconds (Figure 5.9c; Figure 5.10). Moving to the lowest frequency range (0.05-0.1 Hz), imaged energy is even further updip at the beginning of the rupture and never propagates significantly downdip of the epicenter (Figure 5.9c; Figure 5.10). At the end of the rupture, energy

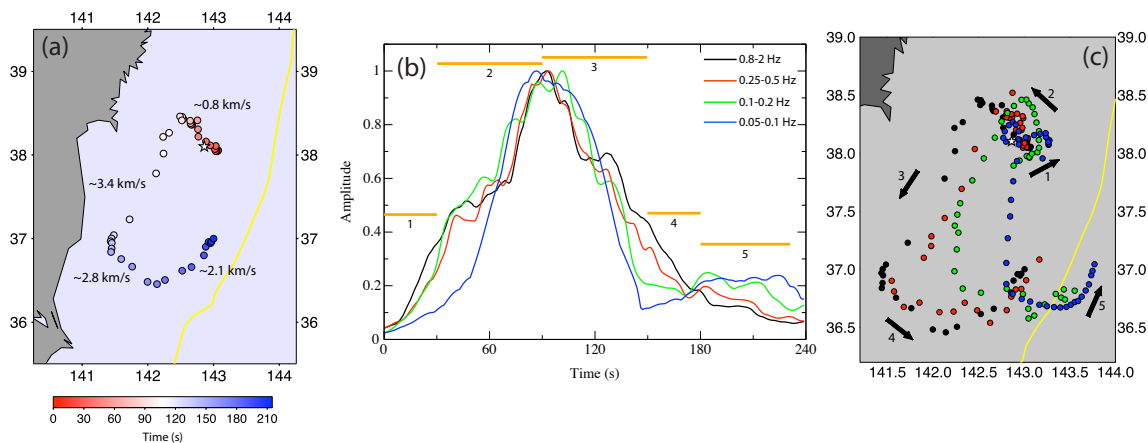


Figure 5.9: (a) Locations (colored dots) of high-frequency (0.8-2 Hz) energy release (5-second intervals). The numbers indicate the average rupture velocities of the four rupture segments described in the main text. The white star is the epicenter of the mainshock and the yellow line is the Japan Trench. (b) Relative amplitude of the back-projection results with respect to the hypocentral time using bandpass-filtered data between 0.8 and 2 Hz (black line), 0.25 and 0.5 Hz (red line), 0.1 and 0.2 Hz (green line), and 0.05 and 0.1 Hz (blue line). The orange horizontal lines show the times of the five rupture episodes of the mainshock shown in (c). (c) Locations of energy release at different times (5-second intervals) during the mainshock using bandpass-filtered data between 0.8 and 2 Hz (black dots), 0.25 and 0.5 Hz (red dots), 0.1 and 0.2 Hz (green dots), and 0.05 and 0.1 Hz (blue dots). The white star is the epicenter and the yellow line is the Japan Trench. The black arrows show general propagation directions of the rupture from the initial updip propagation (1) to the final episode of energy release near the trench (5).

is imaged slightly east of the trench. This energy is interpreted as being on the plate interface and not in the outer-rise region (See Appendix A for a discussion on location uncertainty). The updip shift in the imaged energy at lower frequencies agrees well with other back-projection analyses of this event [Ishii, 2011; Wang and Mori, 2011a]. A final observation worth noting is that as the frequency becomes lower, the relative amplitude of the last episode of energy release (to the south and near the trench) between 180 and 240 seconds increases (Figure 5.9b).

The total area imaged by the four frequency ranges is about 64000 km² (Figure 5.11), and we begin by assuming that this area corresponds to the total rupture

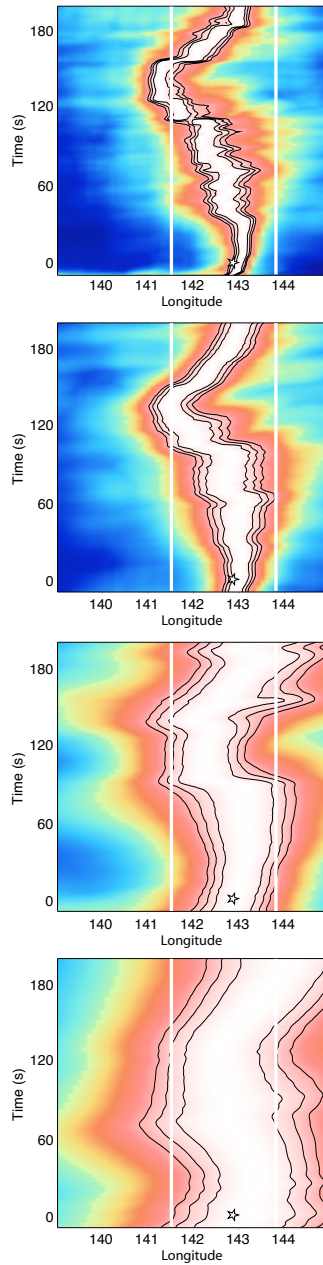


Figure 5.10: From top to bottom: back-projection results of the mainshock with respect to longitude and time using bandpass-filtered data between 0.8 and 2 Hz, 0.25 and 0.5 Hz, 0.1 and 0.2 Hz, and 0.05 and 0.1 Hz. These images demonstrate how resolution degrades at lower frequencies. The imaged energy is normalized at each time step, and the white star is the hypocentral longitude and time. The vertical white lines are the longitudes of the Oshika Peninsula (left) and the trench location at the epicentral latitude (right).

area. Using a circular crack model and typical stress drop of 30 bars [Kanamori and Anderson, 1975], this area gives a moment magnitude of 8.8. This simple approach to estimating magnitude has been successful in previous back-projection studies of the 2004 and 2005 Sumatra earthquakes, and the 2010 Chile earthquake [Ishii et al., 2005, 2007; Kiser and Ishii, 2011], however, the large discrepancy between this magnitude estimate and the magnitude reported by the Japan Meteorological Agency (JMA, 9.0), National Earthquake Information Center (NEIC, 9.0), or the Global CMT catalogue (9.1) for the Tohoku event could be due to slow slip that excites seismic waves at lower frequencies than are considered in this study. Alternatively, the discrepancy could be explained by larger stress drop. If the Mw 9.0 earthquake is occurring over the rupture area obtained by the back-projection method, the required average stress drop is 60 bars. This value is very high for an interplate earthquake [Kanamori and Anderson, 1975], and is consistent with unusually large slip from models of the event [Hayes, 2011; Ammon et al., 2011; Fujii et al., 2011; Ide et al., 2011; Iinuma et al., 2011; Ito et al., 2011; Koper et al., 2011; Lay et al., 2011a,b; Maeda et al., 2011; Ozawa et al., 2011; Simons et al., 2011; Yoshida et al., 2011].

Though little is known about the rupture details, the last earthquake in this region that is thought to have produced a similar-sized tsunami as the March 11th event occurred in 869 AD [e.g., Sawai et al., 2008], and produced maximum wave heights between 6 and 9 meters with a minimum magnitude of 8.4 [e.g., Satake et al., 2008]. Tsunami run-up data are sparse for the 869 AD event, and different studies argue for very different slip distributions, especially with respect to distance from the trench [e.g., Minoura, 2008; Satake et al., 2008]. Therefore, it is not clear if the 869 AD event is a predecessor to the 2011 event. Additional smaller events (Mw 7-8) have occurred along this plate interface in the past 200 years that also produced tsunamis (Figure 5.11). Our high-frequency back-projection results suggest that parts of four

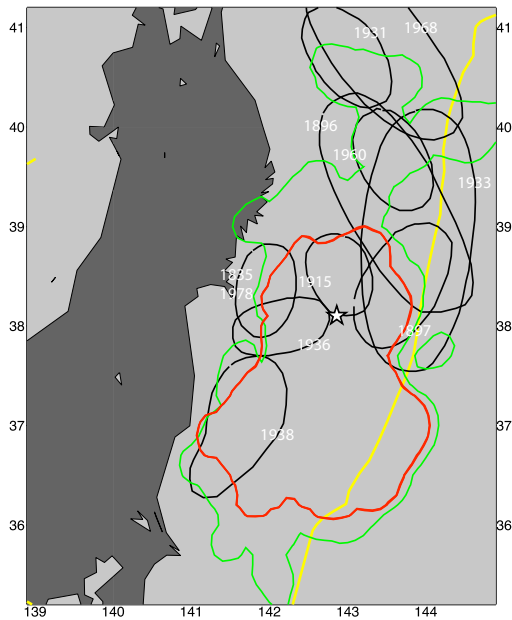


Figure 5.11: The rupture area of the mainshock (red contour) obtained by combining back-projection results from the four frequency ranges (0.05-0.1Hz, 0.1-0.2Hz, 0.25-0.5Hz, 0.8-2Hz) compared with the cumulative rupture distribution for $M \geq 6$ interface events between March 9, 2011 and April 7, 2011 (green contour). The white star is the epicenter of the mainshock and the yellow line is the trench location. The black ovals are approximate rupture areas from tsunamigenic earthquakes for the past 200 years with numbers in white showing historical event years [Hatori, 1987].

of these patches that ruptured in 1915, 1936, 1938 and 1978 [Hatori, 1987] failed again during the 2011 mainshock, while the low-frequency back-projection results suggest that a segment of the plate interface near the trench that last ruptured in 1897 is also involved in the 2011 earthquake [Hatori, 1987, Figure 5.11]. A noticeable gap in the distribution of past tsunamigenic earthquakes occurs updip of the 1938 event (Figure 5.11). This is the region where energy is imaged at all frequencies at the end of the 2011 mainshock. Though additional studies are needed to determine the extent to which this late rupture acted as a tsunami source, the results of this study suggest that this offshore Ibaraki region may be unlikely to produce a tsunamigenic earthquake in the near future assuming the imaged rupture released most of the cumulative strain. In addition, the back-projection results demonstrate that this section of the plate interface can slip seismically, which will be important for evaluating future seismic hazards.

5.4 SUMMARY

The results in this chapter show that different frequency ranges need to be considered to fully assess the complexity of giant earthquakes. One consequence of the frequency-dependent slip behavior is the tsunami generation potential of the earthquake. Tsunamis are known to be more effectively excited by sources involving long-period or low-frequency deformation [e.g., Kanamori, 1972]. For example, based upon our observations of the 2010 Maule earthquake, the region to the south of, and around the epicenter, has higher tsunami potential than that to the north, despite large slip seen to the north in most of the slip modeling results. This simple interpretation may not fully characterize the tsunami potential given the fact that the distance of slip from the trench varies during the rupture and our low frequency may still be relatively high for efficient deformation. However, it does point out that tsunami wave modeling for early warning may need to incorporate frequency-dependent source complexity for giant earthquakes. A second consequence of the results comes from the fact that damage to structures is also frequency dependent [e.g., Stein and Wysession, 2003]. This implies that studies that estimate strong motion and hazard for the purpose of resource allocation of the emergency earthquake response should consider where energy release at relevant frequencies is occurring. Finally, the frequency dependence of the energy release distribution presented in this chapter provides a possible mechanism to resolve the discrepancy between slip models that use seismological and geodetic data. For example, the limited strain release on the northern segments observed for the 2010 Chilean event suggests that the slip mechanism that releases seismic energy predominantly at high frequency does not release strain efficiently. This implies that events with slip with high-frequency energy release do not necessarily reset the recurrence time to the next big earthquake. Similarly, the total slip measured by GPS

instruments over one or more days may not, and in the case of the 2010 Chilean earthquake, is not, equal to the distribution of slip associated with high-frequency energy release easily recorded by the first-arriving seismic waves.

CHAPTER 6

AFTERSHOCK DETECTION

6.1 INTRODUCTION

The detection and characterization of early aftershocks immediately following a giant earthquake are complicated by the arrival of various seismic waves [e.g., Kagan, 2004; Kagan and Houston, 2005; Lolli and Gasperini, 2006; Peng et al., 2007]. This effect can be seen in most earthquake catalogues where gaps in magnitude and time exist directly following large events. For example, in the National Earthquake Information Center (USGS) earthquake catalogue, the first aftershock of the 2004 magnitude 9.1 Sumatra-Andaman earthquake does not occur until nearly 20 minutes after the mainshock. This lack of early aftershock activity is generally considered to be a detection problem, but also has important consequences for the seismic hazards and constitutive relationships acting following the large slip associated with a giant earthquake [e.g., Kagan, 2004; Kagan and Houston, 2005; Lolli and Gasperini, 2006; Peng et al., 2007]. The back-projection method can provide some insight into the aftershock activity shortly after a mainshock rupture by filtering out unwanted seismic energy during the stacking process described in Chapter 2. Application of the technique to the 2004 Mw 9.1 Sumatra-Andaman and 2011 Mw 9.0 Tohoku aftershock sequences detects

numerous events immediately following the mainshocks which are not identified in local or global earthquake catalogues. These unidentified events can be of large magnitude, and are potentially tsunamigenic. In addition to detection, back-projection can be used to study the rupture properties of the largest aftershocks. In particular, the following section will compare the rupture areas of the aftershocks to that of the mainshock of the Tohoku earthquake in an attempt to understand the evolution of plate interface failure.

6.2 2011 TOHOKU, JAPAN AFTERSHOCK SEQUENCE

The seismicity preceding and following the Mw 9.0 mainshock is very vigorous compared to other giant earthquakes in the last 10 years. Between March 11th and April 7th, the aftershock sequence of this event included at least four earthquakes with magnitudes greater than 7, and 70 aftershocks with magnitudes greater than or equal to 6.0 according to the JMA catalogue (Figure 5.8a). These aftershocks have a variety of focal mechanisms, including normal faulting in the outer rise and overriding Okhotsk/North American plate [e.g., Dziewoński et al., 1981; Dziewoński and Woodhouse, 1983; Woodhouse and Dziewonski, 1984; Ekström et al., 2005]. The Mw 9.0 event is also accompanied by a foreshock sequence that includes a Mw 7.3 event north of the mainshock epicenter and 7 additional earthquakes with magnitudes greater than 6.0 (Figure 5.8a).

6.2.1 DATA AND DATA PROCESSING

To understand the relationship between this series of large earthquakes occurring close in time to the mainshock, we apply the coherency function back-projection technique to high-frequency data (0.8-2 Hz) between March 9, 2011 and April 7, 2011. This data

set is recorded by a collection of seismic stations across North America that includes TA (Figure 5.8b). A maximum distance constraint of 92 degrees is applied based upon visual inspection of the quality of waveforms. Beyond this distance, the diffracted P wave is the first to arrive, and the amplitude of this seismic phase rapidly decays. The distance constraint leads to a set of stations with a distance range between 45 and 92 degrees, and an azimuth range between 8 and 59 degrees (Figure 5.8b).

6.2.2 LARGE AFTERSHOCKS AND INTERFACE FAILURE

The level of detail at which seismic events in the source region can be investigated by the back-projection technique is demonstrated in Figure 6.1a where the relative energy release is plotted as a function of time for about a fifty-minute time window after the mainshock. The back-projection approach shows that, in addition to the Mw 9.0 earthquake, both large ($M_w > 6.0$) and smaller ($M_w < 5.5$) aftershocks that are in the JMA catalogue are successfully detected (Figure 6.1a). In addition, two large earthquakes that are reported in the NEIC catalogue, but not the JMA catalogue, are also detected (Figure 6.1a). Furthermore, additional earthquakes that are not detected in either catalogue (JMA or NEIC) are identified during times immediately following large events (Figure 6.1a). A comparison between these detected and undetected events is the subject of Section 6.2.3.

In addition to detecting foreshocks and aftershocks, the spatial distribution of energy release can be investigated for the largest events (Figure 6.2). The JMA catalogue shows that these events have a variety of locations that include along the west coast of Japan and in the outer rise. When these events occurring on the overriding plate, as well as events with normal faulting mechanisms, are removed, the spatial distribution of the remaining energy release for events with $M \geq 6$ between March 9th and April 7th, 2011 shows that there is an almost complete failure of

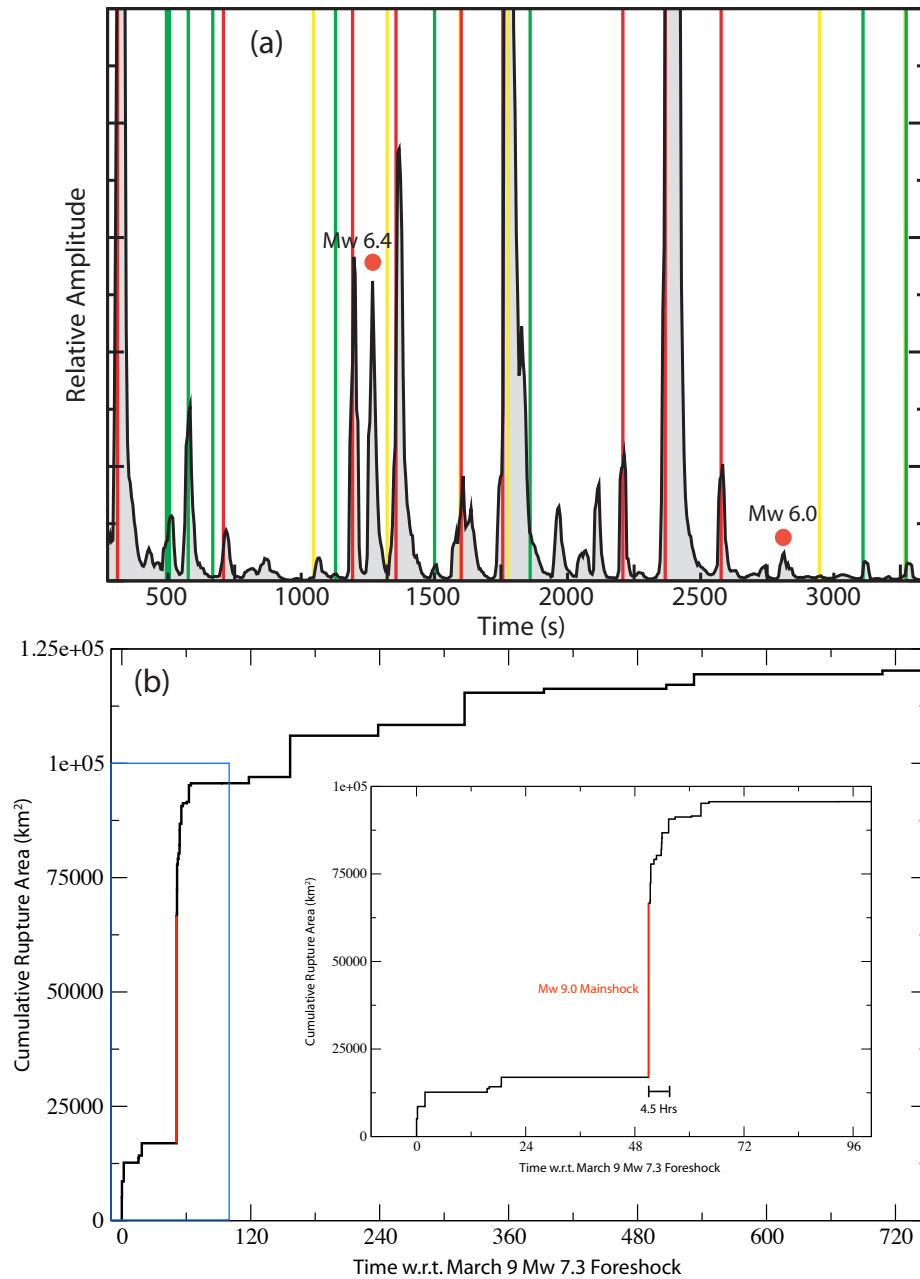


Figure 6.1: (a) Relative amplitude as a function of time with respect to the mainshock hypocentral time during the hour following the M 9.0 event. The vertical lines show the timing of events in the JMA catalogue for magnitudes between 5.0 and 5.4 (yellow), between 5.5 and 5.9 (green), and above 6.0 (red). Two red circles with magnitude estimates are events that exist in the NEIC catalogue but not in the JMA catalogue. (b) The cumulative rupture area as a function of time for $M \geq 6.0$ earthquakes between March 9, 2011 and April 7, 2011. The red line is the contribution from the M 9.0 mainshock. Time is with respect to the March 9th M 7.3 foreshock in units of hours. The inset is a zoom in of the blue box.

the plate interface between 35.0°N and 41.0°N (Figures 5.11 and 6.2). We estimate the area of this failure to be about 120,000 km², about 80% of the total seismogenic zone in this latitude range ($\sim 146,000$ km²) [Heuret et al., 2011]. The majority of the interface failure occurs during the Mw 7.3 foreshock, the Mw 9.0 mainshock, and the series of large events in the 4.5 hours following the mainshock ($\sim 91,000$ km²) (Figure 6.1b). Almost all of the remaining events occur within an area that overlaps with the rupture areas of preceding events. In fact, for many of the regions along the plate interface, high seismicity rates associated with an aftershock sequence do not begin until the cumulative interface failure, as imaged by back-projection, reaches those regions (Figure 6.3). This indicates that the widespread seismicity did not begin due to the large stress changes caused by the mainshock, but from a series of smaller stress changes caused by the largest aftershocks. The northern boundary of interface failure, based upon back-projection results, corresponds to a transition to a region of low interseismic coupling inferred from GPS measurements [e.g., Loveless and Meade, 2010], and the southern boundary of failure matches the location of the northern extent of the subducting Philippine Sea plate [e.g., Shinohara et al., 2011]. In this region, the plate that overrides the Pacific plate changes from the Okhotsk/North American plate to the north to the Philippine Sea plate to the south. It has been suggested that large earthquakes rarely occur along the Pacific plate interface in this region because of the presence of weak serpentized mantle associated with the subducted Philippine Sea plate [Uchida et al., 2009]. This weak material may not accumulate significant strain, which would explain why interface failure stopped in this region.

It has been argued that interactions and synchronization between multiple patches of the subduction interface led to the large magnitude of the 2011 mainshock [Ando and Imanishi, 2011; Aochi and Ide, 2011; Hori and Miyazaki, 2011; Mitsui and Iio,

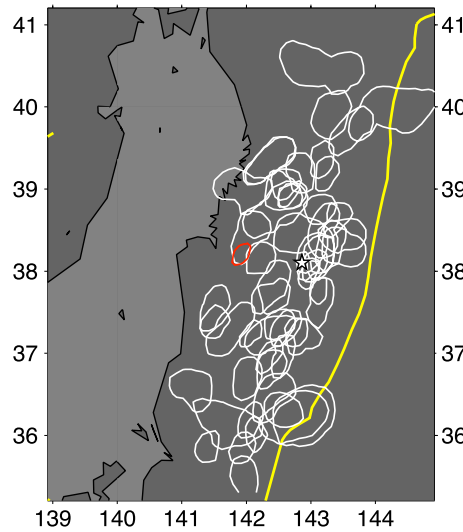


Figure 6.2: Rupture areas (white contours) of foreshocks and aftershocks between March 9th and April 7th. All earthquakes have been identified in the JMA catalogue and have magnitudes greater than or equal to 6. The red contour is the energy kernel of a synthetic point source for reference. The yellow line is the location of the Japan Trench. The white star is the epicenter of the Mw 9.0 mainshock.

2011]. Given the short time delay between the Mw 7.3 foreshock and the 4.5 hours surrounding the mainshock, it seems plausible that the plate interface that ruptured over this time period could have ruptured in a single event. Using the stress drop of 60 bars to match the Mw 9.0 mainshock as an upper bound (See Chapter 5), this hypothetical event would have a moment magnitude of 9.2, and requires failure of multiple asperities that have broken individually in the past. The recurrence times of these patches are very different, ranging from 21 to 750 years (The Headquarters for Earthquake Research Promotion, 2011, Summary of long-term seismic probability for subduction zone earthquakes), and therefore synchronization of segments is necessary for simultaneous failure. Recent work has focused on determining the distribution of asperities along plate interfaces, where coupling between the subducting and overriding plates is high [e.g., Moreno et al., 2010; Lorito et al., 2011], as a way of evaluating the locations and maximum magnitudes of future large earthquakes. The results of this study emphasize the importance of considering time synchronization of adjacent asperities when evaluating future seismic hazards [e.g., Scholz, 2011].

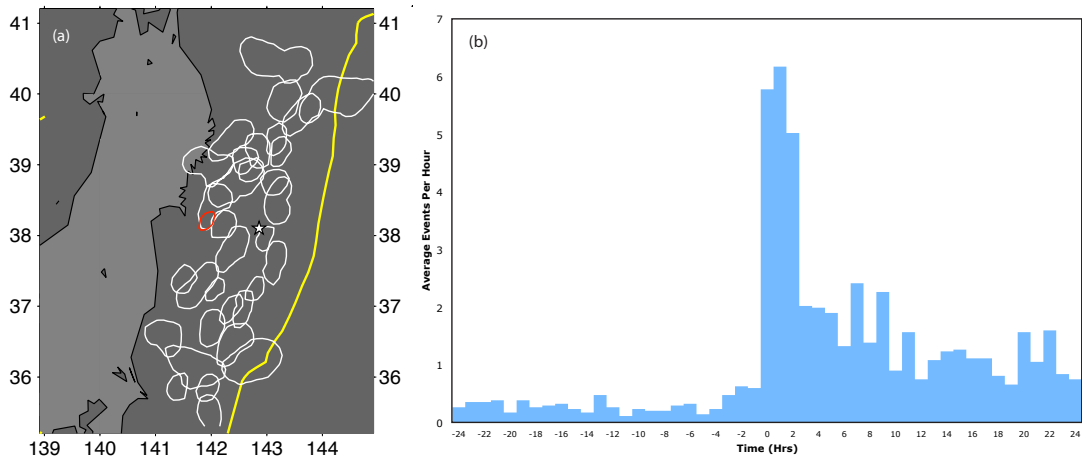


Figure 6.3: (a) Similar to Figure 6.2 except that we have selected foreshocks and aftershocks with rupture areas that do not overlap significantly with previous foreshocks and aftershocks. All symbols are the same as in Figure 6.2. (b) Average seismicity rate of the regions within the contours of (a) for the 48 hours surrounding each large event. Time is with respect to the hypocentral time of each event. This graph shows that seismicity within the contours dramatically increases following these large earthquakes, which lends support to the idea that the interface becomes active through a cascading series of large aftershocks, whose rupture areas are spatially and seismically distinct from the rupture area of the mainshock.

6.2.3 THE FIRST 25 HOURS OF AFTERSHOCKS

As Figure 6.1a shows, events are detected in the back-projection results (henceforth referred to as back-projection events) that are not in other earthquake catalogues. In this section, we extend this comparison between back-projection results and other earthquake catalogues over the first 25 hours of the aftershock sequence. This analysis is performed over a 6° by 6° area around the epicenter of the mainshock. Events are manually picked from the relative source-time function plots (Figure 6.4a). Only those events that have maximum amplitudes at least twice that of the local noise level are initially considered as earthquakes. The time window of the earthquake is selected and the maximum amplitude within this time window is defined as the earthquake time (Figure 6.4a). This definition of earthquake time is probably closer to the centroid time than the epicentral time, though this distinction will only become important for very large aftershocks. The next step in selecting aftershocks is to determine their location (Figures 6.4b and c). The spatial distribution of energy release during the time windows selected in the first step is evaluated. The center of the energy kernel in these plots is selected as the event location (Figures 6.4b and c). In some cases, there are additional events that are clearly separated from the event associated with the peak energy release. If the maximum amplitudes of these events have signal-to-noise ratios of two or greater, then the centers of their energy kernels are selected as earthquake locations. Evaluating the spatial distribution of the back-projection results allows for additional quality control procedures to be performed. Occasionally, energy kernels are at the edge of the back-projection grid. These events are not included, because of the possibility of spatial and temporal bias. In addition, the area of the energy kernel may be much larger than would be expected given the duration of the event. These large features are caused by the arrival of surface waves

from the mainshock, and are discarded.

In total, the back-projection method detects 600 aftershocks during the first 25 hours following the mainshock hypocentral time (Tables B.1 and B.2). The spatial distribution of the aftershocks is very broad with a length of about 500 km along the strike of the Japan Trench (Figure 6.5a). The largest cluster of aftershocks is south and in the updip direction from the epicenter of the mainshock. In addition, there is also a large cluster of events in the outer-rise that has an along trench strike length of about 300 km. Finally, there are a few events that are located within or near the west coast of Honshu that are not associated with the plate interface, or the outer rise, and instead are either shallow events taking place within the overriding Okhotsk/North American plate or deep events that occur within the subducting slab (Figure 6.5). The decay of seismicity rate as a function of time qualitatively follows Omori's law [e.g., Utsu et al., 1995], though more data are needed to model this behavior. There is a dip in the seismicity rate during the second hour of aftershocks that is related to the arrival of surface waves (Figure 6.6). These surface waves obscure events that occur during this time and therefore the decrease in seismicity is an artifact.

6.2.4 COMPARISON WITH THE JMA CATALOGUE

The Japan Meteorological Agency earthquake catalogue lists events in and around Japan using data recorded at stations distributed throughout Japan. In this section, we compare events from the JMA catalogue with the catalogue assembled from the back-projection analysis. In particular, we are interested in determining which events in the back-projection catalogue are also in the JMA catalogue and which events are undetected. To develop a selection criteria, we first look at the distances of back-projection events from JMA events that occur within 100 seconds of each other (Figure 6.7a). Most events within this time window are less than 0.6 degrees from each

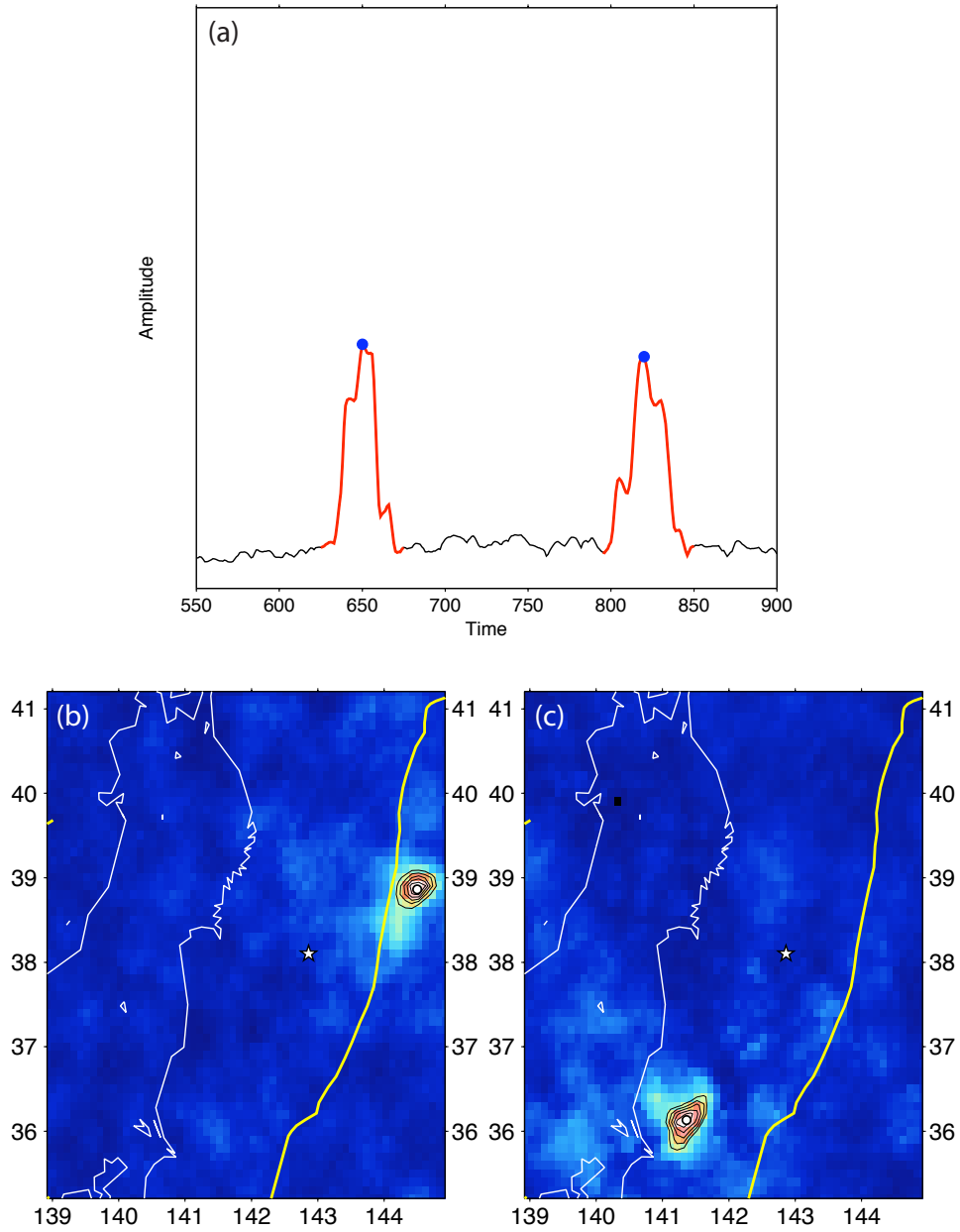


Figure 6.4: (a) A sample of the relative source-time function from the Tohoku aftershock sequence. The time windows of the two aftershocks are shown in red. The local noise level is in black. The blue dots are the peak amplitudes of each event. Time is with respect to March 11th, 19:45:18 UTC. (b) Distribution of energy release for the first event selected in (a). The white dot is the location pick for this event. (c) The same as (b) except for the second event.

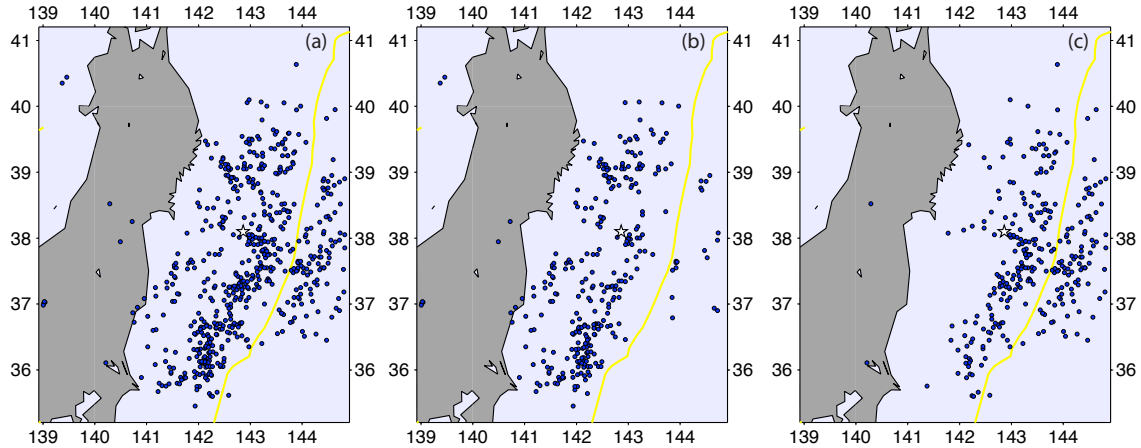


Figure 6.5: (a) Locations (blue dots) of back-projection events from the first 25 hours of aftershocks following the 2011 Tohoku mainshock. The yellow line is the location of the Japan Trench. (b) The same as (a) except only the back-projection events that are also in the JMA catalogue are plotted. (c) The same as (a) except only the back-projection events that are not also in the JMA catalogue are plotted.

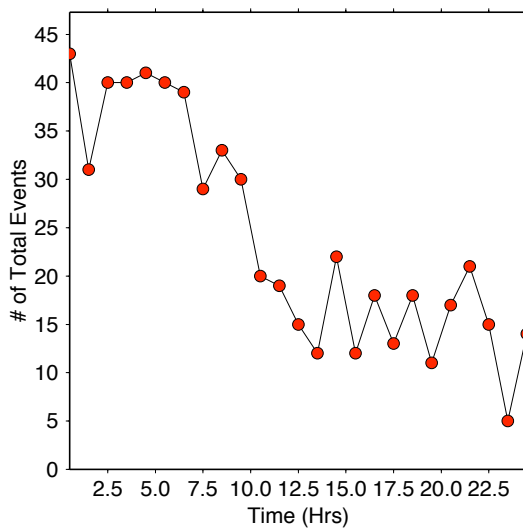


Figure 6.6: The number of back-projection events as a function of time. Time zero is the epicentral time of the mainshock. The data have been gathered into one hour bins.

other, and therefore this is the distance cutoff that is used for earthquake matching. In addition, for the events that fall within this distance, most occur within 50 seconds of each other, and this is chosen as the time limit for detection (Figure 6.7b). Using these selection criteria, about half of the events in the back-projection catalogue are not detected in the JMA catalogue (309 detected and 291 undetected). The events that are detected span almost the entire mainshock region, though there is a noticeable lack of detected events near the trench and in the outer-rise (Figure 6.5b).

Next, we evaluate the magnitudes of JMA earthquakes that can be detected using the back-projection method and the North American seismic array (Figure 6.8a). Most of the detected events have JMA magnitudes that are greater than 4, with a peak at about magnitude 5. It is likely that this peak represents the magnitude of completeness, with the steady decrease at larger magnitudes being a real feature of the aftershock sequence (i.e., the Gutenberg-Richter relationship). The magnitudes in the JMA catalogue can also be evaluated with respect to the peak amplitudes of the coherency function for the detected back-projection events. Figure 6.8b shows that there is a slight correlation between large magnitudes and high coherency function amplitudes, but significant scatter exists. Since the coherency function has little dependence on amplitude information, it is not surprising that the correlation with JMA magnitude is weak. Also, note the systematic increase in the coherency function amplitudes for aftershocks that occur later in the aftershock sequence. This increase in amplitude is likely caused by a decrease in background noise as the seismicity rate decreases. A similar analysis using linear stacking results would likely yield a better correlation with JMA magnitude.

In contrast to the detected events, most of the back-projection events not in the JMA catalogue are located near the trench and in the outer-rise (Figure 6.5c). Besides the spatial distinction, there are only slight differences in the properties of

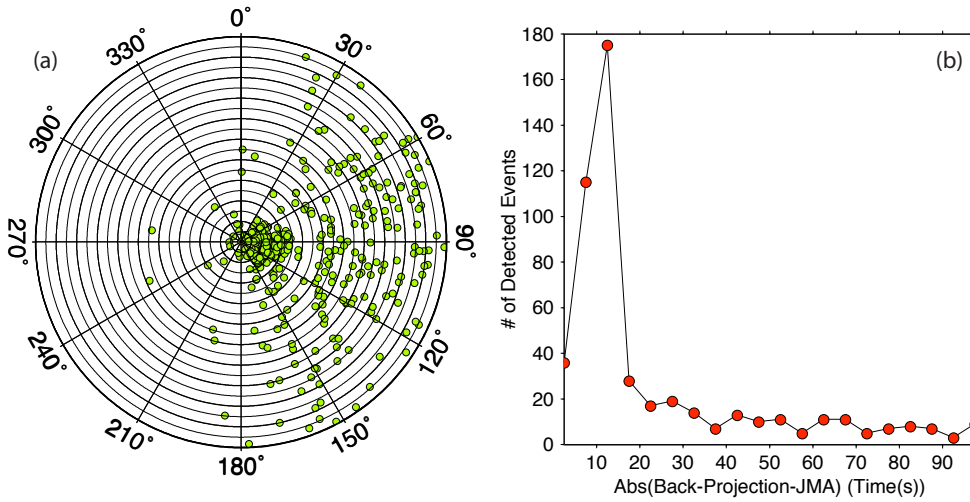


Figure 6.7: (a) Comparison of JMA and back-projection locations. The green dots are the distances and azimuths of the detected back-projection events with respect to their corresponding JMA events plotted in a polar coordinate system. The concentric circles represent distance and have intervals of 0.1 degrees. (b) The number of detected back-projection events as a function of the absolute time difference between JMA and detected back-projection aftershocks. The data have been gathered into 5-second time difference bins.

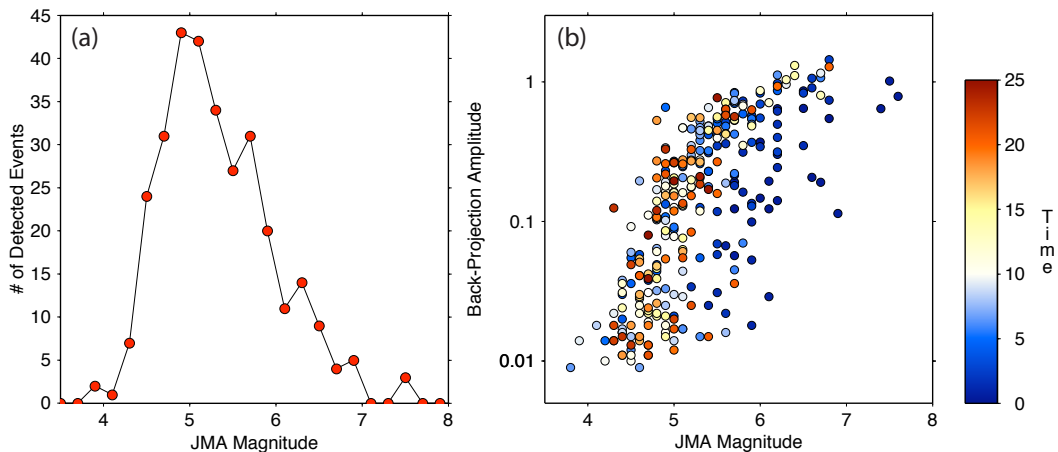


Figure 6.8: (a) The number of detected back-projection events as a function of JMA magnitude. The data have been gathered into 0.2 magnitude bins. (b) Back-projection amplitude versus JMA magnitude for detected events. The colors of the dots represent the times of the aftershocks.

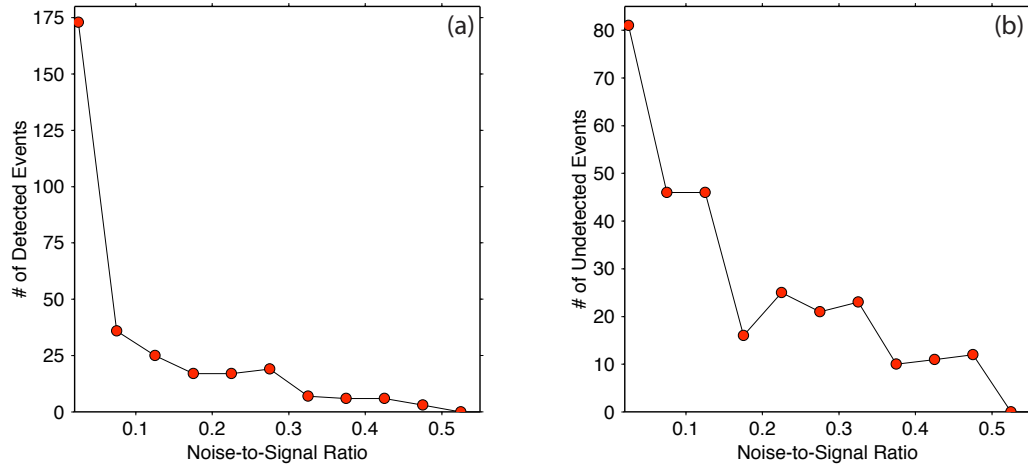


Figure 6.9: (a) The number of back-projection events that are also in the JMA catalogue as a function of noise-to-signal ratio. The data have been gathered into 0.05 noise-to-signal ratio bins. (b) The same as (a) except for events not in the JMA catalogue.

the detected and undetected events. For example, the noise-to-signal ratios of the undetected events have a very similar distribution as the detected events, with most of the events concentrating within the lowest noise-to-signal ratio bin (less than 0.05; Figure 6.9). Surprisingly, the fraction of undetected events only slightly decreases with increasing time from the hypocentral time (Figure 6.10). This near constant detection percentage through time indicates that events are undetected because of their hypocentral location instead of their closeness in time to the mainshock.

An alternative approach to comparing catalogues is to determine the properties of earthquakes in the JMA catalogue that do not have corresponding counterparts in the back-projection catalogue. Most of these events occur near the east coast of Honshu and have magnitudes between 2 and 4.5 (Figures 6.11 and 6.12). There is one event with a magnitude of 6.7 that is not detected by the back-projection analysis. This event takes place during a time period in which the surface waves from the mainshock arrive at the North American stations, and underscores the large degree

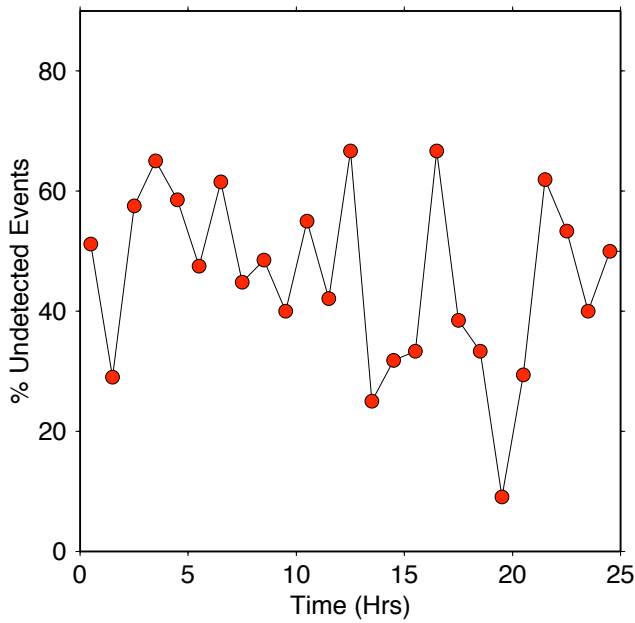


Figure 6.10: The percentage of undetected back-projection events as a function of time. The data have been gathered into one hour bins.

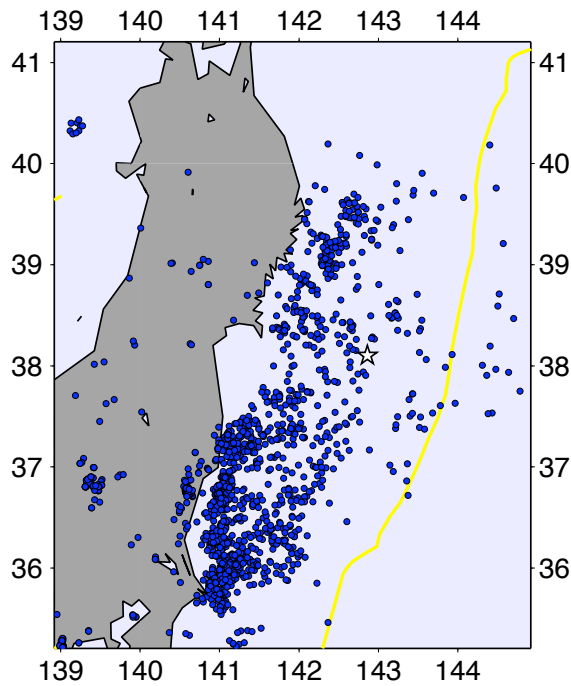


Figure 6.11: Events in the JMA catalogue that do not have corresponding back-projection events.

to which detection is affected during this time.

A final step is to add the back-projection events that are not in the JMA catalogue to the JMA catalogue (Figure 6.13a). When only the JMA events are plotted, there

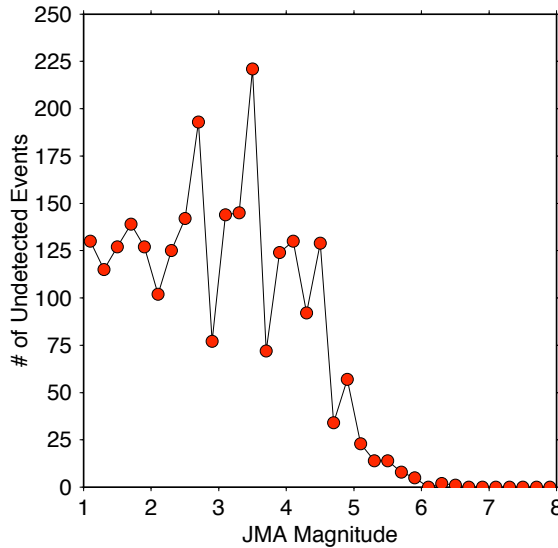


Figure 6.12: The number of JMA events that are not present in the back-projection catalogue as a function of JMA magnitude. The data have been gathered into 0.2 magnitude bins.

is a noticeable absence of events near the trench. This large gap is almost entirely filled when the events detected only by the back-projection technique are included. The interpretations of the spatial distribution of events changes dramatically depending on whether the JMA catalogue or the combined catalogue is used. For example, based upon the JMA catalogue, one would argue that very few seismic events occurred near the trench during the first day of aftershocks. Consequently, the lack of aftershocks may imply that this region undergoes stable sliding immediately following the mainshock, or that in general this region never accumulates significant strain. This has important consequences for the 2011 Tohoku mainshock, because large slip is thought to have occurred near the trench. General paucity of earthquakes near the trench in this region combined with large slip during the mainshock has led some to speculate that dynamic overshoot occurred during the mainshock rupture, and slip only occurred near the trench because of the dynamic energy of the deeper rupture [Ide et al., 2011]. In contrast, including the back-projection events fills in this gap near the trench, which suggests that unstable sliding is a common feature of this region. In this case, the lack of large earthquakes near the trench over the past 200

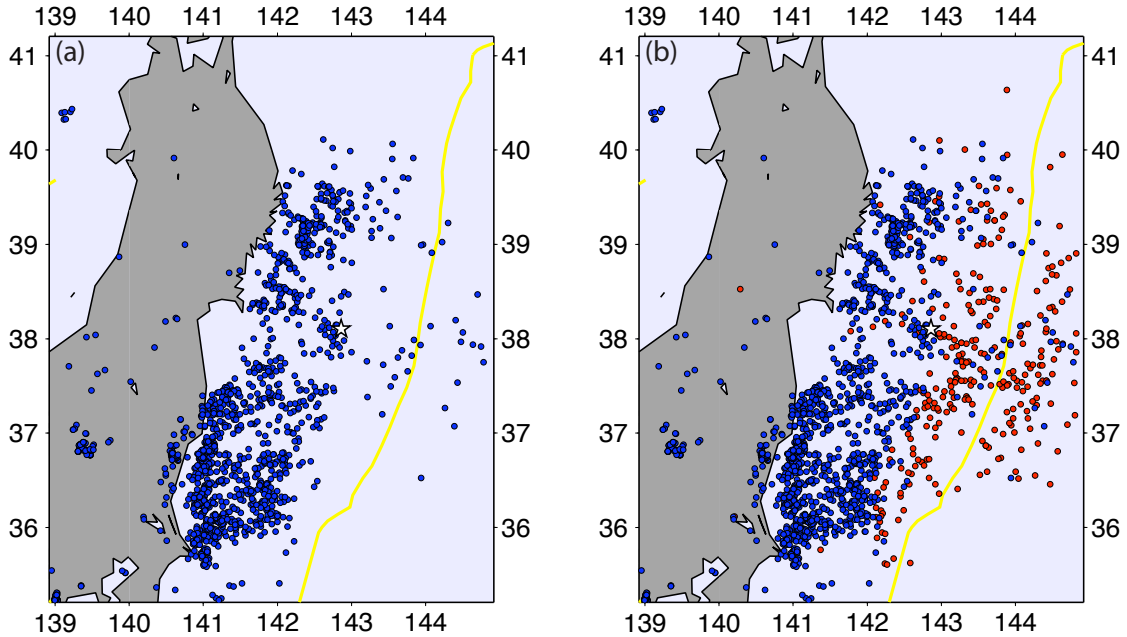


Figure 6.13: (a) Distribution of the first 25 hours of aftershocks (blue circles) from the JMA catalogue. (b) The same as (a) except the first 25 hours of back-projection events that are not in the JMA catalogue have been added (red circles).

years [Hatori, 1987] can be interpreted as an indication of large strain accumulation. A much larger catalogue, which would evaluate the detection issues during times of relative quiescence, is needed to fully understand the seismicity near the trench, and the implications of this seismicity for the 2011 mainshock.

6.2.5 WAVEFORMS FROM UNDETECTED EVENTS IN LOCAL DATA

Though synthetic tests suggest that there is resolution to detect relatively small events (Appendix A), an alternative approach for confirming our back-projection results is to look for waveforms from the events only detected by the back-projection method in the local data. This approach will not only give us more confidence in our results, but may allow us to identify characteristics in the local data that cause these events to be missed by JMA.

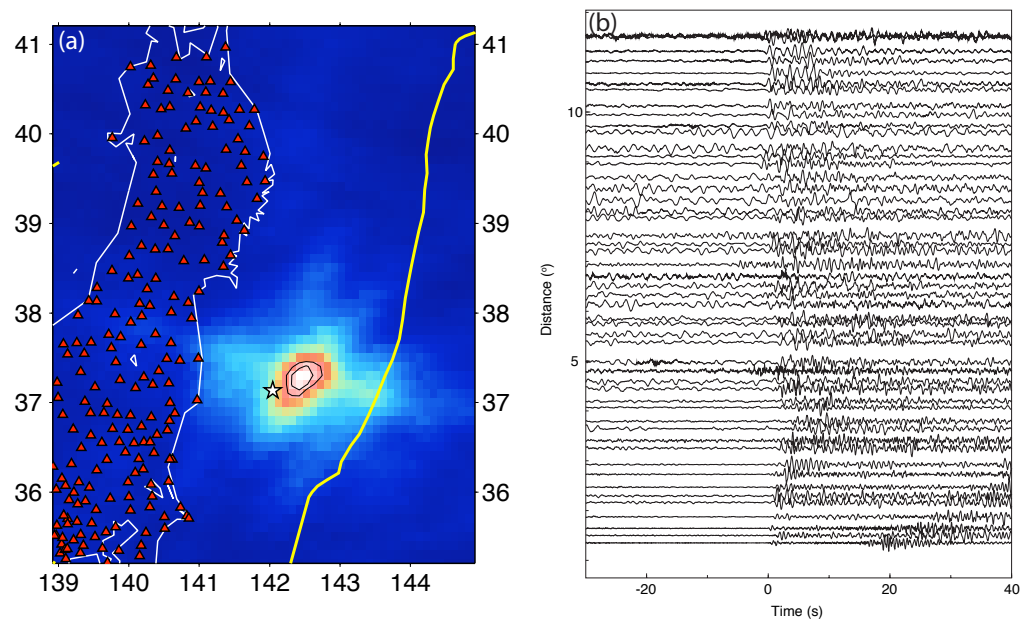


Figure 6.14: (a) Back-projection result (background colors) of a March 11th aftershock that occurred at 08:46:43 UTC. The white star is the epicenter of the JMA earthquake that this event corresponds to, and the triangles are Hi-net stations. (b) Seismograms from the local Hi-net stations aligned at the predicted P wave arrival times based upon the back-projection event location and time.

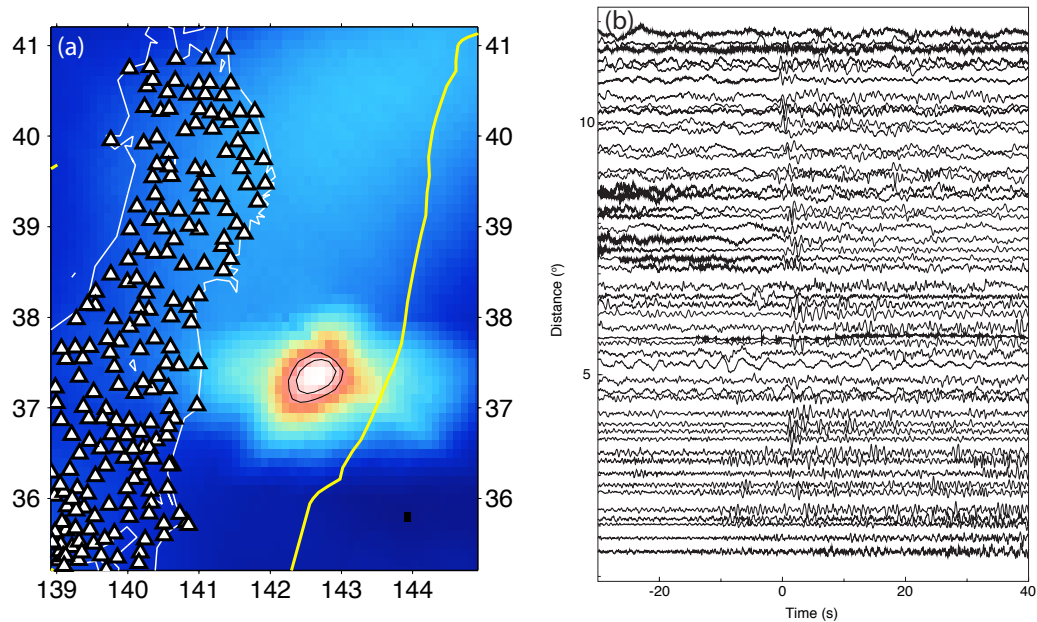


Figure 6.15: (a) Back-projection result of a March 11th aftershock that occurred at 07:23:07 UTC and is not in the JMA catalogue. (b) Seismograms from the local Hi-net stations aligned at the predicted P wave arrival times.

For the sake of comparison, we first look at waveforms from one of the detected events (Figure 6.14). There is a clean P wave arrival associated with this earthquake. This is not surprising given that Hi-net data is also used for the JMA catalogue. In contrast, the waveforms of one of the undetected events are much noisier, and for the closest stations, no P waves can be seen at the predicted times (Figure 6.15). A more thorough analysis is needed to fully understand these features, but these differences seem to be typical. The lack of P wave arrivals for the closest stations, in addition to the spatial clustering of the undetected events, suggest that the local 3-D velocity structure is creating a shadow zone for the closest seismic stations, where ray paths are bent away from these locations. This may be one of the reasons why these earthquakes do not appear in the JMA catalogue.

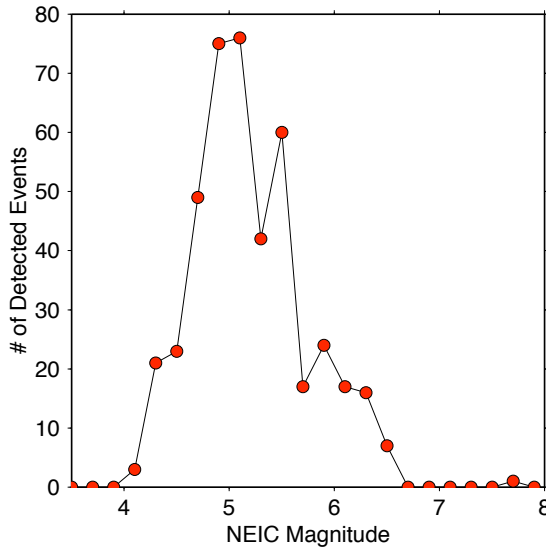


Figure 6.16: The number of detected back-projection events as a function of NEIC magnitude. The data has been gathered into 0.2 magnitude bins.

6.2.6 COMPARISON WITH THE NEIC CATALOGUE

The National Earthquake Information Center (NEIC) catalogue provided by USGS is compiled using global data (<http://earthquake.usgs.gov/regional/neic/>). In general, the magnitude of completeness for this catalogue is higher than the local JMA catalogue. Using the same selection criteria as for the JMA catalogue, the number of back-projection events that have corresponding entries in the NEIC catalogue increases significantly with respect to the comparison with the JMA catalogue (431 detected and 169 undetected). The magnitudes of the NEIC events that match the back-projection catalogue are very similar to the JMA case (Figure 6.16). On the other hand, unlike the JMA case, the spatial distributions of detected and undetected events are very similar (Figure 6.17). The general agreement between back-projection and NEIC aftershocks is not surprising given that teleseismic data are used for both, and may support the idea that the lack of JMA events near the trench is caused by a local velocity feature, though differences in processing techniques between the JMA and NEIC catalogues may also contribute to these results.

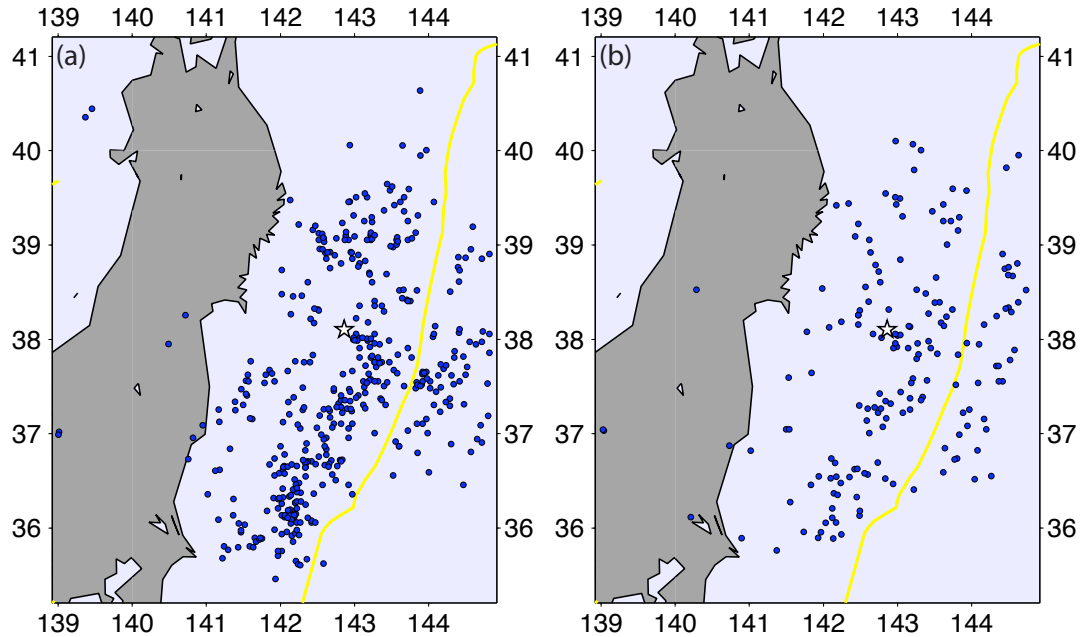


Figure 6.17: (a) Distribution of back-projection events (blue dots) that have counterparts in the NEIC catalogue. (b) The same as (a) except for events not in the NEIC catalogue.

6.3 2004 SUMATRA AFTERSHOCK SEQUENCE

The 2004 Mw 9.1 Sumatra earthquake is different from the 2011 Mw 9.0 Tohoku earthquake in many ways. First, the rupture length and rupture duration of this event is nearly 1300 km and 600 seconds, respectively, compared to 350 km and 220 seconds for the Tohoku event. Second, there was no local network to record the 2004 mainshock, as there was for the Tohoku event. The latter difference means that only a comparison with the NEIC catalogue can be made for the aftershocks detected using the back-projection method. The former difference allows for an investigation of the very early aftershocks near the epicenter of this event, and whether this sequence includes events that occur while the mainshock rupture is still active, but far away from the epicentral region. We refer to these earthquakes as “coseismic aftershocks”.

6.3.1 DATA AND DATA PROCESSING

The initial aftershock sequence of the 2004 Sumatra-Andaman megathrust event is studied using data from the Hi-net array in Japan. These data are filtered between 0.5 and 2 Hz, and only the vertical records are used. As with the 2011 Tohoku aftershock sequence, the coherency function approach is used. No distance constraints are applied to these data, which leads to 703 seismic stations with a distance and azimuthal coverage of 16 and 10 degrees, respectively.

6.3.2 THE FIRST HOUR AND A HALF

The same picking procedure that is outlined in Section 6.2.3 is applied to the first 1.5 hours of aftershocks. The back-projection analysis is applied to a grid area of 14 by 7 degrees that covers the rupture area of the mainshock (Figure 6.18). For the the Sumatra aftershock sequence, a minimum signal-to-noise ratio of 1.25 acts as a good threshold for identifying most of the peaks in the energy release of the back-projection results. In total, 49 earthquakes are recognized during the first 1.5 hours following the mainshock. These events occur within the inferred mainshock rupture area [e.g., Ishii et al., 2005], but also include a few back-arc earthquakes (Figure 6.18a).

6.3.3 COMPARISON WITH THE NEIC CATALOGUE

There are only 14 aftershocks in the NEIC catalogue during the first 1.5 hours. Back-projection events that are within 30 seconds and 0.9 degrees of NEIC events are considered as detected for this comparison. Using these criteria, 13 of the 14 NEIC events are also identified by back-projection (Figure 6.18b). The one event that is not detected takes place very close in space and time to a larger event, so that these two earthquakes cannot be distinguished using the back-projection approach. Taking the

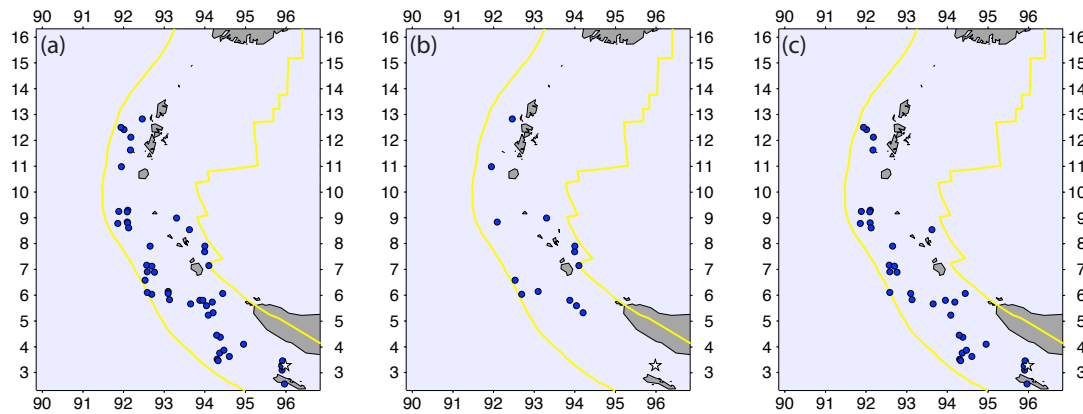


Figure 6.18: (a) Locations (blue dots) of back-projection events from the first 1.5 hours following the 2004 Sumatra mainshock. The yellow lines are the locations of plate boundaries. (b) The same as (a) except only the back-projection events that are also in the NEIC catalogue are plotted. (c) The same as (a) except only the back-projection events that are not in the NEIC catalogue are plotted.

opposite perspective, there are 36 back-projection events that are not in the NEIC catalogue. There is some indication that the back-projection events not in the NEIC catalogue concentrate near the epicenter of the mainshock, but there are not enough earthquakes to make any strong statements about the spatial distinctions of these events (Figure 6.18c).

6.3.4 COSEISMIC AFTERSHOCKS

The large rupture length of the 2004 mainshock means that the rupture leaves the epicentral region well before the rupture ends. This provides a unique opportunity to study the early aftershock activity in this region, and in particular, determine if aftershocks take place while the mainshock rupture is still propagating. The exact timing of the start of the aftershock sequence is important for evaluating the sliding behavior directly following large slip, and the constitutive relationships that govern this behavior [e.g., Dieterich, 1994; Peng et al., 2007]. This analysis is performed by

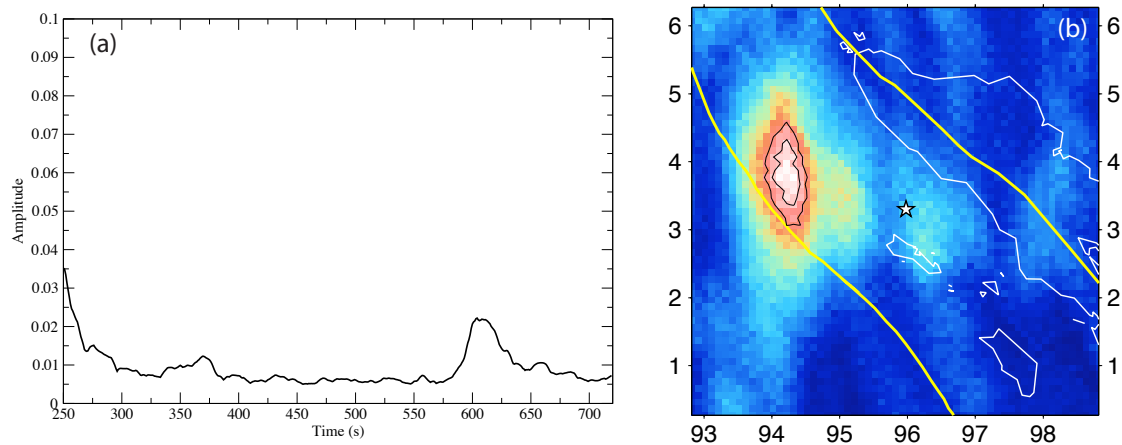


Figure 6.19: (a) Source-time function from the region around the epicenter of the 2004 mainshock. Time is with respect to the mainshock hypocentral time. The peak at around 600 seconds is the first aftershock detected by the back-projection technique. (b) Spatial distribution of energy release from the first aftershock.

back-projecting data to a much smaller region around the epicenter (6 by 6 degrees) than in Section 6.3.2. This smaller grid area makes detecting aftershocks slightly easier by avoiding the large amplitude signal associated with the final part of the mainshock rupture occurring to the north. The relative source-time function has a first peak at around 600 seconds after the epicentral time (Figure 6.19a). This is slightly after the time when the mainshock rupture ends far to the north. In addition to the timing, the location of this event is very interesting from a hazards perspective due to its closeness to the trench (Figure 6.19b).

The analysis that follows will attempt to verify whether there are no events taking place before 600 seconds, or whether it is due to limitations in detection. To determine the time dependence of detection, waveforms from other earthquakes that occurred within this region are inserted into the mainshock signal at different times. These modified data are back-projected to determine whether the inserted events can be detected at the specified times.

The first event to be inserted into the mainshock signal occurred in 2005 and had a moment magnitude of 6.8. This event is inserted at 440 seconds, 490 seconds, and 540 seconds after the mainshock hypocentral time, and separate back-projection results are produced for each modified data set (Figure 6.20). The event is clearly detected at 490 and 540 seconds, but is not observed at 440 seconds (Figure 6.20). This result shows that even when the mainshock rupture is outside of the study region, it is difficult to detect aftershocks. It is also important to recall that there is limited correlation between the amplitude of the coherency function and the magnitude of the event (Figure 6.8b). Therefore, comparing the amplitudes of the 6.8 event to the amplitude of the first aftershock at 600 seconds does not provide much insight into the magnitude of the first aftershock. The large amplitudes in the back-projection results are simply indicating that it is possible to detect a magnitude 6.8 earthquake at times later than 490 seconds after the mainshock hypocentral time, and not possible to detect a magnitude 6.8 event before 490 seconds. Thus this analysis is essentially providing a lower bound on the magnitudes of events at various times. In addition to the magnitude 6.8 event, waveforms from magnitude 7.4, 6.3, and 6.0 events are inserted into the mainshock signal. The magnitude 7.4 event is detected starting at about 290 seconds after the epicentral time (Figure 6.21), the magnitude 6.3 event is detected after about 540 seconds after the epicentral time, and the magnitude 6.0 event is first detected between 590 seconds and 640 seconds. Figure 6.22 summarizes the lower bounds of detectable earthquakes as a function of time. The first aftershock at 600 seconds has a lower-bound magnitude of 6.0. This lower-bound magnitude is relatively large for this aftershock sequence (taking 3 months as the time period of aftershocks) since the largest event to occur within the study region had a magnitude of 6.8. In addition, Figure 6.22 shows that it is possible that very large events ($6.8 < M < 7.4$) can go undetected early in the aftershock sequence.

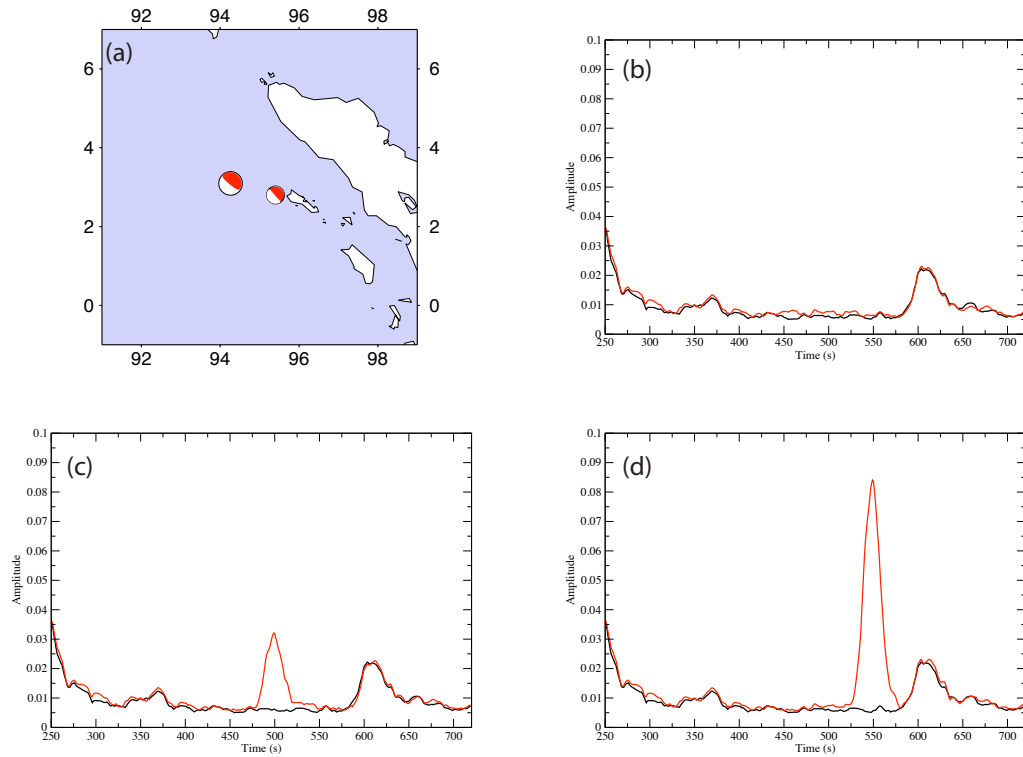


Figure 6.20: (a) Focal mechanisms of the 2004 Mw 9.1 mainshock and 2005 Mw 6.8 aftershock. (b) Relative source-time functions using the original data (black line) and the modified data (red line) where the Mw 6.8 event has been inserted at 440 seconds. The peak at around 600 seconds is the first aftershock detected in the original data. (c) The same as (a) except the Mw 6.8 event has been inserted at 490 seconds. (d) The same as (a) except the Mw 6.8 event has been inserted at 540 seconds.

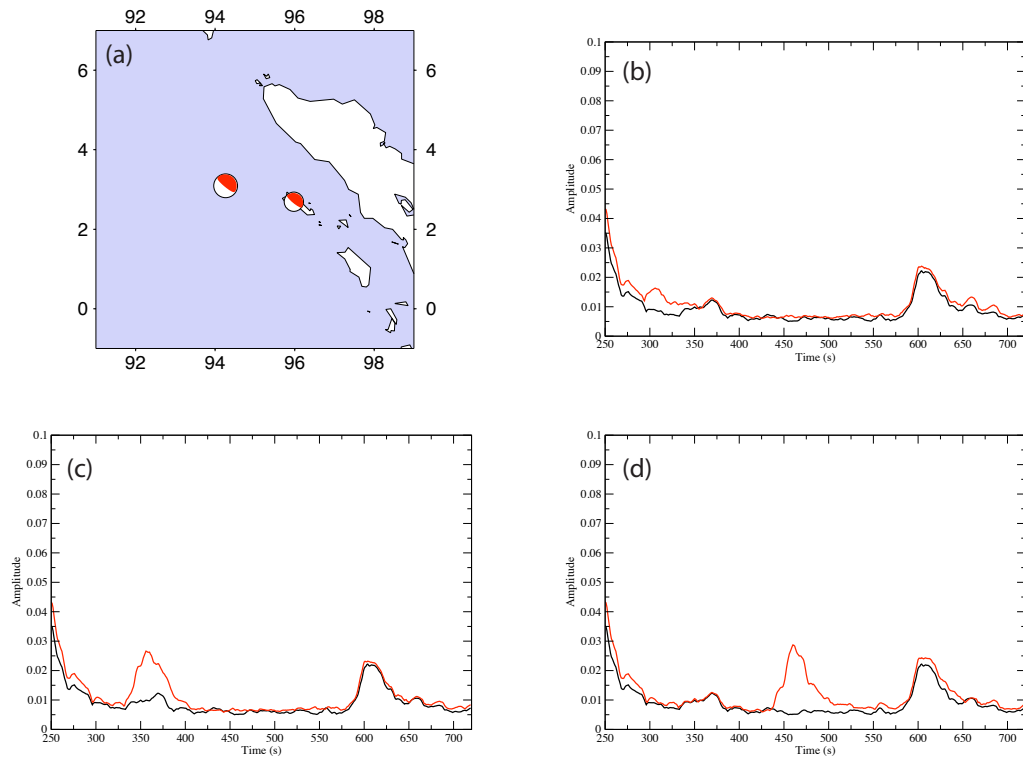


Figure 6.21: (a) Focal mechanisms of the 2004 Mw 9.1 mainshock and 2008 Mw 7.4 aftershock. (b) Relative source-time functions using the original data (black line) and the modified data (red line) where the Mw 7.4 event has been inserted at 290 seconds. The peak at around 600 seconds is the first aftershock detected in the original data. (c) The same as (a) except the Mw 7.4 event has been inserted at 340 seconds. (d) The same as (a) except the Mw 7.4 event has been inserted at 440 seconds.

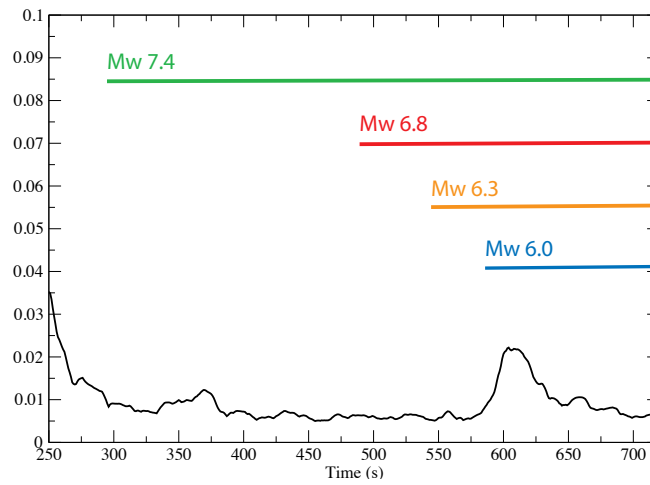


Figure 6.22: The horizontal lines show the times at which earthquakes with the corresponding magnitudes can be detected. The green line is from the Mw 7.4 event, the red line is from the Mw 6.8 event, the orange line is from the Mw 6.3 event, and the blue line is from the Mw 6.0 event.

6.4 SUMMARY

Results in Chapter 6 show the potential of back-projection as an aftershock detection tool. The method can be used to improve the completeness of both local and global catalogues. In particular, based upon the comparison with the JMA catalogue, back-projection can be useful for identifying specific regions where completeness is especially poor. Improving the completeness of earthquake catalogues will lead to more accurate modeling of aftershock sequences [e.g., Utsu et al., 1995], which are commonly used when evaluating the future seismic hazards in a given region. One of the main limitations of the results presented in this chapter is the inability to estimate the magnitudes of the undetected events. This will likely improve when a linear stacking back-projection analysis is combined with the coherency function analysis presented here.

The vigorous aftershock sequence of the 2011 Mw 9.0 Tohoku earthquake produced several relatively large events. The rupture areas of these earthquakes reveal

that activation of the plate interface occurs through a cascading failure of individual segments. Further work in this area should concentrate on determining the rupture directions and velocities of these aftershocks. In particular, spatial and temporal variations in these parameters may be used to describe the stress state of the subduction zone [e.g., Ben-David et al., 2010].

Finally, the early aftershock analysis of the 2004 Mw 9.1 Sumatra earthquake shows that a relatively large event ($M \geq 6$) occurred immediately following the mainshock that is not in any catalogue. In addition, this work shows that large coseismic aftershocks would not be detected, even when using the back-projection method. Therefore, future work on this subject should include the implementation of additional processing steps to improve early aftershock detection. These may include a more thorough procedure for determining the coherency function (See Chapter 2), and the use of more advanced filters for identifying and removing background noise [e.g., Stein and Wysession, 2003, Velocity Filtering].

CHAPTER 7

FUTURE WORK

The results and discussions in Chapters 2-6 demonstrate the capability of back-projection for studying earthquake sources. In this final chapter, discussions of future work on this subject will be presented. In some cases, these discussions will be direct extensions of the results shown in this thesis. However, there is also discussion of general ways in which back-projection should be implemented in the future.

7.1 THE BACK-PROJECTION METHOD

As Chapter 5 demonstrated, back-projection results at low frequencies do not have the same resolution as at high frequencies, but can still provide constraints on the overall behavior of the rupture. Lower frequency seismic waves are not as sensitive to small scale structure and therefore waveform coherency across very large networks is not as much of an issue as at high frequencies. Therefore, at low frequencies, data from the Global Seismic Network could likely be utilized. The use of a global data set presents interesting opportunities to expand the back-projection analysis to put constraints on slip by using the amplitude and polarity information of the waveforms, which is not possible using high-frequency regional array data. For example, once the

times and locations of energy release are determined, specific time windows of the data (both P and S waves) that represent significant subevents of the rupture can be inverted to determine focal mechanisms associated with the different subevents. This approach would give some information regarding the slip behavior, which is a major gap in the current information that can be obtained from a back-projection analysis.

7.2 DEEP EARTHQUAKES

Chapter 3 shows that dynamic triggering during large intermediate-depth earthquakes is common. Additional insight can be gained by investigating dynamic triggering within the subducting slab, far away from the mainshock region. This analysis can determine the sensitivity of the triggering mechanism to seismic wave amplitude, and possibly the relative volatile content throughout the subducting slab. In addition to putting constraints on conditions within the slab, these results will have implications for the water cycle within the mantle.

There are many differences in the characteristics of intermediate-depth and deep-focus earthquakes [e.g., Vidale and Houston, 1993; Persh and Houston, 2004]. From a seismological perspective, it is possible that many of these differences are due to triggered sub-events at intermediate-depths and simple, continuous ruptures at depths between 400 and 700 km. A back-projection study of the rupture properties of deep-focus earthquakes would test this hypothesis and provide additional insights into the mechanisms of these events.

7.3 UNDERSTANDING RUPTURE COMPLEXITY

Though it has been known for decades that earthquake sources are very complex [e.g., Wyss and Brune, 1967], the back-projection results presented in Chapters 4

and 5 show that it is becoming possible to actually quantify this complexity and use it for mitigating and predicting future seismic hazards. From the perspective of back-projection, the critical step for fully exploiting this new information is to link the behavior of energy release with the slip properties and associated hazards of the event. In addition to improving the back-projection method, as is briefly described in Section 7.1, comparisons between slip models using different data sets (e.g., seismic, GPS, and tsunami data) and the back-projection results may help establish this link. In addition, it is important to provide comparisons between the back-projection results and models of the tectonic environments in which the earthquakes occur (e.g., interseismic coupling).

The comparison approach described above may eventually provide a simple way of better understanding back-projection results, however, currently there is significant variation between different slip models for any given earthquake, so it is difficult to know which comparison should be made. An alternative approach to understanding the physical meaning of relative energy release is to back-project synthetic velocity records produced by numerical dynamic models of rupture. An obvious advantage to this type of analysis is that almost every detail of the synthetic rupture can be calculated and compared with the back-projection results. In addition, the constitutive relationships acting during the dynamic rupture can be specified, and therefore it may be possible to establish a link between these relationships and back-projection results [e.g., Bizzarri, 2011].

APPENDIX A

RESOLUTION

A.1 INTRODUCTION

The results presented in Chapters 3-6 show that earthquake sources are extremely complex over a large range of magnitudes and hypocentral depths. This appendix presents synthetic tests that demonstrate which features are resolvable for a given source location. For these synthetic tests, the locations and times of imaged energy from back-projecting synthetic seismograms are compared with the known locations and times of sources used to produce the synthetic seismograms, which can give an indication of the robustness of the recovered features.

A.2 LATERAL RESOLUTION

Back-projection results in Chapter 4 show segmentation during large shallow earthquakes. In this section, we explore the robustness of this complexity by providing and discussing results of synthetic tests that investigate the dependence of lateral resolution on the station distribution, location of the seismic array relative to the earthquake epicenter, and the seismic phases being used. Synthetic seismograms are generated using a simple Ricker wavelet [Ricker, 1953, Figure A.1] with central fre-

quency of 1.0 Hz. The arrival times of the wavelets are determined using a 1-D velocity model of the Earth [Kennett, 1991, IASP91] for a given source location and specified seismic phases. The signal-to-noise ratios of these seismograms are typically around 20, but in some cases are as low as 3.

A.2.1 DISTANCE AND AZIMUTH COVERAGE

The lateral resolution of the back-projection method primarily depends on the distance and azimuthal coverage of the array of stations being used. We illustrate the effect of each criterion by generating synthetic seismograms for hypothetical arrays. To investigate the effect of distance coverage, we generate a synthetic array with stations at distances between 60 and 90 degrees and at a fixed azimuth of 0 degrees (Figure A.2a). The spacing between the stations is 0.1 degrees which leads to an array of 300 stations. The back-projection result from this array shows a circular arc of energy that passes through, and is maximum at, the input point source location (Figure A.2b). As expected, the good distance coverage of the array provides good constraints on the distance of the point source from the array. Conversely, the lack of azimuthal coverage makes it difficult to constrain the azimuth of the point source. The resolution not only depends on the range of distances used, but also on the absolute distances of the stations (Figure A.2c). Here, a synthetic array is set up with the same distance range (30 degrees), but it is closer to the epicenter (40 to 70 degrees; Figure A.2a). The back-projection result from this synthetic array shows that the recovered energy has a larger curvature and less lateral extent than in Figure A.2(b). The improved lateral resolution for closer absolute distances can be understood if one considers a P wave travel time curve (Figure A.2a). The P wave slowness of closer arrays changes more, hence these arrays are more sensitive to changes in the source location. This dependence on slowness becomes more important when considering

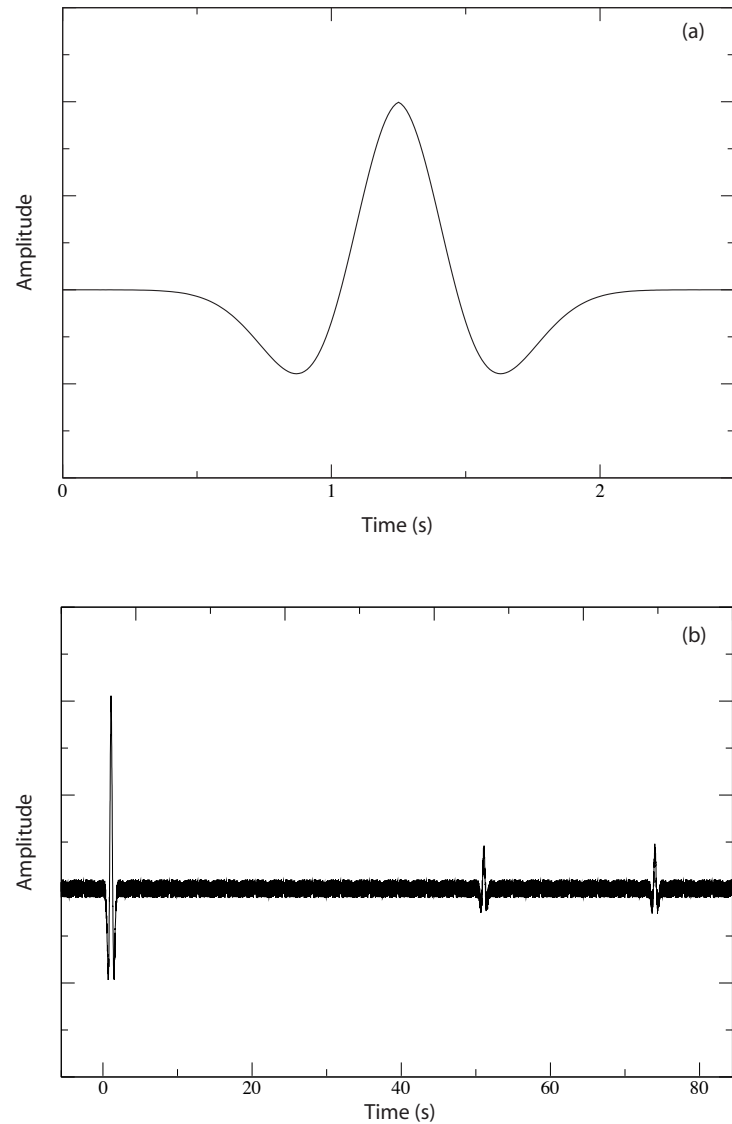


Figure A.1: (a) A Ricker wavelet. (b) Example synthetic seismogram at station TBTH in the Hi-net array from a source at 13.50° S, 166.97° E, and 110 km depth. Time is with respect to the P wave arrival and noise is included with amplitude that is 10% of the input P wave. In addition to P , the seismic phases pP and sP are included in this synthetic seismogram.

distances at which core phases are the first to arrive. For example, the slowness of the core phase *PKIKP* is weakly dependent on distance (Figure 4.2b), and is much less sensitive to changes in source location than the *P* phase.

A similar synthetic test with an array of stations at azimuths between 0 and 30 degrees, a station spacing of 0.1 degrees, and a constant distance of 75 degrees is performed to investigate the effects of azimuthal coverage (Figure A.2d). The recovered energy using this array is now elongated in the direction of the array. This result shows that good azimuthal coverage of the array constrains the azimuth of the point source very well, and poor distance coverage leads to poor distance resolution in the direction of the array (Figure A.2d). For real seismic arrays, the shape and size of a resolution kernel are primarily controlled by the azimuthal and distance coverage, i.e., the shape and size of the array. The synthetic tests also show that absolute distance affects the final result. These results illustrate limitations in using a single array for back-projection studies of source properties. One approach to improve resolution is to increase distance and azimuth coverage by using a global network of stations such as the Global Seismic Network [e.g., Walker et al., 2005; Walker and Shearer, 2009; D'Amico et al., 2010]. However, this data set presents its own challenges due to poor waveform coherence between the stations compared to that within a dense seismic array, especially at high frequencies. Even when care is taken to group stations into subsets with similar waveforms, artifacts can still be an issue [Walker and Shearer, 2009]. In Chapter 4, we have attempted to take advantage of waveform coherence within a given array while improving station coverage by combining two arrays at different azimuths and distances.

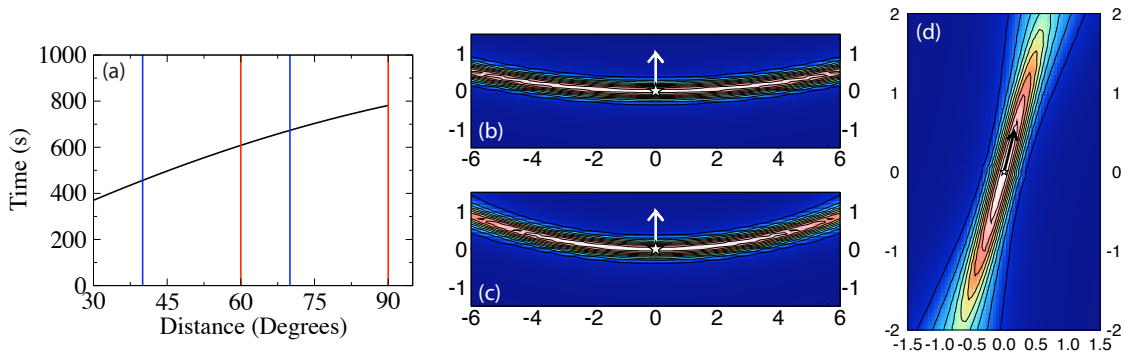


Figure A.2: (a) Synthetic arrays with stations at a range of distances, but all at the same azimuth are generated to determine the effect of poor azimuthal station coverage on back-projection results. This plot shows the range of distances used when generating the synthetic arrays on the travel-time curve (black line). The blue lines show the range for the 40 to 70 degree array, and the red lines show the range for the 60 to 90 degree array. These arrays each have 300 stations with a station spacing of 0.1 degrees. (b) The back-projection result for a point source (white star) using the array with a distance range of 60 to 90 degrees. The colors represent the values of the integrated squared stacks from each grid point. White represents maximum energy and dark blue represents minimum energy. The white arrow is the direction to the array. The latitude/longitude tick marks are with respect to the point source (white star). (c) The same as (b) except using the array with a distance coverage of 40 to 70 degrees. (d) As with (b) and (c), this plot shows the back-projection result for a point source (white star). In this case, the synthetic array used has stations at a constant distance (75 degrees) from the point source, but with an azimuthal coverage of 30 degrees. The black arrow is the direction to the array.

A.2.2 REGIONAL LATERAL RESOLUTION

Lateral resolution using the back-projection method depends upon distance and azimuthal station coverage, and slowness of the phase used (Section A.2.1). In this section we evaluate how the approach of combining arrays improves resolution for the four regions considered in Chapter 4. Each of these regions present unique resolution issues due to their positions relative to Hi-net and TA. Therefore, synthetic tests are presented separately for each region in subsequent sections. For the sake of comparison, we arbitrarily choose the 70% contour of maximum energy to interpret and compare the synthetic results. We estimate the minimum magnitude of an event above which rupture properties can be imaged using the area within this contour [Kanamori, 1977].

Pisco, Peru

319 stations of the Transportable Array are distributed over a distance and azimuth range of 54 to 75 degrees and 321 to 335 degrees, respectively, relative to the epicenter of the August 15, 2007 Mw 8.0 Pisco, Peru event (Figure A.3a). This distance range implies that the P phase is the first to arrive at these stations. On the other hand, the stations of the Hi-net array covers a distance and azimuth range of 133 to 150 degrees and 307 to 323 degrees, respectively. As described in Chapter 4, a distance filter is applied to avoid complications due to the core-phase triplication, resulting in 138 stations with a clean PKP bc phase within a distance and azimuth range of 146 to 150 degrees and 309 to 315 degrees, respectively.

The recovered energy distribution using synthetic seismograms generated for TA and Hi-net from a point source are shown in Figures A.3(b) through (e). By itself, the TA data images the point source very well (Figure A.3b), with an area inside

the 70% contour of 2200 km². In contrast, the result using only Hi-net synthetic seismograms exhibits very poor resolution with an area of 30000 km² inside the 70% contour (Figure A.3c). The poor resolution is primarily a result of the poor azimuth and distance coverage of the array subset used in the analysis, as well as nearly constant slowness. Combining stacks from TA and Hi-net results in some improvement to the TA result (Figure A.3d). The 70% contour area reduces to 1400 km², which corresponds to a moment magnitude of 7.1 [Kanamori, 1977]. This threshold magnitude for imaging rupture properties is much lower than the magnitude of the Pisco, Peru event (Mw 8.0), and therefore details of the rupture should be recoverable using the TA and Hi-net arrays. Finally, a synthetic test is performed including the core phases *PKPab* and *PKIKP* with the *PKPbc* phase in the synthetic seismograms for Hi-net stations to investigate the effects of other core phases not considered during stacking. As Figure A.3(e) shows, these additional phases cause only small changes on the final back-projection result due to the slowness differences between the core phases.

Mentawai Islands

The September 12, 2007 Mw 8.4 Mentawai Islands earthquake occurred at a distance and azimuth range of 45 to 63 degrees and 31 to 40 degrees, respectively, from Hi-net and 122 to 141 degrees and 28 to 46 degrees, respectively, from TA (Figure A.4a). For the 752 stations in Hi-net, the first phase to arrive is *P*, and for TA, there are 346 stations with *PKIKP* as the first arrival. The resolution kernel of a point source using Hi-net data has an area of 3900 km² inside the 70% contour (Figure A.4b). In contrast, the area inside the 70% contour using TA data is 87000 km² (Figure A.4c). This poor resolution from the TA data is caused by the nearly constant slowness of the *PKIKP* phase (Figure 4.2b). Combining the two arrays leads to an energy kernel

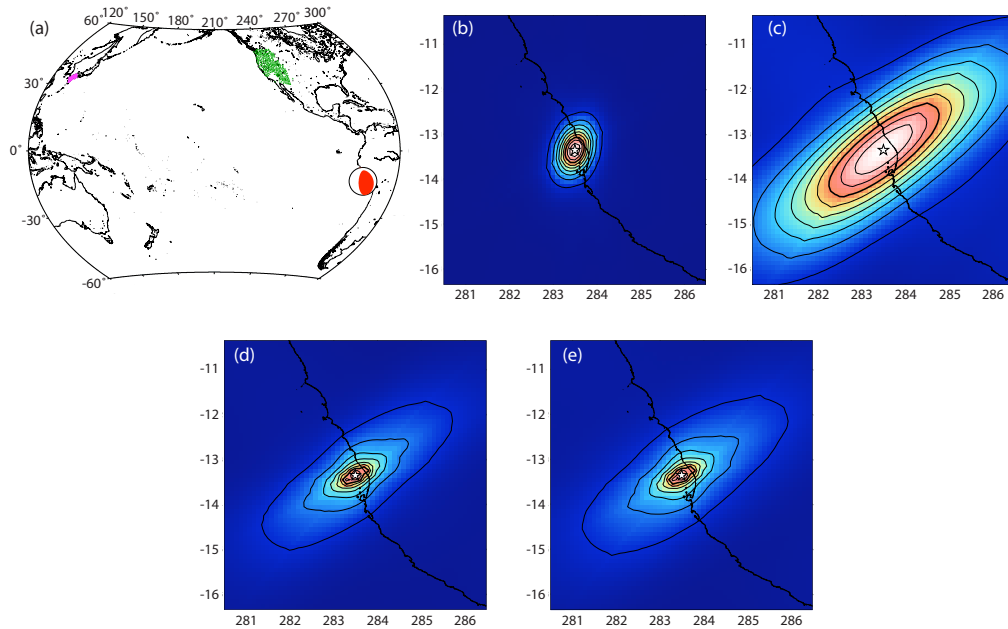


Figure A.3: Back-projection results for a point source input at the hypocenter of the Mw 8.0 2007 Pisco, Peru earthquake. (a) Distribution of stations from TA (green triangles) and Hi-net (pink triangles) with respect to the focal mechanism of the 2007 Peru event (Global CMT Catalogue); [Dziewoński et al., 1981; Dziewoński and Woodhouse, 1983]. Note that there is a distance constraint of 146 to 150 degrees applied to the Hi-net data. (b) Back-projection result from a point source (white star) at the hypocenter of the 2007 Peru event using synthetic TA data. White represents high energy release and dark blue represents low energy release. The light grey lines are the contours of maximum energy release in 10% intervals. The black contour is the 70% contour. The solid black line is the coastline. (c) The same as (b) except using synthetic Hi-net data. (d) The back-projection result when both synthetic TA and Hi-net data are combined. (e) The same as (d) except the core phases *PKIKP* and *PKPab* are included in the synthetic seismograms for Hi-net.

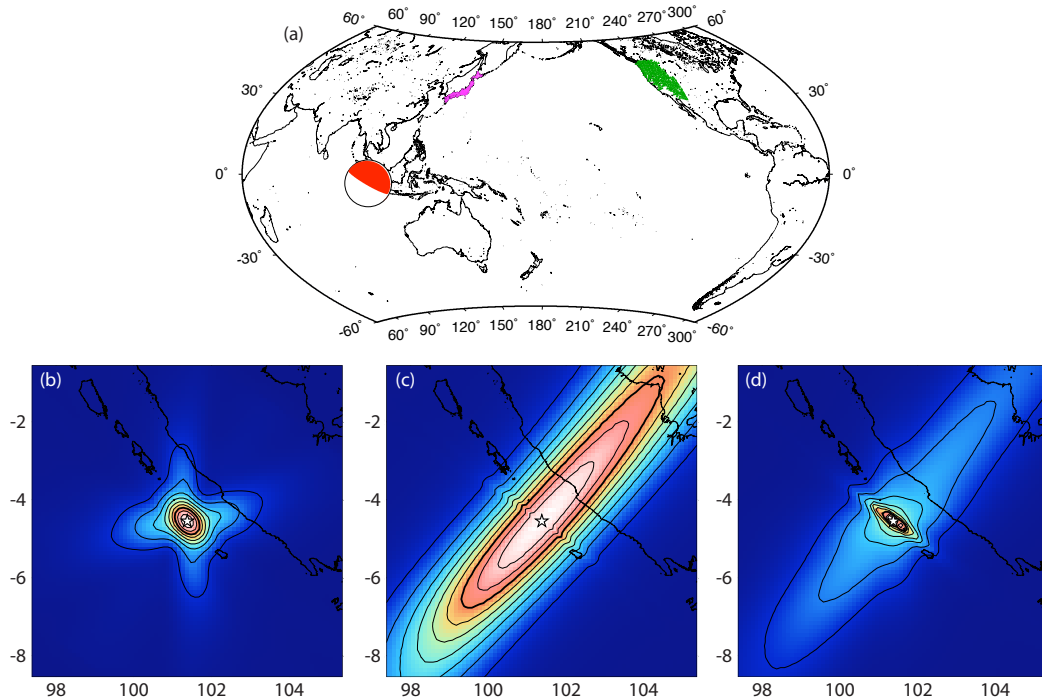


Figure A.4: Back-projection results for a point source at the hypocenter of the Mw 8.4 2007 Mentawai Islands earthquake using synthetic data from both TA and Hi-net. (a) Distribution of stations from TA (green triangles) and Hi-net (pink triangles) with respect to the the focal mechanism of the 2007 Mentawai Islands event (Global CMT Catalogue); [Dziewoński et al., 1981; Dziewoński and Woodhouse, 1983]. (b) Back-projection result from a point source (white star) at the hypocenter of the 2007 Mentawai Islands event using Hi-net synthetic data. The symbols are the same as in Figure A.3. (c) The same as (b) except using TA synthetic data. (d) The back-projection result when both Hi-net and TA synthetic data are used.

with an area of 1700 km^2 , with much better resolution in the dip direction than parallel to the trench (Figure A.4d). Therefore, the minimum earthquake magnitude that can be imaged is 7.2 [Kanamori, 1977]. In addition to imaging the Mw 8.4 event, this means that the data are also capable of imaging the rupture properties of the Mw 7.9 earthquake that occurred 12 hours after the Mw 8.4 event in the same region.

Samoa Islands

The epicenter of the September 29, 2009 Mw 8.1 Samoa Islands event is at a distance and azimuth range of 67 to 75 degrees and 310 to 329 degrees, respectively, from Hi-net, and 71 to 100 degrees and 36 to 60 degrees, respectively, from TA (Figure A.5a). At these distances, the first phase to arrive for both Hi-net and TA is *P*. The number of stations in Hi-net and TA is 802 and 405, respectively. By itself, the TA data images the point source very well (Figure A.5b), giving the area inside the 70% contour of 2300 km². The result using only Hi-net synthetic seismograms also exhibits good resolution with an area of 4700 km² inside the 70% contour (Figure A.5c). In addition to being at *P* phase distances, the arrays also have good distance and azimuthal coverage, which leads to their small resolution kernels. Better resolution using TA is due to the larger distance and azimuth range covered by TA compared to Hi-net. Combining stacks from TA and Hi-net results in a very small energy kernel with an area of 550 km² (Figure A.5d). Using the empirical relationship of Kanamori [1977], the threshold moment magnitude associated with this region is 6.7, much less than the event magnitude on September 29, 2009.

Maule, Chile

The distance and azimuth range of the 390 TA stations from the epicenter of the February 27, 2010 Mw 8.8 Maule, Chile earthquake is 67 to 94 degrees and 323 to 353 degrees, respectively (Figure A.6a). Therefore, the *P* phase is the first to arrive. The distance of stations used from Hi-net is limited to 155 degrees or greater to isolate the *PKIKP* phase. This results in a subset of 384 stations with a distance and azimuth range of 155 to 162 degrees and 263 to 283 degrees, respectively (Figure A.6a). The areas of the point source energy kernels for TA and Hi-net are 1700 km² and

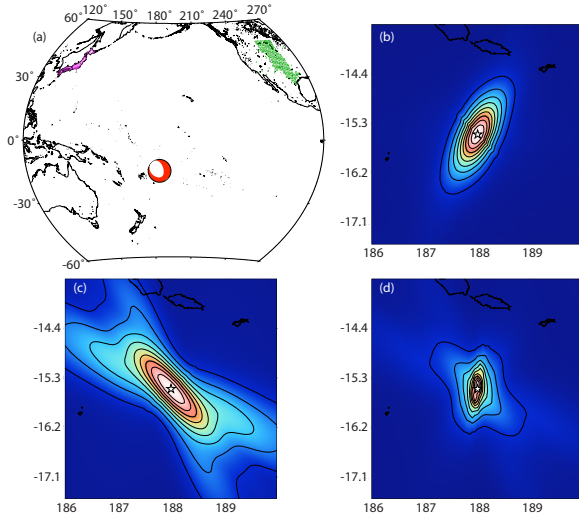


Figure A.5: Back-projection results for a point source at the hypocenter of the Mw 8.1 2009 Samoa Islands earthquake using synthetic data from both TA and Hi-net. (a) Distribution of stations from TA (green triangles) and Hi-net (pink triangles) with respect to the focal mechanism of the 2009 Samoa Islands event (Global CMT Catalogue); [Dziewoński et al., 1981; Dziewoński and Woodhouse, 1983]. (b) Back-projection result from a point source (white star) at the hypocenter of the 2009 Samoa Islands event using TA synthetic data. The symbols are the same as in Figure A.3. (c) The same as (b) except using Hi-net synthetic data. (d) The back-projection result when both TA and Hi-net synthetic data are used.

50000 km², respectively (Figures A.6b and c). As with the Peru event, the limited distance coverage of Hi-net, as well as the slowness of the seismic phase being used, leads to its large resolution kernel. Combining stacks from both arrays leads to a slightly improved area of 1000 km² (Figure A.6d). The associated magnitude of this area is 7.0 [Kanamori, 1977], therefore details of the Mw 8.8 earthquake can be imaged. Additional core phases are included in a final synthetic test to demonstrate that they do not affect the final back-projection results significantly (Figure A.6e).

A.3 DEPTH AND TIME RESOLUTION

The results in Chapter 3 show that earthquake source complexity also extends to intermediate depths. In addition, sub-events have very limited depth extents. This section demonstrates the depth and time resolution that can be achieved when seismic

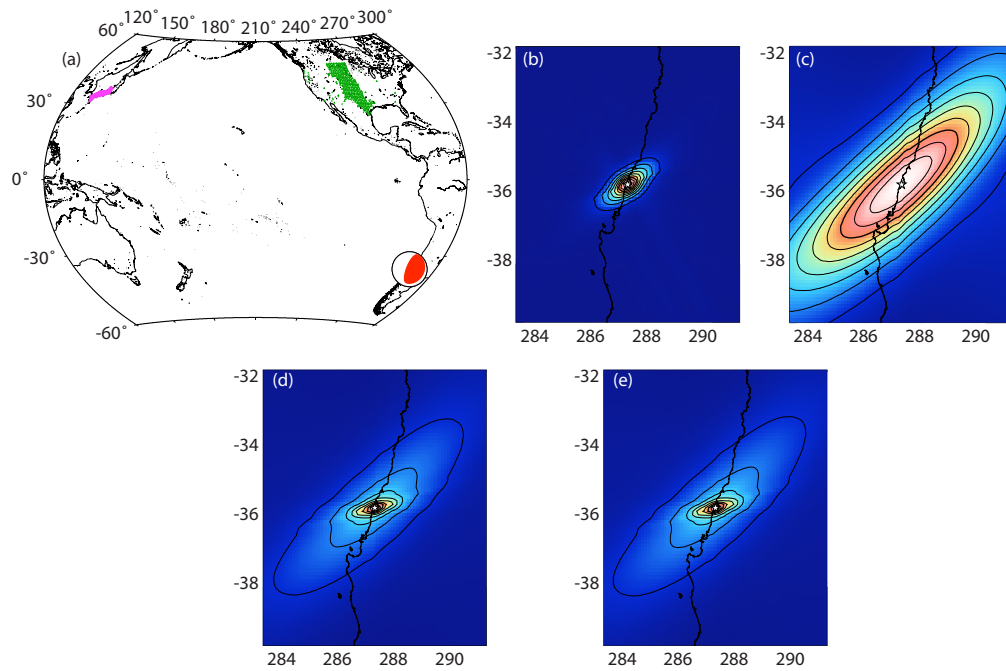


Figure A.6: Back-projection results for a point source at the hypocenter of the Mw 8.8 2010 Maule, Chile earthquake using synthetic data from both TA and Hi-net. (a) Distribution of stations from TA (green triangles) and Hi-net (pink triangles) with respect to the focal mechanism of the 2010 Chile event (Global CMT Catalogue); [Dziewoński et al., 1981; Dziewoński and Woodhouse, 1983]. (b) Back-projection result from a point source (white star) at the hypocenter of the 2010 Chile event using TA synthetic data. The symbols are the same as in Figure A.3. (c) The same as (b) except using Hi-net synthetic data. (d) The back-projection result when both TA and Hi-net synthetic data are used. (e) The same as (d) except the core phases *PKPab* and *PKPbc* are included in the synthetic seismograms from Hi-net.

phases are combined as described in Chapter 2. In addition, it will be shown that a wide variety of rupture behaviors can be recovered, and the limited depth extents presented in Chapter 3 are not artifacts of the method.

To illustrate the depth and time resolution, Figure A.7 compares the depth-time distribution of imaged energy from synthetic tests using individual phases, as well as combinations of phases. These results show that back-projection of a single phase provides no depth resolution. The smearing in these cases is along the ray paths of the different phases (Figure A.7a, b, and c). However, if the *P* phase is combined with one or both of the depth phases, the depth resolution improves dramatically to approximately ± 5 km (Figure A.7d). This uncertainty is valid for all earthquake locations considered in Chapter 3. The time resolution (± 5 seconds) is also very consistent between different source locations, because time resolution is primary dependent on the averaging window used for evaluating the back-projection results and the frequency of the data used. In the case of these synthetic tests, an averaging window of 10 seconds is used, therefore the ± 5 second time resolution. The good resolution in depth and time is the reason why we focus on these two dimensions for the discussion and interpretations of the intermediate-depth earthquakes.

A.3.1 SYNTHETIC RUPTURES IN DEPTH AND TIME

In addition to determining the resolution of a point source, multiple point sources separated in space and time are used to simulate a propagating rupture. Figures A.7(e) through A.7(h) show results of four synthetic tests. For all four of these synthetic tests, the locations and times of the three point sources are assigned to simulate a rupture velocity of 3.6 km/s [Kennett, 1991, 80% of the shear wave speed]. The horizontal rupture result in Figure A.7(e) shows that this rupture looks similar to a point source result, however, the duration reflects the input source duration. The two

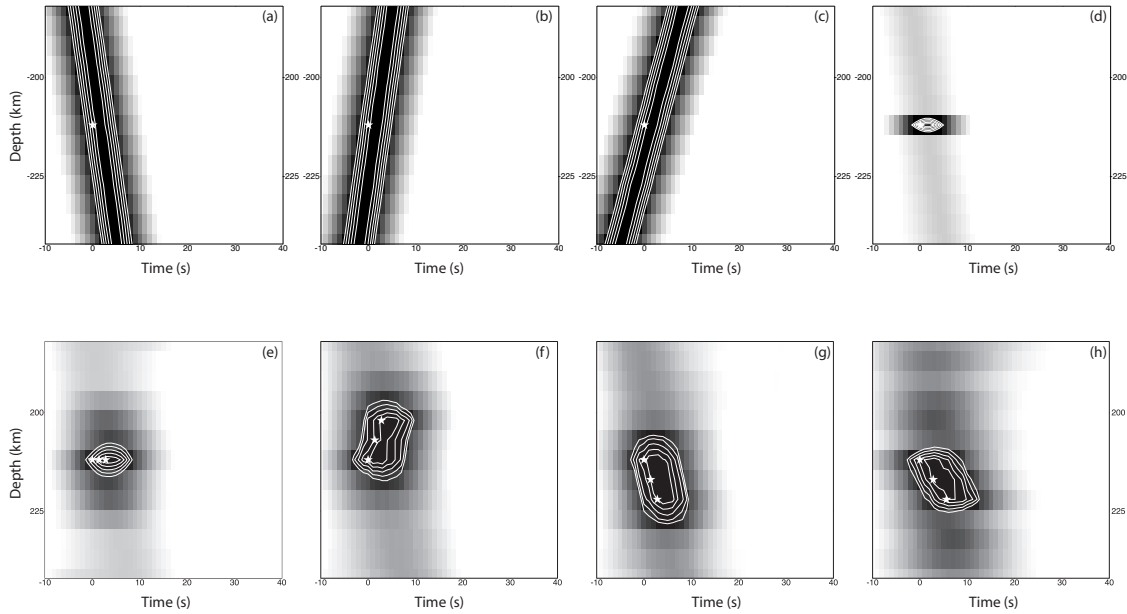


Figure A.7: The white stars are the depths and times of the point sources, and the white lines are 5% contours between 75% and 100% of the maximum value of the squared stack. Time is with respect to the hypocentral time and the background colors indicate high (black) and low (white) stack amplitudes. These plots are made by first creating comprehensive stacks at each depth by selecting the maximum stack amplitude at each time from all of the grid points at a particular depth. Following this, the squared amplitudes of the depth stacks are integrated in 10-second windows. The time interval is 1 second. (a) Synthetic back-projection result of a point source located at 21.08° S, 176.59° W, and 212 km depth using only the P phase. (b) Same as in (a) except for results using only the pP phase. (c) Same as in (a) except for results using only the sP phase. (d) Synthetic back-projection result using all three seismic phases. (e) Synthetic result from three point sources (white stars) separated laterally and in time. This arrangement is meant to simulate a horizontal rupture plane. The three point sources are each separated by 5 km to the east and 1.4 seconds in time. This leads to a rupture velocity of 3.6 km/s in the horizontal direction. The result is obtained by using all three seismic phases considered in this study. (f) Synthetic result from three point sources (white stars) separated in depth and time using all three phases. This arrangement is meant to simulate a vertical plane with rupture propagation upward. The three point sources are each separated by 5 km in depth and 1.4 seconds in time, but have the same latitude and longitude. This leads to a rupture velocity of 3.6 km/s in the vertical direction. (g) Same as in (f) except with propagation downward. (h) Synthetic result from three point sources (white stars) separated in longitude, depth, and time using all three seismic phases. This arrangement is meant to simulate a rupture dipping at 30 degrees. The three point sources are each separated by 8.7 km to the east, 5 km in depth, and 2.8 s in time. This setup is used so that the vertical extent (10 km) and rupture velocity (3.6 km/s) are the same as in (g).

vertical ruptures in Figures A.7(f) and A.7(g) show that back-projection can recover a rupture that propagates upward or downward. Finally, Figure A.7(h) shows the back-projection result for a synthetic rupture that has the same rupture depth extent as Figure A.7(g), but the dip has been changed to 30 degrees. This result shows that if the rupture velocity is constant, we should be able to at least qualitatively recognize differences in the rupture plane dips. Though these synthetic results all have eastward propagating ruptures and common depth extents, the resolution of imaged energy is the same when these parameters are changed (Figure A.8).

An important feature to note is the locations of low amplitude energy for the horizontal and sub-horizontal synthetic ruptures (Figure A.7e and h). In both cases the energy, which falls below the 75 % contour, occurs symmetrically above and below the high amplitude stacks. This is an artifact of the P phase from one point source combining with the depth phase from a different point source. Though these artifacts are low amplitude, they show that symmetric rupture patterns should be met with some degree of skepticism.

A.4 LOW AMPLITUDE DETECTION

The coherency function defined in Chapter 2 has very little dependence on the amplitudes of the seismograms and instead focuses on the coherency of the different seismograms. To illustrate how this approach can be useful for detecting low-amplitude features of large ruptures and aftershocks, a synthetic test using point sources is performed. Here, synthetic data from three relatively close point sources (Figure A.9a) are generated at the North American array stations described in Chapters 5 and 6. The central point source has an amplitude that is ten times larger than the two point sources to the north and south. Back-projection results are then obtained using the

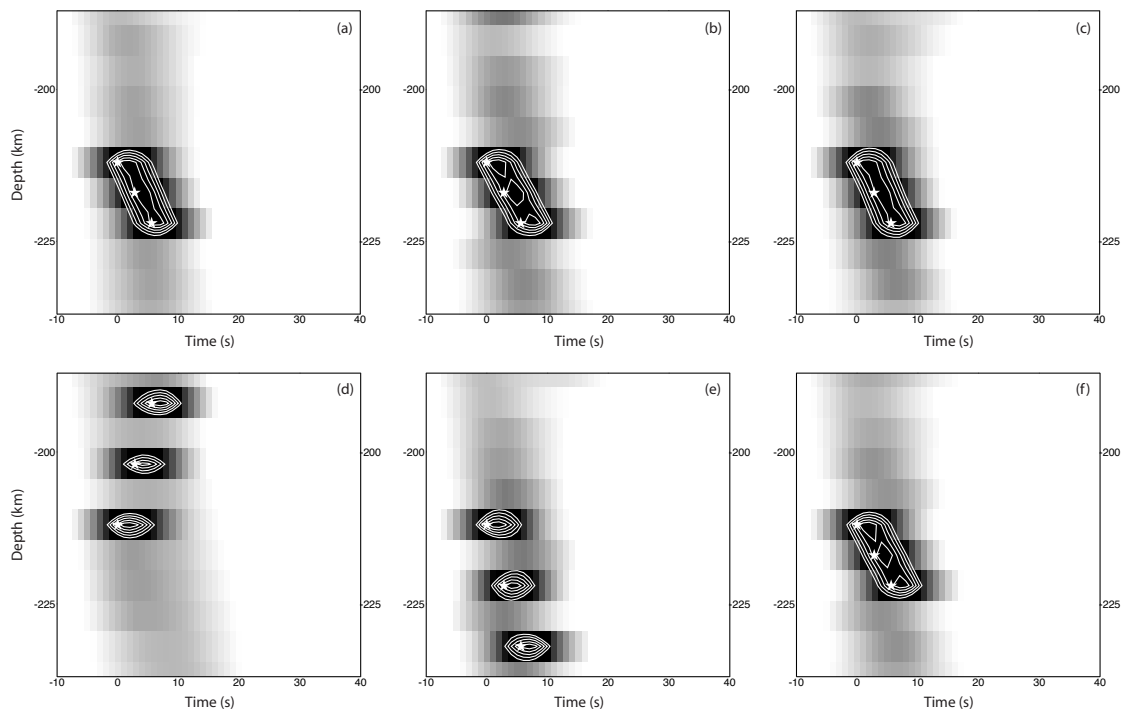


Figure A.8: Back-projection results from three synthetic tests that have the same setup as in Figure A.7(h) (propagation with 30 degree dip), but with dip directions of north (a), south (b), and west (c). (d), (e), and (f) show the back-projection results for synthetic tests similar to those in Figure A.7(f)-(h), with the only difference being that a constant rupture length of 20 km was used instead of a constant depth extent.

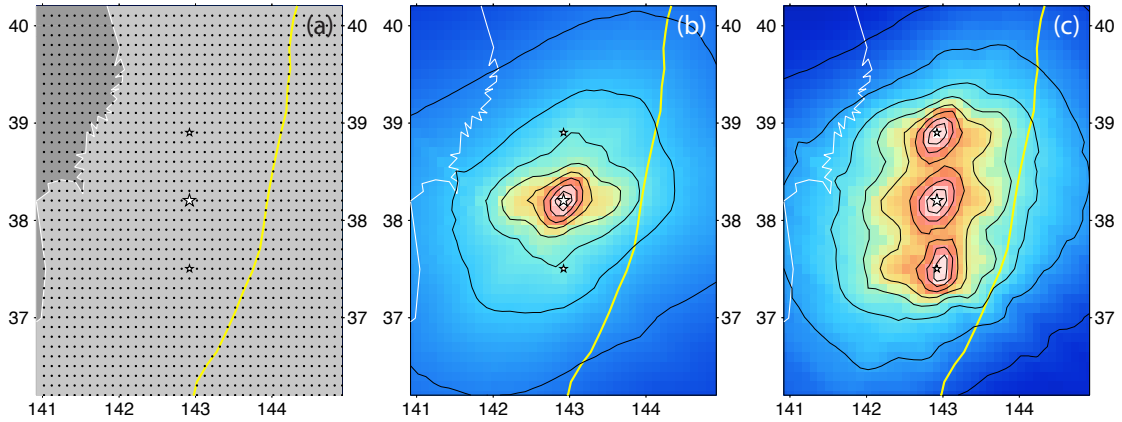


Figure A.9: (a) The black dots are the grid of possible source locations for the back-projection analysis. The three white stars are point source locations, with the northern and southern point sources having amplitudes one-tenth that of the center point source. (b) Back-projection result using linear stacking. (c) The same as (b) expect using the coherency function.

linear stacking approach (Figure A.9b) and the coherency function approach (Figure A.9c). When linear stacking is used, smeared energy from the high-amplitude point source dominates and the low-amplitude point sources are not detected (Figure A.9b). In contrast, when the coherency function is used, all three point sources are imaged with approximately the same amplitude (Figure A.9c). This synthetic test demonstrates that the coherency function works better for detecting low-amplitude features, but not very useful for estimating the relative size of different events.

A.5 THE HORIZONTAL PLANE SETUP

For all of the shallow events studied in this thesis, a horizontal plane of grid points is set up at the hypocentral depth. The setup of a single plane is made, because there is no depth resolution when only P waves are used in the back-projection analysis (See Figure A.7). In addition, the plane of grid points has a constant depth

because smearing of energy occurs along the rays paths, which are nearly vertical at teleseismic distances. This means that if an earthquake source occurs at 10 km depth, but the plane of grid points is at 30 km depth, the energy from the source will be projected onto the deeper plane of grid points where the ray paths intersect this plane (Figure A.10). Since the ray paths are nearly vertical, the lateral location of the projected energy will not differ significantly from the true lateral location. To illustrate this effect, an aftershock from the 2011 Tohoku earthquake is imaged using a horizontal plane of grid points and a dipping plane of grid points that mimics the orientation of the subduction interface. This particular aftershock is an extreme case because its depth from the JMA catalogue is 4 km while the depth of the horizontal plane used in the back-projection analysis is 65 km. The energy projected onto the deeper horizontal plane is slightly shifted to the northeast, which is the direction towards the seismic array (Figure A.11). This example shows that even when there is a large depth separation between the earthquake source and the horizontal plane, the horizontal plane setup does not affect the epicentral location significantly when using teleseismic data.

A.6 THE EFFECT OF DEPTH PHASES ON SHALLOW EVENTS

The back-projection analysis for the 2010 Maule earthquake shows high-frequency energy preceding lower-frequency energy for the northern rupture of the event (Chapter 5). In this section, we determine how interference between depth phases, which have lower frequencies, and the P phase may influence this result. We perform a multi-frequency back-projection analysis using synthetic seismograms that are produced from waveforms of aftershocks of the 2010 Maule event. Using waveforms from real earthquakes for our synthetic seismograms allows us to reproduce the effects of

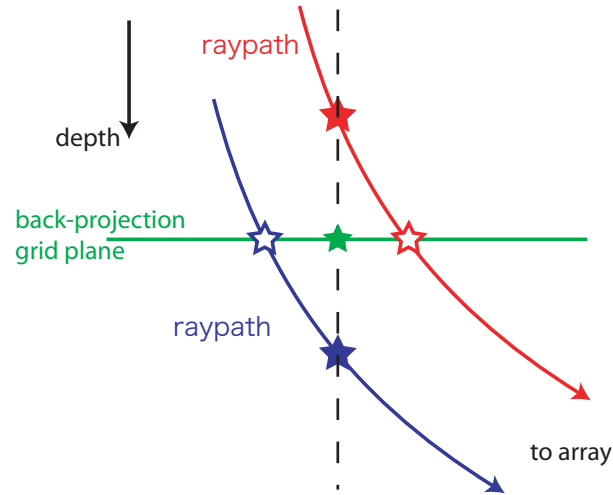


Figure A.10: Effect of discrepancy between earthquake depth and back-projection source grid depth on hypocentral time and lateral location. Depth cross section of back-projection set up, source grid plane (green line) with respect to the hypocenters of two earthquakes, one shallower than the grid depth (solid red star) and another deeper than the grid depth (solid blue star). Due to the depth difference, the back-projected energy will be shifted toward (shallow event case, star with red outline) or away from (deeper event case, star with blue outline) the array direction. This is caused by the fact that energy stacks coherently along the raypath of the seismic phase being considered.

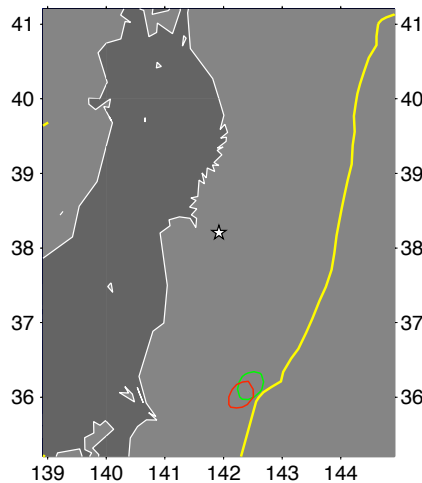


Figure A.11: Rupture areas of a M 6.0 March 11th aftershock using a horizontal plane of grid points (green contour) and a dipping plane of grid points that corresponds to the subduction interface (red contour). The horizontal plane set up causes translation of energy towards the seismic array (northeast).

3-D structure on waveforms from this region at the relatively high frequencies being considered. The locations and times of the input sources are those of peak energy release from the back-projection results of the mainshock using data filtered between 1 and 5 Hz. This leads to 9 point sources, 3 from Segment 1 and 6 from Segment 2 (Figure A.12a). The synthetic seismograms generated from the 9 point sources and with aftershock waveforms are filtered between 1 to 5 Hz (high frequency) and 0.5 to 1 Hz (intermediate frequency). By comparing the latitudes of the high- and intermediate-frequency back-projection results at different times, we can determine if the lag behind of intermediate-frequency energy reported in Chapter 5 is an artifact of depth phases or 3-D structure. We perform this analysis for multiple aftershocks with thrust mechanisms similar to that of the mainshock and depths between 15 and 35 km. Results for one of these aftershocks is shown in Figure A.12, and show that intermediate-frequency energy tends to precede high-frequency energy. This general observation does not change when different aftershocks are used, and is caused by the relatively high amplitude depth phases at intermediate frequencies. This result is in contrast to those presented in Chapter 5 for which the high-frequency energy precedes the intermediate-frequency energy for Segments 1 and 2 of the Mw 8.8 mainshock (Figures A.12b and c). Therefore, these observations are unlikely to be artifacts of depth phases or 3-D structure, but are associated with the source mechanism.

A.7 DIRECTIVITY

For some of the shallow events studied in this thesis, most notably the 2010 Maule earthquake, the azimuth of the seismic array location is similar to the rupture propagation direction. In such a source-receiver geometry, it is important to determine how the directivity effect influences the back-projection results. In addition to the

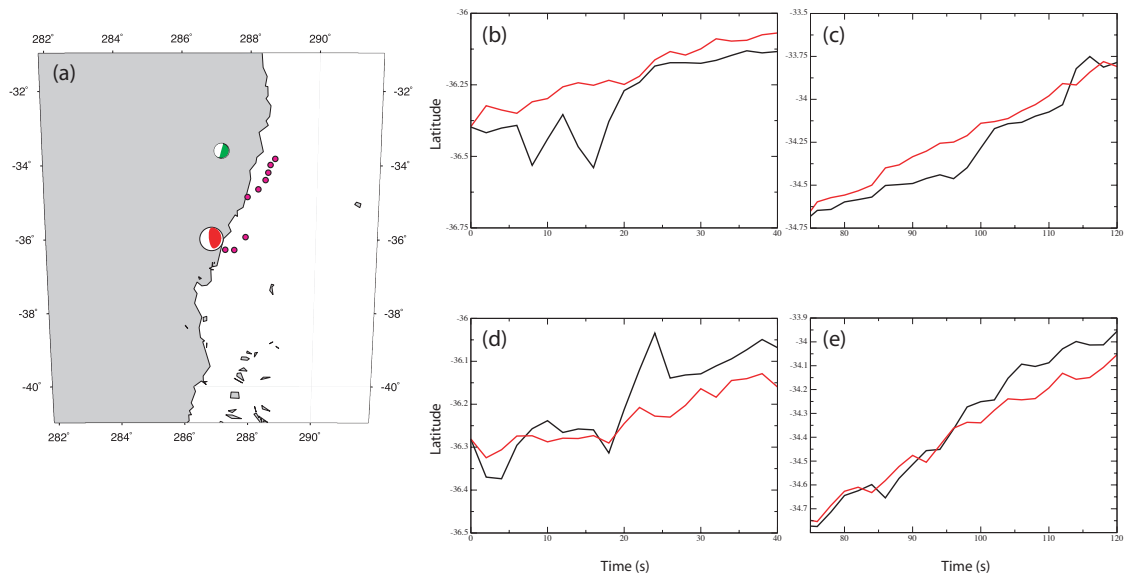


Figure A.12: (a) CMT solutions of the Mw 8.8 mainshock (red focal mechanism) and an Mw 5.6 aftershock (green focal mechanism) that occurred on March 10, 2010 [e.g., Dziewoński et al., 1981; Dziewoński and Woodhouse, 1983]. The pink dots are the locations of the input point sources, which are the peak energy release locations from the high-frequency back-projection results of the mainshock. There are 3 points from Segment 1 and 6 points from Segment 2. (b) Latitudes and times of the imaged energy from Segment 1 of the Mw 8.8 mainshock using TA data filtered from 1 to 5 Hz (red line) and 0.5 to 1 Hz (black line). (c) The same as (b) except for Segment 2. (d) Latitudes and times of the imaged energy from a synthetic test that uses 3 point source locations from Segment 1 and waveform data from the aftershock that occurred on March 10, 2010. (e) The same as (d) except using 6 point source locations from Segment 2.

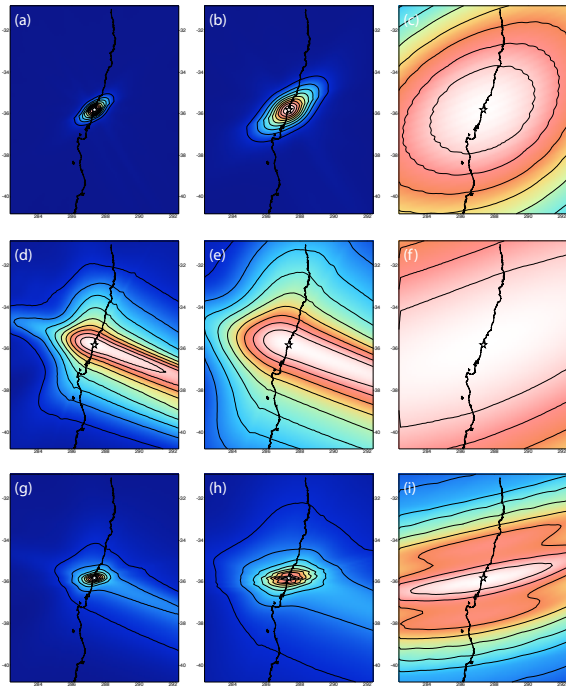


Figure A.13: (a) Back-projection result for a point source (white star) using TA synthetic seismograms with a central frequency of 1.0 Hz. The synthetic seismograms include only P wave arrivals from the point source. (b) The same as (a), except using TA synthetic seismograms with a central frequency of 0.5 Hz. (c) The same as (a), except using TA synthetic seismograms with a central frequency of 0.05 Hz. (d) The same as (a), except using distance constrained (150° - 153°) Hi-net synthetic seismograms and the $PKPbc$ phase. (e) The same as (d), except using Hi-net synthetic seismograms with a central frequency of 0.5 Hz. (f) The same as (c), except using F-net synthetic seismograms and the $PKPdf$ phase. (g) Back-projection result when stacks from (a) are combined with those from (d). (h) Back-projection result when stacks from (b) are combined with those from (e). (i) Back-projection result when stacks from (c) are combined with those from (f).

single point source synthetic tests (Figure A.13), we have performed a test in the 2010 Maule, Chile study region with 71 point sources, using Ricker wavelets, which are offset in time to mimic a bilateral rupture with a propagation speed of 2.8 km/s. The synthetic seismogram includes P , pP , and sP phases from each point source, and waveforms of all phases are produced with the same amplitude and central frequency (1 Hz). This approach produces waveform distortion associated with the directivity effect (large amplitude and high frequency for rupture moving toward the array).

The results using synthetic data show that the recovered northern rupture has a much higher amplitude than the southern rupture as expected (Figure A.14a). This

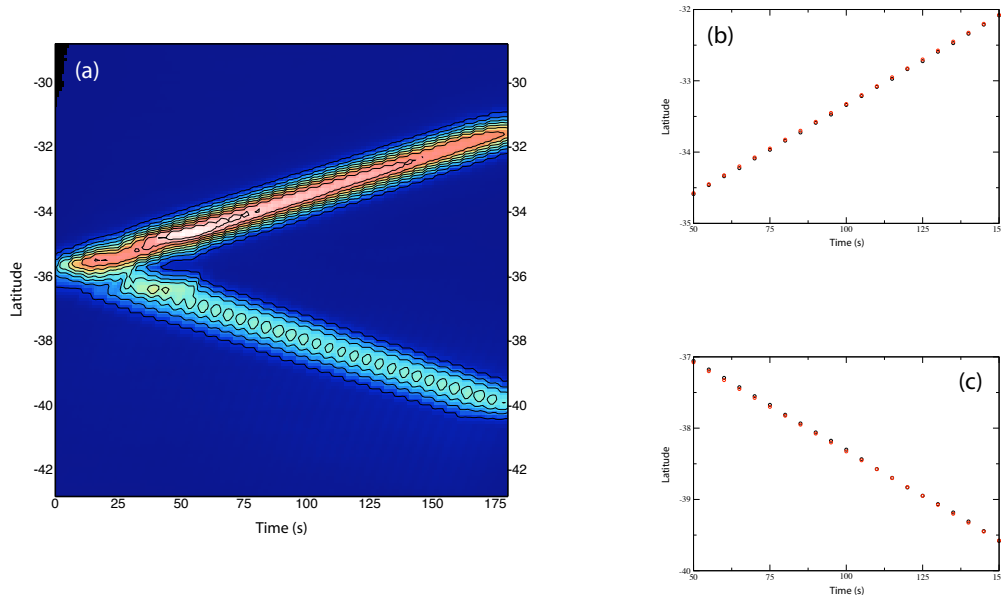


Figure A.14: 71 point sources are used to simulate a synthetic bilateral rupture. The total length of the synthetic rupture is about 974 km (487 km north and 487 km south of the epicenter). The spacing between each point source is about 14 km. The timing between each point source is 5 seconds. This setup simulates a rupture velocity of 2.8 km/s. Each point source contributes a P , pP , and sP wavelet to the TA synthetic seismograms, and the wavelets all have the same central frequency (1 Hz) and amplitude. Before the back-projection analysis, the synthetic seismograms are bandpass filtered between 1 and 5 Hz. (a) Back-projection results for the synthetic bilateral rupture with respect to latitude and time. The warmer colors (red and white) represent high energy release and the colder colors (dark blue) represent low energy release. The higher amplitudes near the epicenter are caused by the interference between the waves of the northern and southern ruptures. (b) Latitudes and times of the input point sources (black circles) and imaged energy (red circles) from the northern synthetic rupture. (c) The same as (b) except for the southern synthetic rupture.

result demonstrates that the directivity effect on recovered amplitude can be quite strong when the azimuth of the seismic array is similar to the rupture propagation direction. Note that this effect only influences the amplitude of relative energy release and not its location (Figures A.14b and c).

The results of these synthetic tests show that the relative amplitude of the 2010

Chile event imaged using TA data may be influenced by the rupture directivity. However, note that this directivity effect would be present at any frequency, i.e., rupture north of the epicenter would be biased toward high amplitude. In addition, we have examined results from the Hi-net and F-net data, which are located nearly perpendicular to the rupture direction. We have tested the directivity effect on these two arrays from the same combination of point sources that were used for the TA case. Unlike the TA, there is little directivity effect on the Hi-net and F-net arrays from a north/south bilateral rupture in this region (Figures A.15a and A.15b). Since the real high-frequency Hi-net result images energy mostly north of the epicenter, and the low frequency F-net result images energy mostly south of the epicenter (Figure 5.7), we rule out directivity as the primary cause of the frequency-dependent results discussed for the 2010 Maule, Chile earthquake.

A.8 SUMMARY

The resolution of the back-projection method is dependent on the general features of the seismic array used in the analysis, and the specific location of the earthquake being studied. The most important features of a seismic array are the distance and azimuthal coverage of the stations. In this respect, TA is the most valuable array in the world for back-projection studies. In terms of source location, the hypocentral depth, distance from the array, local structure, and relative direction between rupture propagation and the array all contribute to variable resolution, depending upon the region being studied. In general, the combination of multiple seismic arrays can reduce these source location effects on resolution.

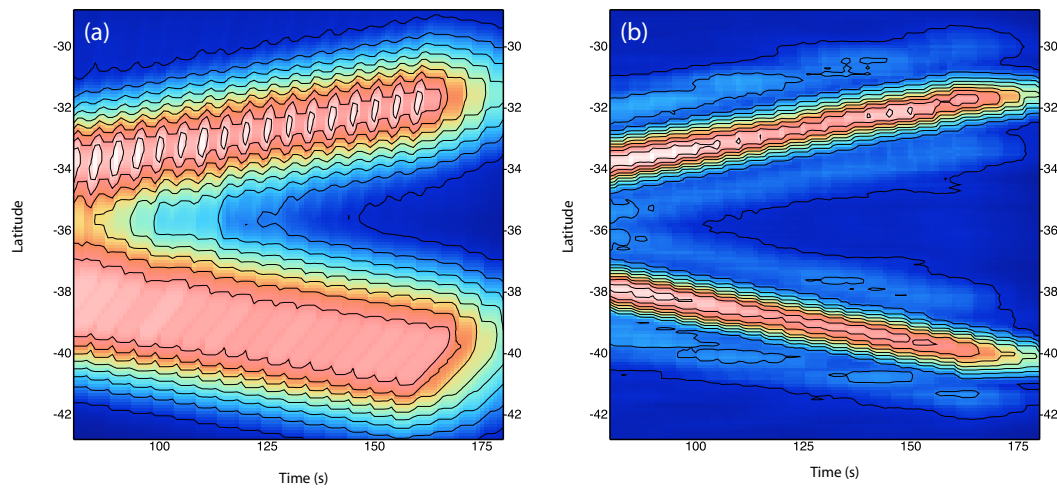


Figure A.15: (a) Back-projection results with respect to latitude and time using Hi-net synthetic seismograms with the distance constraint of 150-153 degrees, and the same point source setup as in Figure A.14. The $PKPbc$ phase is generated from each point source. The distance constraint causes some distortion of the energy kernel of the southern rupture, however, the amplitudes of the northern and southern ruptures are very similar. (b) The same as Figure A.15a, except using F-net synthetic data and the $PKPdf$ phase.

APPENDIX B

TABLES OF MARCH 11TH AND 12TH TOHOKU EVENTS

Table B.1: Catalogue of back-projection events from March 11th after the hypocentral time of the Mw 9.0 Tohoku mainshock. The first column is the time of the back-projection event. The second and third columns are the latitude and longitude of the back-projection event, respectively. The fourth column indicates if the back-projection event has a corresponding counterpart in the JMA catalogue. If there is, columns 5-8 are the latitude, longitude, depth, and magnitude of the JMA event. Finally, the last three columns are the distance (degrees), azimuth, and time (seconds) between the JMA event and back-projection event. Negative values for “Time Diff” indicate that the JMA event occurs before the back-projection event.

Time	Lat	Lon	JMA Cat	JMA Lat	JMA Lon	JMA Dep	JMA Mag	Del	Azi	Time Diff
05:51:41	37.004	142.620	Yes	37.311	142.238	33.0	6.8	0.43	135.1	-21
05:52:32	37.385	143.339	No							
05:53:29	37.904	143.449	No							
05:54:38	37.404	141.549	Yes	37.508	141.353	34.1	6.1	0.19	123.7	-7
05:54:41	37.219	143.074	No							
05:54:47	36.871	140.731	Yes	36.713	140.581	9.5	5.7	0.20	37.2	-5
05:55:53	37.479	143.825	No							
05:55:58	37.004	143.270	No							

Continued on next page

Table B.1 – *Continued from previous page*

Time	Lat	Lon	JMA Cat	JMA Lat	JMA Lon	JMA Dep	JMA Mag	Del	Azi	Time Diff
05:56:02	36.542	142.174	Yes	36.493	141.773	55.0	6.0	0.33	81.2	-9
05:58:17	37.754	142.401	Yes	37.689	141.934	35.2	6.6	0.38	79.9	-12
05:59:30	37.137	142.587	No							
05:59:33	38.391	143.567	No							
05:59:55	38.021	143.037	No							
05:59:58	36.691	142.733	No							
06:00:42	37.792	143.261	No							
06:03:50	37.954	143.270	No							
06:04:06	36.264	142.200	Yes	36.330	141.962	17.1	6.0	0.20	108.9	-8
06:05:05	36.474	142.250	No							
06:06:19	38.917	142.607	Yes	39.045	142.398	28.6	6.5	0.21	128.2	-9
06:07:29	36.371	142.273	Yes	36.302	142.226	20.3	6.5	0.08	28.7	-13
06:09:03	39.795	143.225	Yes	39.821	142.767	32.0	7.4	0.35	94.1	-10
06:09:15	36.051	142.033	Yes	36.078	141.835	26.0	6.2	0.16	99.5	-22
06:10:17	39.950	144.634	No							
06:11:25	36.174	142.190	No							
06:12:43	37.617	144.307	No							
06:13:08	37.121	142.037	Yes	37.228	141.645	38.9	6.7	0.33	108.8	-10
06:13:40	37.584	143.210	No							
06:14:09	38.398	142.611	No							
06:15:32	38.068	144.411	No							
06:15:54	35.957	141.736	Yes	36.121	141.253	42.7	7.6	0.42	112.6	-20
06:16:33	35.889	140.897	Yes	36.077	141.105	39.4	5.7	0.25	221.9	8
06:16:47	35.887	142.132	No							
06:19:04	36.145	142.208	No							
06:20:33	38.654	143.520	No							
06:20:47	36.104	142.120	Yes	36.589	141.724	62.0	5.7	0.58	146.6	-3

Continued on next page

Table B.1 – *Continued from previous page*

Time	Lat	Lon	JMA Cat	JMA Lat	JMA Lon	JMA Dep	JMA Mag	Del	Azi	Time Diff
06:21:35	38.179	143.182	Yes	38.276	142.842	6.0	6.2	0.28	109.9	-8
06:23:14	38.854	142.620	Yes	39.020	142.411	31.0	6.1	0.23	135.5	-9
06:26:04	38.081	144.732	Yes	37.914	144.751	11.0	7.5	0.17	354.9	-20
06:29:23	37.816	144.470	Yes	37.933	143.933	15.0	6.9	0.44	105.3	-8
06:31:56	38.132	143.172	No							
06:33:09	36.644	142.340	Yes	36.605	142.106	43.0	6.1	0.19	78.2	-8
06:38:14	36.044	142.140	Yes	36.183	141.852	24.0	5.6	0.27	120.8	-7
06:41:05	39.440	142.341	Yes	39.333	142.071	48.3	5.9	0.23	62.8	-16
06:48:57	37.984	143.180	No							
06:49:21	37.293	144.287	No							
06:49:50	37.311	144.480	No							
06:50:00	40.066	143.207	Yes	40.110	142.618	6.9	5.9	0.45	95.4	-10
06:52:35	38.054	143.270	Yes	38.400	142.740	0.0	5.9	0.54	129.6	-6
06:55:49	36.621	142.420	Yes	36.579	142.028	79.4	5.4	0.32	82.3	-8
06:57:24	35.792	141.432	Yes	35.819	141.182	27.5	6.2	0.20	97.5	-11
07:01:19	36.587	144.003	No							
07:03:11	38.004	143.170	Yes	38.146	142.790	23.0	5.8	0.33	115.3	-10
07:04:25	38.924	142.670	Yes	38.985	142.428	23.8	5.7	0.20	107.9	-10
07:05:31	38.417	143.707	No							
07:06:07	38.504	144.291	No							
07:10:07	36.704	142.420	Yes	36.671	142.102	23.0	5.5	0.26	82.5	-13
07:11:07	37.718	143.149	Yes	37.819	142.859	27.0	6.2	0.25	113.7	-11
07:13:57	35.915	142.153	Yes	35.952	141.976	50.0	5.8	0.15	104.4	-12
07:14:08	39.154	143.820	No							
07:15:10	36.704	142.370	Yes	36.557	142.041	25.0	6.8	0.30	60.8	-13
07:17:56	37.221	142.837	Yes	37.142	142.592	20.0	6.5	0.21	67.9	-14
07:23:20	37.315	142.787	No							

Continued on next page

Table B.1 – *Continued from previous page*

Time	Lat	Lon	JMA Cat	JMA Lat	JMA Lon	JMA Dep	JMA Mag	Del	Azi	Time Diff
07:25:54	37.971	144.720	Yes	38.064	144.502	40.0	6.2	0.20	118.4	-18
07:28:22	36.893	142.353	Yes	36.891	141.874	44.0	6.2	0.38	89.6	-11
07:29:07	38.891	142.733	Yes	39.022	142.311	17.0	6.6	0.35	111.6	-8
07:30:24	37.304	141.500	Yes	37.365	141.260	27.0	5.9	0.20	107.7	-9
07:33:57	36.204	142.220	Yes	36.291	142.141	19.0	5.2	0.11	143.8	-27
07:34:23	38.787	142.703	Yes	38.888	142.546	24.2	5.6	0.16	129.5	-12
07:35:04	37.918	142.991	Yes	37.977	142.751	13.1	5.7	0.20	107.2	-13
07:36:03	37.104	142.720	Yes	37.060	142.486	28.0	6.0	0.19	76.7	-14
07:38:35	39.104	143.220	Yes	39.254	142.807	16.2	5.8	0.35	115.0	-9
07:43:17	36.115	142.187	No							
07:44:03	37.221	142.737	Yes	37.133	142.539	46.0	5.5	0.18	60.8	-12
07:44:39	36.264	142.200	Yes	36.301	141.901	60.0	5.6	0.24	98.6	-10
07:48:01	38.435	143.643	No							
07:48:02	39.054	143.570	No							
07:50:15	36.113	142.093	Yes	36.555	141.967	34.4	5.5	0.45	167.0	-30
07:54:50	37.621	141.803	Yes	37.669	141.684	35.4	5.5	0.11	117.0	-7
07:56:24	37.104	142.820	Yes	37.049	142.569	11.2	6.2	0.21	74.6	-15
08:00:03	37.304	143.120	No							
08:01:23	36.833	142.620	No							
08:02:13	36.913	143.556	No							
08:03:10	36.820	144.082	No							
08:03:19	36.364	142.140	No							
08:05:03	37.257	142.587	Yes	37.260	142.110	19.2	5.9	0.38	90.3	-10
08:06:32	37.492	143.132	No							
08:10:14	37.904	142.945	Yes	37.883	142.575	37.0	5.5	0.29	85.8	-11
08:10:40	35.891	141.932	Yes	36.057	141.709	18.5	5.4	0.25	132.5	-12
08:10:43	38.716	142.745	No							

Continued on next page

Table B.1 – *Continued from previous page*

Time	Lat	Lon	JMA Cat	JMA Lat	JMA Lon	JMA Dep	JMA Mag	Del	Azi	Time Diff
08:11:27	36.324	142.450	No							
08:11:31	39.354	143.470	No							
08:12:15	36.579	141.987	Yes	36.549	141.386	32.5	6.6	0.48	86.3	-9
08:14:43	37.374	143.170	No							
08:15:47	36.942	144.658	Yes	37.264	144.261	32.0	6.5	0.45	135.4	-4
08:17:31	37.779	144.520	No							
08:19:37	36.113	142.056	Yes	36.157	141.716	35.5	6.8	0.28	99.0	-20
08:21:22	38.316	142.881	No							
08:25:14	37.079	143.945	No							
08:26:48	37.371	143.353	No							
08:27:08	37.664	142.972	Yes	38.033	142.786	30.0	6.2	0.40	158.2	40
08:27:59	37.986	143.038	Yes	38.033	142.786	30.0	6.2	0.20	103.2	-11
08:31:18	37.559	141.538	Yes	37.467	141.377	30.7	5.9	0.16	54.2	-11
08:31:48	37.161	142.849	No							
08:33:09	39.104	143.220	Yes	39.201	142.956	12.1	6.0	0.23	115.3	-10
08:33:48	39.818	144.470	No							
08:33:55	40.101	142.975	No							
08:35:32	36.044	141.440	Yes	36.069	141.133	37.3	5.2	0.25	95.7	-10
08:38:13	37.654	143.920	Yes	37.800	143.628	30.0	5.9	0.27	122.2	-10
08:39:20	37.571	143.220	No							
08:39:36	36.104	142.120	No							
08:40:23	39.596	143.745	No							
08:41:03	37.471	141.473	Yes	37.424	141.273	29.9	6.0	0.17	73.5	-9
08:42:16	37.977	143.420	No							
08:44:10	36.130	142.488	Yes	36.270	142.088	0.0	6.0	0.35	113.3	-17
08:46:55	37.354	142.820	Yes	37.449	142.393	15.0	5.9	0.35	105.5	-11
08:48:34	36.693	142.353	Yes	36.732	142.110	28.0	5.3	0.20	101.2	-12

Continued on next page

Table B.1 – *Continued from previous page*

Time	Lat	Lon	JMA Cat	JMA Lat	JMA Lon	JMA Dep	JMA Mag	Del	Azi	Time Diff
08:51:14	38.921	142.637	Yes	39.143	142.405	29.7	4.7	0.29	140.9	-3
08:51:16	37.754	143.370	No							
08:52:34	36.691	142.333	Yes	36.772	141.948	0.1	5.6	0.32	104.6	-14
08:53:00	37.071	142.803	No							
08:53:07	38.126	142.076	No							
08:54:13	37.644	141.840	Yes	37.660	141.676	39.5	5.0	0.13	97.0	-6
08:55:16	36.671	141.853	No							
08:56:36	39.575	143.934	No							
09:00:37	37.515	143.787	No							
09:02:24	37.262	142.778	No							
09:04:20	37.554	143.120	No							
09:06:09	37.804	143.070	No							
09:07:10	36.054	142.170	No							
09:09:22	37.671	143.531	No							
09:11:41	37.564	143.200	No							
09:12:18	35.954	141.970	No							
09:14:48	35.620	142.583	No							
09:16:35	37.947	140.491	Yes	37.904	140.343	6.8	5.1	0.12	69.7	-11
09:17:41	39.947	143.891	No							
09:18:54	36.054	142.420	Yes	36.137	141.935	58.7	4.6	0.40	101.8	-9
09:19:18	37.444	144.100	No							
09:20:58	39.004	143.670	No							
09:24:47	36.204	141.970	Yes	36.238	141.644	39.9	4.4	0.27	97.3	-21
09:26:00	36.129	142.120	Yes	36.161	141.870	53.8	4.8	0.20	98.9	-10
09:27:46	38.216	142.408	Yes	38.297	142.193	36.2	5.4	0.19	115.6	-9
09:28:04	37.354	143.320	No							
09:31:24	36.664	142.600	Yes	36.744	142.036	12.5	4.9	0.46	99.9	-9

Continued on next page

Table B.1 – *Continued from previous page*

Time	Lat	Lon	JMA Cat	JMA Lat	JMA Lon	JMA Dep	JMA Mag	Del	Azi	Time Diff
09:33:59	38.612	144.412	No							
09:34:16	37.754	143.270	No							
09:35:42	37.516	143.908	No							
09:37:17	35.933	142.020	Yes	36.032	141.774	30.5	5.3	0.22	116.4	-11
09:39:13	36.521	142.837	No							
09:40:25	37.061	142.491	Yes	37.329	142.311	9.0	5.1	0.30	151.8	-17
09:41:05	36.524	142.100	No							
09:41:47	36.624	142.460	No							
09:42:30	39.459	142.938	Yes	39.497	142.754	24.0	5.6	0.15	104.9	-10
09:45:33	36.715	142.687	No							
09:45:39	37.304	144.070	No							
09:47:10	39.579	143.478	Yes	39.592	143.260	28.0	5.7	0.17	94.4	-12
09:49:23	39.429	143.620	No							
09:49:24	37.904	143.143	No							
09:51:12	36.279	142.220	Yes	36.287	141.966	44.0	4.4	0.20	92.2	-9
09:51:35	38.334	144.500	No							
09:52:49	37.664	142.100	Yes	37.685	141.852	32.3	4.9	0.20	96.0	-8
09:53:48	37.554	144.420	No							
09:55:14	37.995	142.984	Yes	38.094	142.638	20.0	5.4	0.29	109.9	-11
09:55:32	36.689	142.158	Yes	36.750	141.801	0.0	5.4	0.29	101.9	-11
09:58:41	37.044	141.500	Yes	37.064	141.297	40.1	4.7	0.16	97.0	-9
10:00:01	38.747	144.449	No							
10:00:04	36.679	142.658	Yes	36.654	142.299	36.0	5.0	0.29	84.9	-12
10:00:38	37.354	143.370	No							
10:04:43	36.716	142.307	No							
10:05:19	36.621	142.037	Yes	36.768	141.343	32.7	4.6	0.58	104.6	1
10:10:46	39.217	142.247	Yes	39.334	142.152	43.8	6.2	0.14	147.8	-7

Continued on next page

Table B.1 – *Continued from previous page*

Time	Lat	Lon	JMA Cat	JMA Lat	JMA Lon	JMA Dep	JMA Mag	Del	Azi	Time Diff
10:13:03	38.537	141.987	Yes	38.625	141.918	45.8	5.3	0.10	148.5	9
10:16:24	36.204	142.120	No							
10:19:36	36.804	144.570	No							
10:20:02	35.979	141.920	Yes	36.114	141.777	26.0	4.5	0.18	139.4	-12
10:20:37	36.954	142.620	Yes	36.908	142.288	11.7	5.8	0.27	80.1	-13
10:21:16	37.249	142.302	Yes	37.346	141.906	22.0	5.5	0.33	107.0	-9
10:22:03	38.016	143.107	No							
10:22:16	36.716	142.807	No							
10:24:12	37.564	143.400	No							
10:27:02	36.733	141.920	Yes	36.755	141.492	45.8	4.5	0.34	93.5	-9
10:28:28	37.904	143.720	No							
10:28:52	39.313	143.856	No							
10:32:40	39.054	142.620	Yes	39.203	142.398	28.0	4.8	0.23	130.8	-8
10:34:36	38.244	144.340	No							
10:35:06	38.037	143.003	No							
10:35:45	37.154	141.620	Yes	37.070	141.343	49.1	5.1	0.24	69.1	-9
10:39:20	38.844	143.040	No							
10:39:28	35.944	142.200	No							
10:40:02	37.429	143.145	No							
10:41:05	36.721	142.837	No							
10:41:06	37.044	144.200	No							
10:42:26	37.471	142.931	No							
10:44:08	38.354	143.370	No							
10:45:53	35.804	141.587	Yes	35.882	141.393	29.8	4.9	0.18	116.3	-32
10:45:53	38.404	143.753	No							
10:47:22	37.554	143.320	No							
10:48:19	38.314	143.740	No							

Continued on next page

Table B.1 – *Continued from previous page*

Time	Lat	Lon	JMA Cat	JMA Lat	JMA Lon	JMA Dep	JMA Mag	Del	Azi	Time Diff
10:52:16	38.516	143.607	No							
10:54:04	37.044	141.540	Yes	37.084	141.298	49.8	4.2	0.20	101.6	7
10:56:01	37.264	142.900	No							
10:58:13	38.957	142.533	Yes	39.017	142.367	32.2	4.9	0.14	114.9	-9
10:58:29	36.564	142.600	No							
10:59:46	37.424	142.760	No							
11:00:24	37.479	144.020	No							
11:00:59	37.671	141.853	Yes	37.722	141.730	46.1	5.5	0.11	117.6	-6
11:02:36	39.054	143.220	Yes	39.169	142.960	22.0	5.3	0.23	119.6	-11
11:03:54	37.554	144.370	No							
11:04:04	38.174	143.590	No							
11:06:18	38.054	143.020	Yes	38.116	142.699	13.0	5.0	0.26	103.7	-14
11:07:17	37.266	143.143	No							
11:08:55	37.444	142.940	Yes	37.485	142.504	11.0	5.0	0.35	96.6	-12
11:09:54	36.554	143.520	No							
11:11:08	35.645	142.208	Yes	35.731	142.115	27.9	5.9	0.11	138.7	-14
11:13:21	36.333	142.120	Yes	36.320	141.947	37.0	5.6	0.14	84.6	-11
11:16:01	39.054	143.720	Yes	39.067	143.537	35.0	5.4	0.14	95.2	-10
11:16:58	36.654	142.053	Yes	36.627	141.708	42.5	5.5	0.28	84.3	-9
11:19:04	37.837	143.820	No							
11:19:15	36.587	143.620	No							
11:19:31	37.254	143.970	No							
11:21:09	35.766	141.295	Yes	35.795	141.200	38.5	5.6	0.08	110.6	-10
11:21:37	37.504	143.400	No							
11:22:09	38.186	142.243	No							
11:22:41	38.079	141.776	No							
11:25:52	35.612	142.237	No							

Continued on next page

Table B.1 – *Continued from previous page*

Time	Lat	Lon	JMA Cat	JMA Lat	JMA Lon	JMA Dep	JMA Mag	Del	Azi	Time Diff
11:26:04	38.254	142.470	Yes	38.443	142.292	34.5	5.0	0.23	143.5	-6
11:27:30	39.079	143.578	Yes	39.265	143.290	0.0	5.7	0.29	129.7	-10
11:28:59	38.604	142.370	Yes	38.696	142.258	35.2	5.2	0.13	136.4	-7
11:29:50	37.944	144.100	No							
11:30:32	39.129	143.828	Yes	39.290	143.625	0.0	5.7	0.23	135.6	-16
11:31:20	38.254	140.720	Yes	38.182	140.490	8.6	5.2	0.19	68.2	-13
11:32:34	38.975	143.520	Yes	39.071	143.270	11.0	5.7	0.22	116.2	-10
11:36:50	39.095	142.884	Yes	39.230	142.579	23.6	6.7	0.27	119.6	-11
11:39:32	38.304	142.491	Yes	38.330	142.248	25.3	5.8	0.19	97.7	-5
11:42:21	39.312	142.987	Yes	39.354	142.817	15.5	5.7	0.14	107.7	-12
11:44:37	36.704	142.820	Yes	36.696	142.451	13.0	5.7	0.30	88.3	-14
11:46:53	36.033	141.520	Yes	36.062	141.175	41.2	5.4	0.28	95.8	-10
11:49:33	37.971	144.553	No							
11:53:36	39.137	142.887	Yes	39.203	142.632	21.5	4.9	0.21	108.4	-11
11:54:09	37.054	142.920	No							
11:55:41	36.379	142.220	Yes	36.281	141.675	40.3	5.3	0.45	77.3	32
11:55:44	38.524	143.260	No							
11:56:22	36.179	141.820	Yes	36.281	141.675	40.3	5.3	0.16	131.0	-9
11:56:44	37.704	143.291	No							
11:57:23	39.159	142.438	Yes	39.272	142.311	28.7	5.3	0.15	138.9	-9
11:59:03	35.604	142.270	No							
12:00:22	35.761	141.372	No							
12:01:22	37.754	143.320	No							
12:01:54	37.884	144.580	No							
12:02:04	39.089	143.000	Yes	39.209	142.575	24.2	5.1	0.35	109.9	-19
12:02:51	39.304	143.070	Yes	39.198	142.507	36.1	4.5	0.45	76.2	0
12:04:25	36.454	142.920	No							

Continued on next page

Table B.1 – *Continued from previous page*

Time	Lat	Lon	JMA Cat	JMA Lat	JMA Lon	JMA Dep	JMA Mag	Del	Azi	Time Diff
12:08:04	38.271	143.420	No							
12:08:49	37.104	142.970	No							
12:10:27	38.854	144.720	No							
12:12:09	37.844	143.540	No							
12:13:03	38.015	142.987	No							
12:13:14	37.295	142.484	Yes	37.225	142.218	26.0	6.2	0.22	71.6	-11
12:15:38	39.292	143.833	No							
12:15:51	39.054	142.520	Yes	39.125	142.405	23.4	5.9	0.11	128.5	-9
12:20:46	36.271	141.553	Yes	36.326	141.219	42.7	3.8	0.27	101.4	-5
12:20:53	37.240	142.665	No							
12:21:36	37.592	141.533	Yes	37.482	141.300	23.2	4.9	0.22	59.2	-15
12:22:22	39.233	142.834	No							
12:24:46	36.513	142.193	Yes	36.460	141.874	23.0	5.2	0.26	78.2	-11
12:26:18	38.239	143.661	No							
12:27:33	37.629	142.845	No							
12:28:53	36.191	142.132	Yes	36.203	141.861	23.0	5.1	0.22	93.1	-12
12:29:43	36.733	143.806	No							
12:30:33	36.547	144.268	No							
12:33:24	37.987	143.003	Yes	38.067	142.757	10.0	5.1	0.21	112.4	-14
12:34:45	37.986	143.465	No							
12:35:34	39.071	143.776	No							
12:35:59	39.221	142.470	No							
12:42:05	37.954	142.970	Yes	38.014	142.719	12.0	4.6	0.21	106.8	-10
12:49:10	36.133	142.020	Yes	36.243	141.762	35.5	5.3	0.24	117.8	-10
12:49:31	38.044	143.040	No							
12:51:08	39.421	143.537	No							
12:52:22	38.154	142.470	No							

Continued on next page

Table B.1 – *Continued from previous page*

Time	Lat	Lon	JMA Cat	JMA Lat	JMA Lon	JMA Dep	JMA Mag	Del	Azi	Time Diff
12:54:59	38.461	142.291	Yes	38.504	142.145	39.3	5.1	0.12	110.6	-8
12:56:14	37.831	142.438	Yes	37.793	142.048	29.0	5.3	0.31	82.8	-11
12:59:30	36.093	142.153	Yes	36.148	141.914	35.0	5.3	0.20	105.8	-12
13:02:52	36.637	142.337	Yes	36.571	142.121	55.0	4.8	0.19	69.1	-13
13:08:22	39.054	142.920	Yes	39.178	142.567	26.4	4.8	0.30	114.2	-10
13:13:15	37.837	143.587	No							
13:14:47	37.629	143.920	Yes	37.876	143.684	53.0	4.8	0.31	142.9	-8
13:15:52	37.275	142.320	Yes	37.315	141.927	25.8	5.2	0.32	97.2	-9
13:16:58	36.417	142.207	Yes	36.427	141.843	28.0	5.7	0.29	91.8	-10
13:18:26	37.634	143.190	No							
13:21:09	36.537	142.353	Yes	36.466	141.859	63.0	4.4	0.40	79.7	-11
13:21:24	37.237	142.964	No							
13:22:19	36.544	142.340	Yes	36.469	141.776	80.0	4.4	0.46	80.4	-10
13:23:52	37.537	141.787	Yes	37.397	141.464	29.8	4.5	0.29	61.3	-12
13:25:04	37.154	143.970	No							
13:26:40	35.666	142.358	No							
13:29:21	36.937	142.587	No							
13:32:03	36.475	142.234	Yes	36.450	141.856	46.0	4.6	0.31	85.2	-9
13:32:04	39.244	143.240	No							
13:33:03	38.391	144.632	No							
13:33:51	36.459	142.211	Yes	36.285	141.930	23.0	5.6	0.29	52.4	41
13:34:43	36.133	142.063	Yes	36.285	141.930	23.0	5.6	0.19	144.7	-11
13:35:54	39.254	143.620	No							
13:42:46	37.441	143.045	No							
13:43:19	38.871	144.403	Yes	39.022	144.225	39.0	5.7	0.20	137.4	-12
13:48:47	38.293	143.398	No							
13:49:45	37.957	143.936	No							

Continued on next page

Table B.1 – *Continued from previous page*

Time	Lat	Lon	JMA Cat	JMA Lat	JMA Lon	JMA Dep	JMA Mag	Del	Azi	Time Diff
13:50:42	37.371	144.287	No							
13:52:18	36.644	142.040	Yes	36.673	141.831	45.0	4.9	0.17	99.8	-8
13:53:39	36.415	142.031	Yes	36.403	141.824	58.4	4.5	0.17	85.8	0
13:54:54	38.554	142.570	Yes	38.630	142.340	31.2	4.4	0.20	112.8	-8
13:55:36	37.917	143.207	No							
13:56:05	37.171	142.670	No							
13:56:11	37.637	141.887	Yes	37.666	141.722	46.4	5.3	0.13	102.5	-6
13:58:58	36.648	142.098	Yes	36.685	141.837	35.9	5.1	0.21	99.9	-10
14:00:45	36.086	141.165	Yes	36.148	140.879	43.4	5.4	0.24	104.9	-8
14:02:15	37.254	143.170	No							
14:07:43	39.071	142.587	Yes	39.242	142.392	29.4	4.4	0.23	138.5	-4
14:09:08	36.864	143.600	No							
14:10:48	37.487	142.303	Yes	37.505	141.996	31.1	5.2	0.24	94.1	-10
14:13:56	37.944	143.340	No							
14:15:07	36.347	142.191	Yes	36.035	141.709	33.0	4.1	0.50	51.1	41
14:19:17	36.254	142.020	Yes	36.269	141.852	35.0	4.6	0.14	96.3	-11
14:20:35	37.544	143.440	No							
14:21:31	36.987	142.553	No							
14:26:43	37.454	142.720	No							
14:27:53	37.229	144.157	No							
14:28:52	38.264	142.140	Yes	38.330	142.026	41.8	4.9	0.11	126.4	-3
14:31:03	38.016	142.783	Yes	38.275	142.350	29.0	5.0	0.43	127.1	-6
14:32:08	35.954	141.470	Yes	36.044	141.283	26.0	4.6	0.18	120.7	-10
14:32:18	39.364	143.400	No							
14:33:19	37.716	144.333	No							
14:37:46	38.764	144.400	Yes	38.911	144.083	30.0	5.1	0.29	120.7	-8
14:38:00	37.221	143.887	No							

Continued on next page

Table B.1 – *Continued from previous page*

Time	Lat	Lon	JMA Cat	JMA Lat	JMA Lon	JMA Dep	JMA Mag	Del	Azi	Time Diff
14:38:38	39.054	143.170	Yes	39.214	142.951	10.5	5.0	0.23	133.2	-11
14:42:27	39.544	142.840	Yes	39.607	142.558	32.0	4.4	0.23	106.1	-6
14:44:16	36.614	141.182	Yes	36.645	140.979	47.3	4.9	0.17	100.7	-7
14:46:03	37.344	142.840	No							
14:49:22	38.104	144.420	No							
14:52:36	37.316	142.908	No							
14:54:13	38.054	142.970	No							
14:54:13	35.924	142.250	Yes	36.006	142.137	13.0	5.4	0.12	131.8	-15
14:56:24	35.893	141.653	Yes	35.972	141.570	31.2	5.8	0.10	139.6	-11
15:01:45	38.954	142.570	Yes	39.108	142.405	29.4	4.9	0.20	140.2	-7
15:04:07	38.004	143.220	Yes	38.145	142.800	0.8	5.1	0.36	113.0	-10
15:06:32	37.204	142.120	Yes	37.291	141.759	35.2	4.8	0.30	106.7	-8
15:07:51	36.316	141.908	Yes	36.377	141.525	40.6	5.4	0.31	101.1	-10
15:10:22	35.854	141.670	Yes	36.021	141.492	28.4	3.9	0.22	139.2	3
15:12:15	37.054	142.270	Yes	37.133	142.012	42.0	4.3	0.22	110.9	-10
15:13:25	35.957	142.087	Yes	36.054	142.001	22.8	6.7	0.12	144.3	-13
15:20:15	36.279	142.278	Yes	36.417	141.911	0.0	6.3	0.33	114.9	-11
15:21:29	38.387	143.503	No							
15:22:35	35.704	141.970	Yes	35.908	141.772	12.0	4.9	0.26	141.7	-11
15:26:11	37.279	142.820	No							
15:29:26	38.524	140.287	No							
15:32:43	37.264	142.650	Yes	37.307	142.173	13.6	5.3	0.38	96.3	-12
15:32:58	36.454	141.833	No							
15:34:39	38.671	144.553	No							
15:36:24	38.804	143.070	Yes	38.919	142.712	13.2	5.0	0.30	112.3	-10
15:38:42	38.771	143.053	Yes	38.913	142.709	37.3	4.2	0.30	117.8	-10
15:39:57	38.679	144.495	No							

Continued on next page

Table B.1 – *Continued from previous page*

Time	Lat	Lon	JMA Cat	JMA Lat	JMA Lon	JMA Dep	JMA Mag	Del	Azi	Time Diff
15:39:58	36.404	142.170	Yes	36.376	141.880	62.0	4.5	0.24	83.1	-11
15:41:01	38.524	143.660	No							
15:42:16	36.104	142.100	Yes	36.130	141.902	16.4	5.5	0.16	99.2	-14
15:44:16	37.840	143.284	No							
15:44:30	38.521	144.737	No							
15:45:23	39.089	142.428	Yes	39.189	142.390	33.5	4.5	0.10	163.6	-19
15:46:12	36.054	142.220	Yes	36.128	141.870	17.0	4.7	0.29	104.6	-11
15:48:57	36.354	142.970	No							
15:51:09	37.475	142.720	Yes	37.526	142.270	13.9	5.0	0.36	98.0	-12
15:51:52	38.604	143.237	No							
15:55:34	36.671	142.153	Yes	36.697	141.824	44.3	4.7	0.27	95.5	-9
15:57:10	36.421	142.220	No							
16:00:48	38.516	143.845	No							
16:02:23	36.793	143.853	Yes	36.523	143.940	69.0	5.1	0.28	345.5	-20
16:05:01	39.191	144.595	No							
16:07:27	38.137	143.153	Yes	38.095	142.577	8.0	4.9	0.46	84.5	-14
16:08:33	37.333	144.234	No							
16:11:40	39.504	143.670	Yes	39.566	143.605	2.1	5.8	0.08	141.0	-17
16:18:10	37.687	144.203	No							
16:21:01	36.244	142.340	Yes	36.257	142.038	25.0	4.9	0.24	93.0	-12
16:25:18	37.104	143.920	No							
16:27:03	38.054	144.820	No							
16:31:10	38.829	143.145	Yes	38.867	142.699	0.0	4.5	0.35	96.1	-6
16:34:29	39.454	143.620	Yes	39.357	143.465	13.0	4.9	0.15	50.9	-12
16:37:09	36.404	143.220	No							
16:42:25	38.404	143.270	Yes	38.447	142.862	7.2	4.8	0.32	97.5	-7
16:45:13	37.871	144.353	No							

Continued on next page

Table B.1 – *Continued from previous page*

Time	Lat	Lon	JMA Cat	JMA Lat	JMA Lon	JMA Dep	JMA Mag	Del	Azi	Time Diff
16:47:27	37.554	143.920	Yes	37.818	143.812	42.0	4.9	0.28	162.0	-9
16:49:26	35.971	141.470	Yes	36.072	141.232	45.3	4.6	0.22	117.6	-10
16:53:08	36.075	142.420	No							
16:56:01	37.754	143.470	Yes	37.758	143.210	30.0	5.1	0.21	91.0	-11
16:56:52	38.171	142.453	Yes	38.272	142.203	42.0	5.3	0.22	117.1	-8
17:00:01	37.804	144.349	No							
17:00:03	38.764	144.500	No							
17:11:45	38.354	143.270	Yes	38.468	142.959	18.7	4.6	0.27	115.0	-8
17:12:49	37.490	144.163	No							
17:15:04	38.921	142.637	Yes	39.048	142.421	26.4	5.0	0.21	127.0	-9
17:17:05	36.887	144.303	No							
17:17:38	35.457	141.936	Yes	35.403	142.028	22.0	6.1	0.09	305.8	-15
17:23:05	36.654	142.770	No							
17:24:06	35.975	142.220	Yes	36.119	141.924	32.0	5.2	0.28	120.9	-11
17:30:57	37.421	141.537	Yes	37.412	141.310	18.3	5.0	0.18	87.1	-11
17:32:20	36.904	144.720	Yes	37.069	144.389	43.0	5.8	0.31	121.9	-6
17:35:27	36.954	142.920	No							
17:38:02	39.354	143.670	No							
17:38:34	36.464	142.940	Yes	36.427	142.499	45.0	4.4	0.36	83.9	-8
17:47:23	37.544	143.840	No							
17:50:35	35.929	142.245	No							
17:51:32	36.864	142.600	Yes	36.792	142.083	32.0	5.0	0.42	80.0	-12
17:56:57	37.624	141.560	Yes	37.476	141.317	29.6	4.4	0.24	52.4	-10
18:02:36	36.775	142.620	No							
18:04:56	37.187	144.803	No							
18:10:32	38.024	144.060	No							
18:11:35	37.191	142.533	Yes	37.171	142.026	25.5	6.0	0.40	87.0	-10

Continued on next page

Table B.1 – *Continued from previous page*

Time	Lat	Lon	JMA Cat	JMA Lat	JMA Lon	JMA Dep	JMA Mag	Del	Azi	Time Diff
18:13:50	36.361	142.449	No							
18:17:15	36.187	142.103	Yes	36.258	141.804	16.0	5.7	0.25	106.3	-12
18:17:53	38.484	143.380	No							
18:34:25	37.087	144.703	No							
18:39:47	37.954	143.270	No							
18:43:09	39.004	143.570	No							
18:44:14	36.837	141.320	Yes	36.871	141.154	47.3	5.0	0.14	104.3	-6
18:55:24	35.754	142.020	Yes	35.946	141.828	15.8	4.8	0.25	140.9	-13
18:59:31	37.018	139.013	Yes	36.986	138.598	8.4	6.7	0.33	84.4	-16
19:03:08	39.292	143.233	Yes	39.353	142.938	8.5	6.3	0.24	104.9	-11
19:08:04	36.579	142.557	No							
19:08:51	36.354	141.020	Yes	36.286	140.948	34.7	5.2	0.09	40.4	-10
19:12:57	37.031	139.038	Yes	37.032	138.672	12.1	4.3	0.29	90.1	-13
19:24:39	35.675	141.220	Yes	35.759	141.041	35.1	5.7	0.17	120.0	-11
19:30:36	36.054	142.270	Yes	36.222	141.929	5.0	4.4	0.32	121.3	-11
19:32:08	36.987	139.003	Yes	36.949	138.572	0.8	5.9	0.35	83.6	-13
19:35:20	38.691	143.432	No							
19:40:19	37.504	143.670	No							
19:45:33	37.554	141.920	Yes	37.490	141.666	25.7	5.2	0.21	72.3	-11
19:47:02	40.442	139.458	Yes	40.394	139.089	3.9	6.4	0.28	80.2	-16
19:56:08	38.864	144.500	Yes	39.225	144.305	45.0	4.7	0.39	157.2	-4
19:58:58	36.133	141.363	Yes	36.256	141.053	42.5	4.8	0.28	116.1	-9
20:01:41	38.054	144.070	No							
20:08:42	40.354	139.370	Yes	40.327	139.143	28.4	4.8	0.18	81.1	-13
20:11:34	38.893	143.053	Yes	38.972	142.755	6.1	6.4	0.24	108.7	-13
20:17:17	37.154	144.170	No							
20:22:47	38.479	142.020	Yes	38.567	141.882	50.0	4.6	0.14	129.1	-6

Continued on next page

Table B.1 – *Continued from previous page*

Time	Lat	Lon	JMA Cat	JMA Lat	JMA Lon	JMA Dep	JMA Mag	Del	Azi	Time Diff
20:23:04	37.277	142.693	Yes	37.441	142.528	52.0	4.9	0.21	141.3	-9
20:23:52	35.754	141.970	Yes	35.958	141.663	9.7	5.4	0.32	129.3	-9
20:25:31	37.092	142.233	Yes	37.083	141.886	28.4	5.1	0.28	88.0	-10
20:26:28	37.640	143.575	No							
20:26:41	38.054	142.670	No							
20:28:11	39.429	142.982	No							
20:33:27	37.754	143.270	No							
20:34:51	37.122	141.175	Yes	36.947	141.224	49.1	5.1	0.18	347.4	-10
20:36:19	37.804	143.220	Yes	37.803	142.727	4.0	5.6	0.39	89.7	-10
20:41:44	37.633	143.920	No							
20:42:35	37.039	139.026	Yes	36.973	138.590	3.8	5.3	0.35	79.1	-16
20:42:50	38.316	142.508	Yes	38.457	142.263	33.6	5.0	0.24	126.2	-9
20:45:23	36.675	142.477	Yes	36.650	142.169	23.0	4.8	0.25	84.1	-12
20:46:13	39.054	142.870	Yes	39.183	142.579	26.2	4.9	0.26	119.7	-6
20:47:07	39.064	143.240	Yes	39.090	142.887	21.7	4.9	0.28	95.3	-11
20:50:09	37.354	142.870	Yes	37.311	142.554	27.0	4.7	0.25	80.2	-5
20:51:32	38.954	144.570	Yes	38.995	143.966	0.0	5.1	0.47	94.8	-9
20:54:58	38.729	144.420	Yes	38.990	143.941	38.0	4.8	0.46	124.8	-4
21:00:54	38.924	142.950	Yes	39.019	142.705	11.9	5.5	0.21	116.4	-13
21:03:42	37.821	143.237	No							
21:14:06	36.647	142.649	No							
21:29:34	39.204	142.470	Yes	39.164	142.345	32.8	4.7	0.10	67.5	-6
21:30:45	37.404	142.820	No							
21:31:18	38.854	142.970	No							
21:34:32	37.554	141.570	Yes	37.452	141.309	22.6	4.8	0.23	63.7	-10
21:42:08	37.279	142.758	Yes	37.276	142.525	2.0	5.6	0.19	89.0	-14
21:47:36	38.904	144.820	No							

Continued on next page

Table B.1 – *Continued from previous page*

Time	Lat	Lon	JMA Cat	JMA Lat	JMA Lon	JMA Dep	JMA Mag	Del	Azi	Time Diff
21:48:52	35.804	141.240	Yes	35.870	140.957	11.2	4.6	0.24	106.0	-12
21:56:44	37.804	143.770	No							
22:04:13	38.304	142.520	Yes	38.427	142.280	37.9	4.4	0.22	123.1	-5
22:08:20	39.617	143.508	No							
22:12:09	40.637	143.887	No							
22:14:43	37.715	144.364	No							
22:14:59	36.112	140.212	No							
22:18:07	37.029	143.720	No							
22:18:54	36.864	142.000	Yes	36.726	141.554	34.9	4.6	0.38	68.7	-17
22:19:44	36.304	141.970	No							
22:19:57	37.264	142.600	Yes	37.262	142.290	14.0	4.8	0.25	89.4	-11
22:22:44	39.129	143.220	Yes	39.157	143.005	23.2	4.7	0.17	99.5	-11
22:29:51	38.354	143.070	No							
22:33:50	37.521	144.337	No							
22:37:04	37.004	143.987	No							
22:43:05	37.554	144.020	No							
22:43:27	39.492	143.033	Yes	39.450	142.785	40.4	5.2	0.20	77.5	-11
22:46:48	39.454	142.920	No							
22:49:48	37.944	144.640	No							
22:54:37	36.504	142.745	Yes	36.489	142.538	68.0	5.3	0.17	84.8	-12
23:05:17	39.475	142.134	Yes	39.619	142.152	47.4	4.9	0.14	185.5	-7
23:12:04	37.254	141.170	Yes	37.180	140.974	10.2	4.6	0.17	64.6	-12
23:12:50	36.954	140.820	Yes	36.743	140.624	5.1	4.6	0.26	36.6	-13
23:21:30	39.037	143.587	Yes	39.169	143.385	30.8	5.1	0.20	130.0	-10
23:24:16	36.844	143.640	No							
23:26:58	38.918	142.963	Yes	39.012	142.693	13.1	5.3	0.23	114.0	-12
23:28:37	36.987	143.837	No							

Continued on next page

Table B.1 – *Continued from previous page*

Time	Lat	Lon	JMA Cat	JMA Lat	JMA Lon	JMA Dep	JMA Mag	Del	Azi	Time Diff
23:32:03	39.104	143.270	Yes	39.281	143.070	39.0	4.8	0.24	138.7	-13
23:36:28	39.454	144.070	No							
23:40:20	37.104	143.845	Yes	37.196	143.416	27.0	5.2	0.35	104.9	-10
23:52:20	39.644	143.440	Yes	39.512	143.199	13.5	4.6	0.23	54.5	-12
23:52:56	37.554	144.420	No							
23:53:37	38.804	142.820	Yes	38.951	142.586	37.0	5.1	0.23	128.8	-10
23:54:54	37.384	142.180	Yes	37.431	141.881	40.0	5.0	0.24	101.1	-9
23:56:34	37.744	143.340	No							
23:58:11	38.404	143.720	Yes	38.523	143.432	57.0	4.8	0.25	117.7	-8
23:59:31	36.573	142.058	Yes	36.498	141.480	28.4	5.5	0.47	80.7	-10

Table B.2: The same as Table B.1, except for events on March 12th.

Time	Lat	Lon	JMA Cat	JMA Lat	JMA Lon	JMA Dep	JMA Mag	Del	Azi	Time Diff
00:01:05	36.544	141.940	Yes	36.562	141.734	65.3	4.5	0.17	96.1	-9
00:01:37	38.140	143.629	No							
00:08:03	37.064	142.700	Yes	37.008	142.137	12.3	4.4	0.45	82.7	-10
00:10:29	39.122	142.520	Yes	39.202	142.343	29.5	4.6	0.16	120.2	-9
00:21:54	38.804	144.620	No							
00:25:16	37.764	142.200	Yes	37.765	141.978	22.7	4.8	0.18	90.3	-11
00:28:45	37.537	144.087	No							
00:39:46	37.261	142.949	No							
00:40:43	38.324	142.460	Yes	38.462	142.318	37.0	5.0	0.18	141.1	-8
00:43:17	39.504	143.170	Yes	39.547	142.842	14.0	4.7	0.26	99.5	-10
00:45:19	36.134	142.190	Yes	36.162	141.932	20.0	5.6	0.21	97.6	-12
00:57:40	36.104	142.370	Yes	36.118	142.003	17.0	4.7	0.30	92.6	-14
01:04:06	37.764	141.600	Yes	37.901	141.524	58.2	4.8	0.15	156.3	-4
01:11:05	37.537	143.187	No							
01:12:21	37.087	140.953	Yes	37.013	140.738	11.1	4.8	0.19	66.6	-12
01:14:04	37.337	141.387	Yes	37.323	141.222	30.1	4.9	0.13	83.9	-8
01:17:10	37.904	143.070	Yes	37.978	142.900	37.0	5.1	0.15	118.8	-12
01:24:27	37.754	142.320	Yes	37.708	142.038	17.0	5.0	0.23	78.3	-18
01:25:12	36.321	142.037	Yes	36.330	141.878	60.0	5.0	0.13	94.0	-11
01:34:19	38.704	143.200	Yes	38.833	142.889	0.0	6.2	0.27	117.9	-12
01:36:36	36.754	142.520	Yes	36.722	142.079	10.0	5.5	0.35	84.7	-12
01:43:28	36.315	141.987	Yes	36.365	141.676	59.8	4.9	0.26	101.2	-9
01:46:29	37.333	142.106	Yes	37.367	141.825	36.4	5.2	0.23	98.6	-9
01:47:26	37.537	143.167	Yes	37.476	142.754	0.0	6.8	0.33	79.3	-14
01:52:50	38.687	143.203	No							

Continued on next page

Table B.2 – *Continued from previous page*

Time	Lat	Lon	JMA Cat	JMA Lat	JMA Lon	JMA Dep	JMA Mag	Del	Azi	Time Diff
01:56:28	36.821	142.337	No							
01:59:53	37.404	143.053	Yes	37.434	142.649	19.0	5.5	0.32	95.2	-10
02:05:02	36.554	141.920	Yes	36.539	141.434	0.0	4.6	0.39	87.7	-9
02:07:31	37.804	143.320	Yes	37.855	143.002	29.0	5.2	0.26	101.4	-11
02:13:59	37.654	143.970	No							
02:14:50	39.254	143.132	Yes	39.382	143.003	12.6	5.7	0.16	142.0	-11
02:17:44	37.644	143.940	Yes	37.651	143.760	46.0	5.4	0.14	92.8	-8
02:27:55	37.704	144.520	Yes	38.131	144.067	46.0	5.0	0.56	139.9	-3
02:30:07	38.454	142.170	Yes	38.523	142.118	46.0	4.7	0.08	149.4	-6
02:34:16	36.779	142.057	Yes	36.744	141.613	45.7	5.2	0.36	84.2	-12
02:37:06	36.515	144.042	No							
02:37:41	40.059	142.938	Yes	40.021	142.748	35.0	5.1	0.15	75.3	-11
02:37:50	36.724	143.770	No							
02:43:18	39.034	142.590	Yes	39.200	142.433	28.1	4.9	0.21	143.7	-8
02:47:43	37.515	143.853	Yes	37.589	143.586	40.0	5.9	0.22	109.2	-9
02:49:11	38.904	144.420	No							
02:50:41	36.733	142.106	No							
02:51:56	37.721	144.237	No							
02:52:46	37.247	141.391	Yes	37.225	141.151	15.7	5.1	0.19	83.4	-12
02:54:09	38.154	144.170	No							
02:56:34	37.161	141.591	Yes	37.214	141.152	15.5	4.7	0.35	98.5	-12
02:57:42	37.504	143.891	No							
02:59:28	37.624	144.500	No							
03:01:57	39.504	143.020	Yes	39.567	142.888	11.0	5.6	0.12	121.7	-13
03:06:40	39.068	142.756	Yes	39.037	142.697	42.0	5.2	0.06	55.9	-15
03:07:42	40.004	143.320	No							
03:08:12	36.179	142.495	No							

Continued on next page

Table B.2 – *Continued from previous page*

Time	Lat	Lon	JMA Cat	JMA Lat	JMA Lon	JMA Dep	JMA Mag	Del	Azi	Time Diff
03:09:45	39.504	142.970	No							
03:12:08	35.875	141.720	Yes	35.983	141.611	37.1	5.6	0.14	140.7	-10
03:13:34	39.254	143.720	No							
03:16:37	38.987	143.487	No							
03:21:52	37.733	144.163	No							
03:25:24	37.379	143.020	No							
03:28:53	36.054	142.470	Yes	36.097	142.163	64.0	4.3	0.25	99.7	-7
03:41:28	40.004	143.970	Yes	39.914	143.833	48.0	5.0	0.14	49.4	-14
03:53:06	37.344	142.940	Yes	37.376	142.452	36.0	4.5	0.39	94.6	-9
03:54:06	38.324	144.460	No							
03:54:56	35.792	141.632	Yes	35.929	141.445	15.9	5.0	0.20	132.1	-11
03:57:49	38.221	143.020	No							
04:01:59	36.454	142.570	No							
04:04:07	36.564	142.700	Yes	36.688	142.342	11.0	4.3	0.31	113.2	-2
04:06:16	38.733	142.020	Yes	38.736	142.167	40.0	5.3	0.11	268.5	-8
04:06:53	39.419	142.175	No							
04:09:32	36.454	144.470	No							
04:20:32	38.604	142.770	No							
04:21:27	37.584	143.980	No							
04:29:00	36.654	142.220	Yes	36.655	141.915	35.0	4.5	0.24	90.1	-4
04:34:13	39.254	143.720	No							
04:37:45	36.304	141.366	Yes	36.257	141.133	40.3	4.4	0.19	75.9	-24
04:43:11	35.887	141.753	Yes	35.992	141.430	37.4	4.3	0.28	111.8	-8
04:47:27	35.891	141.733	Yes	36.046	141.508	28.4	4.9	0.24	130.3	-9
04:53:06	40.054	143.650	Yes	40.063	143.556	8.0	5.7	0.07	97.1	-14
05:14:58	36.726	140.759	Yes	36.753	140.651	9.8	4.8	0.09	107.3	-12
05:29:18	36.864	143.600	No							

Continued on next page

Table B.2 – *Continued from previous page*

Time	Lat	Lon	JMA Cat	JMA Lat	JMA Lon	JMA Dep	JMA Mag	Del	Azi	Time Diff
05:31:02	38.137	144.087	No							
05:47:09	38.287	144.537	No							
05:59:05	37.617	144.132	No							
06:00:33	36.344	142.140	Yes	36.328	141.961	26.0	5.3	0.15	83.6	-12
06:06:47	37.304	143.420	No							
06:18:50	39.117	142.567	Yes	39.158	142.705	44.0	5.5	0.11	249.1	-11
06:23:22	39.544	143.140	Yes	39.540	142.980	24.0	5.4	0.12	88.1	-11
06:28:16	35.854	142.170	Yes	36.204	141.778	0.0	NA	0.47	137.7	-22
06:28:22	38.254	142.470	No							
06:29:17	39.075	142.577	No							
06:36:08	39.592	143.733	Yes	39.697	143.767	50.0	5.0	0.11	194.0	-11
06:39:32	37.554	143.270	No							
06:40:48	37.529	144.795	No							
06:40:54	36.818	141.020	Yes	36.773	140.934	23.4	4.7	0.08	56.8	-9
06:44:12	36.604	141.120	Yes	36.595	141.029	43.2	4.7	0.07	82.9	-12
06:49:19	38.754	142.670	Yes	38.648	142.694	46.0	4.7	0.11	350.0	-11
06:53:58	37.854	144.820	No							

BIBLIOGRAPHY

- Abers, G., 1992. Relationship between shallow- and intermediate-depth seismicity in the eastern Aleutian subduction zone. *Geophys. Res. Lett.* 20, 2019–2022.
- Aki, K., Richards, P., 2002. *Quantitative Seismology*. University of Science Books, Sausalito, California.
- Allmann, B., Shearer, P., 2007. A high-frequency secondary event during the 2004 Parkfield earthquake. *Science* 318, 1279–1283.
- Ammon, C., Lay, T., Kanamori, H., Cleveland, M., 2011. The rupture model of the great 2011 Tohoku earthquake. *Earth Planets Space First Results of the 2011 Off the Pacific Coast of Tohoku Earthquake*.
- Ando, R., Imanishi, K., 2011. Possibility of Mw 9.0 mainshock triggered by diffusional propagation of after-slip from Mw 7.3 foreshock. *Earth Planets Space First Results of the 2011 Off the Pacific Coast of Tohoku Earthquake*.
- Antolik, M., Douglas, D., Romanowicz, B., 1999. Rupture processes of large deep-focus earthquakes from inversion of moment rate functions. *J. Geophys. Res.* 104, 863–894.
- Aochi, H., Ide, S., 2011. Conceptual multi-scale dynamic rupture model for the 2011 Tohoku earthquake. *Earth Planets Space First Results of the 2011 Off the Pacific Coast of Tohoku Earthquake*.
- Araujo, M., Suarez, G., 1994. Geometry and state of stress of the of the subducted Nazca plate beneath central Chile and Argentina: evidence from teleseismic data. *Geophys. J. Int.* 116, 283–303.
- Baker, T., Granat, R., Clayton, R., 2005. Real-time earthquake location using Kirchhoff reconstruction. *Bull. Seismol. Soc. Am.* 95, 699–707.
- Barrientos, S., Ward, S., 1990. The 1960 Chile earthquake: inversion for slip inversion from surface deformation. *Geophys. J. Int.* 103, 589–598.
- Beavan, J., Wang, X., Holden, C., Wilson, K., Power, W., Prasetya, G., Bevis, M., Kautoke, R., 2010. Near-simultaneous great earthquakes at Tongan megathrust and outer rise in September 2009. *Nature* 466, 959–963.

- Beck, S., Barrientos, S., Kausel, E., Reyes, M., 1998. Source characteristics of historic earthquakes along the central Chile subduction zone. *J. S. Am. Earth Sci.* 11, 115–129.
- Ben-David, O., Cohen, G., Fineberg, J., 2010. The Dynamics of the Onset of Frictional Slip. *Science* 330, 211–214.
- Beresnev, I., 2003. Uncertainties in finite-fault slip inversions: to what extent to believe? (a critical review). *Bull. Seismol. Soc. Am.* 95, 2445–2458.
- Bergeot, N., Bouin, M., Diament, M., Pelletier, B., Regnier, M., Calmant, S., Ballu, V., 2009. Horizontal and vertical interseismic velocity fields in the Vanuatu subduction zone from GPS measurements; evidence for a central Vanuatu locked zone. *J. Geophys. Res.* 114.
- Bevis, M., Taylor, F., Schutz, B., Recy, J., Isacks, B., Helu, S., Singh, R., Kendrick, E., Stowell, J., Taylor, B., Calmant, S., 1995. Geodetic observations of very rapid convergence and back-arc extension at the Tonga Arc. *Nature* 374, 249–251.
- Biggs, J., Robinson, D., Dixon, T., 2009. The 2007 Pisco, Peru, earthquake (Mw8.0): Seismology and geodesy. *Geophys. J. Int.* 176, 657–669.
- Bizzarri, A., 2010. On the relations between fracture energy and physical observables in dynamic earthquake models. *J. Geophys. Res.* 115, B10307.
- Bizzarri, A., 2011. On the Deterministic Description of Earthquakes. *Rev. Geophys.* 49, 1–32.
- Boatwright, J., Choy, G., 1986. Teleseismic estimates of the energy radiated by shallow earthquakes. *J. Geophys. Res.* 91, 2095–2112.
- Bos, A., Nolet, G., Rubin, A., Houston, H., Vidale, J., 1998. Duration of deep earthquakes determined by stacking of global seismograph network seismograms. *J. Geophys. Res.* 103, 21059–21065.
- Brantut, N., Sulem, J., Schubnel, A., 2011. Effect of dehydration reactions on earthquake nucleation: stable sliding, transient and unstable slip. *J. Geophys. Res.* 116, B05304.
- Brodsky, E., Kanamori, H., 2001. Elastohydrodynamic lubrication of faults. *J. Geophys. Res.* 106, 16,357–16,374.
- Brune, J., 1970. Tectonic stress and the spectra of seismic shear waves from earthquakes. *J. Geophys. Res.* 75, 4997–5009.
- Campus, P., Das, S., 2000. Comparison of the rupture and radiation characteristics of intermediate and deep earthquakes. *J. Geophys. Res.* 105, 6177–6189.

- Carpenter, E., 1965. A historical review of seismometer array development. *Proc IEEE* 53, 1816–1821.
- Cassidy, J., Waldhauser, F., 2003. Evidence for both crustal and mantle earthquakes in the subducting Juan de Fuca plate. *Geophys. Res. Lett.* 30, 1095.
- Chernak, L., Hirth, G., 2010. Deformation of antigorite serpentinite at high temperature and pressure. *Earth Planet. Sci. Lett.* 296, 23–33.
- Chlieh, M., Avouac, J., Sieh, K., Natawidjaja, D., Galetzka, J., 2008. Heterogeneous coupling of the Sumatran megathrust constrained by geodetic and paleogeodetic measurements. *J. Geophys. Res.* 113, B05305.
- Christensen, D., Beck, S., 1994. The Rupture Process and Tectonic Implications of the Great 1964 Prince William Sound Earthquake. *PAGEOPH* 142, 29–53.
- Christensen, D., Ruff, L., 1986. Rupture process of the March 3, 1985 Chilean earthquake. *Geophys. Res. Lett.* 13, 721–724.
- Claerbout, J., 1976. *Fundamentals of Geophysical Data Processing*. McGraw-Hill, New York.
- Cocco, M., Rice, J., 2002. Pore pressure and poroelasticity effects in Coulomb stress analysis of earthquake interactions. *J. Geophys. Res.* 107, 2030.
- Cohee, B., Beroza, G., 1994. Slip distribution of the 1992 Landers earthquake and its implications for earthquake source mechanics. *Bull. Seismol. Soc. Am.* 84, 692–712.
- Comte, D., Dorbath, L., Pardo, M., Monfret, T., Haessler, H., Rivera, L., Frogneux, M., Glass, B., Meneses, C., 1999. A double-layered seismic zone in Arica, Northern Chile. *Geophys. Res. Lett.* 26, 1965–1968.
- Contreras-Reyes, E., Grevemeyer, I., Flueh, E., Reichert, C., 2008. Upper lithospheric structure of the subduction zone offshore of southern Arauco peninsula, Chile, at 38S. *J. Geophys. Res.* 113, B07303.
- Cotton, F., Campillo, M., 1995. Frequency domain inversion of strong motions: Application to the 1992 Landers earthquake. *J. Geophys. Res.* 100, 3961–3975.
- Creager, K., Boyd, T., 1991. The geometry of Aleutian subduction; three-dimensional kinematic flow model. *J. Geophys. Res.* 96, 2293–2307.
- Cruciani, C., Carminati, E., Doglioni, C., 2005. Slab dip vs. lithosphere age; no direct function. *Earth Planet. Sci. Lett.* 238, 298–310.
- D’Amico, S., Koper, K., Herrmann, R., Akinci, A., Malagnini, L., 2010. Imaging the rupture of the Mw 6.3 April 6, 2009 L’Aquila, Italy earthquake using back-projection of teleseismic P-waves. *Geophys. Res. Lett.* 37, L03301.

- Delouis, B., Legrand, D., 2007. Mw 7.8 Tarapaca intermediate depth earthquake of 13 June 2005 (northern Chile); fault plane identification and slip distribution by waveform inversion. *Geophys. Res. Lett.* 34.
- Delouis, B., Nocquet, J.-M., Vallee, M., 2010. Slip distribution of the February 27, 2010 Mw = 8.8 Maule Earthquake, central Chile, from static and high-rate GPS, InSAR, and broadband teleseismic data. *Geophys. Res. Lett.* 37, L17305.
- Di Toro, G., Goldsby, D., Tullis, T., 2004. Friction falls towards zero in quartz rock as slip velocity approaches seismic rates. *Nature* 427, 436–439.
- Dieterich, J., 1994. A constitutive law for rate of earthquake production and its application to earthquake clustering. *J. Geophys. Res.* 99, 2601–2618.
- Dziewoński, A., Chou, T., Woodhouse, J., 1981. Determination of earthquake source parameters from waveform data for studies of global and regional seismicity. *J. Geophys. Res.* 86, 2825–2852.
- Dziewoński, A., Woodhouse, J., 1983. An experiment in systematic study of global seismicity; centroid-moment tensor solutions for 201 moderate and large earthquakes of 1981. *J. Geophys. Res.* 88, 3247–3271.
- Ekström, G., 1994. Anomalous earthquakes on volcano ring-fault structures. *Earth Planet. Sci. Lett.* 128, 707–712.
- Ekström, G., Dziewoński, A., Maternovskaya, N., Nettles, M., 2005. Global seismicity of 2003: centroid-moment-tensor solutions for 1087 earthquakes. *Phys. Earth Planet. Int.* 148, 327–351.
- Ekström, G., Nettles, M., Abers, G., 2003. Glacial earthquakes. *Science* 302, 622–624.
- Engdahl, E., Scholz, C., 1977. A double Benioff zone beneath the central Aleutians: an unbending of the lithosphere. *Geophys. Res. Lett.* 4, 473–476.
- Famin, V., Nakashima, S., Boullier, A., Fujimoto, K., Hirono, T., 2008. Earthquakes produce carbon dioxide in crustal faults. *Earth Planet. Sci. Lett.* 265, 487–497.
- Flinn, E., Engdahl, E., 1965. A proposed basis for geographical and seismic regionalization. *Rev. Geophys.* 3, 123–149.
- Fournier, T., Freymueller, J., 2007. Transition from locked to creeping subduction in the Shumagin region, Alaska. *Geophys. Res. Lett.* 34, L06303.
- Frankel, A., 2004. Rupture process of the M 7.9 Denali Fault, Alaska, earthquake: Subevents, directivity, and scaling of high-frequency ground motions. *Bull. Seismol. Soc. Am.* 94, 234–255.

- Fritz, H., Kalligeris, N., Borrero, J., Broncano, P., Ortega, E., 2008. The 15 August 2007 Peru tsunami runup observations and modeling. *Geophys. Res. Lett.* 35, L10604.
- Frohlich, C., 1987. Aftershocks and temporal clustering of deep earthquakes. *J. Geophys. Res.* 92, 13944–13956.
- Frohlich, C., 1989. The nature of deep-focus earthquakes. *Ann. Rev. Earth Planet. Sci.* 17, 227–254.
- Frohlich, C., 2006. *Deep Earthquakes*. Cambridge University Press, The Edinburgh Building, Cambridge CB2 2RU, UK.
- Fromm, R., Alvarado, P., Beck, S., Zandt, G., 2006. The April 9, 2001 Juan Fernandez Ridge (Mw 6.7) tensional outer-rise earthquake and its aftershock sequence. *J. Seismol.* 10, 163–170.
- Fujii, Y., Satake, K., Sakai, S., Shinohara, M., Kanazawa, T., 2011. Tsunami source of the 2011 off the Pacific coast of Tohoku, Japan earthquake. *Earth Planets Space First Results of the 2011 Off the Pacific Coast of Tohoku Earthquake*.
- Fukao, Y., Furumoto, M., 1979. Stress drops, wave spectra and recurrence intervals of great earthquakes - implications of the Etorofu earthquake of 1958 November 6. *Geophys. J. Roy. Astron. Soc.* 57, 23–40.
- Green, H., Burnley, P., 1989. A new self-organizing mechanism for deep-focus. *Nature* 341, 733–737.
- Green, H., Houston, H., 1995. The mechanics of deep earthquakes. *Ann. Rev. Earth Planet. Sci.* 23, 169–213.
- Gu, Y., 2009. *Arrays and Array Methods in Global Seismology*. Springer, Dordrecht Heidelberg London New York.
- Habermann, R., Wyss, M., 1984. Earthquake triggering during preparation for great earthquakes. *Geophys. Res. Lett.* 11, 291–294.
- Hacker, B., Peacock, S., Abers, G., Holloway, S., 2003. Subduction factory 2. Are intermediate-depth earthquakes in subducting slabs linked to metamorphic dehydration reactions? *J. Geophys. Res.* 108.
- Han, R., Shimamoto, T., Hirose, T., Ree, J.-H., Ando, J., 2007. Ultralow friction of carbonate faults caused by thermal decomposition. *Science* 316, 878–881.
- Hartzell, S., Heaton, T., 1983. Inversion of strong ground motion and teleseismic waveform data for the fault rupture history of the 1979 Imperial Valley, California, earthquake. *Bull. Seismol. Soc. Am.* 73, 1553–1583.

- Hartzell, S., Helmberger, D., 1982. Strong-motion modeling of Imperial Valley earthquake of 1979. *Bull. Seismol. Soc. Am.* 72, 571–596.
- Hasagawa, A., Umino, N., Takagi, A., 1978. Double-planed structure of the deep seismic zone in the northeastern Japan arc. *Tectonophysics* 47, 43–58.
- Hatori, T., 1987. Intensity and tsunami distribution of Miyaga-oki Earthquake in Kansei 5 (A.D. 1793). *Bull. Earthquake Res. Inst. Univ. Tokyo* 62, 297–309.
- Hayes, G., 2011. Rapid Source Characterization of the 03-11-2011 Mw 9.0 Off the Pacific Coast of Tohoku Earthquake. *Earth Planets Space First Results of the 2011 Off the Pacific Coast of Tohoku Earthquake*.
- Hébert, H., Reymond, D., Krien, Y., Vergoz, J., Schindel e, F., Roger, J., Loevenbruck, A., 2009. The 15 August 2007 Peru earthquake and tsunamis: Influence of the Source Characteristics on the Tsunami Heights. *Pure Appl. Geophys.* 166, 211–232.
- Heuret, A., Lallemand, S., Funicello, F., Piromallo, C., Faccenna, C., 2011. Physical characteristics of subduction interface type seismogenic zones revisited. *Geochem. Geophys. Geosyst.* 12, Q01004.
- Hino, R., Azuma, R., Ito, Y., Yamamoto, Y., Suzuki, K., Tsushima, H., Suzuki, S., Miyashita, M., Tomori, T., Azizono, M., Tange, C., 2009. Insight into complex rupturing of the immature bending normal fault in the outer slope of the Japan Trench from aftershocks of the 2005 Sanriku earthquake (Mw = 7.0) located by ocean bottom seismometry. *Geochem. Geophys. Geosyst.* 10.
- Hiratsuka, S., Sato, T., 2011. Alteration of stress field brought about by the occurrence of the 2011 off the Pacific coast of Tohoku earthquake (Mw 9.0). *Earth Planets Space First Results of the 2011 Off the Pacific Coast of Tohoku Earthquake*.
- Hirose, T., Bystricky, M., 2007. Extreme weakening of faults during dehydration by coseismic shear heating. *Geophys. Res. Lett.* 34, L14311.
- Hobbs, B., Ord, A., 1988. Plastic instabilities: Implications for the origin of intermediate and deep focus earthquakes. *J. Geophys. Res.* 93, 10521–10540.
- Holcombe, C., 1977. Earthquake foci distribution in the Sunda arc and the rotation of the backarc area. *Tectonophysics* 43, 169–180.
- Honda, R., Aoi, S., 2009. Array back-projection imaging of the 2007 Niigataken Chuetsu-oki earthquake striking the world’s largest nuclear power plant. *Bull. Seismol. Soc. Am.* 99, 141–147.

- Honda, R., Yukutake, Y., Ito, H., Harada, M., Aketagawa, T., Yoshida, A., Sakai, S., Nakagawa, S., Hirata, N., Obara, K., Kimura, H., 2011. A complex rupture image of the 2011 Tohoku earthquake revealed by the MeSO-net. *Earth Planets Space First Results of the 2011 Off the Pacific Coast of Tohoku Earthquake*.
- Hori, T., Miyazaki, S., 2011. A possible mechanism of M 9 earthquake generation cycles in the area of repeating M 7-8 earthquakes surrounded by aseismic sliding. *Earth Planets Space First Results of the 2011 Off the Pacific Coast of Tohoku Earthquake*.
- Houston, H., 1993. The non-double-couple component of deep earthquakes and the width of the seismogenic zone. *Geophys. Res. Lett.* 20, 1687–1690.
- Houston, H., 2001. Influence of depth, focal mechanism, and tectonic setting on the shape and duration of earthquake source time functions. *J. Geophys. Res.* 106, 11137–11150.
- Houston, H., Benz, H., Vidale, J., 1998. Time functions of deep earthquakes from broadband and short-period stacks. *J. Geophys. Res.* 103, 29895–29913.
- Houston, H., Vidale, J., 1994. The temporal distribution of seismic radiation during deep earthquake rupture. *Science* 265, 771–774.
- Ide, S., Baltay, A., Beroza, G., 2011. Shallow Dynamic Overshoot and Energetic Deep Rupture in the 2011 Mw 9.0 Tohoku-Oki Earthquake. *Science* 332, 1426–1429.
- Iinuma, T., Ohzono, M., Ohta, Y., Miura, S., 2011. Coseismic slip distribution of the 2011 off the Pacific coast of Tohoku Earthquake (M9.0) estimated based on GPS data Was the asperity in Miyagi-oki rupture? *Earth Planets Space First Results of the 2011 Off the Pacific Coast of Tohoku Earthquake*.
- Ishii, M., 2011. High-Frequency Rupture Properties of the Mw 9.0 Off-the-Pacific-Coast-of-Tohoku Earthquake. *Earth Planets Space First Results of the 2011 Off the Pacific Coast of Tohoku Earthquake*.
- Ishii, M., Shearer, P., Houston, H., Vidale, J., 2005. Extent, duration and speed of the 2004 Sumatra-Andaman earthquake imaged by the Hi-net array. *Nature* 435, 933–936.
- Ishii, M., Shearer, P., Houston, H., Vidale, J., 2007. Teleseismic P wave imaging of the 26 December 2004 Sumatra-Andaman and 28 March 2005 Sumatra earthquake ruptures using the Hi-Net array. *J. Geophys. Res.* 112, B11307.
- Ito, T., Ozawa, K., Watanabe, T., Sagiya, T., 2011. Slip distribution of the 2011 Tohoku earthquake inferred from geodetic data. *Earth Planets Space First Results of the 2011 Off the Pacific Coast of Tohoku Earthquake*.

- Ivandic, M., Grevemeyer, I., Bialas, J., Petersen, J., 2010. Serpentinization in the trench-outer rise region offshore of Nicaragua; constraints from seismic refraction and wide-angle data. *Geophys. J. Int.* 180, 1253–1264.
- Ji, C., Wald, D., Helmberger, D., 2002. Source description of the 1999 Hector Mine, California, earthquake, part I: Wavelet domain inversion theory and resolution analysis. *Bull. Seismol. Soc. Am.* 92, 1192–1207.
- Jiao, W., Silver, P., Fei, Y., Prewitt, C., 2000. Do intermediate- and deep-focus earthquakes occur on preexisting weak zones? An examination of the Tonga subduction zone. *J. Geophys. Res.* 105, 28125–28138.
- Johnson, J., Satake, K., 1993. Source Parameters of the 1957 Aleutian Earthquake from Tsunami Waveforms. *Geophys. Res. Lett.* 20, 1487–1490.
- Johnson, J., Tanioka, Y., Ruff, L., Satake, K., Kanamori, H., Sykes, L., 1994. The 1957 Great Aleutian Earthquake. *PAGEOPH* 142, 3–28.
- Jung, H., Green, H., Dobrzhinetskaya, L., 2004. Intermediate-depth earthquake faulting by dehydration embrittlement with negative volume change. *Nature* 428, 545–549.
- Kagan, Y., 2004. Short-term properties of earthquake catalogues and models of earthquake source. *Bull. Seismol. Soc. Am.* 94, 1207–1228.
- Kagan, Y., Houston, H., 2005. Relation between mainshock rupture process and Omori's law for aftershock moment release rate. *Geophys. J. Int.* 163, 1039–1048.
- Kanamori, H., 1970. The Alaska Earthquake of 1964: Radiation of Long-Period Surface Waves and Source Mechanism. *J. Geophys. Res.* 75, 5029–5040.
- Kanamori, H., 1972. Mechanism of tsunami earthquakes. *Phys. Earth Planet. Int.* 6, 346–359.
- Kanamori, H., 1977. The Energy Release in Great Earthquakes. *J. Geophys. Res.* 82, 2981–2987.
- Kanamori, H., Anderson, D., 1975. Theoretical basis of some empirical relations in seismology. *Bull. Seismol. Soc. Am.* 65, 1073–1095.
- Kanamori, H., Heaton, T., 2000. Microscopic and Macroscopic physics of earthquakes. Open-File Report U. S. Geological Survey Report: OF 00-0129, 1–41.
- Kao, H., Liu, L.-G., 1995. A hypothesis for the seismogenesis of a double seismic zone. *Geophys. J. Int.* 123, 71–84.

- Kao, H., Rau, R.-J., 1999. Detailed structures of the subducted Philippine Sea plate beneath northeast Taiwan: a new type of double seismic zone. *J. Geophys. Res.* 104, 1015–1033.
- Kao, H., Shan, S.-J., 2004. The source-scanning algorithm: mapping the distribution of seismic sources in time and space. *Geophys. J. Int.* 157, 589–594.
- Kao, H., Shan, S.-J., 2007. Rapid identification of earthquake rupture plane using Source-Scanning Algorithms. *Geophys. J. Int.* 168, 1011–1020.
- Kao, H., Wang, K., Chen, R.-Y., Wada, I., He, J., Malone, S., 2008. Identifying the Rupture Plane of the 2001 Nisqually, Washington, Earthquake. *Bull. Seismol. Soc. Am.* 98, 1546–1558.
- Kato, N., Seno, T., 2003. Hypocenter depths of large interplate earthquakes and their relation to seismic coupling. *Earth Planet. Sci. Lett.* 210, 53–63.
- Kawakatsu, H., 1985. Double seismic zone in Tonga. *Nature* 316, 53–55.
- Keleman, P., Hirth, G., 2007. A periodic shear-heating mechanism for intermediate-depth earthquakes in the mantle. *Nature* 446, 787–790.
- Kennett, B., 1991. IASPEI 1991 Seismological Tables. Research School of Earth Sciences, Australia National University, Canberra, Australia.
- Kennett, B., Engdahl, E., 1991. Traveltimes for global earthquake location and phase identification. *Geophys. J. Int.* 105, 429–465.
- Kirby, S., Stein, S., Okal, E., Rubie, D., 1996. Metastable mantle phase transformations and deep earthquakes in subducting oceanic lithosphere. *Rev. Geophys.* 34, 261–306.
- Kiser, E., Ishii, M., 2011. The 2010 Mw 8.8 Chile earthquake: Triggering on multiple segments and frequency-dependent rupture behavior. *Geophys. Res. Lett.* 38.
- Kiser, E., Ishii, M., 2012a. Combining seismic arrays to image the high-frequency characteristics of large earthquakes. *Geophys. J. Int.* 188, 1117–1128.
- Kiser, E., Ishii, M., 2012b. The March 11, 2011 Tohoku-oki earthquake and cascading failure of the plate interface. *Geophys. Res. Lett.* 39, doi:10.1029/2012GL051170.
- Kiser, E., Ishii, M., Langmuir, C., Shearer, P., Hirose, H., 2011. Insights into the Mechanism of Intermediate-Depth Earthquakes from Source Properties as Imaged by Back-Projection of Multiple Seismic Phases. *J. Geophys. Res.* 116.
- Kobayashi, K., Nakanishi, M., Tamaki, K., Ogawa, Y., 1998. Outer slope faulting associated with the western Kuril and Japan trenches. *Geophys. J. Int.* 134, 356–372.

- Konca, A., Avouac, J.-P., Sladen, A., Meltzner, A., Sieh, K., Fang, P., Li, Z., Galetzka, J., Genrich, J., Chlieh, M., Natawidjaja, D., Bock, Y., Fielding, E., Ji, C., Helmberger, D., 2008. Partial rupture of a locked patch of the Sumatra megathrust during the 2007 earthquake sequence. *Nature* 456, 631–635.
- Koper, K., Hutko, A., Lay, T., Ammon, C., Kanamori, H., 2011. Frequency-dependent rupture process of the 11 March 2011 Mw 9.0 Tohoku earthquake: Comparison of short-period P wave backprojection images and broadband seismic rupture models. *Earth Planets Space First Results of the 2011 Off the Pacific Coast of Tohoku Earthquake*.
- Koulakov, I., Sobolev, S., 2006. A tomographic image of Indian lithosphere break-off beneath the Pamir-Hindukush region. *Geophys. J. Int.* 164, 425–440.
- Kuge, K., Kase, Y., Urata, Y., Campos, J., Perez, A., 2010. Rupture characteristics of the 2005 Tarapaca, northern Chile, intermediate-depth earthquake: Evidence for heterogeneous fluid distribution across the subducting oceanic plate? *J. Geophys. Res.* 115, B09305.
- Lachenbruch, A., 1980. Frictional heating, fluid pressure, and the resistance of fault motion. *J. Geophys. Res.* 85, 6097–6112.
- Lay, T., Ammon, C., Hutko, A., Kanamori, H., 2010a. Effects of kinematic constraints on teleseismic finite-source rupture inversion: Great Peruvian earthquakes of 23 June 2001 and 15 August 2007. *Bull. Seismol. Soc. Am.* 100, 969–994.
- Lay, T., Ammon, C., Kanamori, H., Koper, K., Sufri, O., Hutko, A., 2010b. Teleseismic inversion for rupture process of the 27 February 2010 Chile (Mw 8.8) earthquake. *Geophys. Res. Lett.* 37, L13301.
- Lay, T., Ammon, C., Kanamori, H., Rivera, L., Koper, K., Hutko, A., 2010c. The 2009 Samoa-Tonga great earthquake triggered doublet. *Nature* 466, 964–968.
- Lay, T., Ammon, C., Kanamori, H., Xue, L., Kim, M., 2011a. Possible large near-trench slip during the great 2011 Tohoku (Mw 9.0) earthquake. *Earth Planets Space First Results of the 2011 Off the Pacific Coast of Tohoku Earthquake*.
- Lay, T., Yamazaki, Y., Ammon, C., Cheung, K., Kanamori, H., 2011b. The great 2011 off the Pacific coast of Tohoku (Mw 9.0) Earthquake: Comparison of deep-water tsunami signals with finite-fault rupture model predictions. *Earth Planets Space First Results of the 2011 Off the Pacific Coast of Tohoku Earthquake*.
- Lolli, B., Gasperini, P., 2006. Comparing different models of aftershock rate decay: The role of catalogue incompleteness in the first times after mainshock. *Tectonophysics* 423, 43–59.

- Lorenzo-Martin, F., Roth, F., Wang, R., 2006. Inversion for rheological parameters from post-seismic surface deformation associated with the 1960 Valdivia earthquake, Chile. *Geophys. J. Int.* 164, 75–87.
- Lorito, S., Romano, F., Atzori, S., Tong, X., Avallone, A., McCloskey, J., Cocco, M., Boschi, E., Piatanesi, A., 2011. Limited overlap between the seismic gap and coseismic slip of the great 2010 Chile earthquake. *Nature Geosci.* 4, 173–177.
- Loveless, J., Meade, B., 2010. Geodetic imaging of plate motions, slip rates, and partitioning of deformation in Japan. *J. Geophys. Res.* 115, B02410.
- Luyendyk, B., 1970. Dips of downgoing lithospheric plates beneath island arcs. *Geol. Soc. Am. Bull.* 81, 3411–3416.
- Ma, K.-F., Brodsky, E., Mori, J., Ji, C., Song, T.-R., Kanamori, H., 2003. Evidence for fault lubrication during the 1999 Chi-Chi, Taiwan, earthquake (Mw7.6). *Geophys. Res. Lett.* 30.
- MacAyeal, D., Okal, E., Aster, R., Bassis, J., Brunt, K., Cathles, L., Drucker, R., Fricker, H., Kim, Y.-J., Martin, S., Okal, M., Sergienko, O., Sponsler, M., Thom, J., 2006. Transoceanic wave propagation links iceberg calving margins of Antarctica with storms in tropics and northern hemisphere. *Geophys. Res. Lett.* 33, L17502.
- Madariaga, R., 1977. High-frequency radiation from crack (stress drop) models of earthquake faulting. *Geophys. J. Roy. Astron. Soc.* 51, 625–651.
- Maeda, T., Furumura, T., Sakai, S., Shinohara, M., 2011. Significant tsunami observed at the ocean-bottom pressure gauges at 2011 Off the Pacific Coast of Tohoku Earthquake. *Earth Planets Space First Results of the 2011 Off the Pacific Coast of Tohoku Earthquake.*
- Mai, P., Burjanek, J., Delouis, B., Causse, M., Cirella, A., Festa, G., Francois-Holden, C., Monelli, D., Uchide, T., Zahradnik, J., 2007. Earthquake Source Inversion Blindtest: Initial Results and Further Developments. paper presented at 2007 Fall AGU meeting, San Francisco, Ca.
- Mase, C., Smith, L., 1987. Effects of frictional heating on the thermal, hydrologic, and mechanical response of a fault. *J. Geophys. Res.* 92, 6249–6272.
- Masson, D., 1991. Fault patterns at outer trench walls. *Mar. Geophys. Res.* 13, 209–225.
- McCann, W., Nishenko, S., Sykes, L., Krause, J., 1979. Seismic Gaps and Plate Tectonics: Seismic Potential for Major Boundaries. *PAGEOPH* 117, 1082–1147.
- McGuire, J., Wiens, D., 1995. A double seismic zone in New Britain and the morphology of the Solomon plate at intermediate depths. *Geophys. Res. Lett.* 22, 1965–1968.

- McKenzie, D., Brune, J., 1972. Melting of fault planes during large earthquakes. *Geophys. J. Roy. Astron. Soc.* 29, 65–78.
- McMechan, G., Luetgert, J., Mooney, W., 1985. Imaging of earthquake sources in Long Valley caldera, California, 1983. *Bull. Seismol. Soc. Am.* 75, 1005–1020.
- Melosh, H., 1996. Dynamical weakening of faults by acoustic fluidization. *Nature* 379, 601–606.
- Meng, L., Inbal, A., Ampuero, J.-P., 2011. A window into the complexity of the dynamic rupture of the 2011 Mw 9 Tohoku-Oki earthquake. *Geophys. Res. Lett.* 38.
- Minoura, K., 2008. Quantitative analysis of tsunami by the Jogan earthquake. Report of Research Project, Grant-in-Aid for Scientific Research (B) 1.
- Mitsui, Y., Iio, Y., 2011. How did the 2011 Off the Pacific Coast of Tohoku Earthquake start and grow? Role of conditionally stable area -. *Earth Planets Space First Results of the 2011 Off the Pacific Coast of Tohoku Earthquake.*
- Moreno, M., Rosenau, M., Oncken, O., 2010. 2010 Maule earthquake slip correlates with pre-seismic locking of Andean subduction zone. *Nature* 467, 198–202.
- Motagh, M., Wang, R., Walter, T., Buergermann, R., Fielding, E., Anderssohn, J., Zschau, J., 2008. Coseismic slip model of the 2007 August Pisco earthquake (Peru) as constrained by wide swath radar observations. *Geophys. J. Int.* 174, 842–848.
- Nakahara, H., Sato, H., Nishimura, T., Fujiwara, H., 2011. Direct observation of rupture propagation during the 2011 off the Pacific coast of Tohoku, Japan, earthquake (Mw 9.0) using a small seismic array. *Earth Planets Space First Results of the 2011 Off the Pacific Coast of Tohoku Earthquake.*
- Nelson, P., Aoi, S., Hiroyuki, F., 2008. Rupture process of the 2007 Notohanto earthquake by using an isochrones back-projection method and K-NET/KiK-net data. *Earth Planets Space* 60, 1035–1040.
- Nielsen, S., Di Toro, G., Hirose, T., Shimamoto, T., 2008. Frictional melt and seismic slip. *J. Geophys. Res.* 113, B01308.
- Obara, K., Kasahara, K., Hori, S., Okada, Y., 2005. A densely distributed high-sensitivity seismograph network in Japan: Hi-net by National Research Institute for Earth Science and Disaster Prevention. *Rev. Scientific Instruments* 76, 021301.
- Ogawa, M., 1987. Shear instability in a viscoelastic material as the cause of deep focus earthquakes. *J. Geophys. Res.* 92, 13801–13810.

- Okada, Y., Kasahara, K., Hori, S., Obara, K., Sekiguchi, S., Fujiwara, H., Yamamoto, A., 2004. Recent progress of seismic observation networks in Japan: Hi-net, F-net, K-NET and KiK-net. *Earth Planet. Sci. Lett.* 56, xv–xxviii.
- Okal, E., Fritz, H., Synolakis, C., Borrero, J., Weiss, R., Lynett, P., Titov, V., Foteinis, S., Jaffe, B., Liu, P., Chan, I., 2010. Field survey of the Samoa tsunami of 29 September 2009. *Seismol. Res. Lett.* 81, 577–591.
- Olson, A., Apsel, R., 1982. Finite fault and inversion theory with applications to 1979 Imperial Valley earthquake. *Bull. Seismol. Soc. Am.* 72, 1969–2001.
- Ozawa, S., Nishimura, T., Suito, H., Kobayashi, T., Tobita, M., Imakiire, T., 2011. Coseismic and postseismic slip of the 2011 magnitude-9 Tohoku-Oki earthquake. *Nature* 475, 373–377.
- Pavlis, G., Das, S., 2000. The Pamir-Hindu Kush seismic zone as a strain marker for flow in the upper mantle. *Tectonics* 19, 103–115.
- Peacock, S., 2001. Are the lower planes of double seismic zones caused by serpentine dehydration in subducting oceanic mantle? *Geology* 29, 299–302.
- Peng, Z., Vidale, J., Ishii, M., Helmstetter, A., 2007. Seismicity rate immediately before and after main shock rupture from high-frequency waveforms in Japan. *J. Geophys. Res.* 112, B03306.
- Perfettini, H., Avouac, J.-P., Tavera, H., Kositsky, A., Nocquet, J.-M., Bondoux, F., Chlieh, M., Sladen, A., Audin, L., Farber, D., Soler, P., 2010. Seismic and aseismic slip on the central Peru megathrust. *Nature* 465, 78–81.
- Persh, S., Houston, H., 2004. Strongly depth-dependent aftershock production in deep earthquakes. *Bull. Seismol. Soc. Am.* 94, 1808–1816.
- Polet, J., Kanamori, H., 2000. Shallow subduction zone earthquakes and their tsunamigenic potential. *Geophys. J. Int.* 142, 684–702.
- Pritchard, M., Fielding, E., 2008. A study of the 2006 and 2007 earthquake sequence of Pisco, Peru, with InSAR and teleseismic data. *Geophys. Res. Lett.* 35, L09308.
- Raleigh, C., Paterson, M., 1965. Experimental deformation of serpentinite and its tectonic implications. *J. Geophys. Res.* 70, 3965–3985.
- Ranero, C., Morgan, J., McIntosh, K., Reichert, C., 2003. Bending-related faulting and mantle serpentinization at the Middle American Trench. *Nature* 425, 367–373.
- Ranero, C., Villasenor, A., Morgan, J., Weinrebe, W., 2005. Relationship between bend-faulting at trenches and intermediate-depth seismicity. *Geochem. Geophys. Geosyst.* 6.

- Rempel, A., Rice, J., 2006. Thermal pressurization and onset of melting in fault zones. *J. Geophys. Res.* 111, B09314.
- Reyners, M., Robinson, R., McGinty, P., 1997. Plate coupling in the northern South Island and southernmost North Island, New Zealand, as illuminated by earthquake focal mechanisms. *J. Geophys. Res.* 102, 15197–15210.
- Rhie, J., Dreger, D., Bürgmann, R., Romanowicz, B., 2007. Slip of the 2004 Sumatra-Andaman Earthquake from Joint Inversion of Long-Period Global Seismic Waveforms and GPS Static Offsets. *Bull. Seismol. Soc. Am.* 97, S115–S127.
- Rice, J., 2006. Heating and weakening of faults during earthquake slip. *J. Geophys. Res.* 111, B05311.
- Richards, P., 1976. Dynamic motions near an earthquake fault: a three-dimensional solution. *Bull. Seismol. Soc. Am.* 66, 1–32.
- Ricker, N., 1953. The form and laws of propagation of seismic wavelets. *Geophysics* 18, 10–40.
- Rietbrock, A., Scherbaum, F., 1994. Acoustic imaging of earthquake sources from the Chalfant Valley, 1985, aftershock series. *Geophys. J. Int.* 119, 260–268.
- Ringwood, A., 1975. *Composition and Petrology of the Earth's Mantle*. McGraw Hill, New York.
- Romesburg, H., 1984. *Cluster Analysis for Researchers*. Lulu Press, Northern California.
- Ruff, L., Kanamori, H., 1983. The rupture process and asperity distribution of three great earthquakes from long-period diffracted P-waves. *Phys. Earth Planet. Int.* 31, 202–230.
- Samowitz, I., Forsyth, D., 1981. Double seismic zone beneath the Mariana island arc. *J. Geophys. Res.* 86, 7013–7021.
- Satake, K., Namegaya, Y., Yamaki, S., 2008. Numerical simulation of the A.D. 869 Jogan tsunami in Ishinomaki and Sendai plains (in Japanese). *Katsudansou Kojishin Kenkyuu Houkoku* 8, 71–89.
- Sato, M., Ishikawa, T., Ujihara, N., Yoshida, S., Fujita, M., Mochizuki, M., Asada, A., 2011. Displacement Above the Hypocenter of the 2011 Tohoku-Oki Earthquake. *Science* 332, 1395.
- Savage, J., 1966. Radiation from a realistic model of faulting. *Bull. Seismol. Soc. Am.* 56, 577–592.

- Savage, J., 1969. The mechanics of deep-focus faulting. *Tectonophysics* 8, 115–127.
- Sawai, Y., Fujii, Y., Fujiwara, O., Kamataki, T., Komatsubara, J., Okamura, Y., Satake, K., Shishikura, M., 2008. Marine incursions of the past 1500 years and evidence of tsunamis at Suijin-numa, a coastal lake facing the Japan Trench. *The Holocene* 18, 517–528.
- Schmidt, M., Poli, S., 1998. Experimentally based water budgets for dehydrating slabs and consequences for arc magma generation. *Earth Planet. Sci. Lett.* 163, 361–379.
- Scholz, C., 2010. Large Earthquake Triggering, Clustering, and the Synchronization of Faults. *Bull. Seismol. Soc. Am.* 100, 901–909.
- Scholz, C., 2011. Large Earthquake Triggering, Clustering, and the Synchronization of Faults. *Bull. Seismol. Soc. Am.* 100, 901–909.
- Sekiguchi, H., Irikura, K., Iwata, T., Kakehi, Y., Hoshihara, M., 1996. Minute locating of faulting beneath Kobe and the waveform inversion of the source process during the 1995 Hyogo-ken Nanbu, Japan, earthquake using strong ground motion records. *J. Phys. Earth* 44, 473–487.
- Shinohara, M., Yamada, T., Nakahigashi, K., Sakai, S., Mochizuki, K., Uehira, K., Ito, Y., Azuma, R., Kaiho, Y., No, T., Shiobara, H., Hino, R., Murai, Y., Yakiwara, H., Sato, T., Machida, Y., Shinbo, T., Isse, T., Miyamachi, H., Obana, K., Takahashi, N., Kodaira, S., Kaneda, Y., Hirata, K., Yoshikawa, S., Obara, K., Iwasaki, T., Hirata, N., 2011. Aftershock observation of the 2011 off the Pacific coast of Tohoku Earthquake by using ocean bottom seismometer network. *Earth Planets Space First Results of the 2011 Off the Pacific Coast of Tohoku Earthquake*.
- Sibson, R., 1973. Interactions between temperature and fluid pressure during earthquake faulting A mechanism for partial or total stress relief. *Nature* 243, 66–68.
- Sibson, R., 1977. Kinetic shear resistance, fluid pressures and radiation efficiency during seismic faulting. *Pure Appl. Geophys.* 115, 387–400.
- Sibson, R., 1982. Fault zone models, heat flow, and the depth distribution of earthquakes in the continental crust of the United States. *Bull. Seismol. Soc. Am.* 72, 151–163.
- Simons, M., Minson, S., Sladen, A., Ortega, F., Jiang, J., Owen, S., Meng, L., Ampuero, J.-P., Wei, S., Chu, R., Helmberger, D., Kanamori, H., Hetland, E., Moore, A., Webb, F., 2011. The 2011 Magnitude 9.0 Tohoku-Oki Earthquake: Mosaicking the Megathrust from Seconds to Centuries. *Science* 332, 1421–1425.

- Sladen, A., Tavera, H., Simons, M., Avouac, J., Konca, A., Perfettini, H., Audin, L., Fielding, E., Ortega, F., Cavagnoud, R., 2010. Source model of the 2007 Mw 8.0 Pisco, Peru earthquake: Implications for seismogenic behavior of subduction megathrusts. *J. Geophys. Res.* 115, B02405.
- Smith, S., Knapp, J., McPherson, R., 1993. Seismicity of the Gorda plate, structure of the continental margin, and an eastward jump of the Mendocino triple junction. *J. Geophys. Res.* 98, 8153–8171.
- Starovoit, O., Yunga, S., Gabsatova, I., Chepkunas, L., 2002. Destructive earthquake in Afghanistan (Hindu Kush) on March 25, 2002. *Orfeus Newsletter* 4, 11.
- Stein, S., Wysession, M., 2003. *An Introduction to Seismology, Earthquakes, and Earth Structure*. Blackwell Publishing, Malden, Massachusetts.
- Suzuki, S., Kasahara, M., 1996. Unbending and horizontal fracture of the subducting Pacific Plate, as evidenced by the 1993 Kushiro-oki and the 1981 and 1987 intermediate-depth earthquakes in Hokkaido. *Phys. Earth Planet. Int.* 93, 91–104.
- Tibi, R., Bock, G., Estabrook, C., 2002. Seismic body wave constraint on mechanisms on intermediate-depth earthquakes. *J. Geophys. Res.* 107, 23.
- Uchida, N., Nakajima, J., Hasegawa, A., Matsuzawa, T., 2009. What controls inter-plate coupling?: Evidence for abrupt change in coupling across a border between two overlying plates in the NE Japan subduction zone. *Earth Planet. Sci. Lett.* 283, 111–121.
- Utsu, T., Ogata, Y., Matsu'ura, R., 1995. The centenary of the Omori formula for a decay law of aftershock activity. *J. Phys. Earth* 43, 1–33.
- Venkataraman, A., Kanamori, H., 2004. Observational constraints on the fracture energy of subduction zone earthquakes. *J. Geophys. Res.* 109, B05302.
- Vidale, J., Houston, H., 1993. The depth dependence of earthquake duration and implications for rupture mechanisms. *Nature* 365, 45–47.
- von Huene, R., Corvalan, J., Flueh, E., Hinz, K., Korstgard, J., Ranero, C., Weinrebe, W., 1997. Tectonic control of the subducting Juan Fernandez Ridge on the Andean margin near Valparaiso, Chile. *Tectonics* 16, 474–488.
- Wadati, K., 1929. Shallow and deep earthquakes. *Geophys. Mag.* 2, 1–36.
- Walker, K., Ishii, M., Shearer, P., 2005. Rupture details of the 28 March 2005 Sumatra Mw 8.6 earthquake imaged with teleseismic *P* waves. *Geophys. Res. Lett.* 32, L24303.

- Walker, K., Shearer, P., 2009. Illuminating the near-sonic rupture velocities of the intracontinental Kokoxili Mw 7.8 and Denali Mw 7.9 strike-slip earthquakes with global P-wave back projection imaging. *J. Geophys. Res.* 114, B02304.
- Wang, D., Mori, J., 2011a. Frequency-dependent energy radiation and fault coupling for the 2010 Mw8.8 Maule, Chile, and 2011 Mw9.0 Tohoku, Japan, earthquakes. *Geophys. Res. Lett.* 38.
- Wang, D., Mori, J., 2011b. Rupture Process of the 2011 off the Pacific Coast of Tohoku Earthquake (Mw 9.0) as Imaged with Back-Projection of Teleseismic P-waves. *Earth Planets Space First Results of the 2011 Off the Pacific Coast of Tohoku Earthquake.*
- Wark, D., Watson, E., 2000. Effect of grain size on the distribution and transport of deep-seated fluids and melts. *Geophys. Res. Lett.* 27, 2029–2032.
- Warren, L., Hughes, A., Silver, P., 2007. Earthquake mechanics and deformation in the Tonga-Kermadec subduction zone from fault plane orientations of intermediate- and deep-focus earthquakes. *J. Geophys. Res.* 112, B05314.
- Warren, L., Langstaff, M., Silver, P., 2008. Fault plane orientations of intermediate-depth earthquakes in the Middle America Trench. *J. Geophys. Res.* 113, B01304.
- Woodhouse, J., Dziewonski, A., 1984. Mapping the upper mantle; three-dimensional modeling of Earth structure by inversion of seismic waveforms. *J. Geophys. Res.* 89, 5953–5986.
- Wyss, M., Brune, J., 1967. The Alaska Earthquake of 28 March 1964: A Complex Multiple Rupture. *Bull. Seismol. Soc. Am.* 57, 1017–1023.
- Yoshida, Y., Ueno, H., Muto, D., Aoki, S., 2011. Source process of the 2011 Off the Pacific Coast of Tohoku earthquake with the combination of teleseismic and strong motion data. *Earth Planets Space First Results of the 2011 Off the Pacific Coast of Tohoku Earthquake.*
- Zeng, Y., Anderson, J., 1996. A composite source model of the 1994 Northridge earthquake using genetic algorithms. *Bull. Seismol. Soc. Am.* 86, S71–S83.
- Zhang, H., Zengxi, G., Ding, L., 2011. Three Sub-Events Composing the 2011 off the Pacific Coast Tohoku Earthquake (Mw 9.0) Inferred from Rupture Imaging by Back Projecting Teleseismic P Waves. *Earth Planets Space First Results of the 2011 Off the Pacific Coast of Tohoku Earthquake.*